Escape-Time Electrometry: High Precision Measurement of Electrical Charge on Single Molecules in Solution

---

Dissertation

zur

Erlangung der naturwissenschaftlichen Doktorwürde
(Dr. sc. nat.)

vorgelegt der

Mathematisch-naturwissenschaftlichen Fakultät

der

Universität Zürich

von

Francesca Ruggeri

aus

Italien

Promotionskommission

Prof. Dr. Madhavi Krishnan (Vorsitz)

Prof. Dr. Peter Hamm

Prof. Dr. Ben Schuler

Zürich, 2018

A Babbo e Mamma.
(In ordine alfabetico)

“Science, my boy, is made up of mistakes, but they are mistakes which it is useful to make, because they lead little by little to the truth.”.

Journey to the Center of the Earth
Jules Verne

Abstract

This thesis describes a new experimental methodology, the Escape Time Electrometry (ET*e*) approach, developed to measure the effective charge of single macromolecules in solution. This method is based on the Electrostatic Fluidic Trap technique [1, 2], previously used to confine the 3D location of nanometer sized objects in free solution, and relies on simple wide-field fluorescence detection.

Our single molecule trap is created in a fluid-filled gap between two charged walls. Nanoscale patterning of one of the surfaces leads to a modulation of the local electrostatic potential, creating a deep thermodynamic potential well for a like-charged entity. With ET*e* we measure the time that a charged molecule takes to leave the potential well, whose depth is linearly proportional to the effective charge of the molecule [3]. This technique can be applied to a variety of macromolecules, ranging from small DNA fragments to highly charged proteins, and used to measure them at the single-molecule level, in real time.

Different macromolecules can be measured simultaneously and distinguished by spectrally splitting their fluorescence emission signal [4]; by doing so, minute differences ($< 5\%$) between species can be easily detected and we can perform a fast, high throughput, "calibrated measurement", which requires minimum characterization of the system parameters.

We have further expanded the concept of Single-Molecule Electrometry in order to obtain a simultaneous measurement of hydrodynamic radius from the same escape-time trajectory [5]. Finally, tuning the geometry of the trapping cavity, we have been able to study molecules as small as single dye [6], increasing the dynamic range of the technique. This, combined with an unprecedentedly high measurement precision and extremely low amount (pM concentrations) of molecules required, makes ET*e* a great new tool for ultrasensitive, rapid structural studies on biological macromolecules in the fluid phase.

Die Kurzfassung

Die vorliegende Arbeit beschreibt die Fluchtzeitelektrometrie (Escape Time Electrometry, ET*e*) – eine neue experimentelle Methode zur Bestimmung der effektiven Ladung von einzelnen Makromolekülen in Lösung. Die Methode basiert auf der elektrostatischen Fluidfalle [1, 2], die bereits genutzt wurde, um die 3D-Position von nanometergrossen Objekten in Lösung zu ermitteln, und verwendet Fluoreszenz als Detektionsmechanismus.

Unsere Einzelmolekülfalle wird in einem flüssigkeitsgefüllten Spalt zwischen zwei geladenen Oberflächen generiert. Das lokale elektrostatische Potential wird durch Nano-Strukturierung einer dieser Oberflächen so verändert, dass ein tiefer thermodynamischer Potentialtopf für ein gleichgeladenes Objekt geschaffen wird. ET*e* misst die Zeit, die ein geladenes Molekül braucht, um den Potentialtopf zu verlassen. Die Tiefe des Potentialtopfes – und damit die Verweildauer in der Falle – ist linear proportional zur effektiven Ladung des Moleküls [3]. Wir zeigen, dass die Ladung einzelner biologischer Makromoleküle (DNA und stark geladene Proteine) damit in Echtzeit bestimmt werden kann.

Verschiedene Makromoleküle können im gleichen Experiment gemessen werden, indem ihr Fluoreszenzemissionssignal nach Wellenlänge gesplittet wird [4]. Auf diese Weise können kleine Ladungsunterschiede ($< 5\%$) zwischen verschieden

Spezies zuverlässig detektiert werden. Wir nutzen diese Präzision für eine schnelle Kalibrierung der Messzelle, die eine minimale Charakterisierung der Systemparameter erfordert.

Darüber hinaus haben wir das Konzept der Einzelmolekül-Elektrometrie um die gleichzeitige Messung des hydrodynamischen Radius des gefangenen Moleküls erweitert [5]. Weiterhin konnten wir durch Anpassung der Fallengeometrie sogar sehr kleine Objekte wie einzelne organische Farbstoffe einfangen, und den Dynamikumfang der Technik damit erhöhen [6]. Diese Eigenschaften, sowie die beispiellose Messpräzision und der extrem niedrige Probenverbrauch (pikomolare Konzentrationen), machen ET*e* zu einem vielversprechenden Werkzeug für die schnelle, ultra-empfindliche strukturelle Untersuchung biologischer Makromoleküle in Lösung.

List of Publications

Peer-reviewed publications included in this thesis:

- Entropic trapping of a singly charged molecule in solution
  Ruggeri F. and Krishnan M., *Nano Letters*, DOI: 10.1021/acs.nanolett.8b01011
- Spectrally resolved single-molecule electrometry
  Ruggeri F. and Krishnan M., *J. Chem. Phys.* 148 (2018) 123307
- Lattice diffusion of a single molecule in solution
  Ruggeri F. and Krishnan M., *Physical Review E* 96 (2017) 062406
- Single-molecule electrometry
  Ruggeri F. et al., *Nature Nanotechnology* 12 (2017) 488-495

Contents

1
Introduction

> "Research is what I'm doing when I don't know what I'm doing."
>
> ---
>
> *Wernher von Braun*

1.1 Studying Biomolecules in Solution

Studying the properties of biomolecules holds incredible significance in chemistry, biology and medicine. Understanding the function and structure of proteins or nucleotide strands has huge practical bioengineering relevance, allowing us to manipulate soft matter at the nanometer scale with application ranging from molecular motors [7, 8] and DNA scaffolds [9], to bio-transistors [10]. Biological entities like proteins are dynamic systems which may undergo large conformational changes to fulfil their function [11]. For enzymes, for example, activity and structure are deeply connected [12] and the ability to investigate their configuration can guide the design of ligand-protein docking process for drug delivery applications [13].

But what are the important parameters that define a biomolecule? For example we can study how *big* the molecule is, what is its *shape*, its *function* and under which conditions it is active. Local parameters such as pH, salt concentration, temperature or macromolecular crowding can affect the overall response [14].

Another important aspect of macromolecules, focus of this dissertation, is their *charge* in solution. Electrostatic interactions play an important role in biochemistry [15] and are responsible, for example, for protein solubility, complexes formation, selective ion transport or even crystallization [16]. As a matter of fact, on average a third of the aminoacids on the surface of a globular protein are charged [17]. Furthermore, high surface charge can impart increased stability against aggregation or precipitation: a recent work from Liu and collaborators has shown that supercharged mutants of Green Fluorescent Protein are characterized by unusual resilience to abrupt temperature changes [18]. Effective charge (discussed in the next section) and structure of a molecule in solution are quantities deeply related [19] and, as mentioned above, the 3D structure is a key parameter for predicting the molecule behaviour [20].

Over the years a number of characterization techniques have been developed to investigate different aspects of macromolecules. These methods include NMR, crystallography, spectroscopy, mass-spec and chromatography, to name only a few. These ensemble-averaging approaches usually necessitate high amounts of biomolecules ($\sim$ micrograms), a requirement that is often challenging to meet in the case of samples which are inherently difficult to express or purify (e.g. hydrophobic membrane proteins or toxic proteins).

At the single molecule level, the challenge is posed by the necessity of "capturing" a molecule for long enough time to perform, at all, a measurement. In solution, nanometer sized objects undergo fast thermal fluctuations, making it hard to detect them either optically or electrically (e.g. through a solid state nanopore [21]). Alternatively, single molecule studies of molecules tethered to a surface have explored fundamental molecular properties such as kinetics of protein folding [22, 23], and conformational changes in DNA strands [24, 25].

1.1.1 The Effective Charge of Biomolecules

The structural charge, q_{str}, of a biomolecule in solution is of trivial calculation, and corresponds to the sum of all the chargeable groups as a function of pH as follows:

$$q_{\mathrm{str}} = \sum_i \frac{z_i e}{1 + 10^{z_i(\mathrm{pH} - \mathrm{p}K_i)}} \tag{1.1}$$

here K_i is the negative logarithm of the acid dissociation constant, e is the elementary charge and $z_i = +1$ or -1 indicates the valence of a basic or an acidic group.

While the building blocks of proteins are neutral, negatively and positively aminoacids with various pK_{a}s, DNA owes its negative charge to phosphates groups on its backbone, which are very acidic (p$K_{\mathrm{a}} \sim 2$) and thus fully charged in physiological conditions. In this case, the number of structural charges simply correspond to the number of bases, plus any additional phosphate groups at the 5' ends.

A novel approach to calculating charge in solution, intended as an "*interaction charge*", was recently published by M. Krishnan [19] and includes two distinct phenomena, namely charge regulation and charge renormalization, which have been long studied theoretically. Both affect the molecular structural charge in solution, resulting in a reduced, "effective" charge, q_{eff}.

Charge regulation deals with an alteration of the charged state of a ionizable group, due to its surrounding in the molecular environment. For a molecule, immersed in an electrolyte and carrying identical ionizable groups on its surface, interaction among these solvent-exposed groups leads to a local non-zero surface electrical potential, ψ_0. Given constant chemical potential of the protons throughout the system, for high value of ψ_0 the local pH experienced by the groups will be different from the pH in the bulk, causing a departure of their degree of ionization, by a factor α_r [26]:

$$\alpha_r = \frac{1}{1 + 10^{z_i(\mathrm{pH} - \mathrm{p}K)} \exp(z_i e \psi_0 / k_{\mathrm{B}} T)} \tag{1.2}$$

Here k_{B} is Boltzmann's constants and T is the temperature of the system. This factor predicts significant regulation for example for compact, densely charged globular proteins in solution [19].

Charge renormalization, on the other hand, has been extensively modelled for various shape of charged entities, and deals with the non-linear charge screening due to the counterions in the surrounding electrolyte [27, 28].

A key length scale for this phenomenon is the Bjerrum length, distance upon with two charges within a medium of dielectric constant ϵ_m experience a $k_{\mathrm{B}}T$

worth of interaction. The Bjerrum length is defined as $l_{\mathrm{B,m}} = (e^2/4\pi\epsilon_m\epsilon_0 k_{\mathrm{B}}T)$ and is 7.14 Å, in water at 25° C. In the case of a long rod of linear constant charge density, b, (e.g. for DNA) this distance defines the degree of renormalization as $b/l_{\mathrm{B,m}}$.
It results that q_{eff}, in absence of regulation, is $\approx (b/l_{\mathrm{B,w}})q_{\mathrm{str}}$ [27, 29], with corrections for finite-size effects [30].
Double-stranded DNA has a charge spacing b of 1.7 Å, while for ssDNA $b \sim 4$ Å. For infinitely long nucleotide strands, the effective charge of dsDNA is expected to be roughly a quarter of its structural charge. It is worth noting that for ssDNA, given that the distance between bases is not clearly defined, a measurement of effective charge would directly yield the unknown parameter b.

While we have theoretical predictions of q_{eff}, this quantity has long been challenging to directly determine at the experimental level. Simple approaches like pH-titration, based to the reversible binding of protons and hydroxyls ions to the charged groups of the molecule of interest, only give qualitative results [31]. Capillary electrophoresis has also been implemented to measure charge ladders in solution, but the electrophoretic mobility response is typically at best linear with effective charge and tends to saturate for higher q_{eff} ranges [32] or even show a non-monotonic behaviour [33].

Given the limited scope of available experimental techniques, the goal of this thesis work has been to develop a novel method, capable to directly determine the effective charge of a molecule in solution with high precision, and on a single-molecule scale. This quantity, thus far elusive, can yield important informations about the molecule structure. The next section will focus on the general experimental methodology used.

1.2 Other Trapping Techniques

As mentioned at the beginning of this chapter, single molecule imaging methods, ranging from super-resolution microscopy to FRET (Förster resonant energy transfer) [34], often require immobilization of the molecule of interest to a substrate, in order to be able to observe it for long enough time. The immobilization scheme used however may introduce unwanted surface artifacts and some efforts are required in order to minimize interactions of the molecules with the substrate [35, 36]. To circumvent the need of surface immobilization altogether, and to be able to study molecule in their free-solution state, alternative approaches involving *single molecule trapping* have been developed over the years. To this end, in most cases an external field – e.g. optical [37, 38], electrical [39, 40], hydrodynamic [41] or thermophoretic [42] – is applied in order to confine the location of a nanometer sized object in solution. Importantly, the trapped object is still free to undergo thermal fluctuations. As well as imaging, the trapping principle has been also combined with electrical detection, for example in the context of nanopores [43, 44] or optical antennas [45].

1.3 The Electrostatic Fluidic Trap

Trapping techniques based on polarizability dependent external-field suffer from an unfavourable a^3 scaling of trap depth [46], where a is the size of the object, and thus often limit their range of applicability. It has also been reported that high external fields can be disruptive for small biological molecules [47]. Furthermore, feed-back based techniques [40] heavily relies on the ability to image and track the object of interest, often challenging for fast diffusing nanometer-sized entities.

The Electrostatic Fluidic Trap principle, first shown by Krishnan and collaborators [1, 2], relies of the electrostatic potential that naturally developes between two parallel plates in contact with aqueous solution, without any further field applied. The strength of the trap, in this case, depends weakly on the size of the object, while it scales strongly with the molecule effective charge – our measurable of interest. Recently we have applied it to molecule of charge magnitude ranging from 1 to 100e and size as small as a single fluorophore [6].

In our case, the electrostatic potential is due to the charging of two SiO_2 surfaces in contact with aqueous solution, which occurs via ionization/dissociation of the surface groups [48]. Recently, the same trapping concept has been also implemented with different surface coatings, such as negatively charged polymers [49] and cationic polyelectrolytes [50].

In order to maintain electroneutrality in the system, the surface charge is balanced in the solution by equal amount of counterions of opposite charge, partially absorbed to the surface in the so called Stern Layer, partially forming the diffuse electrical double-layer.

The distribution of counterions of valence z at any coordinate x is arranged according to the Boltzmann formulation:

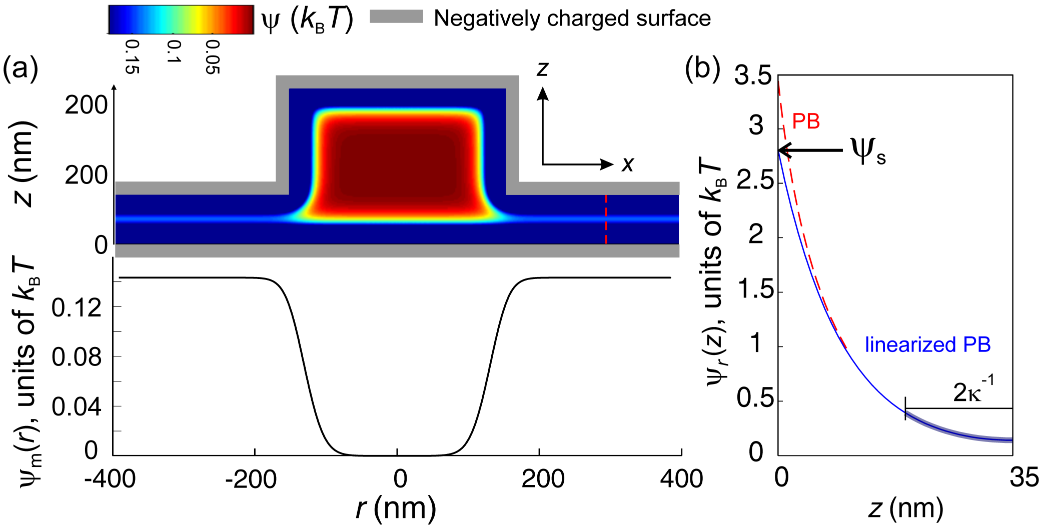

Figure 1.1: (a) Electrostatic potential, ψ calculation in the trapping nanostructure (cross-sectional view). The geometry is axis-symmetric. Solid grey indicates the charged silica surfaces. $\psi_{m,r}$ is the midplane potential at any radial coordinate, $r = \sqrt{x^2 + y^2}$. (b) Electrostatic full PB calculation across the red dashed line in (a) in the half-slit space are compared with the analytical linearized form of Eqn.1.8 (solid blue line), using an effective surface potential ψ_s. A charged object sampling the slit is typically confined within a middle region of extent $\sim 1 - 2\kappa^{-1}$ [6], where the linearized and full PB expression are in excellent agreement.

$$n = n_0 \exp(-ze\psi/k_\mathrm{B}T) \tag{1.3}$$

Where ψ is the electrostatic potential and n_0 is the number density of molecules at the surface.

Combining Eqn.1.3 with the following Poisson Equation for the net excess charge density ρ at any coordinate x:

$$\rho = zen = -\epsilon\epsilon_0(d^2\psi/dx^2) \tag{1.4}$$

we obtain the Poisson-Boltzmann (PB) equation in 1D,

$$d^2\psi/dx^2 = -(zen_0/\epsilon\epsilon_0)\exp(-ze\psi/k_\mathrm{B}T) \tag{1.5}$$

where ϵ is the dielectric constant of the medium and ϵ_0 the dielectric constant of vacuum.

This expression can be generalized for any aqueous electrolyte containing different types of ions i of valency z_i, as long as the total ionic number density at any point x is taken in account as $\sum n_{xi}$ [48].

The PB equation simplifies for a 1:1 electrolyte (in 3D) to:

$$\nabla^2\psi = \frac{k_\mathrm{B}T}{e}\kappa^2 \sinh(e\psi/k_\mathrm{B}T) \tag{1.6}$$

Where κ is the inverse Debye length. $\kappa^{-1} = \sqrt{\epsilon_\mathrm{w}\epsilon_0 k_\mathrm{B}T/2cN_\mathrm{A}e^2}$ is typically 10-30 nm in our work. N_A is Avogadro's number, $\epsilon_\mathrm{w} = 78.5$ the dielectric constant of water and c is the bulk salt concentration in the experiment, expressed in moles per liter.

For potential lower than 25 mV, PB is well approximated by the linearized Debye-Hückel expression:

$$\nabla^2\psi = \kappa^2\psi \tag{1.7}$$

Furthermore, in the case of flat surfaces, the electrostatic potential in 1D can be approximated by $\psi = \psi_s exp(-\kappa x)$.

We essentially exploit the electrostatic potential described so far as follows: if a – negatively – charged object is placed between two close – negatively – charged surfaces of gap $2h$, it will be repelled by both surfaces and experience a potential minimum at the half slit, h, resulting in a confinement in that dimension. By creating a local indentation (the pocket) of depth, d, and radius, R, the electrostatic potential is modulated also in the (x, y) plane, creating effectively a thermodynamic potential well (Fig. 1.1a), which confines the position of the test object in 3D.
The electrostatic potential in z (Fig. 1.1a) far away from the charged surfaces at any radial location in the slit, can be approximated by two overlapping exponentially decaying functions [51]:

$$\psi_r(z) = \psi_s[\exp(-\kappa z) + \exp(-\kappa(2h - z))] \tag{1.8}$$

Figure 1.1b compares the result of a finite-element calculation of the potential from Eqn.1.6 with the linearized version of Eqn.1.8. The single pK charge regulation model for silica [52], with pK = 9.5 and chargeable group density $\Gamma = 8e/\mathrm{nm}^2$ (see Chapter 2.2.3), corresponds to an effective surface potential $\psi_s = 2.8k_\mathrm{B}T$.
The midplane potential ψ_m represents the electrostatic barrier per unit of charge and according to Eqn.1.8 is espressed by:

$$\psi_m = 2\psi_s \exp(-\kappa h) \tag{1.9}$$

assuming that the potential minimum in the pocket region is zero. The midplane potential can be tuned by means of κh in order to increase the trap depth [3]. The total electrostatic free-energy for a molecule of charge q_eff is thus given by $q_\mathrm{eff}\psi_\mathrm{m}$ [19].

1.3.1 First Steps Toward Trapping and Studying a Small Molecule: Quantum Dots

The initial aim of this PhD project has been to use the Electrostatic Fluidic Trap technique – previously applied to nanoparticles of $\sim$ 20 nm in size and lipid vesicles [1, 2] – for studying smaller and lesser charged molecules. As a first step, we optimized the experimental conditions. We have increased the midplane potential by working in a regime of $\kappa h \sim 4$ and using a high pH buffer, suited for biomolecules (1 mM Tris, pH $\sim$ 8.8), which also results in

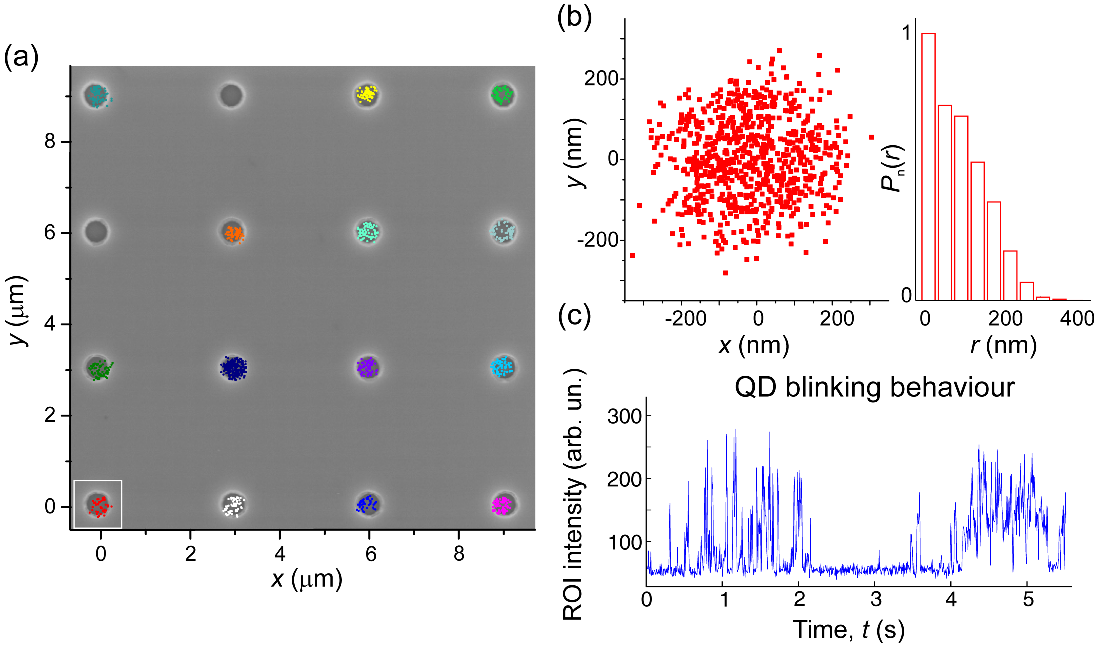

Figure 1.2: (a) The panel depict the (x, y) coordinates of 14 Quantum Dots trapped for 24 hours and monitored once every minute. The individual scatterplots are overlayed over an Scanning Electron Microscopy (SEM) image of the patterned surface. (b) The bottom left scatterplot in (a) is presented together with the normalized radial position probability distribution, $P_\mathrm{n}(r)$ of the particle. (c) The plot presents the fluorescence intensity fluctuations of a trapped Quantum Dot over time, in a separate experiment in which we imaged the particle with higher time resolution. The blinking behaviour observed is typical of a single emitter [56].

a higher surface charge for the $\mathrm{SiO_2}$ nanoslit walls, whose $\mathrm{p}K_\mathrm{a}$ is estimated as $\sim 7.5-9.5$ [53, 54, 55]. We patterned nanoslits of 5-20 µm in width with circular indentation of $R = 150-300$ nm and $d = 100-300$ nm, creating pocket lattices of regular pitch $\lambda \approx 1-2$ µm. In order to achieve the desired low κh conditions, we mostly worked with channel heights, $2h \sim 70$ nm. By doing so, we have been able to stably trap biomolecules ranging from small DNA fragments, proteins and even individual fluorophores carrying down to a single charge.

Our first result of stable trapping of a small, weakly charged objects was achieved studying Fluorescent Nanocrystal (Trilite™ Cytodiagnostic, emission = 575 nm) which are $\sim$ 6 nm in diameter and are functionalized with approximately 25 carboxylic acid group per particle, thus reminiscing in both size and charge of a small protein. In particular, we have managed to trap and track the position of few trapped Quantum Dots over the course of 24 hours (Fig.1.2). Achieved this first milestone, we have focused our efforts to develop a new method to precisely measure the effective charge of trapped entities.

Charge measurement of passively trapped nanoparticles was shown by Mojarad and Krishnan in previous work [2]. This experimental approach relied on 3D tracking of confined gold nanospheres in order to infer the trap stiffness $k \propto q_{\text{eff}}$. However, the relationship between measured stiffness and effective charge, which is linear and tend to saturate for high q_{eff}, only offers limited precision and hinges on careful localization of the object. In the case of weak emitters with limited photon budget, such as fluorescently labelled biomolecules, tracking cannot be achieved with the required nanometer precision for an extended period of time.

Our recently developed Escape-Time Electrometry (ET*e*) approach sidesteps the need of tracking and uses a telegraphic "on-off" approach (see Chapter 4) which works for Signal-to-Noise Ratio (SNR) down to ~ 3. Importantly, with ET*e* we measure a quantity, the escape time t_{esc}, which depends exponentially on the molecule charge, yielding unprecedented precision and capability of distinguishing minute differences between molecular species.

1.4 The Escape-Time Electrometry Approach

In brief, the ET*e* approach consists in measuring the time that a charged molecule takes to leave our geometry-induced thermodynamic potential, once first captured: this is the so-called escape-time, t_{esc}.

A molecule undergoing Brownian motion will reside in a trap of depth W for a time, t_{esc}, given by Kramers' analytical expression [57]:

$$t_{\text{esc}} = t_{\text{r}} \exp(W/k_{\text{B}}T) \tag{1.10}$$

where t_{r} is the position relaxation time of the molecule, a quantity that depends on the diffusion coefficient, $D = k_{\text{B}}T/6\pi\eta r_{\text{H}}$, of the molecule and the geometry of the trapping lattice. Here r_{H} is the molecule hydrodynamic radius and η is the viscosity of the medium. In essence, this quantity roughly represents the

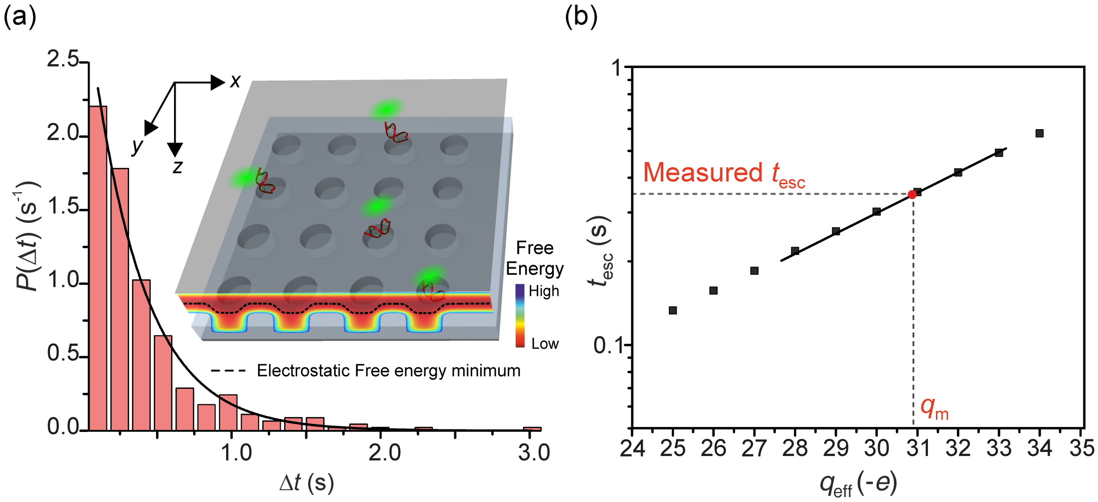

Figure 1.3: Figure adapted from Ref.[3] (a) Escape time probability distribution $P(\Delta t)$, where Δt is the duration of an escape event, obtained monitoring an electrostatic landscape of traps. The inset shows a schematic of the trapping device. The molecules, which carry two fluorophores, give a high fluorescence signal when confined within a trap. The free energy minimum profile is indicated by a black dashed line. (b) t_{esc} is readily converted into a measurement of effective charge, q_{m}.

time a particle would take to diffuse across a distance corresponding to the width of the well, in absence of any thermodynamic potential.
In turn the well depth W is function of the molecule effective charge as follows:

$$W = q_{\text{eff}}\psi_{\text{m}} + f \tag{1.11}$$

Here ψ_{m} is the electrostatic potential minimum in the slit, described above, and f is the contribution to the well depth due to the spatial fluctuations in z of the molecule, which is mostly entropic in origin. This quantity can be tuned by varying the physical depth of the trapping nanostructure [6] and it's typically $\sim 30\%$ of the total well depth.

A fluorescently-labelled molecule or radius $\sim$ 5 nm, monitored with wide-field microscopy (see Chapter 3), will spread its signal over an area of a $\sim$ 4 μm^2 during an observation time of a few milliseconds, when freely diffusing: in these case, its signal is likely be lost in the background [5]. On the other hand, when the molecule gets captured in any of the traps in the lattice, its intensity is confined within a much tighter area, comparable with the Point Spread Function (PSF) size of the imaging system, giving rise to an higher signal within a Region-Of-Interest (ROI) centered around the occupied pocket (see Details in Chapter 4). When the molecule escapes due to thermal fluctuations, returning in the "field-free" area or getting captured in a neighbouring trap, the intensity within the ROI decreases again. The duration of the intensity bursts thus correspond to the duration of the trapping events, or hops, which follow an exponentially decaying probability distribution and can be averaged to obtain the mean escape-time t_{esc} (Fig. 1.3a).

The measured timescale is then converted into a measured welldepth – and thus q_{eff} – by means of a Brownian Dynamics simulation (Fig.1.3b). It is worth pointing out that the exponential relationship between escape time and charge allows unprecedented precision in the determination of q_{eff}. To give a rough estimate, for a modest number of event $N = 100$, the expected error on q_{eff} is lower than 2% [3] (See Section 3.3 for details). It is clear however that accurate determination of this quantity depends on the knowledge of the midplane potential, ψ_{m} (Eqn. 1.11), since they affect the measured W in a multiplicative fashion. In turn this quantity, expressed by Eqn.1.9, is function of the salt concentration ($\kappa \propto \sqrt{c}$), and channel height ($2h$) as well as the SiO_2 surface potential (ψ_s). All these parameters can be accurately measured or estimated, as illustrated in the next Chapter.

1.5 Dissertation Outline

Chapter 2 describes how we fabricate the nanofluidic trapping device and thoroughly characterize it.

Chapter 3 illustrates our simple optical setup and describes the experimental protocol of an ET*e* experiment.

Chapter 4 shows our data analysis procedure and the key features that need to be captured by a Brownian Dynamics simulation in order to correctly convert the experimental t_{esc} into a measured charge value.

Chapter 5 introduces the our first published application of ET*e*, the paper *Single-molecule electrometry* [3], in which we measure the effective charge of a variety of molecules, distinguish between charge mutants of a small protein and monitor the charge of a single molecule in real-time.

In **Chapter 6** we introduce the concept of *Spectrally resolved single-molecule electrometry* [4]. With the aid of a second excitation wavelength, we can image and measure at the same time two populations of molecules, each labelled with a different dye. This allow us to perform a “calibrated” experiment, in which one molecule – of known charge – is used as standard, circumventing the need of knowing the midplane potential and substantially improving the accuracy of the method.

Chapter 7 expands on the concept of configurational entropy in the trap, effectively captured by the quantity f in Eqn.1.11. By increasing this quantity, by means of effectively making the trapping nanostructure geometrically deeper, we are able to trap a small singly charged molecule and to improve the dynamic range of the method, as described in our recently published work *”Entropic trapping of a singly charged molecule in solution”*.

Chapter 8 introduces the finding of our paper *”Lattice diffusion of a single molecule in solution”* [5]. Here we explain how, by expanding the concept of single-molecule ETe, we can look at a single molecular trajectory determine not only charge, but also the hydrodynamic radius of the object.

Finally **Chapter 9** describes future potential applications of ETe.

2

Device Fabrication and Characterization

> “In One Dimensions, did not a moving Point produce a Line with two terminal points? In two Dimensions, did not a moving Line produce a Square with four terminal points? In Three Dimensions, did not a moving Square produce - did not the eyes of mine behold it - that blessed being, a Cube, with eight terminal points?
>
> ---
>
> *Flatland*
> *Edwin A. Abbott*

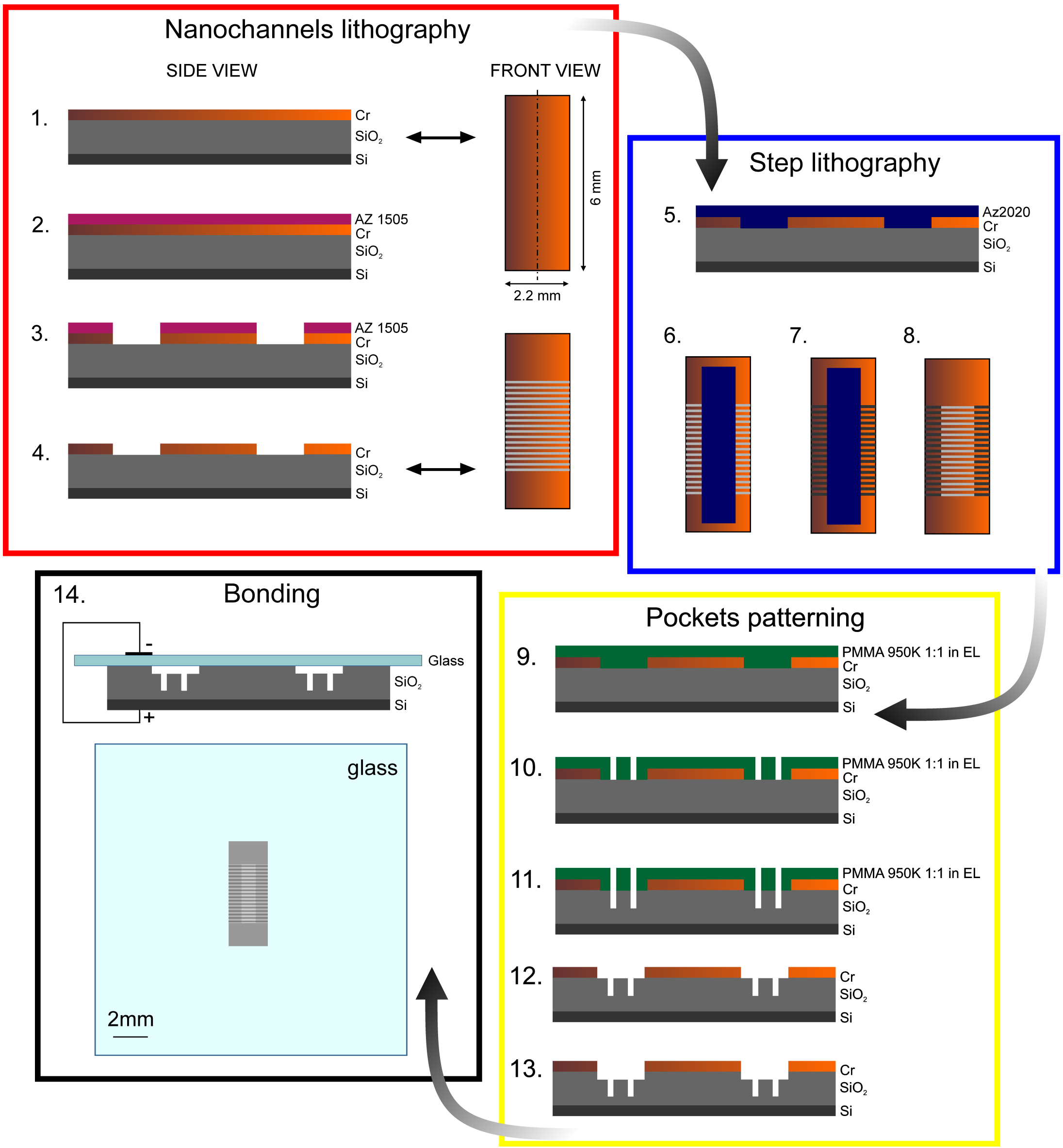

Figure 2.1: Fabrication flowchart: the 4 panels represent the main stages of fabrication, described in details in the main text. We typically pattern substrates of 20x20mm in size. Each substrate gives approximately 20 individual ET*e* devices.

2.1 Fabrication of Microfluidic Devices

The fabrication process of the ETe devices used for trapping and studying single molecules is based on standard silicon nanofabrication techniques. The protocol flowchart, depicted in Fig. 2.1, is described below (for further details see also Appendix).

- 1. The starting point is a silicon wafer with 400 nm of thermal oxide. The wafer is covered by a Chrome layer 40 nm thick, deposited using an Electron Beam Evaporator.
  2. The wafer is covered by the positive resist AZ1505, span to a thickness of approximately 300 nm and patterned with DUV lithography in order to define the nanoslits.
  3. The exposed area of the Chrome Layer are then etched using chemical Chrome Etch. The Chrome acts as a hard mask so that the underlying silicon oxide can be etched using Reactive Ion Etching (RIE) during Step 13. The channels typically have a width, w_c, ranging from 5 to 20 µm, alternating with supporting walls of the same width.
  4. The residual resist is removed from the substrate.

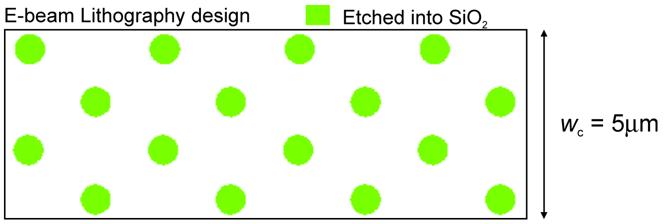

Figure 2.2: Design of lattice of trapping nanostructures pockets for E-beam lithography. The circular features, in green, will be etched in the silica substrate.

In order to avoid collapsing of the nanoslits (discussed later in Section 2.2.1) as well as facilitating the entry of the molecules in the bonded device (see Chapter 3), we create a deeper region along the sides of each device, that we refer to as the “Step Region” (Fig. 2.4).

- 5. The substrate is span with the negative resist AZ2020, to a thickness of approximately 2 µm.
  6. This resist protects the middle $\sim$ 600 µm of the devices (later patterned with trapping nanostructures).
  7. The exposed area of the slits is etched with RIE to a depth, $2h_{\mathrm{s}}$ of $\sim$ 250 nm in order to create a the Step Region.
  8. The residual resist is cleaned off.

  The cleaned substrate is now ready to be patterned with nanostructures, typically of circular shape.

- 9. The substrate is span with a resist suitable for Electron Beam Lithography (E-beam), namely PMMA 950K diluted 1:1 in Ethyl Lactate. The thickness of the span resist is $\sim$ 100 nm.
  10. Circular pockets of typical radius, $R = 150 - 300$ nm are patterned in a regular arrangement in the middle area of the device with E-beam. We typically pattern an area of 300x100 µm, with $\sim$ 2000 pockets per device.
  11. After developing the resist, the substrate is etched in the RIE to define the pocket depth, d.
  12. The substrate is stripped of any residual resist.
  13. Final the channel depth of the middle region, $2h$ is defined with a further RIE etch. The Chrome layer, patterned previously, protects the area in between channels, which acts as supporting walls (Fig. 2.4).

- 14. The Chrome layer is removed, and the substrate is ready to be diced in individual devices of typical size 6x2.2mm. Each device is anodically bonded to a small glass substrate. During bonding, the device is placed on a hotplate at 350°C and 1400 V are applied between the glass and the Si- SiO_2 device for 3 minutes. The combination of high voltage and heat creates a covalent bond at the interface.

The high electrical field created in the nanoslits during bonding can be strong enough to pull the glass, made more fluid by the high temperature, and for the nanostructure to collapse (see Section 2.2.1).
Figure 2.3 shows the dimensions of a bonded device.

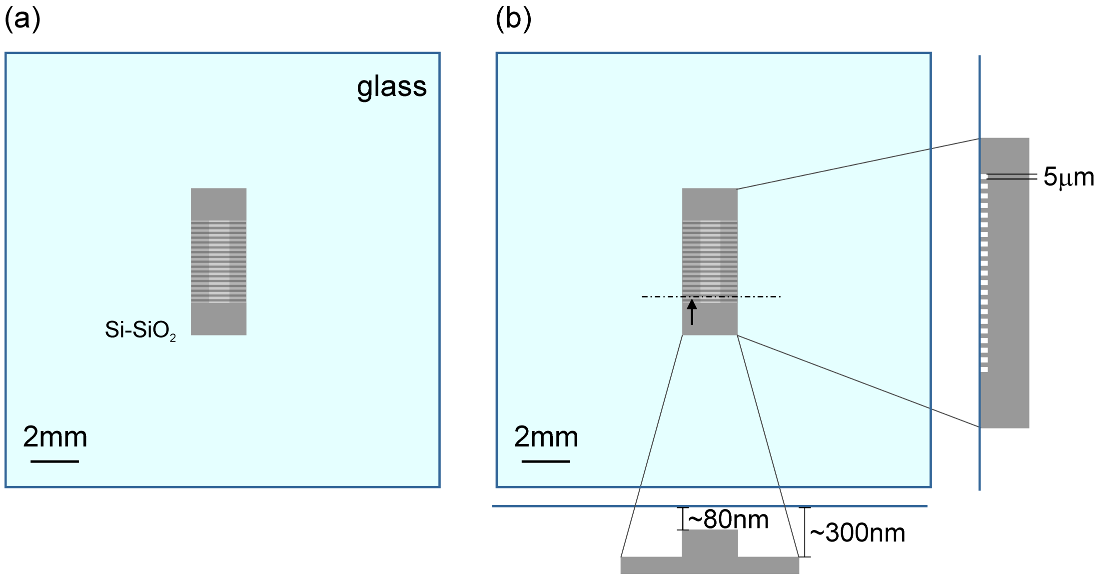

Figure 2.3: (a) Schematic of a bonded device. (b) The cross-section view shows the typical channel width (5 µm). The middle region of the device, which is patterned with circular indentations, is shallower than the "Step Region".

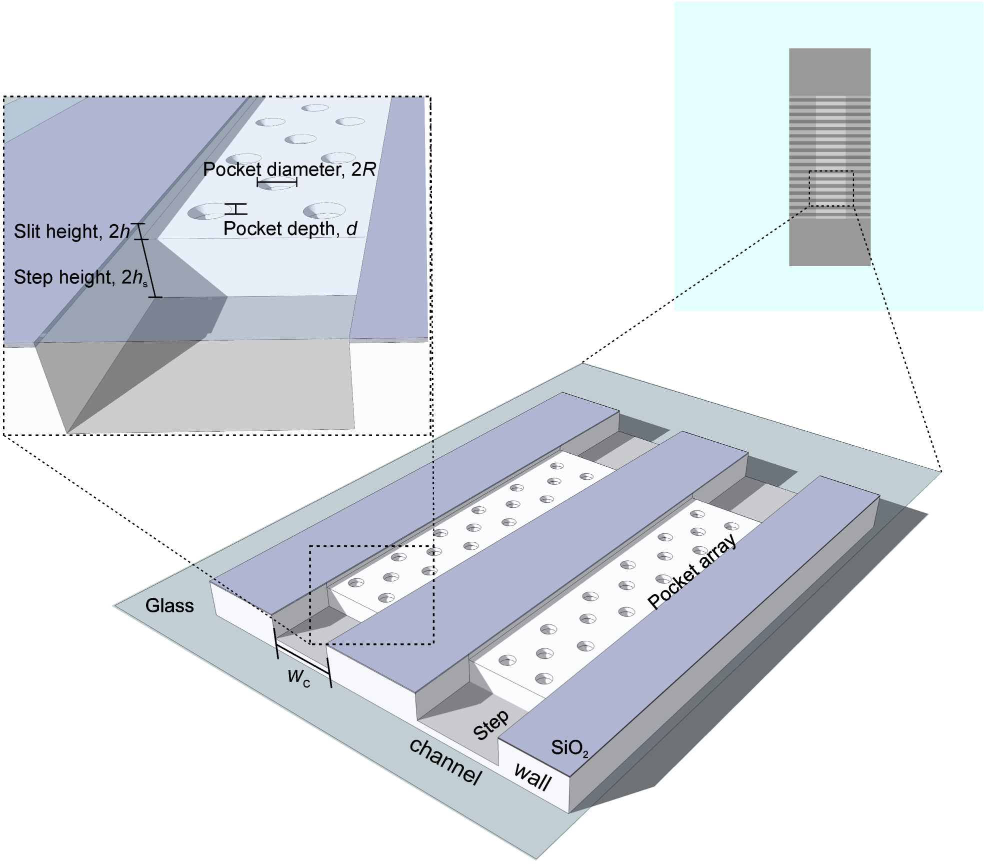

Figure 2.4: The 3D schematic presents a small section of a bonded device, in which the main geometrical parameters are indicated. The inset indicates the important features of the circular indentations, such as the radius R, the pocket depth d, and the slit height, $2h$. The Step Region is typically etched further, to a depth $2h_s \sim 250$ nm.

2.2 Characterization

2.2.1 Channel height

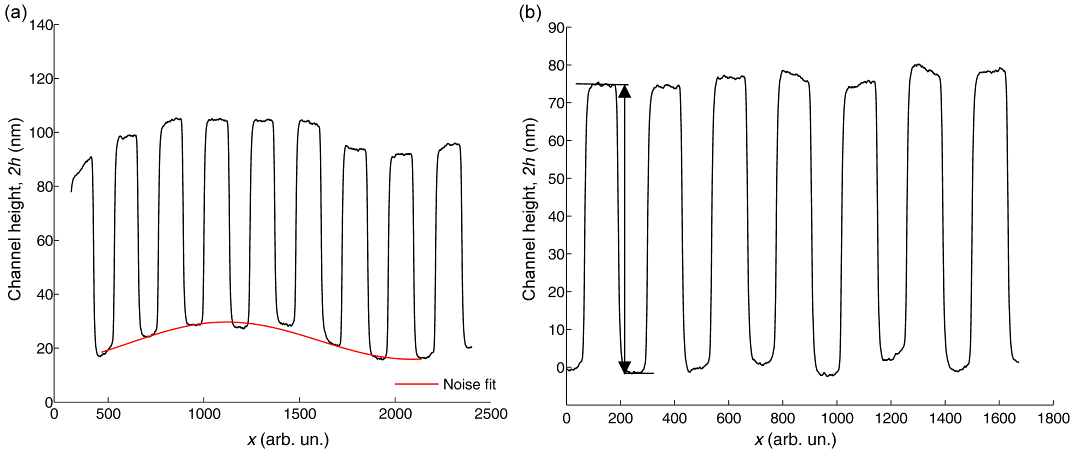

Figure 2.5: (a) A profilometer scan of the channels. (b) The underlying noise is fit to a sinusoidal shape and subtracted from the trace. The channel height, $2h$, is defined as the average distance from the top of the walls to the channels bottom.

Before bonding, every devices is mapped using a Profilometer (Dektak Profilometer, Bruker) in order to precisely determine the average channel height, $2h$, in the region patterned with pockets. We usually scan a 300x100 µm area, with 20 scan lines and at a scanning speed of 5 µm/s. As discussed in Chapter 3, the channel height variability is the dominant source of error in an ETe measurement. Each scan line is then analyzed separately.

Figure 2.5 shows a representative profilometer scan. The underlying noise is most probably an artifact due to how the sample is mounted in the instrument, rather than to a real etch heterogeneity. To eliminate this noise, every scan is fit to a sinusoidal function and baseline-subtracted: $2h$ is then defined as the average difference in height from the bottom and the top of a given channel (see Figure 2.5b), averaged over all channels and scans. We find that the typical height Standard Deviation, S.D., is 1-2% of the total height, which corresponds to 1 nm for $2h = 70$ nm, typical in our experiments.

This value however probably overestimates the real height variability across a given device, which is supposedly much smaller when using an RIE etch [4] and is estimated to be roughly $\sim$ 0.3 nm across a millimeter-sized substrate.

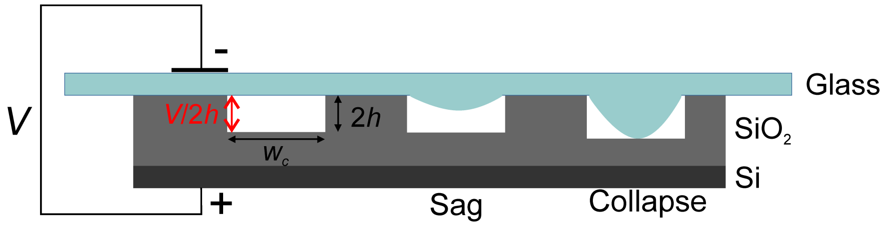

Figure 2.6: Schematic of the bonding configuration. A voltage V is applied across the device, developing an Electric Field at the gap, $V/2h$, which combined with high temperature can induce sag or complete collapse of the glass substrate.

In fact, we register the same height variability even when simply repeating a profilometer scan multiple times over the same channel: this indicates that the recorded heterogeneity is mostly due to an instrumental imprecision, which defines how accurately we can know the channel height in an absolute sense.
Even though we are able to determine the channel height before bonding with nanometer precision, it is not clear whether the same gap height will be maintained upon bonding. In fact, the use of high temperature, combined with the high electric field which develops at the interface, are known to create either sag or complete collapse of the glass substrate [58].
Some efforts have been dedicated to being able to create narrow gaps (< 100 nm) for nanofluidics application [59]. It has been previously shown that the expected degree of collapse for an anodically bonded slit is function of its width, height, and the electrical field developed at the gap, as well as the dimension of the supporting walls [60] (Fig. 2.6).

We have ourselves investigated this effect by comparing the slit height measured with profilometer before bonding, with a direct observation of the gap – after bonding – via cleavage of the device. By doing so, we could study the channels cross-section in SEM, as depicted in Figure 2.7. As a first step, we indented the bonded devices with a diamond scriber and then proceeded to separate the two halves with a blade, applying pressure through the middle. We then sputter-coated the two halves of the device with Au/Pd for enhancing contrast in SEM. By varying temperature, voltage and duration of the bonding, we observed the effects on channel of different widths (w_c = 5-100 µm).
We have found that bonding for relatively short times (3 min), under fairly low temperature (350° C) and high voltage (1400 V), gives the most reproducible results. Channels of $w_c = 100\,\mu\text{m}$ always appear fully collapsed for $2h = 200$ nm under these bonding conditions. 20 µm channels appear slightly sagged, while

(a)

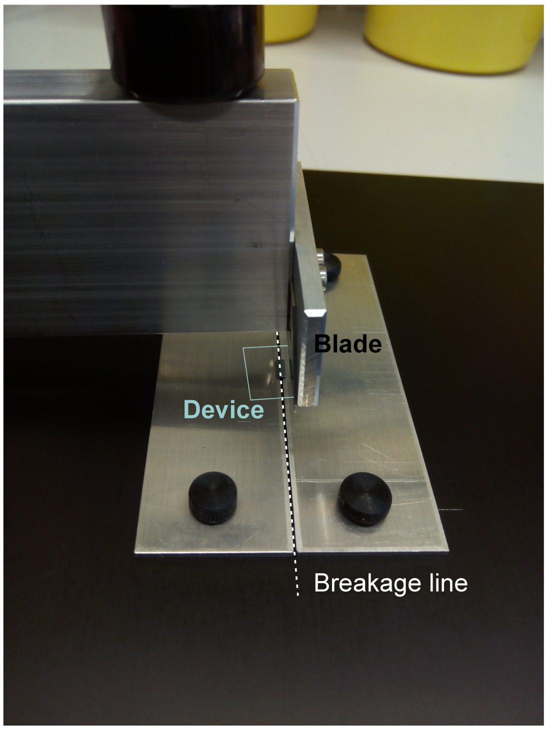

(b)

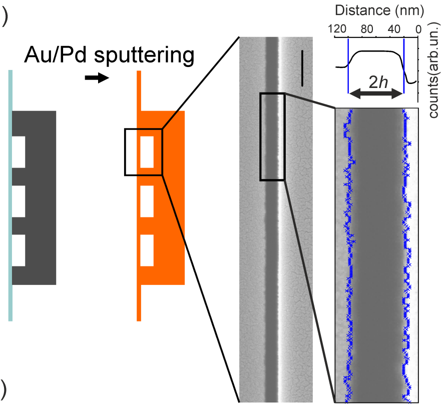

(c)

PROFILOMETER, 2*h* (nm)	SEM, 2*h* (nm)
66.6±0.7	66.2± 1.1
68.8±1.0	68.2±1.1
81.7±1.0	82.1±2.3
79.9±0.9	82.4±1.1

Figure 2.7: (a) A home-made cleaving apparatus is used to break the devices in half, perpendicular to the channel direction, after bonding. A blade is connected to a metallic arm that can be used in order to impart enough force to break the chip (highlighted in light blue) cantilevered between two metallic slides, across the breakage line (dashed white line). (b) The two halves of the device are then sputter-coated with Au/Pd to enhance contrast in SEM. We can directly image the cross-section of the channels and compare the gap, $2h$, with the value obtained by profilometer measurements. (c) The table summarizes a few representative results, showing that the channel height is not affected by the bonding procedure for $w_c = 5$ µm and gaps $2h > 65$ nm.

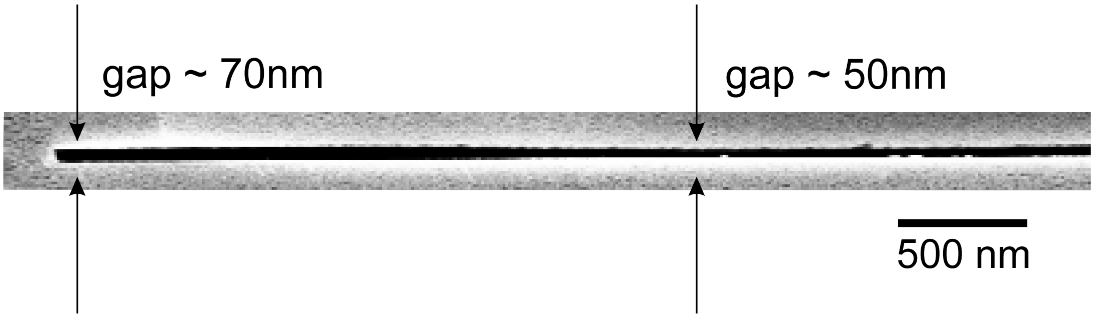

Figure 2.8: An SEM image of the cross section of a 10 µm semi-collapsed channel. The profilometer measured height was 73±1nm. The middle of the slit is clearly narrower than the left edge.

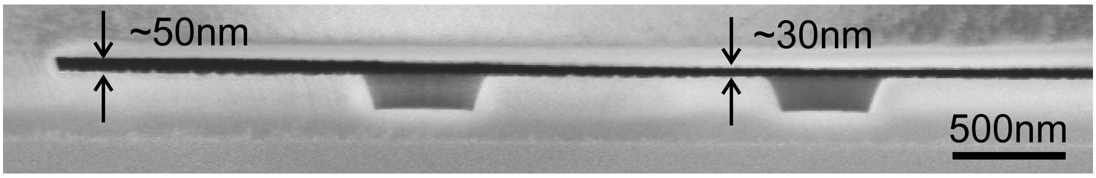

Figure 2.9: An SEM image of the cross section of a 5 µm partially collapsed channel. The cross-section of two trapping nanostructure is also visible. The profilometer measured height was 55±1nm in this case. Clearly the whole structure has sagged, particularly in the center.

10 µm slits typically survive. For shallower channel heights, close to our range of interest ($\sim$ 70-80 nm), even 10 µm channels show signs of severe sag (Fig. 2.8). Finally we have found that narrower channels of 5 µm in width can withstand the bonding procedure without any sign of collapse for a large range of height (65 nm and above), as shown in Fig. 2.7c and Fig. 2.11, and were in fact used for vast majority of our ET*e* experiments. For narrower gaps, even 5 micron channels tend to collapse as shown in Fig. 2.9.

We found that the presence of sag and collapse can be also assessed by fluorescence imaging with our wide-field microscopy setup. When exciting the area of the devices with a 532 nm laser, we find high fluorescence in the wall region, bonded to the glass. This fluorescence is broad, red-shifted, and partially overlaps with the fluorescence of the dye used to label our macromolecules (ATTO 532). In the channels, instead, usually the auto-fluorescence signal is weak and can be attenuated using a short pass filter, cutting emission above 694 nm (de-

tails about the fluorescence setup can be found in Chapter 3. This ensures high SNR (~ 10) for double-labelled fluorescent molecules trapped in the patterned slits.
Interestingly, in the case of severe sag, the auto-fluorescence in the channel region dramatically increases, as shown in Figure 2.10b. Here the spurious signal from the device is high and uniform across both channel and wall regions – so much so that the position of the pockets, etched deeper, is clearly visible.

Figure 2.11 summarizes the regime of slit height in which 5 micron channels have been studied, and survive bonding. The sag behaviour limits, for now, the range of midplane potentials that can be explored reproducibly in a ET*e* measurement, as discussed later in Section 5.3.

2.2.2 Trapping Nanostructures

The shape of the pockets patterned with E-beam (Fig. 2.12) is characterized via both Atomic Force Microscopy (AFM)(Fig. 2.13) and direct imaging of both the top view and cross-section in SEM (Fig. 2.14). We have found both shape and depth of the pockets to be very homogeneous across the patterned area (Fig. 2.12b).

From the SEM cross-sectional view (Fig. 2.14a, bottom panel) it is clear that pockets have a slightly tapered shape, as previously reported in literature for similar etching recipe [61]. In order to obtain a straighter etch, we have verified that the usage of Argon gas, as well as CHF_3, is a good etching strategy (Fig. 2.14b). In this case, however, it is necessary to use a thicker resist layer; for example non diluted PMMA gives a 4-fold increase in thickness. The selectivity of the RIE etch in the case of CHF_3 alone is 1.5:1 for SiO_2:PMMA, while is about 1:1 when including Argon.

Finally, looking closely at the cross-section of a pocket etched without Argon, we also noted a slight micro-trenching, as reported in literature for etching of small cavities with chlorine gas [62]. This phenomenon, due to reflection of ions by the sides of the patterned cavity, creates a slightly deeper etch (by $\sim$6% in our case) at the very edges, as shown in Fig. 2.15.

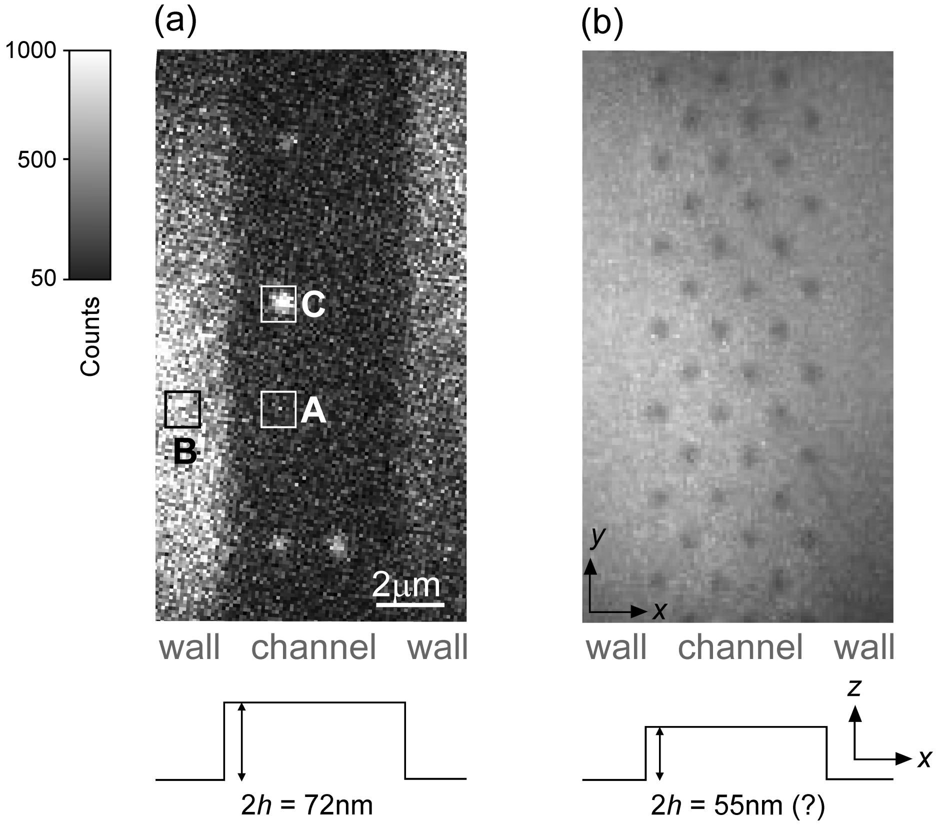

Figure 2.10: (a) Fluorescence image recorded with an Electron Multiplying CCD Camera, under 532 nm laser excitation, of a representative nanoslit during an ET*e* experiment. Under typical illumination conditions – laser power 0.5kW/cm^2, detector exposure time = 5ms – the background in the channel is usually low: if we examine an area of 15x15 pixels (corresponding to roughly 2x2 µm in our field of view, square "A"), we record on average 100±40 counts. In the region of the silica walls, bonded to glass, we always record high auto-fluorescence, of spectrum mostly overlapping with the emission of the fluorophore used to label the molecules. The intensity in the this region ("B"), is 700±150. The same area, centered on a trapped molecule ("C"), gives 400±100 counts, ensuring a Signal-to-Noise Ratio ∼ 10. In this frame we clearly see 4 trapped molecules. (b) A fluorescence image, under the same illumination conditions as (a), of a sagged channel, of nominal height 55 nm. In this height range, even 5 µm channels cannot withstand the bonding procedure, and the collapsing behaviour results in high background, ∼ 600 counts, everywhere.

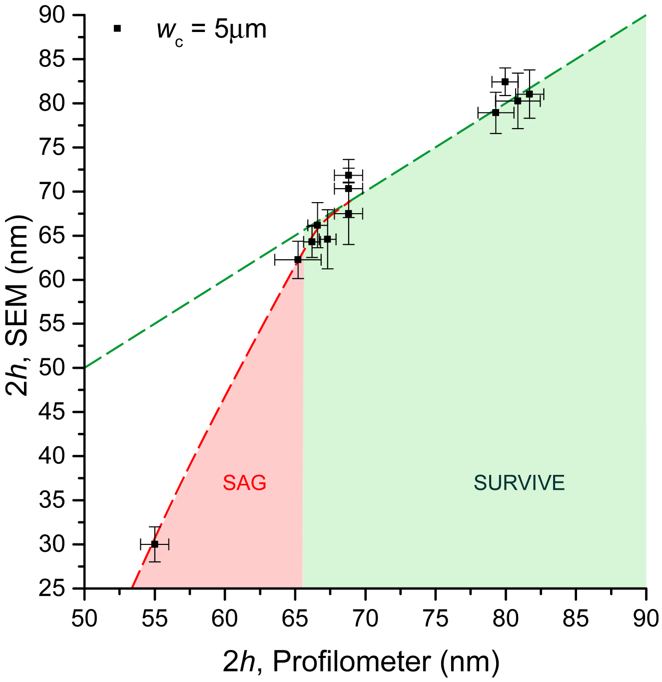

Figure 2.11: The plot summarizes the sag behaviour for slits of $w_c = 5\,\mu\text{m}$, by comparison of their height before bonding – via profilometer characterization – and after bonding, imaging their cross-section in SEM. The green dashed line indicates identity. For $2h > 65$ nm the channels withstand bonding without any sign of deformation, while narrower gaps tend to collapse.

(a) Lithography design

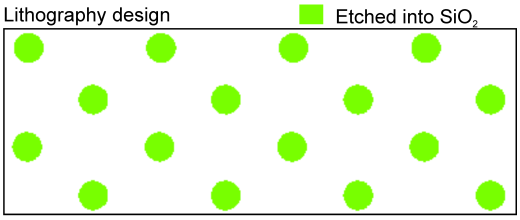

(b) SEM image

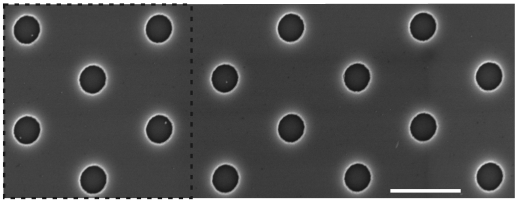

(c) Projected fluorescence stack

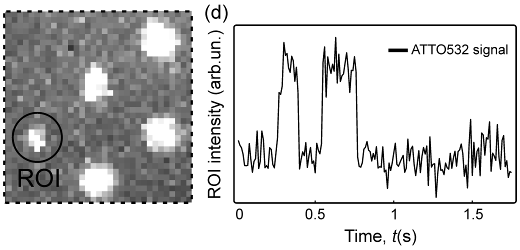

Figure 2.12: (a) E-beam lithography design. The array of circular indentations to be patterned onto the SiO_2 wafer are arranged in a regular zig-zag pattern to maximize space within a 5 µm channel. (b) The resulting array, after RIE etching, imaged with SEM. Scale bar is 1 µm. (c) Once occupied by a fluorescent molecules, the intensity of the lattice – observed via wide-field microscopy – reveals the location of the pockets. Monitoring the intensity fluctuations within a given ROI centered on a trap allow us to study t_{esc}, as described in Chapter 3.

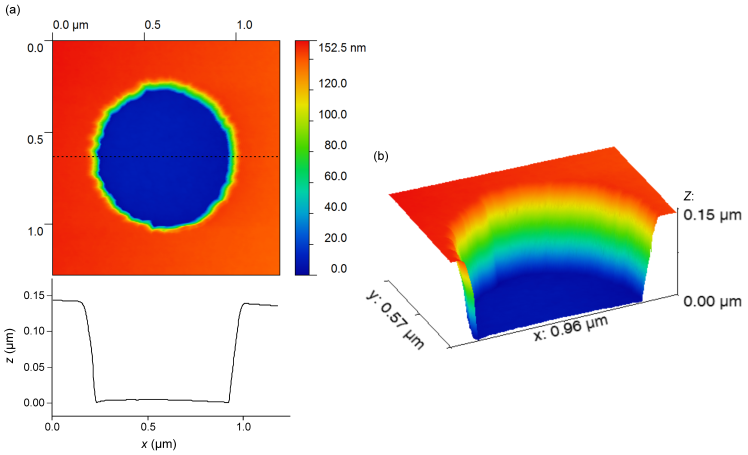

Figure 2.13: (a) Atomic Force Microscopy (AFM) scan of a trapping nanostructure of $R = 400$ nm. The z-profile is depicted in the bottom panel. (b) 3D view of the half-structure.

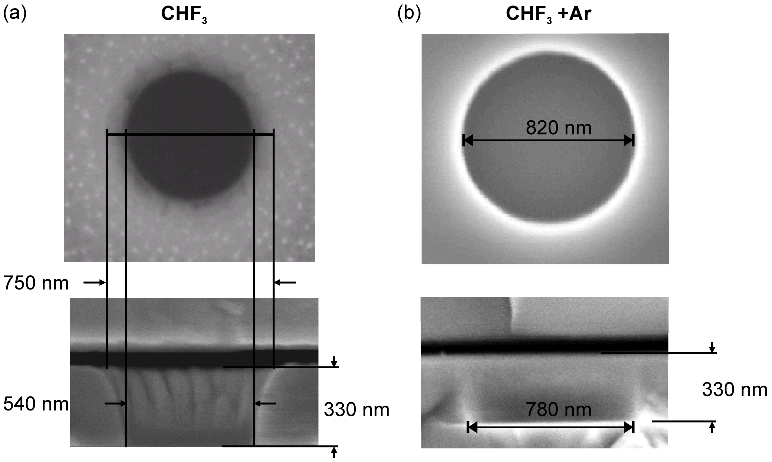

Figure 2.14: (a) Top-view (top panel) and cross-sectional view (bottom panel) of a pocket etched in SiO_2 using CHF_3 gases. The profile appears tapered in this case. The bottom of a pocket of $d = 330$ nm is almost 200 nm narrower in diameter, compared to the mouth of the aperture. This correspond to a taper of $\sim$ 66% (cone angle $\sim$ 35°).(b) The addition of Argon gas during the etching process gives straighter edges and reduces tapering. The top and bottom diameter of the indentation are comparable.

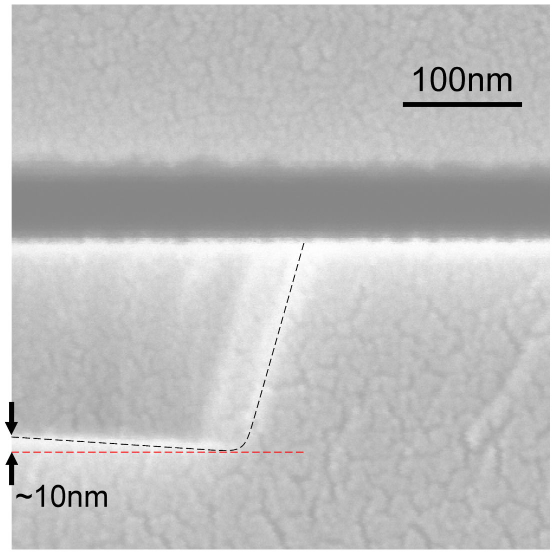

Figure 2.15: SEM image of half of the cross-section of a circular nanostructure of $d = 150$ nm and $R = 300$ nm, etched with CHF_3. Microtrenching effect gives a deeper etch at the edges of the structure, by ∼10 nm.

It's worth pointing out that this peculiar shape might explain the skewed radial position probability distribution, $P(r)$, of a large trapped nanoparticle sampling a similar nanostructure reported in Ref.[1]. In this work, instead of a smooth sigmoidal distribution – expected given the shape of the underlying potential – the probability maximum was found shifted toward the edge, approximately 50 nm away from the physical boundary of the pocket. This is in fact roughly where we also observe the deeper point of the pocket cross-section, due to the combined effect of tapering and microtrenching during the etch process. However it is also possible that the effect arises from imaging conditions [63] or other unknown effects.

2.2.3 Surface potential

After we have characterized all the geometrical parameters of an ETe device, we need to evaluate the response of the SiO_2 walls in our system to estimate an effective surface potential, ψ_s, needed as input of Eqn.1.9.

To do so, we have used the classical single pK Charge Regulation Model, developed by Behrens and Grier [52]. This model, which describes the oxide behaviour with salt concentration and pH, has been previously applied to silica particles measurement [64] and nanoslits systems similar to ours [53]. The surface charge of silica originates from the de-protonation of silanol groups according to:

$$\mathrm{SiOH} \leftrightarrow \mathrm{SiO}^- + \mathrm{H}^+ \tag{2.1}$$

The single pK model for the wall surface potential, ψ_w describes the dissociation of the silanol groups using a constant, pK, and discarding the contribution of the Stern layer, according to:

$$\psi_w(\sigma) = \frac{k_\mathrm{B}T}{e}\ln\Big(\frac{-\sigma}{e\Gamma + \sigma}\Big) + \frac{\ln(10)}{e/k_\mathrm{B}T}(\mathrm{p}K - \mathrm{pH}) \tag{2.2}$$

where Γ is the density of chargeable groups and σ the surface charge density. In the case of an isolated surface, where no double layer overlap occurs, the surface charge density is described by the Grahame equation [53]:

$$\sigma(\psi_w) = \frac{2\epsilon\epsilon_0\kappa k_\mathrm{B}T}{e}\sinh\frac{e\psi_w}{2k_\mathrm{B}T} \tag{2.3}$$

Solving Eqn.2.2 and Eqn.2.3 gives σ and ψ_w. The linearized PB equation in this case yields the simplified expression $\sigma = \epsilon\kappa\psi_w$ [65].
In our system, where $\kappa^{-1} \approx h$ and double layer overlap occurs, no analytical solution is available and we solve the non-linear PB equation (Eqn.1.6) numerically with the following boundary condition on the walls at any point $\mathbf{r}$:

$$\sigma(\mathbf{r}) = \frac{\Gamma}{1 + 10^{(\mathrm{pH}-\mathrm{p}K)}\exp\big(\frac{-e\psi(\mathbf{r})}{k_B T}\big)} \tag{2.4}$$

In our calculations, we initially assumed $\Gamma = 8e/\mathrm{nm}^2$ and p$K = 7.5$, resulting in a surface charge density of $\sim 0.3e/\mathrm{nm}^2$ and an "effective" linearized surface potential $\psi_s = 3.7k_\mathrm{B}T$ at pH $= 8.8$ and 1 mM salt [3].

In order to obtain an experimental estimate of σ, we have measured conductance of two aqueous solutions in our devices at different pH values (see Figure 2.16). In the case of low salt concentration ($\sim$ mM) and for small gaps, the number of mobile counterions – that effectively balance the surface charge of the slit – dominates over the bulk ion contribution. Therefore when we apply a voltage, these counterions are responsible for the measured current. The I-V measurement can then be used to estimate the surface charge density of the nanoslit wall, given that the conductance scales as $\approx \sigma\mu_i w_c(1+\frac{4\epsilon\epsilon_0 k_\mathrm{B}T}{e\mu_i\eta})$, where μ_i the ions mobility [66].

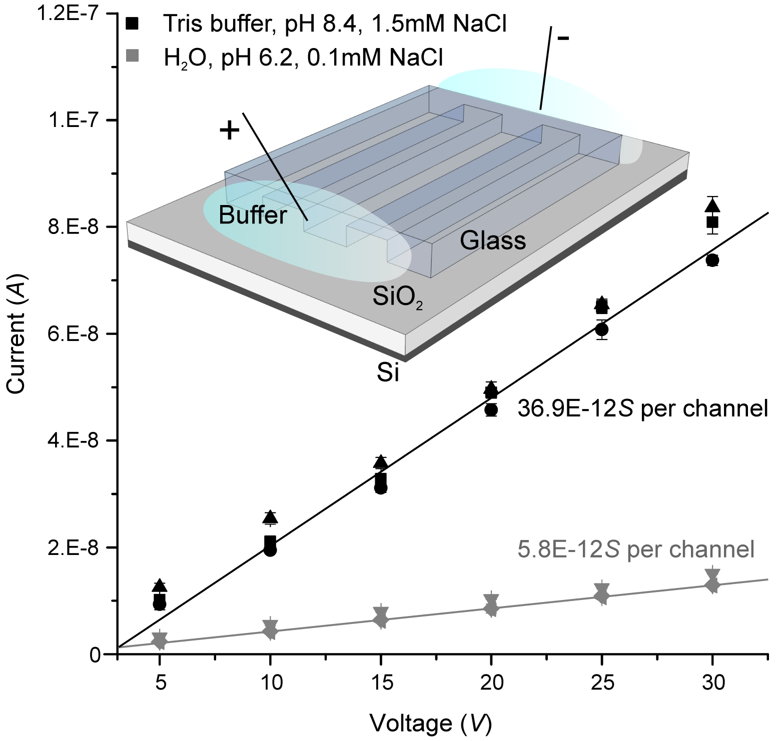

Figure 2.16: I-V curve measurement of the nanoslits of an ET*e* device. The slope carries information on the conductance of each channel. The experiment was performed filling the device with 2 solutions, of different pH and salt concentrations. The applied voltage across the slits was increased from 5 to 30 Volts in steps of 5V. 3 repetitions were performed for of each measurement point, here indicated by different symbols. Black symbols represent measurement of high pH, Tris buffer (pH = 8.4), while grey symbols indicate measurement performed with water at pH = 6.2. The measured conductance values are in good agreement with the results previously reported from Stein et al. [66]

In order to perform this measurement, we have inverted the typical configuration of the device, patterning the glass substrate instead of the silica wafer, in order to avoid contact of the water with the highly conductive silicon layer on the back (Figure 2.16). We have applied an increasing voltage (5 to 30 V) across 75 nanochannels of 2.2 mm in length and 20 µm in width and measured a current at each point, inferring the conductance from the slope of the fitted line according to Ohm's law. The conductance per nanoslit is obtained scaling the measurement by the number of slits. We have found good agreement with the measurements published by Stein et al. [66], who have reported a value of conductance of ~40E-12S/nanoslit for an aqueous solution at pH $\sim$ 8 and corresponding to the aforementioned value of $\sigma \sim 0.3e/\mathrm{nm}^2$.

Conductance measurements on the other hand might not provide an accurate enough description of surface charge. The applied voltage may induce accumulation or depletion of ions at the channel inlets, creating a concentration gradient and hence transient or non-linear responses of the measured currents [67]. Moreover the analytical description of conductance above, treats the ions as point charges, discarding other complicating effects due for example to the finite ions size, which would alter the nominal ion mobility [68].

Furthermore a recent work which involved direct optical measurement of the pK of a glass capillary [54], has shown a broad distribution of pK within a fairly small area of the substrate ($\sim$ 100 µm) and suggested that sample preparation might have a strong impact on the result.

In order to precisely characterize the surface potential in an ETe experiment in equilibrium, we have used a molecule of known effective charge as "calibrator" and directly measured the midplane potential [5, 4]. This experimental approach has actually suggested an higher $\mathrm{SiO_2}$ p$K = 9.5$, corresponding to a surface potential $\psi_s = 2.8k_\mathrm{B}T$. We note however that, since we are not able to independently measure Γ and pK, it is possible that other combinations of these two parameters yield the same value of surface potential.

3

Optical Setup and Experimental Protocols

> “Life isn’t black and white. It’s a million gray areas, don’t you find?”
>
> *Ridley Scott*

3.1 Optical Setup

The Optical Setup used to perform ET*e* measurement is a simple home-build wide-field fluorescence microscope. Figure 3.1 illustrates the setup. The laser source used is a diode-pumped solid-state (DPSS) laser from Pusch OptoTech GmbH. We purchased Achromatic Lenses and Silver Mirrors from Thorlabs. We used an high Numerical Aperture (NA = 1.32) Objective from Leitz (Leitz Wetzlar PL Fluator), with 100X Magnification. The beam was expanded 5 times, before being focused on the back-focal aperture of the objective by the Wide-Field lens (focal length = 25 cm) upon reflection by a Dichroic Mirror (F38-532, AHF). The emission was then band-passed by a combination of Long Pass (F76-534, AHF) and Short Pass filters (FF01-694/SP-25, Semrock) – the latter used to reduce red auto-fluorescence arising from the silicon oxide substrate – and then focused on the Electron Multiplying CCD Camera (EMCCD,

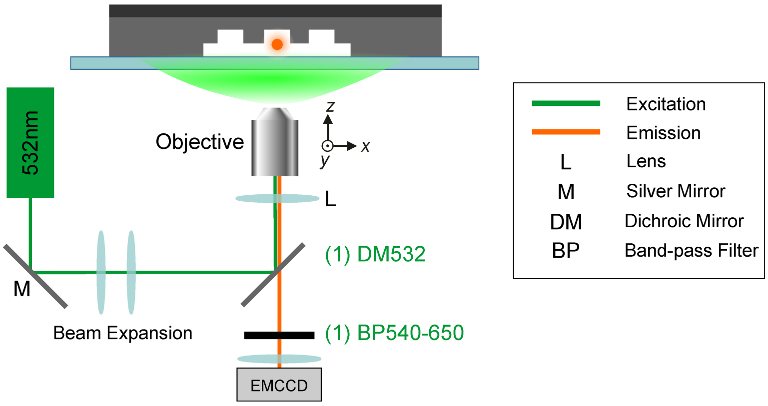

Figure 3.1: Schematic of the wide-field fluorescence setup used for electrometry measurements. We have a single wavelength (532nm) to excite the molecules – here depicted in orange – typically carrying two ATTO 532 dyes. The setup was later modified to incorporate a second laser source (488 nm), as described in Chapter 6.

Ixon Ultra, Andor) with a lens of 50 cm focal length. The obtained pixel size on the detector was $\sim$ 120 nm, close to the size of the PSF of the system [69], illuminating a field of view of approximately 20 by 20 µm. We typically use a laser power of 0.5kW/cm^2 and camera exposure times of 5-10 ms, with a EM gain = 150.

3.2 Experimental Procedures

3.2.1 Biomolecules Purification and Labeling

We have used ET*e* to measure a variety of biomolecules, including DNA fragments and proteins (Figure 3.2). The ssDNA strands were purchased already labelled and purified via high-pressure liquid chromatography from either Microsynth AG, or IBA-lifescience. We annealed the complementary strands to form dsDNA in a buffer of 10 mM Tris pH 7.5, 5 mM MgCl2 and 50 mM NaCl, heated at 95°C for 3 minutes and cooled down to room-temperature. The DNA purity was verified with Native Polyacrylamide gel electrophoresis (PAGE)(see also Chapter 6 and Ref.[4]). All molecules were stored in water at -20°C. For long storage, stock solutions were kept either lyophilized or dissolved in annealing buffer.

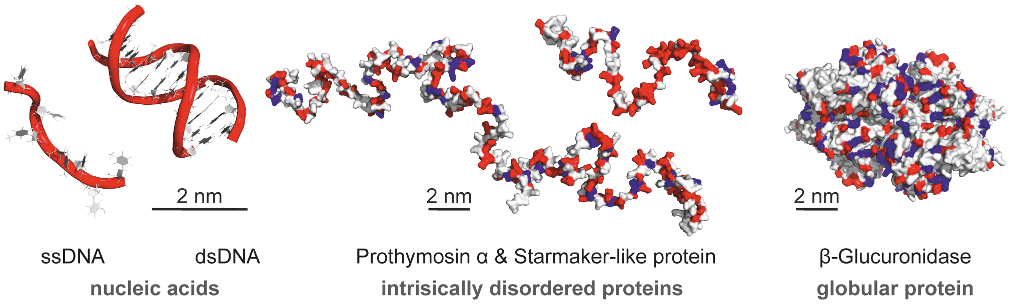

Figure 3.2: PyMol Surface representation of the molecules used, adapted from Ref.[3]. Negatively charged aminoacids are colored in red, positively charged in blue.

The intrinsically disordered protein (IDP) ProTα [70] (Fig. 3.2) was mutated with site-directed mutagenesis, according to the Protocol in Ref.[71] to produce the E59K mutant [3], carrying a Lysine (K) residue instead of a Glutamate (E) on position 59. This created a difference of $+2e$ in the structural charge of the mutant (see Supporting Information of Ref.[3] for further details). We also generated a second mutant, E59KE60K, carrying a similar mutation on the next Glutamate ($\Delta q_{\text{str}} = -4e$)

These proteins were labelled at the two cysteine residues with either ATTO 532 (ATTO-TEC GmbH, q_{str} = -1e), Cy3B (Lumiprobe, q_{str} = 0e) or Alexa 546 (Thermo Fisher Scientific, $q_{\text{str}} = -2e$).

The intrinsically disordered Starmaker-like protein (Stm-l) was generously gifted to us from Prof. Andrzej Ożyhar [72]. Stock solutions of both IDPs were stored in 10 mM Tris (pH 7.5). The globular protein β-glucuronidase (Gusβ) was purchased from Sigma Aldrich and purified with Size Exclusion Chromatography (column: Superdex200 10/300, GE Healthcare) and labelled at the exposed cysteine residues with an average of $\sim$ 2 ATTO 532 dyes per molecule. The molecule, prone to aggregation, was kept in a buffer of 100 mM NaCl, 150 mM Tris and 2-fold excess of 2-Mercaptoethanol and dissolved in measuring buffer only shortly before each experiment.
All proteins were stored at -80°C.

3.2.2 ETe: from Escape Time to Effective Charge

Once the nanofluidic devices are ready (Chapter 2), an ETe measurement requires little further preparation. The bonded devices are prepared applying hydrophobic ink (Super PAP Pen, Cat. no. 24230-1 from Polysciences) along

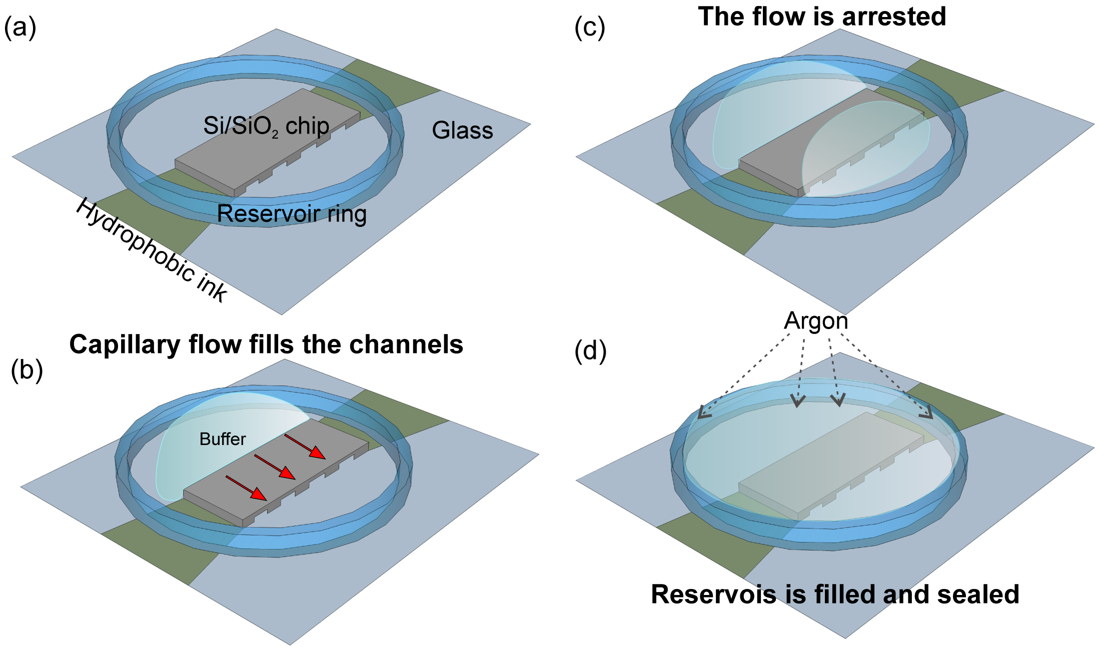

Figure 3.3: Schematic of the experimental procedure. (a) Hydrophobic ink is applied along the edges of the silica chip and a reservoir ring is used to enclose the aqueous buffer. (b) The solution is loaded on one side of the device and fills the channels by capillary force. (c) Adding solution to the other side of the device stops the flow. (d) The reservoir is filled with buffer, sealed and a weak Argon gas flow protects the buffer from oxidation.

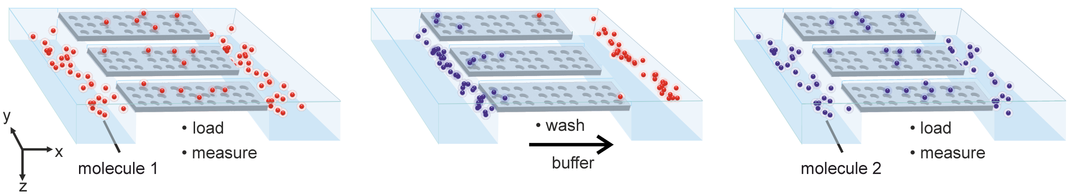

Figure 3.4: Schematic of the experimental procedure: different species can be measured in the same device, one after the other, using capillary flow to load them and flushing with empty buffer in between measurements. Adapted from Ref. [3].

the sides of the silica chip – perpendicularly to the channels – in order to create a barrier for the buffer (Fig.3.3a). We typically also create a buffer reservoir by sticking on the device either a home made plexiglass ring or a commercial plastic well (Press-to-Seal Silicone Isolator, Cat. no. P-24743 from Thermo Scientific). The device is first loaded with buffer via capillary flow; the buffer is left to fill and rinse the channels for about 10 minutes (Fig.3.3b). We then swap the solution to a buffer containing the molecule of interest, at a concentration of 50-100 pM. In a few tens of seconds, the molecules will reach the area of the device containing the pockets; once the desired molecule density is obtained (2-3 per nanoslit), the flow is stopped adding liquid to the other side (Fig.3.3c). Finally the reservoir is filled with about 200 µL of the same buffer, sealed with Parafilm tape and flooded with Argon in order to avoid oxidation of the buffer (Fig.3.3c). After approximately 20 minutes of equilibration time, we proceed to measure, imagining the molecule in the active area.

We usually monitor an area of 20x20 µm, which spans 3 nanoslits, populated by 2-3 molecules each. We use an exposure time, t_{exp} = 5-10 ms and a variable lag-time between frames, t_{lag}, such that the total cycle-time, t_{cycle} is $\approx 0.25 t_{\mathrm{esc}}$. For single-molecule measurements, characterized by fast dynamics, usually $t_{\mathrm{cycle}} = t_{\mathrm{exp}}$. We have characterized the bleaching time of the fluorophores used to label the macromolecules (see SI of Ref. [3]): under our typical illumination conditions, described above, the number of frames to bleaching for a molecule double-labelled with ATTO 532 is approximately 300, much larger than the number of frames-to-escape, which is typically 4. After the movies are recorded, we measure conductivity and pH of the buffer in the reservoir. We find that, upon sealing and under continue Argon flow, a device is stable and impervious to salt concentration drift for at least 30 min to 1 hour.

An ETe nanofluidic device can be used several times in order to measured different molecular species, in a sequential fashion. In order to exchange to a new molecule solution, we simply repeat the capillary flow step in Fig.3.3b for approximately 10-20 minutes, loading empty buffer in order to completely remove the first species. Afterwards, a solution containing the second type of macromolecules of interest is added (see Fig.3.4) and the sealing procedure is repeated as above. We can routinely measure 3-4 molecular species sequentially in the same device.

3.3 The Sources of Error in the ETe Experiment

This section illustrates the dominant sources of uncertainty in an ETe experiment.
In general, the measurement error, x_e on a quantity x, which is a function of the variables f, g, h, etc., each with uncertainties f_e, g_e, h_e, etc., can be expressed as follows:

$$x_\mathrm{e} = \sqrt{\left(\frac{\partial x}{\partial f}\right)^2 f_\mathrm{e}^2 + \left(\frac{\partial x}{\partial g}\right)^2 g_\mathrm{e}^2 + \left(\frac{\partial x}{\partial h}\right)^2 h_\mathrm{e}^2 + ...} \tag{3.1}$$

In the regime of $W \geq 5k_\mathrm{B}T$, the relationship between measured escape time, t_esc, and molecule effective charge, noted here as q, is well described by Kramers' analytical expression, given by:

$$q\psi_\mathrm{m} + f = k_\mathrm{B}T \ln\left(\frac{t_\mathrm{esc}}{t_\mathrm{r}}\right) \tag{3.2}$$

In the regime of $W < 5k_\mathrm{B}T$ however the dependence of t_esc on W is weaker and can be represented by a more generic expression of the form:

$$t_\mathrm{esc} = t_r \exp\left(\frac{\nu W}{k_\mathrm{B}T}\right) = t_r \exp\left[\frac{\nu(q\psi_\mathrm{m} + f)}{k_\mathrm{B}T}\right] \tag{3.3}$$

This fit parameter ν is < 1 for $W \leq 5k_\mathrm{B}T$ and is equal to 1 for $W > 5k_\mathrm{B}T$, where the Kramers' prediction well describes the behavior. Most of the experimental results presented in this thesis were performed in the high well depth regime,

except the data included in Chapter 7 [6], corresponding to weakly charged molecules, and performed in a regime of $W < 4k_\mathrm{B}T$, where $\nu \approx 0.6$.
We write the fractional error q_e/q according to Eqn.3.1 as:

$$\frac{q_\mathrm{e}}{q} = \sqrt{\left(\frac{1}{q^2}\right)\left(\frac{\partial q}{\partial \psi_\mathrm{m}}\right)^2 \psi_\mathrm{m,e}^2 + \left(\frac{1}{q^2}\right)\left(\frac{\partial q}{\partial t_\mathrm{esc}}\right)^2 t_\mathrm{esc,e}^2 + \left(\frac{1}{q^2}\right)\left(\frac{\partial q}{\partial t_\mathrm{r}}\right)^2 t_\mathrm{r,e}^2} \quad (3.4)$$

The first term on the RHS of Eq.3.4, represents the uncertainty in determining the electrical potential at the midplane of the slit, ψ_m. This aspect has been discussed at length in the Supporting Information of Ref.[3]. Given $\psi_m \approx 2\psi_s \exp(-\kappa h)$, the dominant source of error resides in the estimation of the system parameter κh. We can directly determine the inverse Debye length, $\kappa = \sqrt{2cN_\mathrm{A}e^2/\epsilon_\mathrm{w}\epsilon_0 k_\mathrm{B}T} = \sqrt{c}/0.301$ at room temperature, via measuring the conductivity of the aqueous solution, with an uncertainty of roughly $\sim 0.5\%$. We then convert the conductivity into a molar concentration value, c, using a calibration curve [3].

On the other hand, as described in Chapter 2, we are not able of determining the slit height ($2h$) with an accuracy better than $h_\mathrm{e} = 1$ nm. The corresponding error on ψ_m is thus estimated to be about 5% when averaging over 4-5 independent experiments, and for $\kappa h \sim 3.5$. In a single experiment however where the nominal height of the slit may depart from the mean value by as much as 2 or $3h_\mathrm{e}$, so this (single) measurement inaccuracy can be as large as 15%.

The second term of Eqn.3.4, that we denote as $(q_e/q)_{t_\mathrm{esc}}$, arises from statistical uncertainty in measuring t_esc in a temporally limited experiment. Given that the escape events Δt are exponentially distributed, the measurement error $t_\mathrm{esc,e}$ on their average value, t_esc, is function of the number of detected hops, N, as follows:

$$t_\mathrm{esc,e} = \frac{t_\mathrm{esc}}{\sqrt{N}} \quad (3.5)$$

According to Eqn.3.3, $(\partial q/\partial t_\mathrm{esc}) = (k_\mathrm{B}T/\nu t_\mathrm{esc}\psi_\mathrm{m})$. Using Eqn.3.5, $(q_e/q)_{t_\mathrm{esc}}$ gives

$$\left(\frac{q_e}{q}\right)^2_{t_\mathrm{esc}} = \left(\frac{1}{q^2}\right)\left(\frac{k_\mathrm{B}T}{\nu t_\mathrm{esc}\psi_\mathrm{m}}\right)^2 t_\mathrm{esc,e}^2 = \left(\frac{k_\mathrm{B}T}{\sqrt{N}\nu q\psi_\mathrm{m}}\right)^2 \quad (3.6)$$

Note that in this analysis we assume that f in Eq.3.3 is constant, since the fluctuation contribution is largely charge-independent as discussed in Chapter 7.

We finally analyze the last term of Eqn.3.4, denoted by $(q_e/q)_{t_\mathrm{r}}$, which represents the fractional error contribution given by the uncertainty in determining the position relaxation time, t_r.

This quantity represents the time a molecule, under purely diffusive conditions, would take to move away from a region of the same spatial extent as the trap. The effective radial extent, L, of the trap is function of both pocket radius R and lattice pitch λ and is a fit parameter that can be inferred from a 2D Brownian Dynamics simulation. Hence $t_\mathrm{r} \approx L^2/4D$, and according to the Stokes-Einstein formula the molecule diffusion coefficient $D = k_\mathrm{B}T/6\pi\eta r_\mathrm{H}$, therefore $t_\mathrm{r,e} \propto r_\mathrm{H,e}$.

The hydrodynamic radius, r_H, of the molecules measured is typically determined with an independent two-focus Fluorescence Correlation Spectroscopy (2fFCS) measurement [73] and carries $\sim 5\%$ uncertainty. As described in Chapter 8, we can also directly determine the size of the molecule during and ETe experiment. In this case the error on r_H also trends with the number of recorded events N as roughly $1.7/\sqrt{N}$ [5].

From Eqn. 3.4:

$$\frac{1}{q^2}\left(\frac{\partial q}{\partial t_r}\right)^2 = \left(\frac{1}{\ln\frac{t_\mathrm{esc}}{t_\mathrm{r}}}\right)^2 \left(\frac{t_\mathrm{r,e}}{t_\mathrm{r}}\right)^2 \tag{3.7}$$

The ratio of $\ln(t_\mathrm{esc}/t_\mathrm{r})$ is approximately 5 for a molecule of $r_\mathrm{H} = 5$ nm and $t_\mathrm{esc} = 0.5$ s, resulting in an overall contribution of $\sim 1\%$, given the nominal 2fFCS error on r_H.

The following table summarizes the error contribution of each term discussed, for two experimental cases which only differ by the system parameter κh. This affects both the midplane potential, which is ~ 3 times lower when increasing κh by a unit and – holding the other experimental conditions constant – the escape time, which in this case is decreased by a factor 20.

Sources of Error	**Analytical Expression**	**Error Estimation (*N* = 100, *q* = -30e)**	
		κ*h* = 3.5	**κ*h* = 4.5**
Statistical error on t_{esc} measurement	$\left(\frac{q_e}{q}\right)_{t_{\text{esc}}} = \frac{k_{\mathrm{B}}T}{\sqrt{N}\nu q \psi_{\mathrm{m}}}$	2%	5.6%
Channel height uncertainty	$\left(\frac{q_e}{q}\right)_{\psi_{\mathrm{m}}} \propto \frac{\kappa h_{\mathrm{e}}}{e\psi_{\mathrm{m}}/k_{\mathrm{B}}T}$	5%	14%
Uncertainty on r_{H}	$\left(\frac{q_e}{q}\right)_{t_{\mathrm{r}}} \approx \frac{1}{\ln(t_{\text{esc}}/t_{\mathrm{r}})} \frac{r_{\mathrm{H,e}}}{r_{\mathrm{H}}}$	1%	2.6%
	$\frac{q_e}{q}$	**5.5%**	**15.3%**

Table 3.5: Error contributions in a ETe measurement. The statistical error on the measurement of t_{esc} limits the precision of the method, while uncertainty on the determination of the midplane potential and r_{H} affects the measurement accuracy. $r_{\mathrm{H,e}}$ in this example is the nominal 2fFCS error, 5%. Working with high ψ_{m} (low κh) is desirable to reduce the overall error.

4

Data Analysis and Brownian Dynamics Simulations

> "Science walks forward on two feet, namely theory and experiment. Sometimes it is one foot which is put forward first, sometimes the other, but continuous progress is only made by the use of both..."
>
> *Robert A. Millikan*

4.1 Data Analysis

In our experiment ET*e*, we introduce the molecular species of interest labelled with two fluorescent dye molecules in the patterned nanoslit and after an equilibration time of approximately 20 minutes, we image the dynamics using wide-field fluorescence microscopy. We use a sampling time smaller than the expected t_{esc}, which typically ranges from tens of milliseconds to a few seconds. The traps lattices are usually populated by 5-6 molecules at a time in the case of the "*en-*

semble" measurement, in which we achieve an high throughput, fast and precise, population-averaged q_{m} determination.
Furthermore, if we are interested in the charge of the individual molecules in the sample, either because the population is expected to be heterogenous (see Spectrally Resolved ETe work in Ref. [4]) or because we want to follow the charge evolution of the same molecule over time, ETe can be also used to perform a "*single-molecule*" measurement.

4.1.1 The ETe Ensemble-averaged Measurement

At the practical level, after recording a movie of the dynamics in a lattice of pockets, observed with wide-field microscopy, we can locate the position of the traps by summing the intensity of each frame in the stack. In the resulting image the lattice points, populated by the molecules for longer time compared to the "diffusive" inter-well space, will appear very bright. In the data analysis routine, we center an ROI on each lattice point and monitor the fluorescence intensity over the duration of the recorded movie. The ROI contour roughly corresponds to the radial escape criterion r_{esc}, discussed later.

We use two intensity thresholds to determine the beginning and the end of an escape event, Δt. The background intensity for each ROI (corresponding to when the trap is empty) is subtracted prior to the analysis, and the background noise, S.D.$_{\mathrm{bg}}$, is calculated as the intensity standard deviation over a stretch of 10-20 "dark" frames. The Start of an event is defined when the fluorescence intensity overcomes 30 times S.D.$_{\mathrm{bg}}$, while the End is set when the fluorescence then falls below 15 times S.D.$_{bg}$ (Figure 4.1). In general we find that, given the high SNR (~ 10) typically achieved, the length, Δt,, of an event is very robust to small variations of the intensity thresholds position.
The escape events, exponentially distributed, are then averaged in order to obtain the mean escape-time t_{esc}, which can be converted into a measured well depth, W (and thus q_{m}), with the aid of BD simulations.

4.1.2 The Single-Molecule ETe Measurement

Instead of monitoring many molecules at the same time, we can also operate in a regime in which only one molecule samples the trapping landscape. Doing so, we can directly measure the effective charge of a single molecule and even monitor its evolution over time.

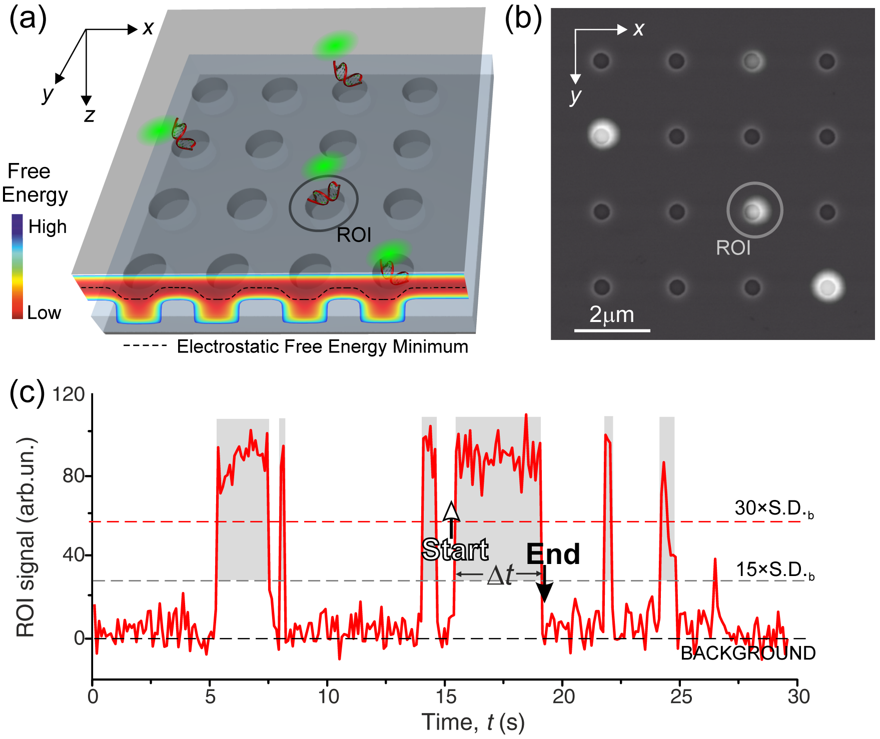

Figure 4.1: (a) Graphic representation of a trapping lattice and a COMSOL calculation of the Electrostatic Free Energy across a row of traps. (b) When the molecules reside in the trap, their fluorescence intensity can be detected. Here a representative fluorescence wide-field image is superimposed with an SEM of the underlying patterned surface. (c) An ET*e* trace of an ROI centered on a trap. Monitoring the intensity over time reveals the presence of trapped molecules. The background standard deviation, S.D.$_{\text{bg}}$, is used to set un upper threshold (red dashed line), which has to be overcome to define the beginning of a trapping event, or “hop”. The event, shaded in grey, ends when the intensity falls below the lower intensity threshold (grey dashed line).

In brief, instead of collecting all the escape events for a final reading of t_{esc} and q_{m}, we can split the molecule trajectory in intervals of N hops each, measure a $t_{\mathrm{esc,N}}$, and have a reading of charge in real time. This approach results in a time resolution which is $\sim Nt_{\mathrm{esc}}$.
In order to do so we have to:

1. Ensure we are following the same object over time.
2. Speed up t_{esc} in order to improve the time resolution.

To satisfy the first point, we work under very diluted conditions, making sure that only one molecule is sampling each nanoslit. Furthermore, when analysing the trajectory, we ensure that each translation from one lattice site to another don't exceed the diffusion length in 2D of the molecule during the observation time t_{exp}, $l_{\mathrm{diff}} = \sqrt{4Dt_{\mathrm{exp}}}$.

The second point is achieved by decreasing the radius of the pocket and creating a very dense lattice (small λ), effectively reducing the position relaxation time of the molecule and thus t_{esc}, without affecting ψ_{m}. The midplane potential needs to be kept high, since the measurement error on charge goes as $\propto 1/\psi_m$ (Chapter 3.3).

When the dimensions of the lattice pitch become comparable with the size of the Point Spread Function of our optical system, it is challenging to assess the exact position of the traps in our field of view, condition needed to define ROIs for the telegraphic "on-off" approach. To sidestep this problem, we directly track the position of the molecule in the lattice. Note, however, that the method is still suited for weak emitters: the required spatial information on the location of the molecule doesn't need to be better than $\sim$ 100 nm, dimension comparable with the radius of a pocket. The tracking routine, in fact, only needs to know in *which* trap the molecule is residing and for how much time, while the exact spatial location *within* a trap is superfluous for our purpose. In general we find that molecules labelled with ATTO 532 dye can be tracked with $\sim 20 - 30$ nm precision for tens of seconds under our typical illumination conditions [74].

In the case of SNR > 6, we are able to perform 2D Gaussian fitting of the raw fluorescence images using a standard tracking routine. When the SNR is lower, the images are usually spot enhanced with a Mexican Hat filter [75] prior to

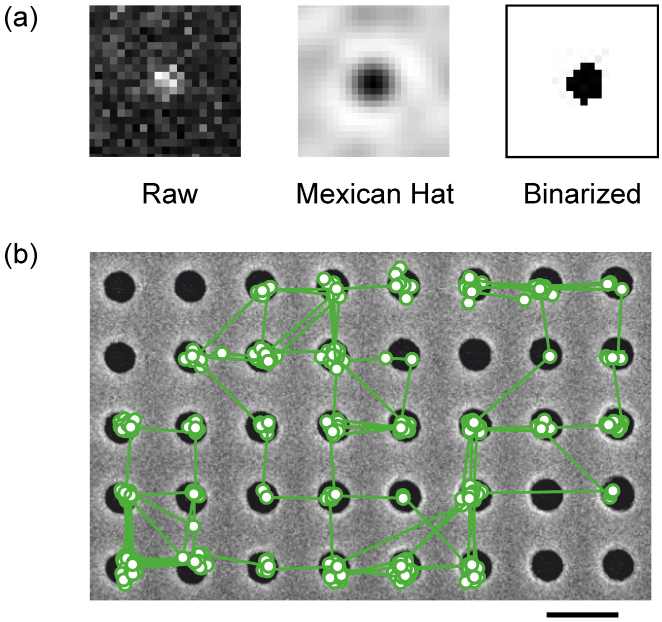

Figure 4.2: (a) The panel present a series of images depicting, from left to right: a raw fluorescence image of a trapped molecule; the same image filtered via a Mexican Hat; a binirized version of the image, based on an intensity threshold. The filtering methods have been implemented in order to facilitate tracking when the SNR is low.(b) Trajectory of a single molecule, overlayed on the SEM images of the nanostructured surface sampled. Scale bar is 500 nm.

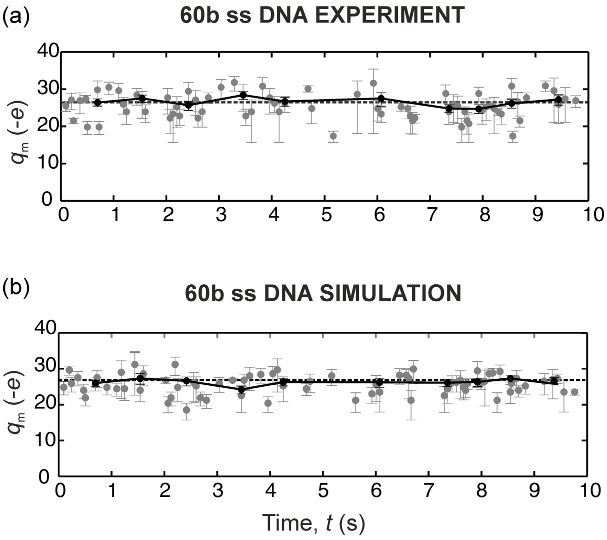

(c)

	Experiment		Simulation	
	$N = 3$	$N = 21$	$N = 3$	$N = 21$
$\frac{\text{S.D.}_{t_{\text{esc,N}}}}{\langle t_{\text{esc,N}} \rangle}$	57.3%	24.9%	51%	21%
$\frac{\text{S.D.}_{q_{\text{m,N}}}}{\langle q_{\text{m,N}} \rangle}$	13.3%	4.5%	11%	4.5%

Figure 4.3: (a) Experimental single 60ss DNA trace acquired with different time resolution. The "hops" are bunched in group of N events, that are then averaged and converted into a well depth to infer q_{m} over time. Error bar indicates standard error of the mean (s.e.m.) and N sets the time resolution of the measurement, which is approximately Nt_{esc}. In the top trace, in grey $N = 3$ and the average time resolution $= 150$ ms, while for the points in black $N = 20$ and the average time resolution $= 1$ s. (b) The simulation result is also presented. (c) The fractional standard deviation, S.D., for both t_{esc} and charge measurement are very close in the two cases, pointing out the detected fluctuations in the experiment are also mostly statistically limited.

fitting. Alternatively, we can set an intensity threshold for each image in the stack and perform a blob fitting of the binirized frame (Fig. 4.2a).
The frames in which the fitting routine fails typically correspond to the times when the molecule is freely diffusing between traps, and can be discarded. This inter-well travel time is what we have named "t_{OFF}" and exploited to infer the molecule r_{H} in a subsequent work [5]. The occurrence of off-times is rare in the dense lattices used in Ref. [3], where $R = 150$ nm and $\lambda = 700$ nm, smaller than l_{diff} of a typical molecule, $\sim 1\,\mu\mathrm{m}$. Similarly as in the ensemble approach, the number of frames spent by the molecule within a given well corresponds to an escape event.

In order to better understand the scope and limits of single-molecule ETe, which could be potentially applied to detect charge and structural fluctuations, we have investigated the origin of measurement noise. To rule out small heterogeneity in the underlying potential landscape sampled by a molecule – e.g. channel height or pocket size variability, which could affect the local escape time and create a larger noise in the measurement – we have compared our experimental and simulated results. In particular we have studied a molecule designed not to form any stable secondary structure, and therefore expected to carry the same q_{eff} throughout the observation time. Figure 4.3 shows an experimental trace and compares it with an ideal noise-free case, in which the hops are generated via a BD simulation (Details in the next Section). This "*in silico*" experiment doesn't suffer from any other external sourcea of noise than the statistically limited one, and thus represents an "ideal" case.

We studied two scenarios, averaging over a number of hops $N = 3$ and $N = 21$. Panel c in Figure 4.3 reports the fractional standard deviation of the measured t_{esc} and q_{m} over the observation time, for both experiment and simulation. The S.D. on t_{esc} is expected to scale like $1/\sqrt{N}$, resulting in 57% and 21% error for $N = 3$ and $N = 21$ respectively. Both simulation and experiment are in excellent agreement with these expected values. The fractional standard deviation in the measurement of effective charge, expected to trend like $1/q_{\mathrm{eff}}\psi_{\mathrm{m}}\sqrt{N}$, with $q_{\mathrm{eff}}\psi_{\mathrm{m}} = 4.4k_{\mathrm{B}}T$ in this case, is thus also in very good agreement with predictions. Given the strong similarities between experiment and simulation, the fluctuations observed in the measured single-molecule trace can be attributed purely to statistical noise, confirming that our method is shot-noise limited.

4.2 Brownian Dynamics Simulations

In order to quantitatively relate the average measured escape time, t_{esc}, of a particle to the depth of the potential well, W, we performed Brownian Dynamics simulations of the escape process. Transport coefficients in a landscape are generally only available for particular analytical functional forms of the underlying potential [76, 77], with closed form expressions limited to 1D problems.
In our system, the features that hinder an analytical, *a priori*, determination of the Kramers' escape prefactor, t_{r}, are the following:

- The shape of the well is not described by an analytical function
- Experimentally we use a finite observation time of the escape process
- In an experiment, the molecule doesn't sample a *single-well*, but rather a *landscape of traps*

4.2.1 "Instantaneous" BD Simulation of Escape from a Single-Well

As a first step, in order to determine the full three-dimensional distribution of electrical potential in a single trap, we solve the nonlinear Poisson-Boltzmann equation in the fluidic nanostructure (Eqn.1.6). Since we have verified by simulation that the dimensionality of the problem can be reduced to two by including an entropic correction for axial fluctuations, f, to the well depth [6], the molecule effectively samples a 2D energy manifold whose value at any point (x, y) is given by the minimum electrostatic energy in z at every radial coordinate.

The molecule, of charge q_{eff}, experiences both thermal fluctuations and a force given by $-\nabla q_{\text{eff}}\psi(\mathbf{r})$ at any point $\mathbf{r}$ in the landscape. Here $\psi(\mathbf{r})$ is the local the electrical potential at $\mathbf{r}$ in the absence of the particle [19].

We simulate a particle trajectory by iteratively solving the discretized overdamped Langevin equation, which reads as follows in one dimension:

$$\mathbf{x}(t+\delta t) = \mathbf{x}(t) - \mu\nabla q_{\text{eff}}\psi(\mathbf{x}(t)) + \sqrt{2D\delta t}\,\mathbf{w}(t) \tag{4.1}$$

Here, $\mathbf{x}(t)$ represents the *instantaneous* position of the molecule at time, t in one dimension, and D is the molecule's diffusion coefficient. $\mathbf{w}(t)$ represents a displacement due to the random thermal force acting on the particle that satisfies $\langle\mathbf{w}(t)\rangle = \mathbf{0}$ and $\langle\mathbf{w}(t)\mathbf{w}^{\top}(t')\rangle = \boldsymbol{I}$ if $\mid t - t' \mid\leq \delta t$, $\mathbf{0}$ otherwise. Further $\mu = \delta t/6\pi\eta r_{\text{H}}$, where the simulation time-step, $\delta t =$ 1-10 µs is much larger than the momentum relaxation time ~10 ns for a typical molecule.

This is the simplest version of the simulation – referred to here as "instantaneous". At $t = 0$, the particle is located in the middle of the pocket, $x = y = 0$. We use Eqn.4.1 to propagate the instantaneous position of the particle, $\mathbf{x}(t)$, forward in time for each spatial dimension, until its radial position $r = \sqrt{x^2 + y^2}$ exceeds an arbitrary radial escape threshold, r_{esc} [5]. The time needed to reach r_{esc} from the bottom of the well corresponds to an escape event, or hop, Δt.

Once the molecule has escaped, the simulation restarts and another escape trajectory is computed: we typically average over a number of hops, $N \sim 10^3$, to obtain the average instantaneous escape time t'_{esc}.

4.2.2 “Time-averaged” BD Simulation

As mentioned, working with an instantaneous trajectory is an over-simplification of the problem. In order to relate experimentally measured escape times, t_{esc}, to measured well depths, we actually perform a 2D BD simulation analysis using time-averaged co-ordinates $< r >_{t_{\mathrm{exp}}}$, rather than instantaneous positions, r. The simulated trajectory is time-averaged over the experimental finite observation time, the exposure time t_{exp}, which is typically 5 ms in our experiments (Figure 4.4).

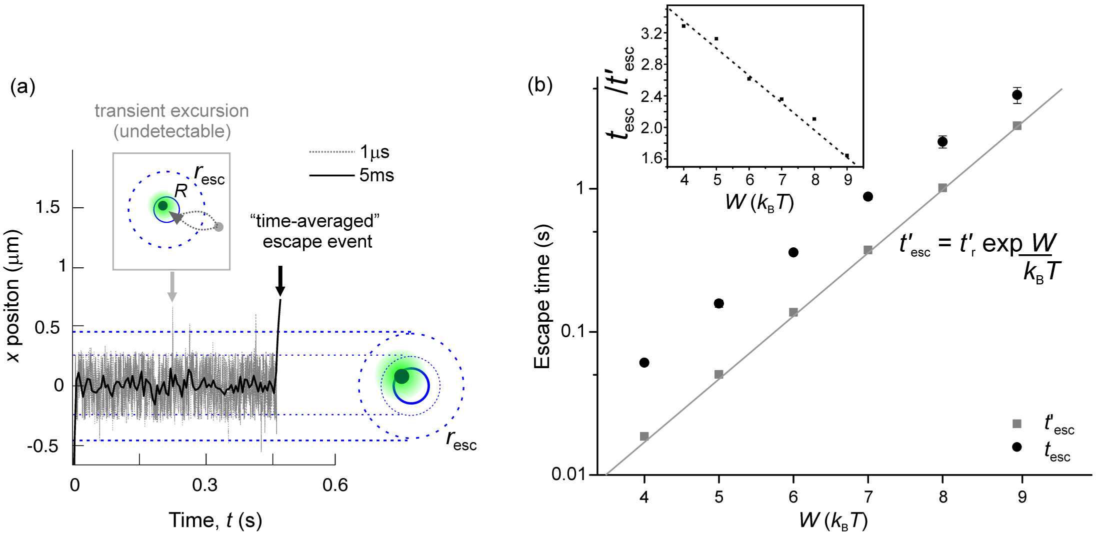

Figure 4.4: The plot, adapted from Ref. [5], represents a simulated x-trajectory of a molecule sampling a trap. R indicates the radius of the pocket circumference, while r_{esc} is the escape boundary. The position of the escape boundary is discussed at length in Ref. [5]. The instantaneous trajectory (grey) shows fast excursion outside r_{esc}, while the time-averaged trajectory (black) is confined in the trap bottom for longer time. (b) The “instantaneous” escape time, t'_{esc}, in grey, is significantly shorter than the “time-averaged” one. Furthermore the ratio of the two timescales depends on well depth, as depicted in the inset.

We point out that in the experiment, a molecule must reside in a given trap for $\Delta t \geq t_{\mathrm{exp}}$ in order to accumulate enough signal on the detector and be recognized as trapped. In the simulation, we use the same criterion on the minimum residence time when analyzing a particle position trajectory [5].

Comparing simulated “instantaneous” and “time-averaged” trajectories (see

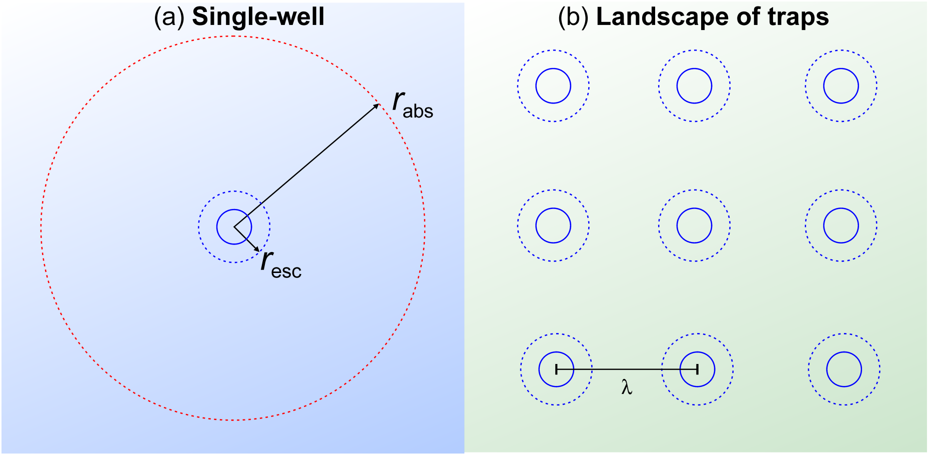

Figure 4.5: (a) Schematics of the important parameters in a single-well simulation. The blue solid line indicate the circumference of the pocket. The blue dashed line delineate the escape boundary r_{esc}. The red dotted line indicates the absorbing boundary condition, r_{abs}. An escape event is concluded when either the particle time-averaged radial position $< r >_{t_{\mathrm{exp}}}$ exceeds r_{esc}, or when the instantaneous coordinate $r > r_{\mathrm{abs}}$. (b) We consider a landscape of traps, of same geometry as in the experiment. The pitch λ is the distance between pocket centers.

Fig.4.4) it is clear why in general, for a given well depth, the "time-averaged" t_{esc} is substantially longer than the "instantaneous" t'_{esc}. This difference is effectively due to a finite return probability of the molecule to the bottom of the trap after an instantaneous, undetectable excursion (Fig.4.4a): this effect is also weakly dependent on well depth (inset in Fig.4.4b). It is intuitive that a particle sampling a shallow trap undergoes more frequent excursions out of the trap, compared with an object sampling a deeper well, tightly confined at the trap bottom and thus less likely to escape, even "instantaneously".

4.2.3 BD Simulation in a Landscape of Traps

Further, we compare a "time-averaged" simulation including only one well (Figure 4.5a), with the translational dynamics in a 2D landscape of traps (Figure 4.5b), corresponding to the experimental geometry.

For the "time-averaged" escape from a single well, we have set – similarly as in the instantaneous case – a radial escape criterion that must be exceeded in order to conclude an escape event. Furthermore we have defined a radial absorbing boundary condition, $r_{\mathrm{abs}} > r_{\mathrm{esc}}$, which also determines the end of an the escape event, if the instantaneous radial position transverses it (Figure 4.5a).

With the “landscape” approach, instead, we study a molecule sampling an array of traps, arranged according to the experimental e-beam design. Furthermore, we find that the time-averaged escape time is fairly insensitive to the position of the escape criterion r_{esc} for both the “single-well” and the “landscape” approaches. However, in the “landscape” case, t_{esc} increases with increasing pitch λ, and we find that two methods give the same simulated escape times only when the position of the instantaneous absorbing boundary conditions r_{abs} is $\approx \lambda$. This observation indicates that the overall dynamic is dominated by the location of the instantaneous absorbing boundary condition, rather than the time-averaged radial escape criterion.

Moreover this suggests that neighbouring wells in the landscape effectively act as equivalent absorbing boundaries for molecules sampling a given well, affecting the instantaneous probability of the particle escaping and returning to the same trap, and needs to be included in order to accurately reconstruct the escape process [5] (see Figure 4.6). Since experimentally we use different trapping geometries and the nanostructures may be arranged in square, rectangular or hexagonal lattices, it is not always straightforward to find the equivalent “single-well” absorbing boundary condition, hence we typically use the 2D “landscape” approach to interpret the experimental data. Furthermore, in our simulation, we also include the effect of the walls at either side of the nanoslit as reflecting boundary conditions.

To verify that the simulation captures correctly the effect of the pitch in the our experiment, we have performed ETe measurements in pocket lattices of identical R but increasing λ (Fig. 4.6) and found that the experimental results show a very similar trend.
In order to give a more general description, instead of decoupling λ and the molecule hydrodynamic radius, we illustrate the observed trends of t_{esc} as a function of a single parameter, $\lambda/l_{\mathrm{diff}}$, where the second term is the average diffusion length of a molecule during an exposure time, $l_{\mathrm{diff}} = \sqrt{4Dt_{\mathrm{exp}}}$ (Fig. 4.6a inset).

When $\lambda/l_{\mathrm{diff}}$ is large, out-of-the-well instantaneous excursions are unlikely to result in a “capture” in the next trap during t_{exp}. These fast, undetectable

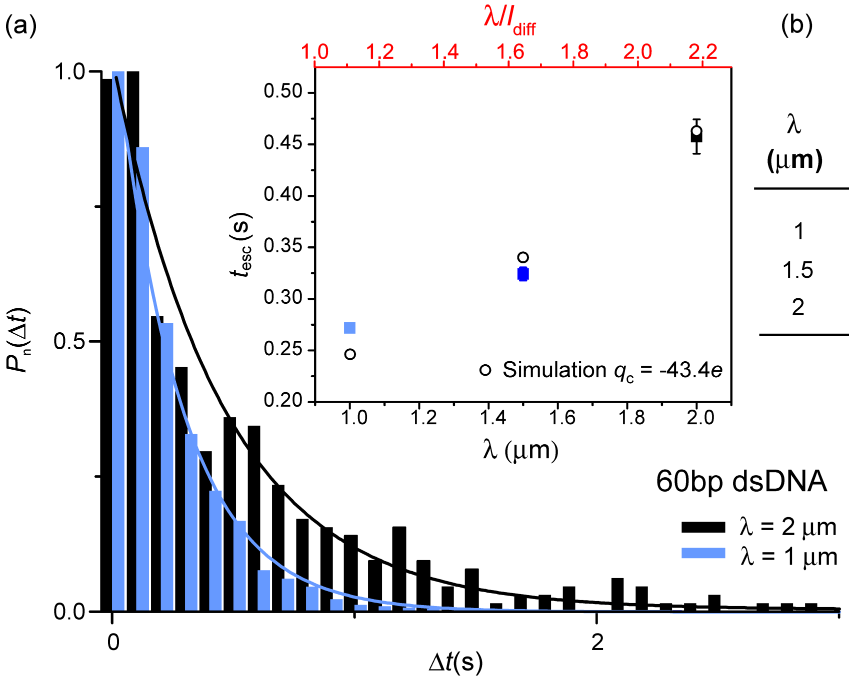

(b)

λ (μm)	$q_{m,sw}$ (-e)	$q_{m,lc}$ (-e)
1	38.2±0.1	43.8±0.2
1.5	39.7±0.2	42.3±0.2
2	42.6±0.4	42.8±0.4

Figure 4.6: Normalized probability distribution of measured escape times for 60 dsDNA molecules sampling 3 different lattices, characterized by the same pocket radius, but different pitch, λ. The inset compares the measurement (full symbols) with the simulation prediction (empty symbols). The top x-axis (in red) denotes the ratio $\lambda/l_{\mathrm{diff}}$ over the range explored. (b) If we don't include the right geometry in our BD simulation and only study escape from a single well with the same absorbing boundary conditions, r_{abs} placed approximately 2 µm away from the center of the trap in all 3 cases, the correct effective charge is inferred only in the case where $\lambda \approx r_{\mathrm{abs}}$. This suggests that the neighbouring traps effectively act as absorbing boundary conditions for a particle sampling a well. In the other cases the effective charge inferred from a single well approach, $q_{\mathrm{m,sw}}$, strongly departs from the true effective charge of the molecule. The values reported in the last column, $q_{\mathrm{m,lc}}$, which are obtained interpreting the measured timescale via a BD simulation which takes in account the different geometries of the lattices, are all in excellent agreement with the calculated value of charge for 60ds DNA, $q_{\mathrm{c}} = -43.4e$.

excursions simply result in a return into the same well and naturally inflate the "time-averaged" escape time, as if the molecule had actually never left the trap (Fig. 4.8b). A molecule sampling a more densely packed lattice ($\lambda/l_{\mathrm{diff}} \leq 1$), instead, has a comparatively lower return probability: this is because, once it instantaneously crosses the escape boundary of a well, it is very likely to be captured in another trap, thus concluding a – shorter – escape event (Fig. 4.8a).

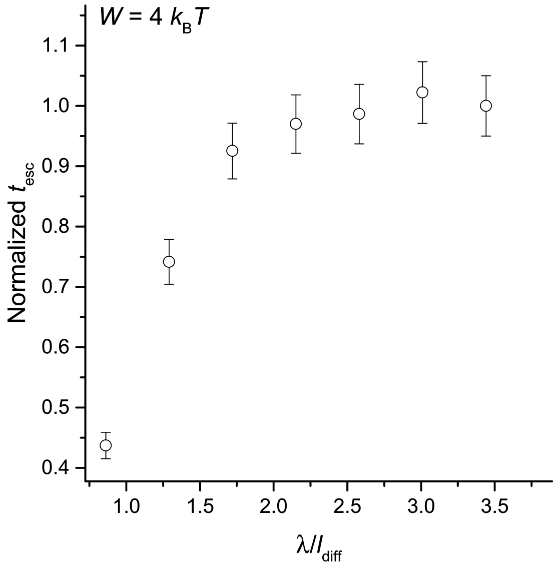

Figure 4.7: Simulated "time-averaged" escape times for a molecule sampling a landscape of traps of well depth, $W = 4k_{\mathrm{B}}T$, normalized against the value of t_{esc} obtained for $\lambda/l_{\mathrm{diff}} = 3.5$. The regime of $\lambda/l_{\mathrm{diff}} = 1 - 2$ was also investigated experimentally (Figure 4.6a). The value of $\lambda/l_{\mathrm{diff}} = 2$ mark the onset of the regime in which capture in a neighbouring pocket is highly unlikely and the trap can be thought as isolated.

To understand this effect more deeply, we have investigated a larger range of $\lambda/l_{\mathrm{diff}}$ by simulation (Figure 4.7). With increasing $\lambda/l_{\mathrm{diff}} > 2$, the simulated data shows that the escape time no longer monotonically increases.

The diffusion length l_{diff} represents the standard deviation of a gaussian probability distribution for two-dimensional diffusion, according to Fick's second law; thus for a particle initially located at (x, y) at time t, and which diffuses to (x', y') at time $t' = t + t_{\mathrm{exp}}$ (Figure 4.8), the probability of displacement $P(\sqrt{(x'-x)^2 + (y'-y)^2} > 2l_{\mathrm{diff}}) < 5\%$. Consequently, capture in a neighbouring pocket happens very rarely from this regime onwards and t_{esc} is maximized.

In essence, while for $\lambda/l_{\mathrm{diff}} < 2$ the neighbouring traps strongly influence t_{esc}, when this parameter is larger than 2, the pocket can be thought as isolated. The escape events, in this case, are not concluded when the molecule has reached another thermodynamic well, but rather when it is found in the "field-free" area between traps. (Fig. 4.8c). We point out that our typical ET*e* experiments are performed in the regime of $\lambda/l_{\mathrm{diff}} \approx 1$, and for this reason the geometry of the lattice is crucial to the right interpretation of the measured timescale.

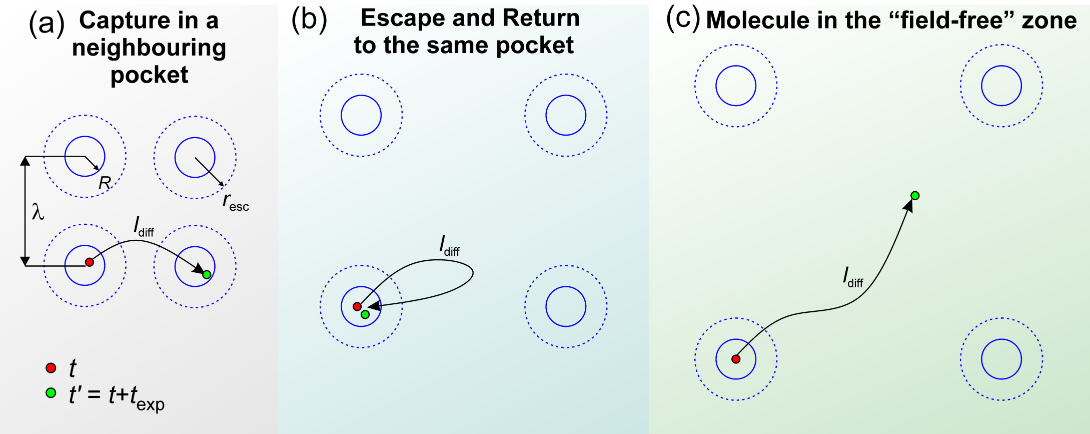

Figure 4.8: (a) Solid blue circle of radius R indicates the physical border of the pocket. Blue dashed circle of radius r_{esc} delimits the escape position threshold. The red dot indicates the (x, y) position at a time t, while the green one is the coordinate after one observation time, $t' = t + t_{\mathrm{exp}}$. For $\lambda < l_{\mathrm{diff}}$, as soon as the instantaneous radial coordinate of the particle crosses r_{esc}, instantaneous return to the same well is unlikely due to capture a neighbouring trap, resulting in shorter average escape time. (b) Frequent instantaneous returns to the same well when λ is large inflate t_{esc}. (c) t_{esc} is constant with increasing λ, for $\lambda > 2l_{\mathrm{diff}}$. At t', the molecule is found freely diffusing in the inter-well space.

We have also found that the time spent by the molecule diffusing from one trap to another, can be exploited to study another property of the object, namely its hydrodynamic radius. We call the "off-time", or t_{OFF}, the time spent by a molecule in the inter-well region, from the moment it escapes the r_{esc} of a pocket to when it is captured in the next well. This timescale is directly related to the diffusion constant of the object and scales roughly as $\lambda^2/4D$. Experimentally, the off-time is easily defined, since a small molecule (of $r_{\mathrm{H}} < 10$ nm), freely diffusing in the nanoslit, typically doesn't accumulate as much signal on the detector as when its fluorescence intensity is confined within a small trap: in practice, when it's not trapped, the molecule is almost invisible.

To conclude, the relationship between input well depth and simulated "time-averaged" t_{esc} in a 2D landscape of traps, gives an effective position relaxation time, depending on both r_{H} and array geometry, which we use to convert the experimentally measured timescales into W according to Eqn.1.10. Furthermore studying the resulting "on-off" signal of a molecule sampling a landscape of carefully spaced traps, we are able to correlate the high intensity stretches with the time spent in a well, while the low intensity intervals, in the same trace, simply correspond to the time spent freely diffusing. These two timescales, understood and modelled via comparison with BD simulations, can give both the molecule charge and its hydrodynamic radius [5].

5

ETe: Escape Time Electrometry

> "How did I escape? With difficulty. How did I plan this moment? With pleasure."
>
> ---
>
> *The Count of Montecristo*
> *Alexandre Dumas*

5.1 Electrometry

In the paper presented in this chapter, *"Single-molecule electrometry"*, [3], we introduce ETe as a novel detection method and apply it to several biomolecular species, ranging from small, weakly charged 10 bases single-stranded DNA to an highly charged intrinsically disordered protein, Stm-l [72]. In order to validate the technique, we have compared the measured charge, q_{m}, with theoretical models and with calculated effective charge, q_{c}, obtained from free-energy calculations. In general, we find that our measured effective charge for DNA molecules is in remarkable agreement with existing theoretical predictions that take charge renormalization into account, depending on the molecule structural charge density. This suggests that ETe can serve to readout the inter-

nucleotides spacing of an arbitrary nucleic acid molecule or polyelectrolyte. Our measurements on ProTα, a disordered one-dimensional polypeptide, also provides unique insight into the charge renormalizing behaviour of short, strongly charged segments within the molecule (see also Section 5.2).
The study of the enzyme Gusβ suggests substantial regulation of the structural charge in a globular molecule, due to the shifted pH experienced by its charged groups, as a result of the local dielectric environment.

Furthermore the exponential dependence of t_{esc} on the charge of the molecule permits us to distinguish between two ProTα variants that differ by a mutation of a single amino acid (E59K, 4% of the structural charge).

The figure below compares the results of effective charge measurements, q_{m}, vs. calculated values, q_{c}.

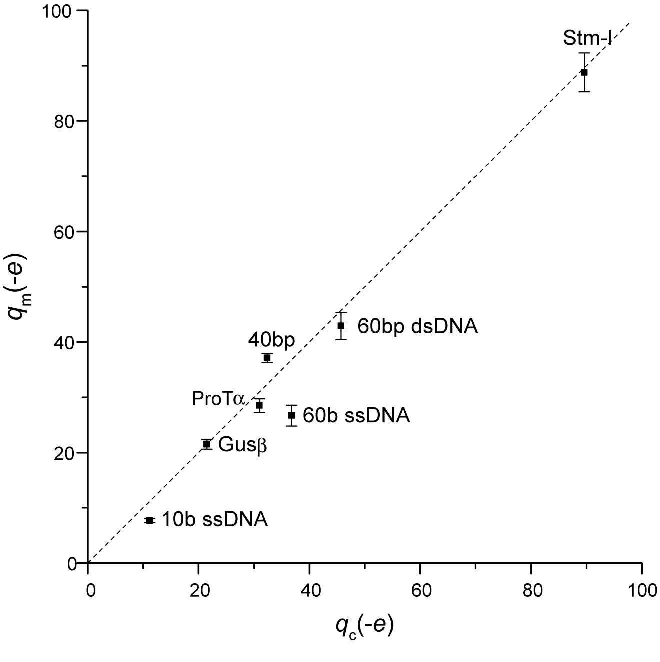

Figure 5.1: Values of measured vs. calculated effective charge for the molecules studied. The dashed line indicates the identity line.

Our manuscript concludes illustrating how ETe can also be applied to measure a single molecule in real time. We ensure that the trapping lattice is sparsely populated and follow the trajectory of an individual molecule, hopping from a lattice site to another. By averaging over few hops at the time ($N \sim 3-10$),

we obtain a reading of charge in real time, with a time resolution which is approximately Nt_{esc}, and is currently around 100 ms to 1 s. Our following paper, introduced in Chapter 8 (see Ref. [5]), develops further the concept of single-molecule ETe measurement and shows the ability of measuring both charge and size of the object from the same trajectory.
We point out that the ability to study a single molecule in real time opens up the possibility of detecting charge (and structure) fluctuations. This concept has been examined *in silico* and is illustrated in the final Chapter of this dissertation.

5.2 Measuring Differences between Protein Mutants

The unparalleled high sensitivity of ETe to the charge of a molecule, combined with the ability of measuring several molecular species one after the other in the same electrometry device, allow us to distinguish minute differences between them. The ability to detect small differences between proteins could have great relevance in biology: point mutations in enzymes, for example, can strongly affect their function and even cause genetic diseases [78].

With ETe we have compared the molecule ProTα ($q_{\mathrm{str}} = -46$e) with a variant that only differs from the original sequence by a point mutation (Glutamate E59 was mutated into a Lysine, K) and has a slightly lower structural charge, $q_{\mathrm{str}} = -44e$. This small difference in structural charge ($< 4\%$) produces a remarkable distinction in escape time. The E59K mutant escapes twice as fast as the original, difference easily detectable in a sequential ETe experiment [3].

In a further investigation, not included in our manuscript, we have also generated an additional ProTα variant, which carries a second mutation on the neighbour Glutamate E60, similarly changed into a Lysine (E59KE60K) and resulting in a structural charge, $q_{\mathrm{str}} = -42e$. (See Figure 5.2). Given this, naively we would expect this mutant to escape with an even faster timescale than the other two proteins, under the same experimental conditions. Interestingly, however, in this case we observed a less intuitive behaviour. Figure 5.3 reports the results of two sequential ETe measurements. While the protein E59K, as reported above [3], shows a considerably faster average escape time compared to the non mutated ProTα moiety – correlated with a lower effective charge – t_{esc} of E59KE60 mutant doesn't simply trend with q_{str}. The escape time of E59KE60K seems to be still slightly faster than the non-mutated ProTα

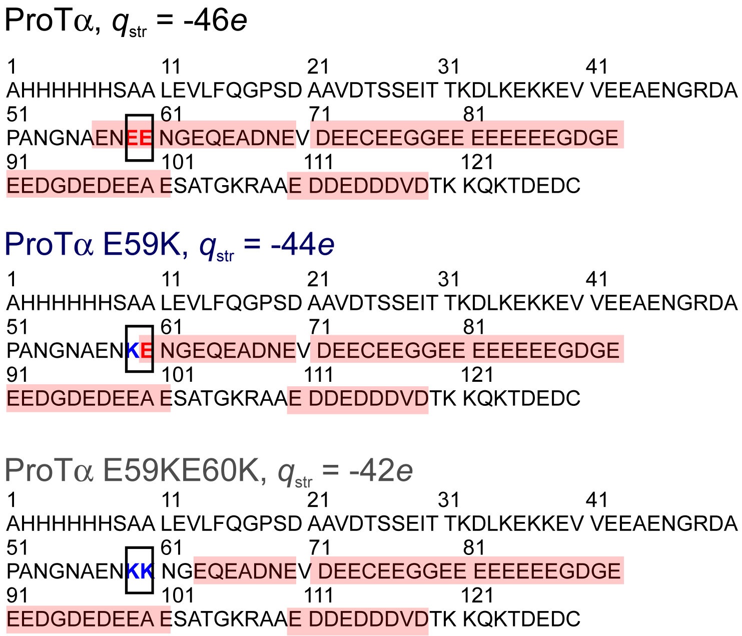

ProTα, q_{str} = -46*e*

1 11 21 31 41
AHHHHHHSAA LEVLFQGPSD AAVDTSSEIT TKDLKEKKEV VEEAENGRDA
51 61 71 81
PANGNAENEE NGEQEADNEV DEECEEGGEE EEEEEEGDGE
91 101 111 121
EEDGDEDEEA ESATGKRAAE DDEDDDVDTK KQKTDEDC

ProTα E59K, q_{str} = -44*e*

1 11 21 31 41
AHHHHHHSAA LEVLFQGPSD AAVDTSSEIT TKDLKEKKEV VEEAENGRDA
51 61 71 81
PANGNAENKE NGEQEADNEV DEECEEGGEE EEEEEEGDGE
91 101 111 121
EEDGDEDEEA ESATGKRAAE DDEDDDVDTK KQKTDEDC

ProTα E59KE60K, q_{str} = -42*e*

1 11 21 31 41
AHHHHHHSAA LEVLFQGPSD AAVDTSSEIT TKDLKEKKEV VEEAENGRDA
51 61 71 81
PANGNAENKK NGEQEADNEV DEECEEGGEE EEEEEEGDGE
91 101 111 121
EEDGDEDEEA ESATGKRAAE DDEDDDVDTK KQKTDEDC

Figure 5.2: Aminoacid sequence of the protein ProTα, of $q_{\text{str}} = -46e$, and its mutant created with site-directed mutagenesis. The molecule E59K, $q_{\text{str}} = -44e$, contains a single point mutation, while E59KE60K, $q_{\text{str}} = -42e$ was modified on two subsequent Glutamates, both mutated into Lysines and creating a difference of structural charge of -4e compared to the un-mutated sequence. Highlighted in red are the high negative charge density aminoacid stretches within the molecule. Square indicates positions of the mutated residues.

	Molecule	κh	t_{esc}(s)	q_{str}(-e)	q_m(-e)
Exp. no. 1	ProTα	3.39	2.30±0.12	46	$31^{\#}$±0.2
	E59K	3.29	1.08±0.03	44	27.7±0.1
	E59KE60K	3.32	1.87±0.11	42	28.3±0.2
	ProTα	3.34	3.53±0.46	46	29.9±0.5
Exp. no. 2	E59K	3.37	0.33±0.04	44	$27.7^{\#}$±0.2
	E59KE60K	3.34	1.12±0.16	42	29.2±0.3
	E59KE60K	3.30	0.85±0.02	42	29±0.2

Figure 5.3: Summary of sequential ETe experiments performed with ProTα (black) and its mutants E59K (blue) and E59KE60K (light grey). In each experiment the molecules were measured sequentially, in the same order as in the table (from top to bottom). Repetitions of the same molecule were performed in order to ensure the absence of artifacts, potentially given by repeatedly flushing the device. Differences in κh from one measurement to another within one round of sequential ETe are due to small variabilities in the measured salt concentration at the end of each measurement. The symbol # indicates that the measured charge of the first molecule was set equal to its calculated value, in order to perform a calibrated measurement of the subsequent ones.

molecule, yet consistently longer that the E59K species.

This behaviour might be due to the specific position of the mutations in the molecule, and could be explained via a more refined calculation of the protein effective charge.

At the moment, in most cases, the input of the calculations of q_{eff} is a uniform net charge distributed over the length of the molecule [19]. This is a good description for a molecule like DNA, in which the chargeable groups – the phosphate on the backbone – are indeed uniformly spaced; for a protein instead the distribution of charged aminoacids within the molecule is unlikely to be so constant. In the case of ProTα, most of the negatively charged aminoacids are actually contained in a stretch of 31 residues at the C-term and two smaller stretches of approximately 10 residues, which renormalize substantially (Figure 5.2). The calculations have already been refined by modeling the segments of the protein with different charge densities, and we in fact found good agreement of the predictions with our measurement of q_{eff} for the un-mutated protein and the E59K variant [3].

Yet, to capture the minute renormalization effects given by neighbouring charged residues, the calculation model would need to be refined further and in the future it will entail assigning the net charge of every individual aminoacid separately. There may be interesting effects in the electrostatics due to the two adjacent aminoacids, both mutated right at the beginning of an "high charge density" stretch within the molecule – as our measurements seem to suggest: this insight, given by the our new precise and fast method, will guide future modeling efforts and likely offer unprecedented understanding of the charge distribution within the molecule.

5.3 Measuring Effective Charge at low κh

As described at the beginning of this chapter, we have measured t_{esc} for a variety of biomolecules; furthermore, we have explored this timescale for a broad range of electrostatic midplane potentials.

Eqn.1.9 indicates that, ψ_{s} remaining constant, the measured well depth is solely a function of κh. We have been able to verify this in experiments (Figure 5.4b), observing that large variation of both salt concentration (and thus κ) and the slit height, $2h$, tuned in order to give the same multiplicative factor κh, result in identical measured well depths and, consequently q_{eff}, for all molecules. On this account, we describe our system – holding the geometry of the trapping nanostructures and the surface potential constant – by a single parameter, κh. Assuming that the effective charge of a molecule is also constant in our range of interest ($c = 0.25 - 2$ mM, pH $= 8.8$ [28]), t_{esc} is expected to increase exponentially with κh. To give a rough estimate, for $\kappa h = 3$, a molecule of $r_{\mathrm{H}} = 4$ nm carrying 40 charges should experience about 13 $k_{\mathrm{B}}T$ worth of well depth, and thus trap for many hours.

Contrarily, when we started exploring this low κh regime, we have observed a rather unexpected behavior. For all molecules studied, t_{esc} grows in the expected fashion only when the electrostatic free energy, $q_{\mathrm{eff}}\psi_m$, is lower than a certain empirical energy threshold $F^* \sim 4k_{\mathrm{B}}T$ (Figure 5.5, 5.6). This is the typical regime in which we perform our ETe measurements, which anyway take advantage of the fast dynamics of molecules sampling shallow wells. For higher interaction potentials however, a much weaker dependance is observed: if we take, for example, a 60ds DNA fragment ($q_{\mathrm{c}} = -43.4e$), measured at $\kappa h = 2.4$, we would expect the molecule to experience a well depth of approximately 22

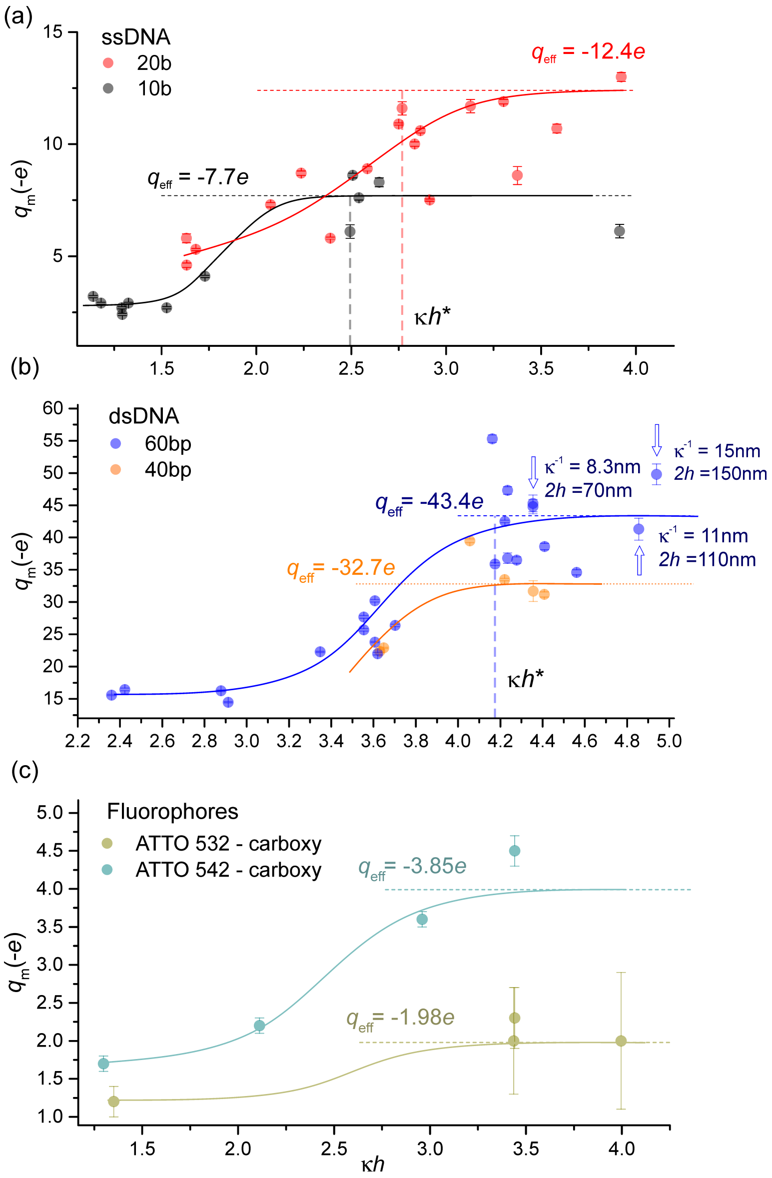

Figure 5.4: ETe measurement of effective charge, q_{m} for ssDNA (a), dsDNA (b), and weakly charged fluorophores (c) [6], over a broad range of κh. Each point represent a single, non calibrated measurement. Error bars indicate the precision of each experimental measurement, arising from statistical noise alone, and are standard error of the mean. All molecules show a considerable reduction of measured charge below a certain κh, noted as κh^*. The saturation value agrees well with calculated values of q_{eff} (dashed lines). Solid lines are a guide to the eye. In (b) the arrows draw attention to a few representative measurements, performed under similar κh conditions, but modulating either κ or $2h$. We find that the measured q_{eff} responds to variations of these parameters is an identical fashion, as long as the multiplicative factor, κh, is kept constant.

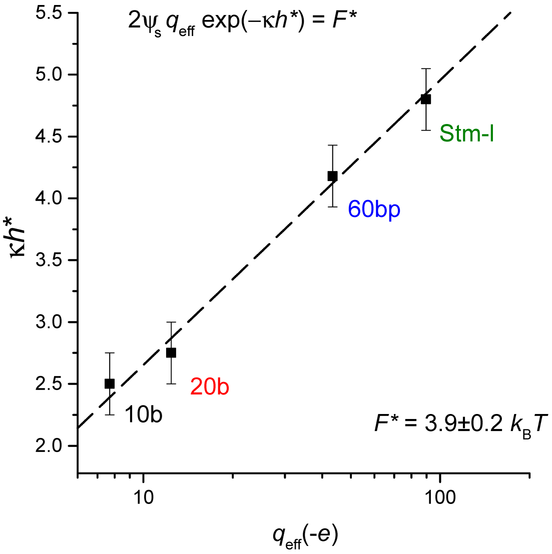

Figure 5.5: The κh threshold, κh^*, above which q_{m} saturates to the calculated value of effective charge, is estimated from Figure 5.4. We have plotted κh^* vs. the measured effective charge of each molecule examined. The error bars correspond to the average resolution at which we measured q_{eff} as function of κh, $\sim 0.25\kappa h$. From a fit of the form $\kappa h^* = \ln(2\psi_{\mathrm{s}} q_{\mathrm{eff}}) - \ln(F^*)$ (dashed line) we find an overall free energy threshold value, F^*, same for all molecule of approximately 3.9 $k_{\mathrm{B}}T$, above which t_{esc} departs from the behaviour expected and consequently $q_{\mathrm{m}} < q_{\mathrm{c}}$.

$k_{\mathrm{B}}T$, which corresponds to *many days* worth of trapping time. Interestingly, the timescale we measure experimentally in this case is only a *few tens of seconds*, which points to a well depth more than twice as small, $\approx 9k_{\mathrm{B}}T$. If we simply convert this well depth to a measurement of charge, assuming the nominal mid-plane potential, this gives a q_{m} value of $\sim -15e$, significantly smaller than the value measured at high κh (Figure 5.4b).

We point out that the inaccuracy of the charge measurement under these conditions is estimated to be fairly small, around 2%. The large discrepancy in the experimentally observed well depth compared to the theoretical expectation could be attributed to a mis-estimation of the system parameters – for example a channel height 50% larger than the value measured with Profilometer – which is highly unlikely. Tuning of the Silicon Oxide charge regulation model for the surface potential (See Eqn.2.4) doesn't give a satisfactory explanation of the overall behaviour, especially in the regime of $\kappa h < 3$ where a deficit of interac-

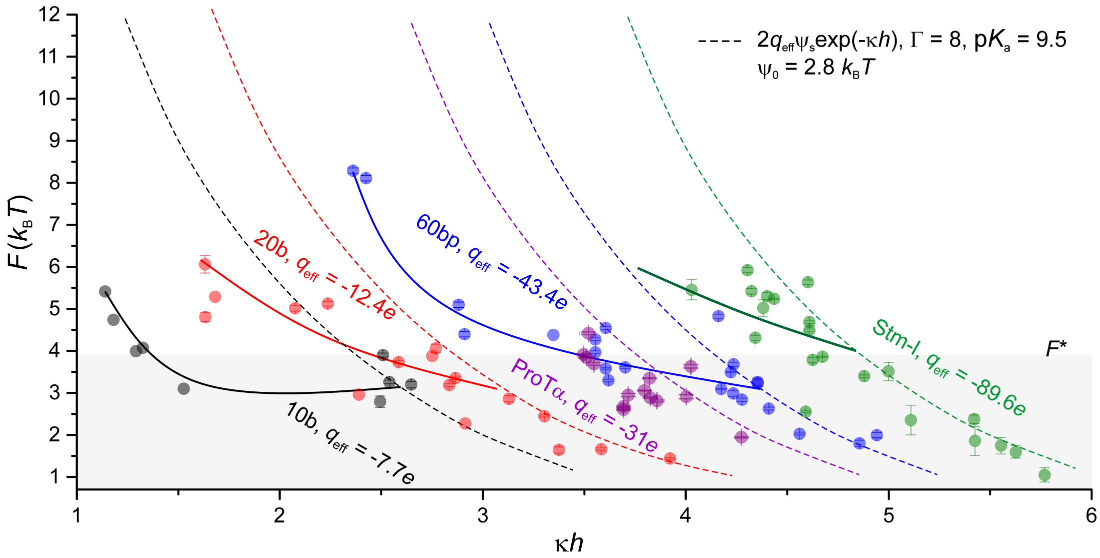

Figure 5.6: Measurement of the electrostatic free energy, F, for a range of molecule, using the nominal midplane potential and the values of effective charge measured previously [3, 4, 6] (Fig. 5.4). The dashed lines indicate the expected behaviour given the our usual midplane potential model and assuming the same q_{eff} of the object over the whole range of κh; the measurement however reveals a strong departure from the expected behaviour above an energy threshold F^*, shaded in grey. Solid lines serve as a guide to the eye.

tion free energy, ΔF, of tens of $k_{\mathrm{B}}T$ is clearly shown from our measurements (Figure 5.7). In addition, we consistently observe this decreasing trend of q_{m} vs. κh for all the molecules studied (Figure 5.4 and Figure 5.6), even down to a weakly charged fluorophores (Figure 5.4c).

We note a κh threshold, κh^*, above which q_{m} saturates to the calculated value of effective charge and is different for each molecule (Figure 5.5). Given the typical fractional error on q_{m}, $\sigma_{\mathrm{q}} = q_{\mathrm{m,e}}/q_{\mathrm{m}} = 6\%$ [3], we estimate κh^* as the lowest point in which a measurement falls within $q_{\mathrm{c}} \pm 2\sigma_{\mathrm{q}}$. Analyzing the relationship of κh^* with the effective charge of the molecules studied, we find an underlying common free energy limit, F^*, above which the measurement of electrostatic free energy, F, strongly departs from the theoretical prediction (Figure 5.6). We remark that F is the component of W due to electrostatics alone. Nevertheless, our ETe experiments intended to accurately measure effective charge [3, 4, 5, 6] are performed in the regime of $\kappa h > \kappa h^*$ for each molecule.

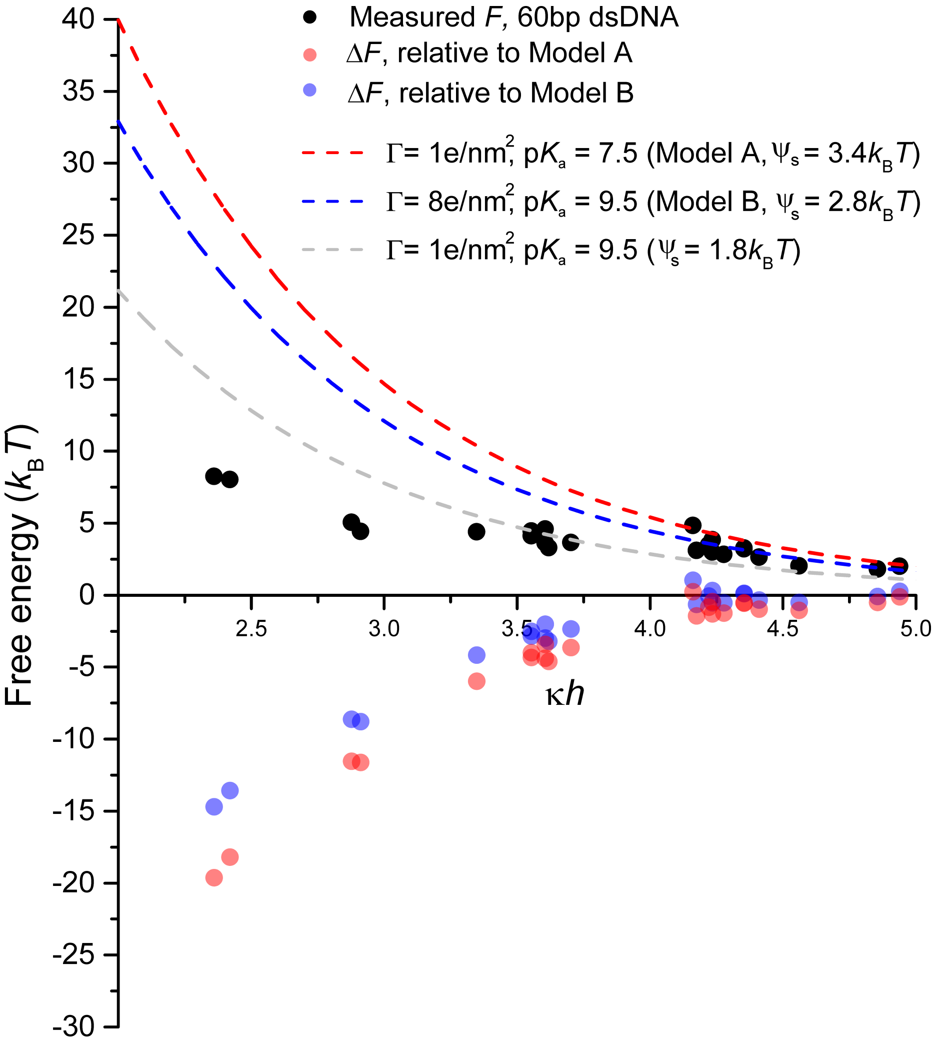

Figure 5.7: Measured electrostatic free energy for 60bp dsDNA compared with the expected behaviour from the SiO_2 regulation model Eqn.2.4, varying chargeable group density, Γ, and pK_a. A simple variation of these two parameters cannot reconcile the behaviour across the whole κh range examined. Deficit in free energy is plot in the negative y axis, relative to two SiO_2 models. The values of effective surface potential, ψ_s, for each model are also reported. A deficit of almost 20 k_BT of energy at $\kappa h = 2$ suggests a missing term in our electrostatic free energy model. Error bars – arising from statistical error alone – on each measurement point are smaller than symbols. Additional error in the measurement is due to inaccuracy in the estimation of the midplane potential, mainly due to uncertainty in the channel height, $2h$ (see Supp. Info in Ref. [3]). This inaccuracy is $\sim 2\%$ for $\kappa h = 2$, $\sim 6\%$ for $\kappa h = 3.5$ and $\sim 25\%$ for $\kappa h = 5$.

Preliminary observation in the regime of even higher electrostatic interaction ($\kappa h < 1$ and $\psi_m > 2k_{\mathrm{B}}T$), indicate absence of trapping. The molecules, including the weakly charged ATTO dyes, probably freely diffuse in the landscape, without experiencing any confining force. The electrostatic potential seems to have vanished, and the small entropic contribution to the well depth arising from z-fluctuations of the object in the nanostructure is simply not enough to provide significant confinement ($f \sim 2k_{\mathrm{B}}T$ for a typical pocket geometry of $\beta \sim 3$ [6]). It is worth mentioning that low values of κh are typically obtained by creating very shallow nanochannels, since the minimum inverse Debye length we have been able to achieve in water, with no added salt, is $\sim 0.04\mathrm{nm}^{-1}$. This implies the need of gaps as narrow as 60 nm to have $\kappa h \sim 1$. As we have discussed in Chapter 2, channels of height < 65 nm are challenging to fabricate, since they typically either sag or fully collapse upon anodic bonding (Fig. 2.8). When this occurs, the experimental results are unpredictable, since often the fluorescence background in the channels is too high to assess the presence of the molecules in the slit (see Fig. 2.10). Alternative approaches to performing experiments in the regime $2h < 65$ nm were not explored in this work.

Finally, by fitting the measured deficit of electrostatic free energy, $\mid \Delta F \mid$ to an exponential function of κh (Figure 5.8), we find the this term grows strongly with κh, as $\exp(-B\kappa h)$, where $B = 1.45$, while F only grows as $\exp(-\kappa h)$. This implies that, if we compare the expected behaviour of F (Figure 5.8 inset) and the deficit term at low κh, for $\kappa h < 1.5$, the latter overcomes in magnitude the electrostatic free energy (Figure 5.8 inset, shaded in red), effectively canceling the trapping potential, as we have experienced experimentally. This measurement of deficit of free energy (Figure 5.7), resulting even in a complete loss of trapping, to our knowledge cannot be reconciled by varying the parameters of the electrostatic model used so far (e.g. $\mathrm{SiO_2}$ pK_{a} value or chargeable group density, Γ, Figure 5.7). We believe that additional effects at low κh may need to be considered in order to justify this unexpected behaviour and describe the whole parameter space: further experimental analysis, investigating for example the response of different materials as well as $\mathrm{SiO_2}$, might unravel the physics of this interesting regime.

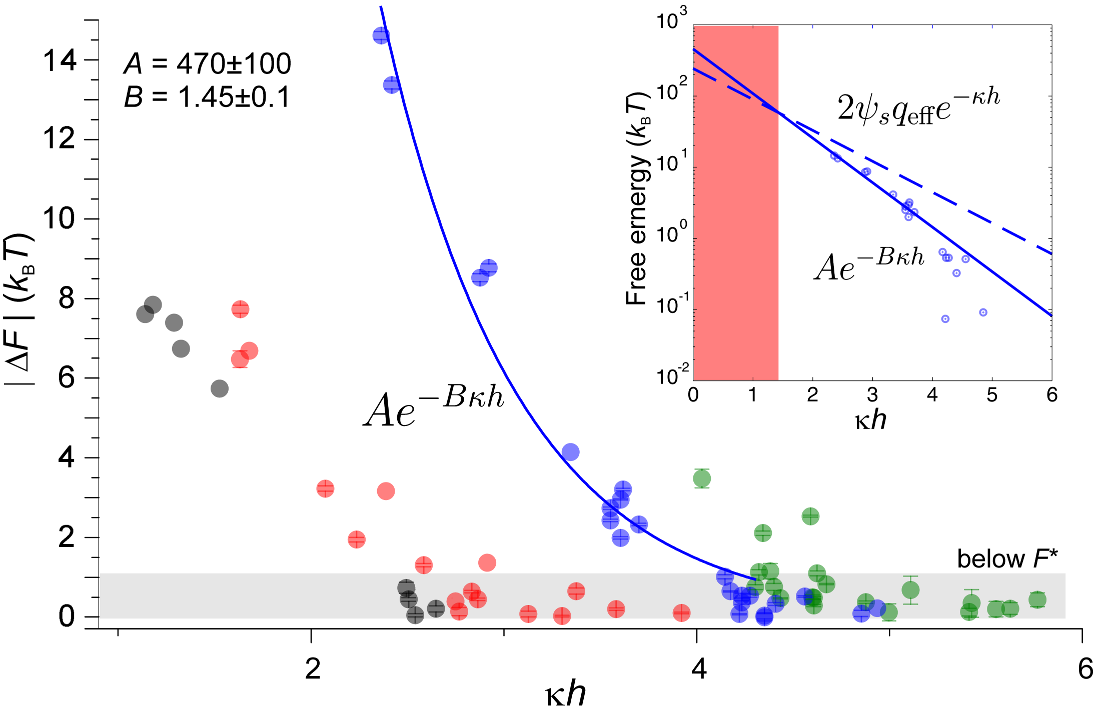

Figure 5.8: Deficit in free energy for the molecules studied, 10ssDNA (black), 20b ssDNA (red), 60bp dsDNA (blue) and Stm-l (green). The data from 60 dsDNA, which spans the larger range of κh, is fit with an exponential form $A\exp(-B\kappa h)$. The deficit term grows faster with κh than the electrostatic free energy, overcoming it for κh lower than 1.5 and hence predicting no trapping under these conditions. We have indeed observed absence of trapping, for this molecule, already in the regime of κh $\sim$ 1.2, although in an irreproducible fashion due to experimental uncertainty on the slit height.

ARTICLES
PUBLISHED ONLINE: 13 MARCH 2017 | DOI: 10.1038/NNANO.2017.26
nature nanotechnology

Single-molecule electrometry

Francesca Ruggeri[1], Franziska Zosel[2], Natalie Mutter[2], Mirosława Różycka[3], Magdalena Wojtas[2,3], Andrzej Ożyhar[3], Benjamin Schuler[2,4] and Madhavi Krishnan[1,4]*

Mass and electrical charge are fundamental properties of biological macromolecules. Although molecular mass has long been determined with atomic precision, a direct and precise determination of molecular charge remains an outstanding challenge. Here we report high-precision (<1e) measurements of the electrical charge of molecules such as nucleic acids, and globular and disordered proteins in solution. The measurement is based on parallel external field-free trapping of single macromolecules, permits the estimation of a dielectric coefficient of the molecular interior and can be performed in real time. Further, we demonstrate the direct detection of single amino acid substitution and chemical modifications in proteins. As the electrical charge of a macromolecule strongly depends on its three-dimensional conformation, this kind of high-precision electrometry offers an approach to probe the structure, fluctuations and interactions of a single molecule in solution.

The electrostatic properties of macromolecules—specifically, their electrical charge and interior dielectric characteristics—are a vital component of their function as they contribute to the physical basis of mechanisms that range from molecular recognition, signalling and enzymatic catalysis to protein folding and aggregation, and are of fundamental relevance in experiment and theory[1–4]. 'Supercharged' isoforms of evolutionarily conserved proteins are known to confer extreme physiological capacities on certain species, presumably because of their enhanced stability to aggregation at high concentrations[5,6]. Moreover, the addition and removal of small amounts of structural charge—in the form of phosphate groups or other post-translational modifications—modulates not only such a basic phenomenon as protein stability, but also subcellular localization or function, and can regulate macroscopic processes such as metabolism at the systemic level[4]. A recent study demonstrated that the addition of as few as two phosphate groups to a protein induced a folding–unfolding transition and altered its binding affinity by orders of magnitude[3]. Not surprisingly, several disease states are correlated with altered phosphorylation of proteins, for example, disordered proteins, such as tau and α-synuclein involved in Alzheimer's and Parkinson's disease, and multimeric proteins, such as the stress-activated p53 implicated both in ageing and cancer[7,8]. A high-precision, direct measurement of the effective charge of a macromolecule in solution would not only permit the detection of minute differences of chemical composition in molecules, but would also offer a new physical dimension to systematically probe three-dimensional (3D) molecular structures and monitor structural changes in real time, which has important biochemical and biophysical implications.

At the simplest level, a direct sum over a macromolecule's charged groups yields a qualitative estimate of its net electrical charge at a given solution pH:

$$q_{\mathrm{str}} = \sum_i \frac{je}{1 + 10^{j(\mathrm{pH} - \mathrm{p}K_i)}} \qquad (1)$$

where i denotes each ionizable group, pK_i is the negative logarithm of its acid dissociation constant and $j = +1$ or -1 for basic or acidic groups, respectively. In practice, however, collective interactions in a densely packed system of charges can dramatically modify the molecule's effective charge in solution via two separate phenomena—namely, charge regulation and charge renormalization. The former concerns an alteration in the charged state of an ionizable group in the context of the molecular environment, whereas the latter deals with the highly nonlinear screening of molecular charge by counterions in the surrounding electrolyte phase. Both phenomena generally result in a reduced effective charge of an electrically charged object, and have received extensive theoretical attention, from polyelectrolytes[9,10] and proteins[11,12] to colloidal particles[10,13–15] and charged surfaces in solution.

Here we present a methodology to measure a macromolecule's electric charge with the precision of a single charge and below (<1e) by exploiting the electrostatic fluidic trap for nanoscale matter in solution[16,17].

Trapping charged macromolecules in solution

The trap is created in a fluid-filled gap between two electrically charged walls. Nanoscale structuring of one of the surfaces leads to a modulation of the local electrostatic potential, which creates a deep thermodynamic potential well for a like-charged molecule (Fig. 1a,b). In our experiment, we introduce the molecular species of interest labelled with two fluorescent dye molecules, at a typical concentration of 50 pM in a solution of total salt concentration $c \sim 1$–3 mM (up to 2.5 mM NaCl, 1 mM Tris, pH 8.7–9.1), into an array of electrostatic fluidic traps and image the dynamics using wide-field fluorescence microscopy. In our current work, the physical dimensions of the geometric perturbation that creates the trap (nanostructure depth and diameter generally 200–600 nm) are much larger than the Debye length, $\kappa^{-1} \sim 10$ nm, the characteristic length scale of electrostatic interactions. As a result, a molecule in a trap inhabits a region of zero electric field and zero electrical potential, and chemical equilibrium ensures that the solution conditions at the bottom of the potential well, where the molecule spends most of its time, are identical to those in the bulk solution.

We achieve stable trapping of biomolecules such as 10–60 base oligonucleotides of ssDNA, dsDNA and intrinsically disordered proteins (IDPs) (prothymosin α (Protα, 10 kDa) (refs 18,19) and starmaker-like protein (Stm-l, 40 kDa) (ref. 20)), and a globular

---

[1]Department of Chemistry, University of Zurich, Winterthurerstrasse 190, CH 8057 Zurich, Switzerland. [2]Department of Biochemistry, University of Zurich, Winterthurerstrasse 190, CH 8057 Zurich, Switzerland. [3]Department of Biochemistry, Faculty of Chemistry, Wrocław University of Technology, Wrocław, Poland. [4]Department of Physics, University of Zurich, Winterthurerstrasse 190, CH 8057 Zurich, Switzerland. *e-mail: madhavi.krishnan@uzh.ch

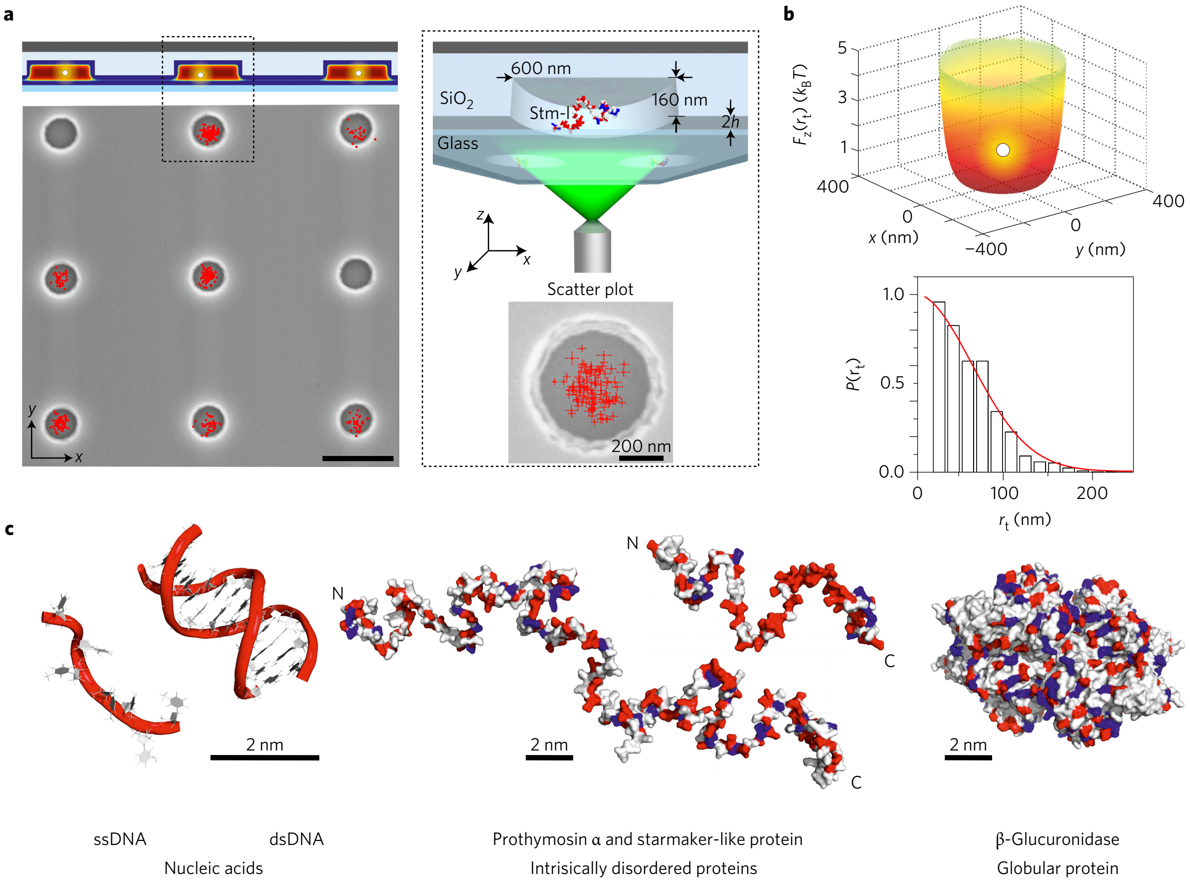

Figure 1 | Long-term trapping of single nucleic acid and protein molecules in solution. **a**, Schematic representation of fluorescently labelled disordered protein Stm-l confined in an electrostatic fluidic trap (top), with a slit height of $2h = 75$ nm, a trapping nanostructure diameter of 600 nm and a depth of 160 nm in a solution of 1 mM Tris (salt concentration, $c = 0.25$ mM). The bottom panels present spatial scatter plots of single confined molecules superimposed on a scanning electron micrograph (SEM) of the surface topography. Scale bar, 1 µm (left panel). Scatter plots were generated from stroboscopic images acquired using exposure times, $t_{exp} = 10$ ms, at a sampling rate of 70 mHz over a total measurement period >30 min using wide-field fluorescence microscopy and single-particle tracking. **b**, The inferred x-y distribution of the minimum axial (z) electrostatic free energy in the confining potential well, $F_z(r_t)$ (top), and measured radial sampling probability, $P(r_t)$, of a single trapped Stm-l molecule (bottom), where $r_t = \sqrt{x^2 + y^2}$. **c**, Structural models of the various biomolecules considered in this study, with charged residues highlighted in red (negative) and in blue (positive).

tetrameric enzyme, β-glucuronidase (Gusβ, 290 kDa) in aqueous solution. The physical properties of interest for all the molecules are summarized in Supplementary Table 1. Figure 1a presents single Stm-l molecules confined in an array of electrostatic fluidic traps on timescales longer than 30 min.

The depth of the potential well, W, determines the time, t_{esc}, spent by the molecule in the trap[21], and can be modulated using either the geometry of the well or the ionic strength of the solution, or both. Decreasing W to approximately $6k_BT$, where k_B is Boltzmann's constant and T is the temperature, permits a transition from the regime of long-term trapping to short dwell times, $t_{esc} \leq 1$ s.

The escape-time electrometry approach

Operating in the rapid escape regime, with a sampling time in imaging smaller than t_{esc}, we can, on timescales of ~100 ms to 1 s, acquire adequate statistics on the escape process (~100 escape events). An exponential fit to the histogram of residence times yields a measurement of t_{esc} that is precise to within 5% (Fig. 2c and Supplementary Movie 1). Thus, we achieve an accurate measurement of the average escape time, t_{esc}, of a few molecules, thermally sampling a high-density array of shallow traps (Fig. 2c and Supplementary Fig. 7).

The depth of the trap, W, links the experimentally measured t_{esc} with the electrical charge of a trapped molecule. In thermally activated escape from a deep potential well, the mean escape time of an object, t_{esc}, depends exponentially on the well depth, W, as illustrated by a Kramers-type expression, $t_{esc} = t_r \exp(W/k_BT)$ (ref. 21). Here t_r is a timescale that depends on the position relaxation of the particle in the well (which depends on its experimentally measured hydrodynamic radius, r_H) (Supplementary Fig. 3 and Supplementary Table 1) and the geometry of the trapping potential. The dominant contribution to W in our experiment is the molecule's spatial electrostatic free energy, $F(r)$. Calculating $F(r)$ as previously described[22], we find that it is well expressed by the relation $F(r) = q_{eff}\psi(r)$ (Supplementary Section 1), where $\psi(r)$ is the local electrostatic potential caused by the nanostructure and q_{eff} denotes the effective electrical charge of the molecule. The nanostructure geometry and salt concentration in the experiment together determine $\psi(r)$ (ref. 16). 3D Brownian dynamics (BD) simulations of the escape of a point object with a friction coefficient $6\pi\eta r_H$, from a potential well whose morphology is given by $F(r)$, yields the theoretically expected relationship between a simulated escape time, t_{sim}, and q_{eff} (Fig. 2d). The t_{sim} versus q_{eff} functional dependence thus readily converts the experimentally measured timescale t_{esc} into a measured effective charge, q_m. BD simulations are a one-time effort and the obtained t_{sim} versus q_{eff} relationship can be simply rescaled to account for variations in trap geometry and salt concentration. Further, although

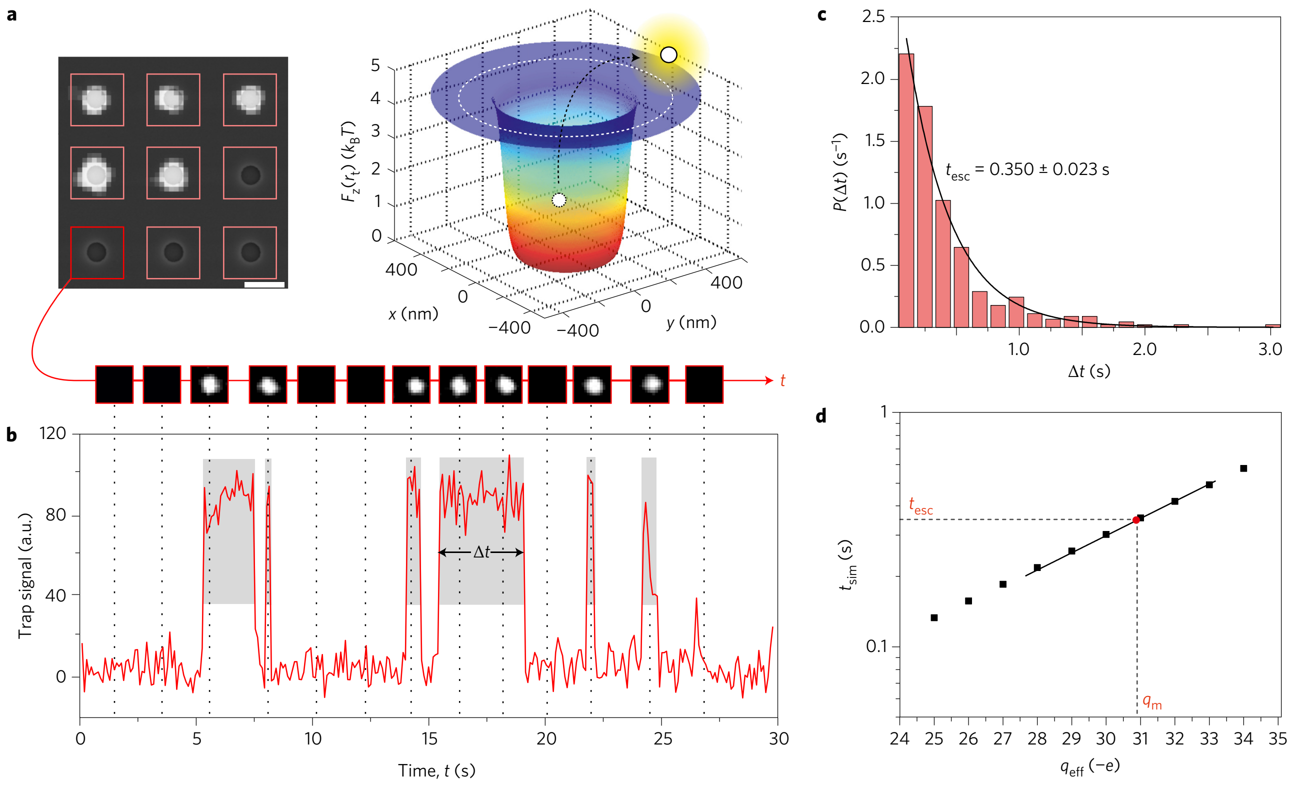

Figure 2 | ETe to determine the electrical charge of a trapped species. a, A single snapshot of fluorescently labelled ProTα molecules sampling a 3 × 3 array of electrostatic fluidic traps (left) with slit height $2h = 76.4$ nm (scale bar, 1 μm). The shape of the inferred confining potential well is given on the right. A series of snapshots of the array acquired using an exposure time of $t_{exp} = 30$ ms at a frequency of 33 Hz over a period of ~30 s is analysed by recognizing the regions of interest defined by the locations of single traps (red squares) and monitoring the average intensity in the region as a function of time. **b**, A representative time trace of a single region-of-interest. The time traces are analysed using a step-finding algorithm that identifies and determines the duration of residence of a molecule in a trap, Δt. **c**, Residence- (escape-) time data recorded for ~10–15 molecules ($N = 300$ escape events) are pooled and the normalized histogram fit with a single exponential of the form $P(\Delta t) = (A/t_{esc})\exp(-\Delta t/t_{esc})$, which represents a Poisson process, in which t_{esc} denotes the average measured escape time and $A \approx 1$ (further details in Supplementary Fig. 7). **d**, 3D BD simulation result of the average escape time, t_{sim}, of a molecule as a function of its effective charge, q_{eff} (black squares). The Brownian walk begins at the electrostatic potential minimum at $r_t = 0$ and the molecule is considered to have escaped the well when it traverses the dotted contour line in **a**. The black line is a linear fit of the obtained t_{sim} versus q_{eff} dependence in the range of interest. In this case, the measured $t_{esc} = 0.35 \pm 0.023$ s (red circle) converts into a measured charge, $q_m = -30.9 \pm 0.4e$ (Supplementary Fig. 8).

the molecule is treated as a point object from the standpoint of the electrostatics, its finite hydrodynamic radius, r_H, is required in the BD simulation to correctly capture the timescales of its diffusive motion in the free-energy landscape.

Crucially, the exponential dependence of t_{esc} on the molecule's solution-phase electrical charge renders possible charge measurements with a precision much better than the elementary charge, e. We thus introduce the concept of 'escape from a potential well' as a measurement principle that offers major advantages over the previously described tracking-based approach to determine the charge of single colloidal particles in solution[17]. Using the functional form of the spatial confining potential to determine the charge of a trapped object requires high signal-to-noise ratio detection of the particle, with the experimentally measured quantity, for example, a spring constant of confinement, depending at best linearly on the entity's charge. The escape-time approach we describe here utilizes a telegraphic 'on–off' signal trace (Fig. 2a,b) and is ideally suited to the measurement of weak emitters, thus enabling the investigation of single molecules.

Overall, the statistically limited experimental error of <5% on t_{esc} implies a precision of <2% in the charge determination in a single measurement. In practice, however, the experimental uncertainty, $h_e \approx 1$ nm, on the slit height (Supplementary Fig. 1) results in an estimated overall single-measurement uncertainty of ~10%, as evidenced by the spread in the measured values from one experiment to the next (Supplementary Fig. 8). This device-related measurement uncertainty can, however, be reduced to the level of 2–6% by averaging, as reflected in Fig. 3. However, a sequential (parallel) measurement on spectrally identical (separable) molecules in a single device would permit us to attain a statistically limited measurement precision and thus distinguish molecular species that carry very similar amounts of charge (see below). Escape-time electrometry (ET*e*) thus offers a direct, rapid, highly sensitive and precise measurement of the charge of a single nano-object or macromolecule in solution. The measurement does not require knowledge of the molecule's composition or structure. Given a protein's amino acid composition, however, we show that the measured charge, q_m, can be compared with the calculated effective charge, q_c, determined from free-energy calculations[22] (Supplementary Section 1), and used to infer the 3D distribution of the charge in the molecule, as well as to estimate a dielectric coefficient of the molecular interior for folded molecules. Thus, observing the 'hopping dynamics' of a single molecule in a well-determined free-energy landscape should yield a wealth of information on its physical and structural properties.

Measuring the effective electrical charge of biomolecules

Double-stranded DNA (dsDNA), a uniformly charged linear polyelectrolyte that possesses negatively charged phosphate

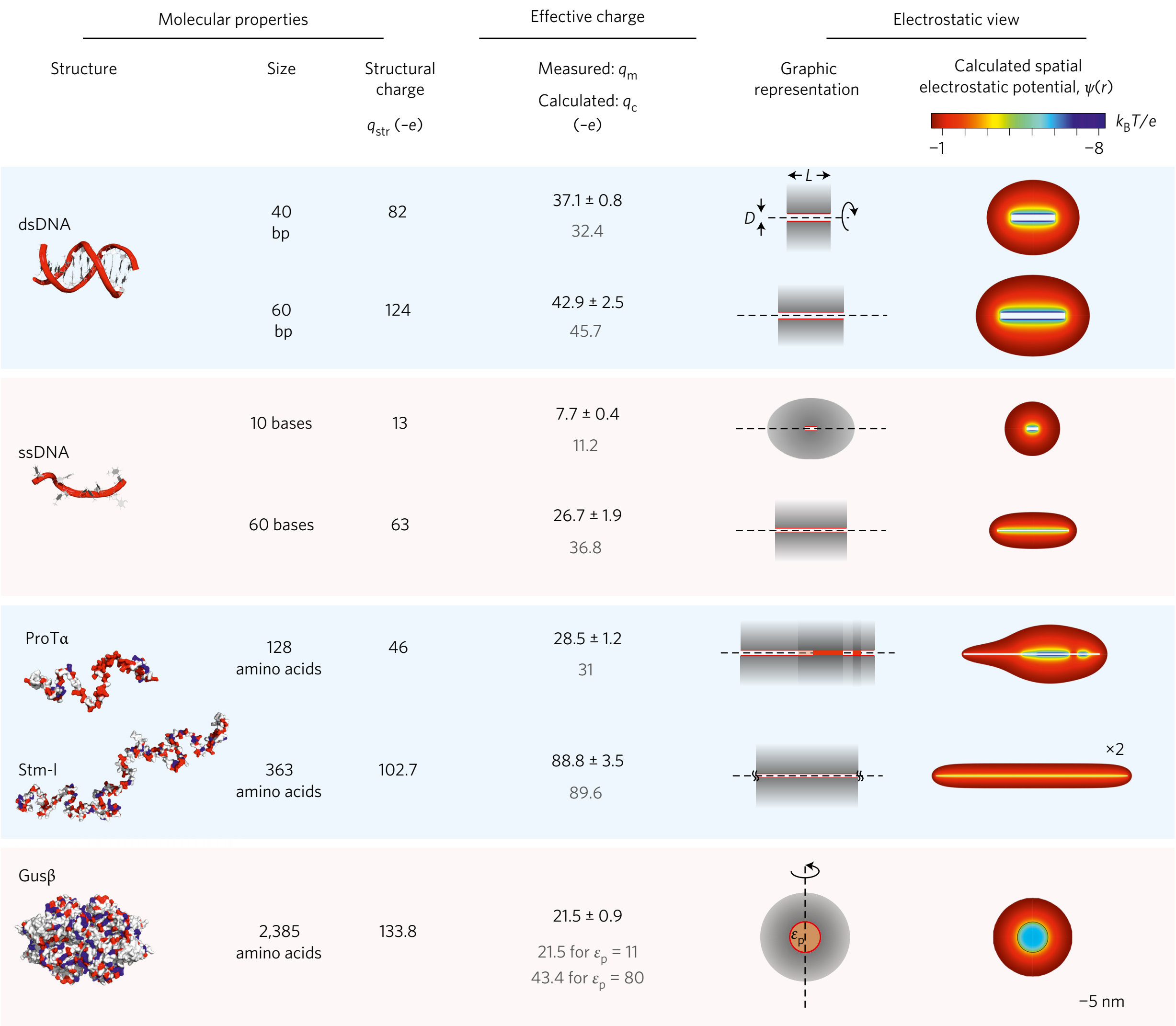

Figure 3 | The effective electrical charge of nucleic acids and proteins measured using ETe. Columns from left to right: structures of the biomolecules in Fig. 1c; the size of the molecule; the structural charge, q_{str}, calculated from equation (1) at the experimental pH, including the contribution of Atto 532 dye molecules; the effective electrical charge, both measured, q_m (top), and calculated, q_c (bottom) (Supplementary Section 1); a molecular electrostatic view with a schematic representation of the modelled molecular geometry on the left, in which the dotted line denotes the axis of cylindrical symmetry, the regions of net negative charge are coloured red and the spatial solution-phase counterion density is in shades of grey, *L* and *D* denote the full contour length and diameter for the linear polyelectrolytes (Supplementary Table 1), and (right) the calculated spatial electrostatic potential distributions, $\psi(r)$, for each molecule under the conditions of the measurement. Spatial scale for Stm-I is reduced by a factor of two. The values for q_m denote averages over several independent measurements listed in Supplementary Fig. 8 and the quoted errors are s.e.m.

groups (p$K_a = 2.2$), serves as an ideal test object for our effective charge measurement. A key length scale in the analysis of the effective charge of polyelectrolytes is the Bjerrum length, $l_{B,m} = (e^2/4\pi\varepsilon_m\varepsilon_0 k_BT)$, which denotes the distance over which two unit charges that interact via a medium of dielectric coefficient, ε_m, experience k_BT worth of interaction energy, where ε_0 is the permittivity of free space ($l_{B,w} = 7.14$ Å in water at 25 °C). Single-stranded DNA (ssDNA) and dsDNA are assumed to have uniform charge spacings, $b = 4$ and 1.7 Å, smaller than $l_{B,w}$, which means that strong charge renormalization is expected[9,23].

We take the structural charge, q_{str} of an unlabelled DNA fragment n bases in length as $n + 1$ for ssDNA and $2n + 2$ for dsDNA, which accounts for an additional negative charge on the 5′-end phosphate group. Further, all the DNA oligomers in our measurements are labelled fluorescently with two Atto 532 dye molecules, which adds an additional two negative charges to the molecule in all cases but one (Supplementary Fig. 4). Measurements were performed in a regime in which the total observation time of a single molecule is much shorter than the photobleaching time of the fluorescent labels (Supplementary Fig. 7). dsDNA fragments 40 base pairs (bp) and 60 bp in length reveal measured effective charges, $q_m = -37.1 \pm 0.8e$ and $-42.9 \pm 2.5e$, respectively, that compare well with the corresponding calculated values of $q_c = -32.4e$ and $-45.7e$. These values are substantially larger than the expected $q_{eff} = (b/l_{B,w})q_{str}$ for infinitely long charged rods[9] because in our experiments we probe the molecules in the regime $\kappa^{-1} \simeq L$, the fully extended length of the molecule. Here finite-size effects make important contributions to the electrostatics[24], as evident in the electrical potential distributions presented in Fig. 3. For 10 base and 60 base fragments of ssDNA, however, our measurements surprisingly reveal values of effective charge that are around 30% smaller than both our calculated q_c values and other theoretical predictions (Supplementary Table 2). The reasons for this discrepancy may lie in the high flexibility of ssDNA and its propensity for

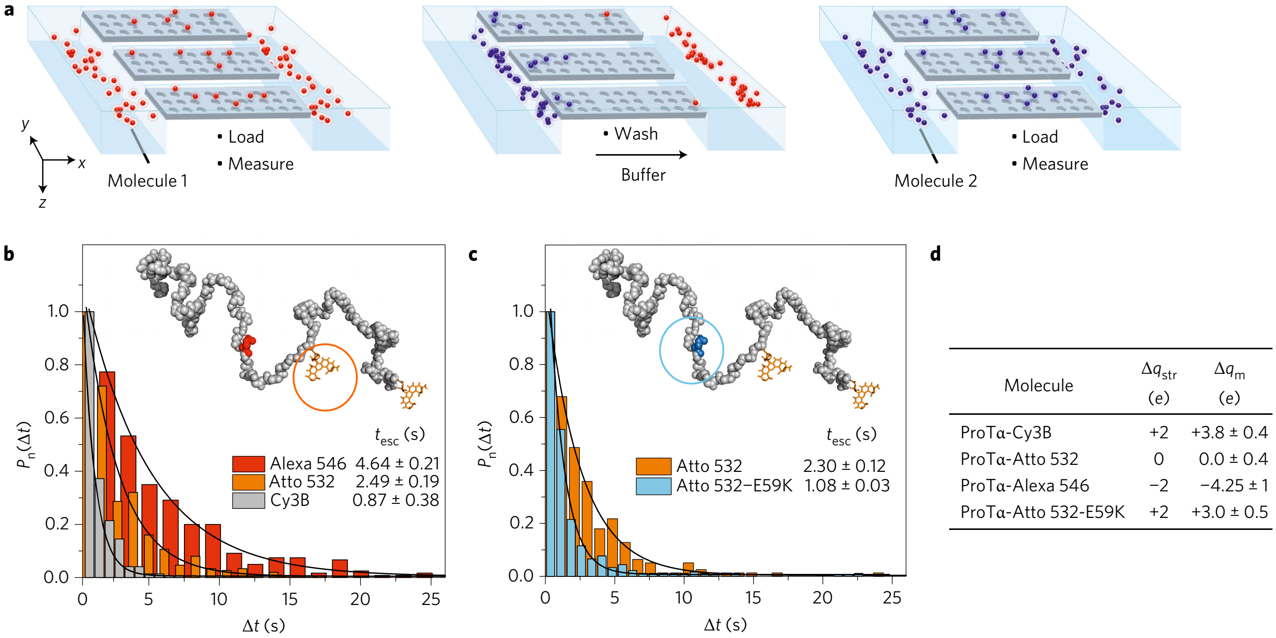

Molecule	Δq_{str} (e)	Δq_m (e)
ProTα-Cy3B	+2	+3.8 ± 0.4
ProTα-Atto 532	0	0.0 ± 0.4
ProTα-Alexa 546	−2	−4.25 ± 1
ProTα-Atto 532-E59K	+2	+3.0 ± 0.5

Figure 4 | Sequential ETe to detect chemical modifications and amino acid exchanges in a disordered protein. a, Schematic depiction of sequential ETe in a single device. The measurements were performed in 1 mM Tris, ~1 mM NaCl, in slits of height $2h = 65$–72 nm. The device is flushed with buffer between measurements of different species. **b**, Measured escape-time histograms, $P_n(\Delta t) = (P(\Delta t)/P_{max}(\Delta t))$, and fit values of t_{esc} for ProTα labelled with Cy3B (0*e*), Atto 532 (−1*e*) and Alexa 546 (−2*e*). The chemical structures of the dye moieties are presented in Supplementary Fig 4. **c**, Histograms and fit values of t_{esc} for ProTα and ProTαE59K, which carry a single amino acid exchange. **d**, Tabulated measured charge differences, Δq_m, for the dye-derivatized molecules and single amino acid exchange, relative to ProTα-Atto 532 ($\Delta q_m = q_{m,mol} - q_{m,ProT\alpha\text{-}Atto\ 532}$). Uncertainties are s.e.m. over 2-3 series of measurements in different devices.

transient long-range intramolecular base pairing, which together render the rigid uniformly charged rod an inadequate description of the electrostatics.

Turning our attention to proteins—macromolecules that can possess complex 3D structures and contain a mixture of charged groups of different pK_a values—we consider the IDPs ProTα and Stm-l and the folded protein Gusβ. ProTα and Stm-l are similar in that both are disordered polyelectrolytes with no secondary structure, but they differ widely in structural charge. Stm-l and the globular protein Gusβ, on the other hand, have nearly the same value of q_{str}, but may be regarded as representing two limiting cases at the level of 3D structure (Fig. 1c). All the proteins are fluorescently labelled with Atto 532, and each dye molecule is chemically coupled to a cysteine residue on the protein. The IDPs carry exactly two dyes per molecule and Gusβ an average of 2.1 dyes per molecule. Performing measurements at pH 8.8 ensures that the labelling leaves the structural charge of the molecule essentially unchanged.

For ProTα and Stm-l, estimates of the mean intercharge spacing, $b = 10$ Å and 12.7 Å $> l_{B,w}$, suggest that, unlike a strongly charged polyelectrolyte like DNA, the electrostatic interactions within these disordered proteins are relatively weak, and charge renormalization is unlikely to play as significant a role. For example, consider ProTα with a structural charge of $q_{str} = -46e$. Assuming a uniform average linear charge density of $1e\ \text{nm}^{-1}$, our calculation suggests an effective charge of around −37.5*e*. The measurement, however, reveals $q_m = -28.5 \pm 1.2e$, a substantially smaller value. Interestingly, we find that the observation can be explained largely by considering the pattern of charge within the primary structure of the molecule, as opposed to merely its residue composition. Rather than a uniformly distributed net charge, ProTα carries most of its net negative charge (−25*e*) within a C-terminal stretch of 31 amino acids, flanked by two shorter stretches of high net negative-charge density (shaded red in Fig. 3, and see Supplementary Fig. 4). With $b = 3.6$ Å, these highly charged segments show substantial charge renormalization, resulting in a calculated effective charge of $q_c = -31e$, which is close to the experimental measurement.

For Stm-l, with a structural charge of $q_{str} = -102.7e$ and $b > l_{B,w}$, Manning theory predicts no renormalization[9], whereas Netz and Orland[10] predict some renormalization, with $q_{theory} = -96e$ (Supplementary Table 2). Indeed, our experimental observation of a comparatively large effective charge, $q_m = -88.8 \pm 3.5e$, reveals little charge renormalization, and agrees remarkably well with our calculated value, $q_c = -89.6e$ (Supplementary Table 2).

We then studied IDPs with sequential ETe on distinct molecular species with the aim of measuring small differences in structural charge between closely related molecular isoforms in a single experiment. We performed escape-time measurements on each molecular species of interest in a sequential manner in a single ETe device, with intermediate steps of flushing with buffer solution, as shown in Fig. 4. We focus on four modified versions of ProTα, three that are labelled with different fluorescent dye molecules, and a fourth carrying a mutation that replaces a negatively charged glutamate (E) residue with a positively charged lysine (K) at a single site. The dye molecules are organic entities that carry net charges of 0 (Cy3B), −1*e* (Atto 532) or −2*e* (Alexa 546) per molecule (Supplementary Fig. 4). Our results demonstrate the ability to easily resolve ~5% differences in charge in the electrostatics of molecular isoforms by direct measurement (Fig. 4), which is much larger than the ~1% precision of the method.

Finally, we focus on Gusβ, a globular tetrameric protein whose charge is dominated by acidic groups distributed fairly uniformly throughout its 3D structure (Protein Data Bank entry 3K46, Supplementary Fig. 5). At pH 8.8, the expected net charge based purely on the molecule's amino acid composition is $q_{str} = -133.8\ e$. Approximating a globular protein of total charge q_{str} by a dielectric sphere of radius *R* filled with a uniform density of acidic groups

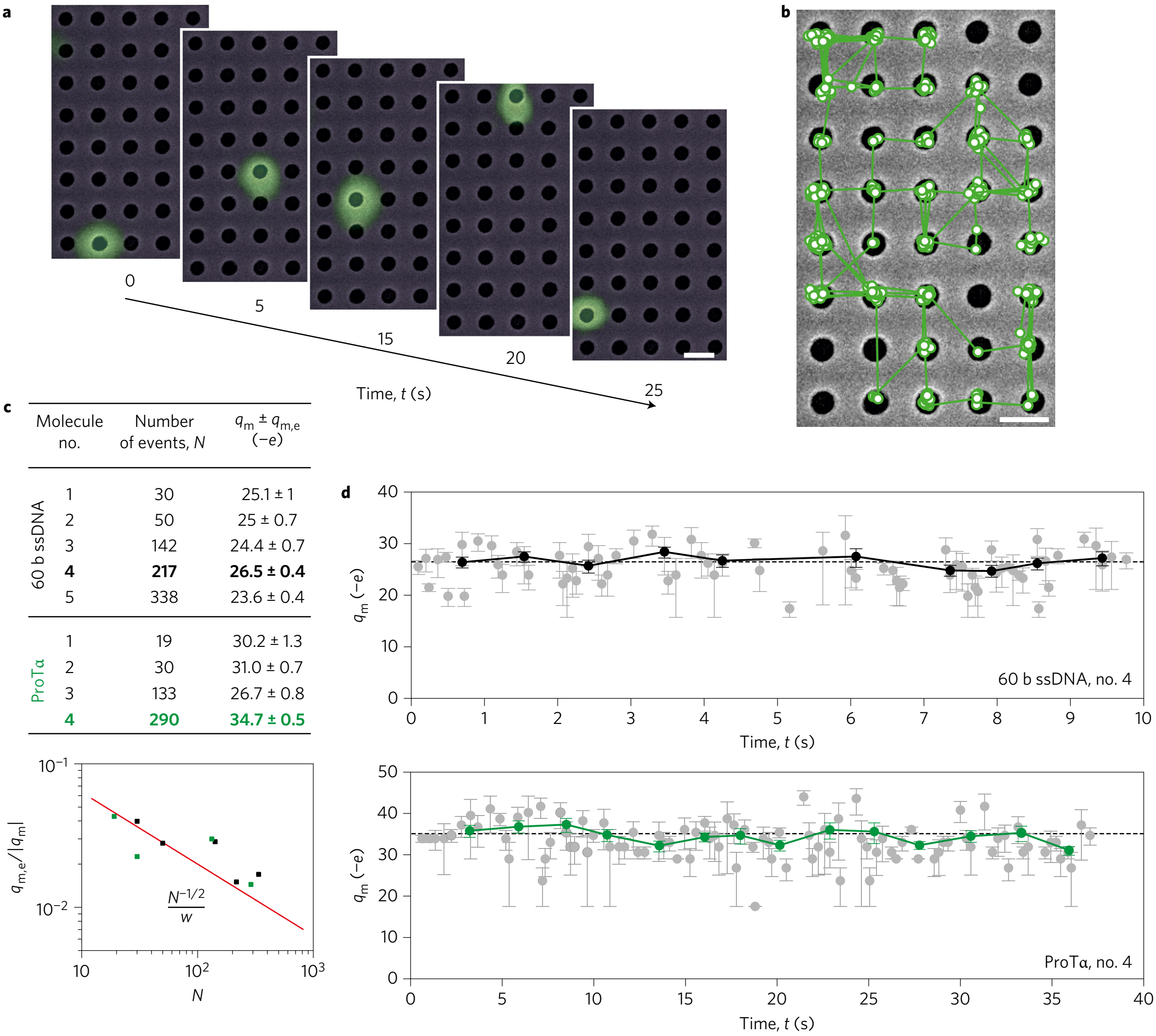

	Molecule no.	Number of events, N	$q_m \pm q_{m,e}$ (−e)
60 b ssDNA	1	30	25.1 ± 1
	2	50	25 ± 0.7
	3	142	24.4 ± 0.7
	4	**217**	**26.5 ± 0.4**
	5	338	23.6 ± 0.4
ProTα	1	19	30.2 ± 1.3
	2	30	31.0 ± 0.7
	3	133	26.7 ± 0.8
	4	**290**	**34.7 ± 0.5**

Figure 5 | Real-time measurement of the electrical charge of a single molecule. a, Optical snapshots of a single 60 base ssDNA molecule (false colour) sampling an array of traps, superimposed on an SEM of the trapping topography where the nanostructure diameter is 300 nm. **b**, The trajectory of the molecule in time is used to generate its escape-time histogram. Scale bars, 500 nm. **c**, q_m for single molecules determined from N recorded escape events or hops. The fractional uncertainty on each measurement, $q_{m,e}/|q_m|$, is plotted below. The red line denotes the dependence ($N^{-1/2}/w$) where, as expected, the fit parameter $w = 5 \pm 0.6$ is close to $(\langle W\rangle/k_BT) = 6.8 \pm 0.8$, the average measured trap depth over all molecules in these measurements. **d**, Binning a long single-molecule trajectory into groups of $N = 3$ and 20 consecutive events yields real-time measurements of q_m at overall average temporal resolutions of ~150 ms (grey symbols) and ~1 s (black symbols) for ssDNA (top), and 370 ms (grey symbols) and 2.5 s (green symbols) for ProTα (bottom). Data are presented for molecule no. 4 in each group. Time-averaged q_m values are plotted as dashed lines in each case. All the images were acquired using exposure times of $t_{exp} = 5$ ms; the experimental timescales were $t_{esc,60\text{ b}} = 34$ ms and $t_{cycle} \approx 5$ ms for 60 base ssDNA and $t_{esc,\text{ProT}\alpha} = 72$ ms and $t_{cycle} = 25$ ms for ProTα. For a given species, the average q_m over all single molecules compares well with the ensemble measurements of Fig. 3. Error bars, s.e.m.

of p$K_a \cong 4$, an analysis at pH 7 suggests a threshold criterion $(|q_{str}|l_{B,p}/eR) \simeq 10$–15 for the onset of charge regulation, where $l_{B,p} = (e^2/4\pi\varepsilon_p\varepsilon_0 k_B T)$ (using Supplementary equation (1)). Taking $q_{str} = -133e$ and $R = r_H = 5.1$ nm, even assuming a high value of $\varepsilon_p = 78.5$ for the dielectric constant of the interior of the protein, suggests substantial charge regulation in the molecule. Remarkably, the measurement reveals t_{esc} values for Gusβ comparable rather to those of ProTα than of Stm-l, with an associated experimentally inferred charge of $q_m = -21.5 \pm 0.9e$. Tuning the value of ε_p in our free-energy calculation, we find that the measurement implies $\varepsilon_p = 11$, which serves as a physical indication of the molecule's compact folded state. By way of comparison, an atomistic calculation of the net charge of Gusβ under the experimental conditions and assuming $\varepsilon_p = 11$ yields $q_{theory} = -24.3e$ (ref. 25) (Supplementary Section 1), which agrees very closely with our prediction. The measurement thus reveals substantial charge regulation for the globular protein, which confirms the theoretical expectations based on a low dielectric interior[26,27].

Measuring the charge of a single molecule in real time

As escape times are exponentially distributed, the fractional measurement uncertainty on t_{esc} from a sample of N statistically independent 'hops' of a molecule is simply $N^{-1/2}$ (Supplementary Fig. 7). For $N = 100$, the logarithmic dependence of q_m on t_{esc} implies ~2% precision in determining q_m. Speeding up the escape process so that $t_{esc} < 20$ ms and binning the entire time trace into consecutive blocks of $N = 2$–100 hops permits a real-time read out of the charge of a single molecule at a time resolution of ~20 ms to 1 s with respective uncertainties on q_m of ~20–2%. From a study of single 60 b ssDNA and ProTα molecules in this fashion, we demonstrate the ability to measure the effective charge of a single molecule in real time (Fig. 5 and Supplementary Movie 2). Comparing our measurements with simulations shows that the temporal charge fluctuations presented in Fig. 5d are largely statistical in origin (Supplementary Fig. 9). At the fundamental level, the concept we propose would enable, for the first time, the observation of equilibrium effective-charge fluctuations of a single molecule in solution that arise from, for example, reactions, interactions or conformational changes.

Conclusions

The similarity in structural charge of Stm-l and Gusβ, but the enormous difference in their measured effective charge, highlights a central feature of this work, namely the experimental demonstration that 3D structure plays a decisive role in the solution-phase electrical charge of a biological macromolecule. Furthermore, in conjunction with atomistic models of the protein interior, a direct measurement of a protein's net charge using ET*e* could be used to probe the local dielectric environment of the protein, and thereby contribute substantially to the calibration of force-field parameters in fully atomistic approaches[28].

Although the measurements reported here were performed in a low salt environment (~2 mM), future experiments with an optimized trap design and the use of alternative dielectrics or lipid bilayers as surface materials will enable charge measurements in the higher salt regime. Moreover, even though a comparison of the resulting measured value of $q_m = -88.8e$ for Stm-l, for instance, with the corresponding theoretically expected value of $q_c = -89.6e$ implies excellent accuracy in the technique, it is nonetheless possible that the measured values in Fig. 3 carry an underestimate of up to ~10%. The uncertainty in a single measurement could be reduced, and the accuracy of the method improved further, by including a calibration molecule in the measurement whose effective charge is accurately known. One possibility would be a linear polyelectrolyte that carries a known number of ionizable groups spaced at a uniform distance, b, significantly larger than the Bjerrum length, l_B. Doing so would circumvent residual uncertainties in slit height and salt concentration, and enable the attainment, in a single measurement, of an accuracy that potentially approaches the high precision offered by the escape-time principle. Additionally, the requirement of the method for a relatively low signal-to-noise ratio of about three is ideally suited to the use of direct optical detection techniques, for example, scattering interferometry, which could in future obviate the need for chemical labelling of the molecule of interest[29,30].

Beyond the individual molecule, these measurements can be readily applied to monitor intermolecular interactions, for example, measuring binding free energies associated with molecular recognition[31,32]. Finally, as previously implemented in mass spectrometry, sequence-specific chemical modification, introduction of amino acid exchanges or proteolytic cleavage could be used to probe the 3D structure of the object of interest, enabling ultrasensitive, rapid structural studies on biological macromolecules and molecular complexes in the fluid phase[33,34].

Data availability. The data that support the plots within this paper and other findings of this study are available from the corresponding author on reasonable request.

Received 25 August 2016; accepted 31 January 2017;

References

1. Perutz, M. F. Electrostatic effects in proteins. *Science* **201,** 1187–1191 (1978).
2. Warshel, A., Sharma, P. K., Kato, M. & Parson, W. W. Modeling electrostatic effects in proteins. *Biochim. Biophys. Acta* **1764,** 1647–1676 (2006).
3. Bah, A. *et al.* Folding of an intrinsically disordered protein by phosphorylation as a regulatory switch. *Nature* **519,** 106–109 (2015).
4. Kamerlin, S. C. L., Sharma, P. K., Prasad, R. B. & Warshel, A. Why nature really chose phosphate. *Q. Rev. Biophys.* **46,** 1–132 (2013).
5. Lawrence, M. S., Phillips, K. J. & Liu, D. R. Supercharging proteins can impart unusual resilience. *J. Am. Chem. Soc.* **129,** 10110–10112 (2007).
6. Mirceta, S. *et al.* Evolution of mammalian diving capacity traced by myoglobin net surface charge. *Science* **340,** 1234192 (2013).
7. Martin, L., Latypova, X. & Terro, F. Post-translational modifications of tau protein: implications for Alzheimer's disease. *Neurochem. Int.* **58,** 458–471 (2011).
8. Bode, A. M. & Dong, Z. G. Post-translational modification of p53 in tumorigenesis. *Nat. Rev. Cancer* **4,** 793–805 (2004).
9. Manning, G. S. Limiting laws and counterion condensation in polyelectrolyte solutions. I. Colligative properties. *J. Chem. Phys.* **51,** 924–933 (1969).
10. Netz, R. R. & Orland, H. Variational charge renormalization in charged systems. *Eur. Phys. J. E* **11,** 301–311 (2003).
11. Lund, M. & Jonsson, B. Charge regulation in biomolecular solution. *Q. Rev. Biophys.* **46,** 265–281 (2013).
12. Ninham, B. W. & Parsegian, V. A. Electrostatic potential between surfaces bearing ionizable groups in ionic equilibrium with physiologic saline solution. *J. Theor. Biol.* **31,** 405–428 (1971).
13. Alexander, S. *et al.* Charge renormalization, osmotic-pressure, and bulk modulus of colloidal crystals—theory. *J. Chem. Phys.* **80,** 5776–5781 (1984).
14. Aubouy, M., Trizac, E. & Bocquet, L. Effective charge versus bare charge: an analytical estimate for colloids in the infinite dilution limit. *J. Phys. A* **36,** 5835–5840 (2003).
15. Belloni, L. Ionic condensation and charge renormalization in colloidal suspensions. *Colloids Surf. A* **140,** 227–243 (1998).
16. Krishnan, M., Mojarad, N., Kukura, P. & Sandoghdar, V. Geometry-induced electrostatic trapping of nanometric objects in a fluid. *Nature* **467,** 692–695 (2010).
17. Mojarad, N. & Krishnan, M. Measuring the size and charge of single nanoscale objects in solution using an electrostatic fluidic trap. *Nat. Nanotech.* **7,** 448–452 (2012).
18. Gast, K. *et al.* Prothymosin-alpha—a biologically-active protein with random coil conformation. *Biochemistry* **34,** 13211–13218 (1995).
19. Mueller-Spaeth, S. *et al.* Charge interactions can dominate the dimensions of intrinsically disordered proteins. *Proc. Natl Acad. Sci. USA* **107,** 14609–14614 (2010).
20. Rozycka, M. *et al.* Intrinsically disordered and pliable starmaker-like protein from Medaka (*Oryzias latipes*) controls the formation of calcium carbonate crystals. *PLoS ONE* **9,** e114308 (2014).
21. Kramers, H. A. Brownian motion in a field of force and the diffusion model of chemical reactions. *Physica* **7,** 284–304 (1940).
22. Krishnan, M. Electrostatic free energy for a confined nanoscale object in a fluid. *J. Chem. Phys.* **138,** 114906 (2013).
23. Manning, G. S. Molecular theory of polyelectrolyte solutions with applications to electrostatic properties of polynucleotides. *Q. Rev. Biophys.* **11,** 179–246 (1978).
24. Manning, G. S. Approximate solutions to some problems in polyelectrolyte theory involving nonuniform charge distributions. *Macromolecules* **41,** 6217–6227 (2008).
25. Gordon, J. C. *et al.* H++: a server for estimating pK_as and adding missing hydrogens to macromolecules. *Nucleic Acids Res.* **33,** W368–W371 (2005).
26. Li, L., Li, C., Zhang, Z. & Alexov, E. On the 'dielectric constant' of proteins: smooth dielectric function for macromolecular modeling and its implementation in DelPhi. *J. Chem. Theory Comput.* **9,** 2126–2136 (2013).
27. Sham, Y. Y., Muegge, I. & Warshel, N. Effect of protein relaxation on charge–charge interaction and dielectric constants in protein. *Biophys. J.* **76,** A198–A198 (1999).
28. Isom, D. G., Castaneda, C. A., Cannon, B. R. & Garcia-Moreno, B. E. Large shifts in pK_a values of lysine residues buried inside a protein. *Proc. Natl Acad. Sci. USA* **108,** 5260–5265 (2011).
29. Piliarik, M. & Sandoghdar, V. Direct optical sensing of single unlabelled proteins and super-resolution imaging of their binding sites. *Nat. Commun.* **5,** 4495 (2014).
30. Arroyo, J. O. *et al.* Label-free, all-optical detection, imaging, and tracking of a single protein. *Nano Lett.* **14,** 2065–2070 (2014).
31. Wang, Q. & Moerner, W. E. Single-molecule motions enable direct visualization of biomolecular interactions in solution. *Nat. Methods* **11,** 555–558 (2014).
32. Gao, J. M., Mammen, M. & Whitesides, G. M. Evaluating electrostatic contributions to binding with the use of protein charge ladders. *Science* **272,** 535–537 (1996).
33. Winston, R. L. & Fitzgerald, M. C. Mass spectrometry as a readout of protein structure and function. *Mass Spectrom. Rev.* **16,** 165–179 (1997).
34. Sharon, M. & Robinson, C. V. The role of mass spectrometry in structure elucidation of dynamic protein complexes. *Annu. Rev. Biochem.* **76,** 167–193 (2007).

Acknowledgements

We acknowledge M. Borgia for the generous gift of unlabelled ProTαC protein, D. Nettels for help with fluorescence correlation spectroscopy (FCS) instrumentation and providing FCS data-analysis software, S. Chesnov from the Functional Genomics Center Zurich for mass spectrometry analysis, A. Caflisch, A. Soranno, G. Manning and R. Netz for discussions, and the Swiss National Science Foundation and University of Zurich for financial support. Nanofabrication was carried out at the FIRST Center for Micro- and Nanoscience, ETH Zurich.

Author contributions

F.R. performed the experiments and analysed the data. F.Z. and F.R. purified and labelled the proteins and nucleic acids and performed and analysed the FCS experiments. N.M., M.R., M.W. and A.O. provided the unlabelled Stm-l protein. F.Z. and B.S. contributed biochemical expertise, including protein selection. M.K. conceived the project, performed the theoretical analysis, interpreted the data and wrote the manuscript. F.R., F.Z. and B.S. provided feedback on the manuscript.

Additional information

Supplementary information is available in the online version of the paper. Reprints and permissions information is available online at www.nature.com/reprints. Correspondence and requests for materials should be addressed to M.K.

Competing financial interests

The authors declare no competing financial interests.

nature nanotechnology
SUPPLEMENTARY INFORMATION
DOI: 10.1038/NNANO.2017.26

Single-molecule electrometry

Francesca Ruggeri, Franziska Zosel, Natalie Mutter, Mirosława Różycka,
Magdalena Wojtas, Andrzej Ożyhar, Benjamin Schuler & Madhavi Krishnan*

*correspondence to: madhavi.krishnan@uzh.ch

This PDF file includes:

Materials and Methods

Supplementary Text

Supplementary Figures 1 to 9

Supplementary Tables 1 to 2

Captions for Supplementary Videos 1 and 2

Other Supplementary Materials for this manuscript includes the following:

Supplementary Videos 1 and 2

1. Materials and Methods

Experimental Methods

Device fabrication and escape-time electrometry (ET*e*) experimental procedure

Devices were fabricated as previously described [1]. Surface nanostructures and nanoslit were extensively characterized by atomic force microscopy (AFM), profilometry and scanning electron microscopy (SEM) (Supplementary Fig. 1). DNA and proteins were purified and labelled as described below. A suspension of the test molecule at a concentration of 50 pM was loaded into the nanoslits by capillary flow. The inlet and outlet reservoirs were filled with fluid to arrest the flow. The device was then sealed, allowed to equilibrate for ca. 10 minutes and maintained in an Argon atmosphere during optical measurements.

Trap arrays were imaged with standard wide-field fluorescence microscopy using a 100 X, NA=1.32 oil immersion objective (Leitz Wetzlar, Germany), 532 nm excitation from a DPSS laser (Pusch OptoTech GmbH, Germany) and an EMCCD camera (iXon, Andor Inc., United Kingdom) for detection. Arrays were illuminated with an intensity of 4 μW/μm^2 and time-lapse videos were recorded using an exposure time, $t_{\mathrm{exp}} = 5$ or 10 ms and a variable lag-time, t_{lag} between frames, such that $t_{\mathrm{cycle}} = t_{\mathrm{exp}} + t_{\mathrm{lag}} \approx 0.25 t_{\mathrm{esc}}$, typically. Solution pH and conductivity of the reservoirs were measured before and after every experiment using microconductivity (Laquatwin, Horiba Scientific, Japan) and micro-pH (Orionstar 215, Thermo Scientific, USA) meters. Calibration of the conductivity meter was performed using NIST-certified NaCl concentration standards (<0.2% uncertainty, Ricca Chemical Co., USA) (Supplementary Fig. 2). Intensity time traces for regions of interest corresponding to the trap locations (Fig. 2b) were analyzed using a step-finding algorithm with tunable threshold values. A single- exponential fit to the histogram of residence times representing 300 escape events in a single measurement yielded the escape time, t_{esc} presented in Fig. 2c.

In the sequential ET*e* experiments, following the measurements of t_{esc}, solution pH and conductivity for one molecular species, the reservoirs were drained and the nanoslits flushed with buffer of the same composition for 5-10 minutes before the second species was loaded and measured as before (Fig. 4a). Hydrodynamic radii (r_{H}) of all molecules in this work were measured using two-focus Fluorescence Correlation Spectroscopy, in solution conditions identical to the ET*e* measurement. The obtained r_{H} values were confirmed in direct single molecule diffusion measurements in one-dimensional “line-traps” in an ET*e* device [1] (Supplementary Fig. 3).

Biochemical procedures for purification and labelling of nucleic acids and proteins

DNA

All DNA oligomers were purchased from Microsynth AG (Switzerland) with Atto 532 attached to the 3' and 5' termini (see Supplementary Fig. 4). The 40 bp ds DNA molecule however carried the Atto532 label only at the 5' end of both strands. The complementary strand for the 60 bp ssDNA was purchased without labels. The integrity of the DNA was examined with anion exchange chromatography on a DNAPac PA100 4x250 mm column (Dionex, USA) at 85 °C (low salt buffer: 5 M urea, 12.5 mM Tris-HCl, pH 7.4; high salt buffer: 5 M urea, 12.5 mM Tris-HCl, 0.5 M sodium perchlorate, pH 7.4). The 40 bp and 60 bp dsDNA was annealed in 10 mM Tris-HCl pH 7.5, 5 mM $MgCl_2$ and 50 mM NaCl at a concentration of 8.5 μM with a 2-fold molar excess of unlabelled complementary strand by heating the sample to 95°C for 3 min and letting it slowly cool down to room temperature.

Fluorescent dyes

The following fluorescent dyes were used in the preparation of labelled protein: Atto 532 maleimide (Atto-Tec, Germany), Alexa Fluor 546 C5 maleimide (Thermo Fisher Scientific, USA), and Cy3B maleimide (GE Healthcare, USA). Prior to labelling, the dyes were dissolved to 10 mg/ml in dry DMSO and sonicated for 2 min to dissociate oligomers.

Protein preparation

ProTα. A double-cysteine mutant of human prothymosin alpha, ProTα, was expressed and purified with an N-terminal His_6-Tag according to published protocols [2]. The protein was enriched with IMAC chromatography, reduced with 5 mM TCEP and purified further with RP-HPLC (Reprosil-Gold 200 C18, 5 μm, 250x4.6 mm, Dr. Maisch, Germany), using gradient elution with water + 0.1% trifluoroacetic acid /acetonitrile. Electro-spray ionization mass spectrometry (ESI-MS) of the purified protein confirmed that the N-terminal methionine was cleaved off during expression. The lyophilized protein was dissolved in 100 mM potassium phosphate buffer (pH 7.0) to a concentration of 150-250 μM. An equimolar amount of fluorescent dye (Atto 532, AlexaFluor 546 or Cy3B) was added to the protein solution. The reaction was incubated for 3 h at room temperature and quenched with 50 mM 2-mercaptoethanol (2-ME) before purification with RP-HPLC (see above). The fraction containing double-labelled protein was collected and dissolved in 20 mM Tris-HCl (pH 7.5) after freeze drying. Proper labelling was confirmed with ESI-MS.

ProTα E59K. A plasmid encoding the E59K mutant of ProTα was produced with site-directed mutagenesis. The protein was expressed and purified analogously to the original ProTα. The E59K variant was double-labelled at the cysteines with Atto 532. The molecular weight of the double-labelled protein was confirmed with ESI-MS.

Starmaker-like. A double-cysteine mutant (A14C/A70C) of the Starmaker-like protein (Stm-l) of *Oryzias latipes* was purified according to published protocols [3]. The protein (200 μM) was labelled for 2 h at room temperature with a 4.5 fold molar excess of Atto

532 in 20 mM Tris-HCl pH 7.5, 150 mM NaCl. After that, the reaction was quenched with 50 mM 2-ME. The free dye was separated from the protein by passing the reaction over a PD MiniTrap G-25 column (GE Healthcare), equilibrated with 20 mM Tris-HCl pH 7.5, 50 mM NaCl. The double-labelled protein was further purified with anion exchange chromatography on a MonoQ 5/50 GL column (GE Healthcare), using a gradient from 50 mM to 1 M NaCl in 20 mM Tris-HCl pH 7.5. The protein was desalted on a G-25 column into 20 mM Tris-HCl, 50 mM NaCl. Double labelling was confirmed by ESI-MS.

β-Glucuronidase. E. coli β-Glucuronidase (Gusβ) was purchased from Sigma (G8295). The protein was dissolved in 50 mM sodium phosphate pH 7, reduced with 5 mM DTT and loaded onto a Superdex 200 10/300 GL column (GE Healthcare) equilibrated with 50 mM sodium phosphate buffer (pH 7.0). The fraction corresponding to tetrameric GUS was collected. The protein (2.5 μM) was labelled immediately after elution with a threefold molar excess of Atto 532. The reaction was incubated at room temperature for 3 h and quenched with 14 mM 2-ME. Residual free dye was removed on a G-25 column equilibrated with 20 mM Tris-HCl pH 7.5, 50 mM NaCl, followed by purification on a Superdex 200 increase 10/300 GL column (GE Healthcare) in the same buffer. The degree of labelling was determined to be 2.1 dyes/molecule via UV/Vis absorbance. The integrity of the protein under ET*e* measurement conditions was confirmed with analytical size-exclusion chromatography on a Superdex 200 increase column in running buffer of composition 20 mM Tris-HCl pH 7.3, 50 mM NaCl (Supplementary Fig. 5a).

Dual-focus fluorescence correlation spectroscopy

Dual-focus fluorescence correlation spectroscopy (2f-FCS) measurements [4] of Atto 532-labelled molecules were performed according to published procedures [5,6] on a MT200 instrument (PicoQuant, Germany). Alternating excitation of the sample with 483 nm was achieved with two orthogonally polarized lasers (LDH-D-C-485, PicoQuant) with a repetition rate of 20 MHz. A differential interference contrast prism (U-DICR, Olympus, Japan) was inserted into the beam to split the two polarization directions into two laser foci. The emitted photons from both foci were separated from the excitation light with a dichroic mirror (HC Triple laser beam splitter BS R405/488/594, Semrock, USA), split according to their polarization and color (595 DCXR (Chroma)) and detected with two avalanche photodiodes for each angle. The two detectors in each path were equipped with either an ET 525/50 filter (Chroma) or a HQ 650/100 filter (Chroma). The signal of the two channels was combined for data analysis, as Atto 532 shows significant emission in both spectral regions. To match the spectral properties of ProTα-Cy3B and ProTα-Alexa 546, the sample was excited alternatingly with two white light continuum sources (SC-450AOTF, Fianium, UK; Solea, PicoQuant) pulsing at 20 MHz, with 15 μW (Alexa 546) or 5 μW (Cy3B) excitation power each (measured at the back aperture of the objective). The appropriate wavelength was selected with a laser cleanup filter for the Fianium lightsource (BrightLine HC 532/3, Semrock) and by setting the tunable bandpass filter of the Solea to 528/7 nm. Emitted photons were separated from the excitation light with a dichroic mirror (triple line beam splitter zt405/530/630rpc, Chroma), split according to their polarization and distributed onto two avalanche photodiodes, both equipped with a 585/65 ET bandpass filter (Chroma).

The detected photons were combined into 100 ms bins to assess signal stability. Occasional aggregates (detectable by a spike in the fluorescence intensity trajectory) were removed from the photon trace prior to further analysis. The data analysis of the auto- and cross-correlation functions of the two foci was conducted according to Refs. [4] and [5] with the addition of a triplet state component [6]. From the molecular diffusion coefficient D_m, the hydrodynamic radius, r_H, of the protein was calculated according to the Stokes-Einstein equation, $r_H = \dfrac{k_\mathrm{B}T}{6\pi\eta D_m}$, where η is the viscosity of water at 22°C. The dominant uncertainty in the diffusion coefficient originates from the uncertainty on the inter-focus distance, an input parameter for the fit which was quantified as 436±20 nm from a calibration based on dynamic light scattering[7]. To assess the resulting uncertainty, we obtained the diffusion coefficient from fitting the correlation functions 1000 times with the inter-focus distance varied randomly by 5% according to a normal distribution with a mean of 436 nm. The standard deviation of this fit corresponds to the error in r_H given in Supplementary Table 1. All measurements were conducted at 2 nM concentration of the labelled species in the relevant buffer conditions (1 mM Tris, ~1 mM NaCl) as in ET*e* experiments.

Theoretical approach

Poisson-Boltzmann model for the spatial electrostatic potential in the trapping nanostructure

We begin modelling our electrostatic single molecule trap by calculating the 3D distribution of electrostatic potential $\psi(\boldsymbol{r})$ throughout the trapping nanostructure using COMSOL Multiphysics as previously described [1,8]. We model the molecule as a 3D object as schematically depicted in Fig. 3, with the relevant geometric parameters listed in Supplementary Table 1. In previous work we treated the surface charge of the trapped object and walls of the system using constant charge or constant potential boundary conditions. Here we employ the charge regulation formalism [9] that permits us to account for the response of the ionizable groups to the local dielectric environment within the molecule as well as the pH of the surrounding electrolyte.

We treat a globular protein as a salt-free sphere of uniform dielectric coefficient ε_p, and radius, *R* equal to the molecule's measured Stokes radius, r_H. The structural charge of the molecule arising from its chemical groups is considered as a charge density distributed uniformly throughout the spherical volume and is given by

$$\rho(\boldsymbol{r}) = \sum_i \frac{je\rho_i(\boldsymbol{r})}{1+10^{j(\mathrm{pH}\text{-}\mathrm{p}K_i)}\exp\left\{\dfrac{je\psi(\boldsymbol{r})+\phi_s+\phi_0}{k_\mathrm{B}T}\right\}} \qquad (1)$$

This relation incorporates the response of the charged groups to the local electrical potential, $\psi(\boldsymbol{r})$ and importantly reflects the uniform chemical potential of the protons throughout the system. Here, ρ_i represents the volumetric number density of ionizable species i, $\mathrm{p}K_i$ represents its acid dissociation constant, j=+1 or -1 indicates a basic or an acidic species, k_B is Boltzmann's constant and T is temperature. For proteins, we use intrinsic $\mathrm{p}K_\mathrm{a}$ values for the charged residues measured for Alanine pentapeptides [10]. $\frac{\phi_\mathrm{s}}{k_\mathrm{B}T}=\frac{l_\mathrm{B,m}}{2r_{\mathrm{A}^-}}\left(\frac{\varepsilon_\mathrm{m}}{\varepsilon_\mathrm{p}}-1\right)$ denotes the difference in solvation energy of the ionized group between the exterior electrolyte and interior dielectric. Here $l_\mathrm{B,m}$ denotes the Bjerrum length in the electrolyte phase, r_{A^-} is the radius of the ionized group and ε_m and ε_p denote the dielectric constants of the exterior electrolyte and interior dielectric medium respectively. ϕ_0 in turn can be used to incorporate additional non-electrostatic energy contributions to the ionization equilibrium, but is set to zero in this work. Electrolyte ions are not permitted to enter the dielectric sphere, and the Poisson equation $\Delta\psi(\boldsymbol{r})=-\frac{\rho(\boldsymbol{r})}{\varepsilon_\mathrm{p}\varepsilon_0}$ describes the electrical potential, $\psi(\boldsymbol{r})$ within the sphere, where ε_0 is the permittivity of free space.

Polypeptide chains, single-stranded and double-stranded nucleic acids are treated as rigid, hollow cylinders of diameters, D = 0.5 nm, 1 nm and 2 nm respectively, whose lengths, L correspond to full extension. We consider the charge of the molecule as a uniform density, $\sigma(\boldsymbol{r})$ all over the cylindrical surface representing the molecule, unless otherwise stated. Thus analogous to the spherical globular protein we have $\sigma(\boldsymbol{r})=\sum_i \frac{je\sigma_i(\boldsymbol{r})}{1+10^{j(\mathrm{pH}\text{-}\mathrm{p}K_i)}\exp\left\{\frac{je\psi(\boldsymbol{r})+\phi_\mathrm{s}+\phi_0}{k_\mathrm{B}T}\right\}}$, where $\sigma_i(\boldsymbol{r})$ represents the local surface number density of ionizable species i, and $\psi(\boldsymbol{r})$ is the local surface potential.

In the solution phase exterior to the object, the non-linear Poisson-Boltzmann equation $\Delta\psi(\boldsymbol{r})=\kappa^2\sinh\psi(\boldsymbol{r})$ governs the spatial electrostatic potential, where $\kappa=\sqrt{\frac{2cN_\mathrm{A}e^2}{\varepsilon_\mathrm{m}\varepsilon_0 k_\mathrm{B}T}}$ denotes the inverse Debye length. Here N_A is Avogadro's number, and we assume a uniform dielectric coefficient of $\varepsilon_\mathrm{m}=78.5$ representing water at 25 °C, with pH and bulk salt concentration, c, corresponding to the experimental conditions. Note that similar to traditional treatments, our dielectric sphere is impervious to salt ions in the aqueous phase [11-13]. But by contrast, protons are permitted to penetrate the sphere, enabling us to account for the pH- and interior dielectric coefficient-dependent titration of charged groups in a single calculation.

Numerically solving for the spatial electrostatic potential and integrating the electric field over the surface of the sphere or cylinder representing the molecule directly yields the charge enclosed by the molecular surface, q_s under a given set of conditions. A low dielectric coefficient entails strong coulombic coupling between charges embedded in the medium. The large excess of negative residues in a globular protein like Gusβ thus leads to strong charge regulation via Supplementary Equation (1), and as a result, q_{s} departs significantly from the structural value, q_{str}. We have validated the net charge predictions of our simple model of the protein interior against a fully atomistic calculation for Lysozyme using the H++ platform[14] (http://biophysics.cs.vt.edu/H++, version 3.2) which employs the methodology proposed in Ref.[12]. The p*K*-1/2 values for individual groups generated by the same atomistic calculation platform were used to determine the value $q_{\mathrm{theory}} = -24.3\ e$ reported for Gusβ in Supplementary Table 2.

Furthermore our model also captures experimentally measured trends of $\mathrm{p}K_{\mathrm{a}}$ shifts reported for acidic[10] and basic proteins[15]. Details on the validation of the model will be presented in a separate publication.

Note that throughout this work we model the SiO_2 walls of the trap using a single p*K* charge regulation model which, in conjunction with Poisson-Boltzmann equation describing the bulk electrolyte, models the response of the SiO_2 surfaces to both the solution ionic strength and pH. The charge density on the walls of the slits is thus $\sigma_{\mathrm{w}}(\boldsymbol{r}) = \dfrac{\Gamma}{1+10^{(\mathrm{pH}\text{-}\mathrm{p}K)}\exp\left\{\dfrac{-e\psi_{\mathrm{w}}(\boldsymbol{r})}{k_{\mathrm{B}}T}\right\}}$, where Γ= -8 e/nm^2 is the number density of surface ionizable groups and p*K*=7.5 [16]. Supplementary Fig. 6 illustrates the influence of σ_{w} on the electrical potential difference $\Delta\psi$ between the shoulders and center of the trap.

Spatial maps of the electrostatic potential due to a single molecule, calculated using the above approach, are shown in Fig. 3.

Numerical model for the effective electrical charge and interior dielectric coefficient of a trapped macromolecule

In order to address the question of how the measured charge q_{m} compares with theoretical expectations, we first calculate $F(\mathbf{r})$, the electrostatic free energy as a function of spatial position *r* of the molecule in the landscape. The electrostatic free energy calculation incorporates the mixing entropy of the counterions in solution as previously described[8].

Since we find that q_{s} remains constant regardless of the object's spatial location in the trap, we calculate differences in the system electrostatic free energy, ΔF between states where the molecule is situated at axial potential minima at the center of the trap and outside the trap - at the shoulders of the potential well - using the constant charge approach previously described[8]. We find that the calculated spatial electrostatic interaction free energy can be cast in the form $F(\mathbf{r}) = q_{\mathrm{c}}\psi(\mathbf{r})$ (2), where q_{c} can be thought of as a calculated molecular "interaction charge". We thus determine q_{c} via the relation $q_c = \frac{\Delta F}{\Delta \psi}$, where ΔF denotes the difference in calculated electrostatic free energy for positions of the molecule at the bottom and shoulders of the potential well and $\Delta \psi$ in turn is the difference in minimum axial (z) electrical potential, between the bottom and shoulders of the trap, in the *absence* of the molecule. Note that the equality in Supplementary Equation (2) also forms the basis of our Brownian Dynamics simulation of escape of a point object of charge, q_{eff} from a trap potential landscape given by $\psi(\mathbf{r})$, where $\psi(\mathbf{r})$ again refers to the spatial electrostatic potential distribution due to the nanostructure alone, in the absence of the molecule. As such, Supplementary Equation (2) represents a parametrization of the electrostatic free energy of interaction in terms of an effective molecular charge which can not only be directly calculated as described above but as we show in our work experimentally inferred from an escape-time measurement.

For low object charge densities we note that $q_c = q_{\text{str}}$, which is expected in the linear regime [17]. For large charge densities however we find that q_c is smaller than q_{str}, indicating charge renormalization. In particular in the point object regime, i.e., object radius, $R <$ Debye length, κ^{-1}, we find that our calculated effective charge, q_c agrees very closely with the "effective charge" discussed in charge renormalization and counterion condensation theories[17-20] (Supplementary Table 2). Thus in our work q_c denotes a calculated effective molecular charge.

For the disordered proteins and double stranded nucleic acids we find remarkable agreement between the measured and calculated charges, q_m and q_c, without any adjustable parameters (Supplementary Table 2). We further note that q_m – or its theoretical counterpart, q_c – is the quantity of interest in "far-field" interactions, e.g., intermolecular or intersegment forces in a long polyelectrolyte or polyampholyte. The true charge of the molecule however is given by the actual charge enclosed by or distributed over the molecular surface, q_s. Depending on the molecule's charge density, its 3D structure, and solution conditions such as ionic strength and pH, q_s can itself on occasion be substantially less than the nominal q_{str}, and may thus be thought of as a regulated molecular charge (Table S2). Finally, while the free energy calculation for linear polyelectrolytes is free of adjustable parameters, for a compactly folded molecule such as a globular protein we do in fact tune the interior dielectric coefficient, ε_p in order to obtain agreement of q_c with q_m.

The numerical error in q_c stems from the error in calculating ΔF. Currently this uncertainty is generally of the order 1%, but can be up to 3-5% for highly charged molecules such as dsDNA.

2. Supplementary Text

Experimental parameters and measurement precision

The inputs to the overall measurement process are the object's Stokes radius, r_{H}, nanostructure geometry, salt concentration in the electrolyte, c and slit surface charge density, σ_{W}: all these parameters can be directly measured and/or controlled. We point out that although σ_{W} can be measured, for highly charged surfaces, the non-linearity of the governing PB equation makes $|\Delta\psi|$ relatively robust to large variations in this parameter (Supplementary Fig. 6). Thus, uncertainties on the slit height, $2h$ hydrodynamic radius of the particle, r_{H} and solution ionic strength, c are the main sources of error in the overall measurement (see section below). We emphasize that unlike other approaches, the escape-time methodology circumvents uncertainty on molecular size (or equivalently, the drag coefficient) in a unique way. The mean escape time, t_{esc} depends exponentially on an object's charge but only linearly on its viscous drag. This means that as long as t_{esc} is much longer than t_{r}, the relaxation time in the trap, even a relatively large uncertainty in the drag coefficient only results in a small correction to the measured charge, e.g., for escape times ≈100 ms and relaxation times ≈ 100 μs, as in these experiments, 10% uncertainty in the drag coefficient results in ≈1% error in charge measurement. Thus with the salt concentration known to within 0.5% (Supplementary Fig. 2), the error in the measurement could stem solely from the statistical nature of escape time determination. In our present work the ~1 second measurement time results in an overall average error of <5% on t_{esc} which in turn translates to <0.5% error in charge determination. In absolute terms this statistical uncertainty ranges from ≈0.05 e for weakly charged matter such as 10 base ssDNA ($q_{\mathrm{eff}} \sim -10\,e$) to ≈0.5 e for a highly charged molecule such as Stm-l ($q_{\mathrm{eff}} \sim -100\,e$). Below we present a more detailed error analysis for the ET*e* measurement that takes into account uncertainties on the system parameters and experimentally measured quantities.

Measurement accuracy and error propagation analysis for ET*e* measurements

The overall uncertainty, g_{e} on a quantity, $g(x, y, ..)$ that is a function of observables x, y, z, etc., each associated with their own uncertainties x_{e}, y_{e} etc. is given by the following equation:

$$g_{\mathrm{e}} = \sqrt{\left(\frac{\partial g}{\partial x}\right)^2 x_{\mathrm{e}}^2 + \left(\frac{\partial g}{\partial y}\right)^2 y_{\mathrm{e}}^2 + \left(\frac{\partial g}{\partial z}\right)^2 z_{\mathrm{e}}^2 + \ldots}$$

In our experiment the measured electrical charge on an object, q_{m} which we denote hereafter as q, depends on system parameters and experimental measurables as follows:

$$q\psi_{\mathrm{m}} + f = k_{\mathrm{B}}T\ln\left(\frac{t_{\mathrm{esc}}}{t_{\mathrm{r}}}\right)$$

Here, ψ_{m} denotes the slit mid-plane potential, which well approximates the trap potential difference $\Delta\psi$, since the electrical potential at the bottom of the trap is zero by design. Further, t_{esc} is the measured escape time, and t_{r}, the particle's position relaxation time in the trap which depends inversely on the measured hydrodynamic radius, r_{H}. $f \sim 2k_{\mathrm{B}}T$ in turn is a fluctuation-governed, predominantly entropic, contribution to the trap depth, W which arises from position fluctuations of the molecule in the axial dimension, and can be regarded as effectively independent of q.

The fractional uncertainty $\frac{q_{\mathrm{e}}}{q}$ on the measured charge can thus be written as

$$\frac{q_{\mathrm{e}}}{q} = \sqrt{\left(\frac{1}{q^2}\right)\left(\frac{\partial q}{\partial \psi_{\mathrm{m}}}\right)^2 \psi_{\mathrm{m,e}}^2 + \left(\frac{1}{q^2}\right)\left(\frac{\partial q}{\partial t_{\mathrm{esc}}}\right)^2 t_{\mathrm{esc,e}}^2 + \left(\frac{1}{q^2}\right)\left(\frac{\partial q}{\partial t_{\mathrm{r}}}\right)^2 t_{\mathrm{r,e}}^2}$$

which simplifies to $$\frac{q_{\mathrm{e}}}{q} = \sqrt{\left(\frac{\psi_{\mathrm{m,e}}}{\psi_{\mathrm{m}}}\right)^2 + \frac{1}{\left\{\ln\left(\frac{t_{\mathrm{esc}}}{t_{\mathrm{r}}}\right)\right\}^2}\left(\frac{t_{\mathrm{r,e}}}{t_{\mathrm{r}}}\right)^2 + \frac{1}{\left\{\ln\left(\frac{t_{\mathrm{esc}}}{t_{\mathrm{r}}}\right)\right\}^2}\left(\frac{t_{\mathrm{esc,e}}}{t_{\mathrm{r}}}\right)^2} \qquad (3)$$

Of the 3 terms in Supplementary Equation (3) the latter two contain experimental measurables t_{esc} and t_{r} and can therefore be directly estimated. The first term Supplementary Equation on the other hand is a function of 3 additional experimental parameters, namely, the inverse Debye length, κ, the height of the channel, $2h$, denoted for now as H, with a corresponding error h_{e}, and the surface charge density of the slit-walls, σ_{w}. Thus, we write in addition,

$$\frac{\psi_{\mathrm{m,e}}}{\psi_{\mathrm{m}}} = \sqrt{\left(\frac{1}{\psi_{\mathrm{m}}^2}\right)\left(\frac{\partial \psi_{\mathrm{m}}}{\partial \kappa}\right)^2 \kappa_{\mathrm{e}}^2 + \left(\frac{1}{\psi_{\mathrm{m}}^2}\right)\left(\frac{\partial \psi_{\mathrm{m}}}{\partial H}\right)^2 h_{\mathrm{e}}^2 + \left(\frac{1}{\psi_{\mathrm{m}}^2}\right)\left(\frac{\partial \psi_{\mathrm{m}}}{\partial \sigma_{\mathrm{w}}}\right)^2 \sigma_{\mathrm{e}}^2}$$

We find that the following linear functions well describe the dependence of ψ_{m} on the parameters κ, H and σ_{w} for perturbations about the nominal values:

$\frac{e\psi_{\mathrm{m}}}{k_{\mathrm{B}}T} = A - B\kappa H$, holding σ_{w} constant, and

$\frac{e\psi_{\mathrm{m}}}{k_{\mathrm{B}}T} = \frac{C\sigma_{\mathrm{w}}}{1 + D\sigma_{\mathrm{w}}}$, holding κ and h constant.

In experiments where c = 1 mM NaCl in slits of height $2h = H = 66.2$ nm, we find the following values for the coefficients: $A = 1$, $B = 0.11$, $C = 9.15$ nm^2/e and $D = 37.91$ nm^2/e.

Furthermore since $\kappa \propto \sqrt{c}$, we note that $\frac{\kappa_\mathrm{e}}{\kappa} = \frac{1}{2}\frac{c_\mathrm{e}}{c}$, where the measured uncertainty on the salt concentration, $\frac{c_\mathrm{e}}{c} \cong 0.5\%$ (Supplementary Fig. 2).

Thus the fractional error on the mid-plane potential, ψ_m can be written as

$$\frac{\psi_\mathrm{m,e}}{\psi_\mathrm{m}} = \sqrt{\frac{B^2}{\left(e\psi_\mathrm{m}/k_\mathrm{B}T\right)^2}\left(H\kappa_\mathrm{e}\right)^2 + \frac{B^2}{\left(e\psi_\mathrm{m}/k_\mathrm{B}T\right)^2}\left(\kappa h_\mathrm{e}\right)^2 + \frac{C^2}{\left\{\left(1+D\sigma\right)^2 \frac{e\psi_\mathrm{m}}{k_\mathrm{B}T}\right\}^2}\sigma_\mathrm{e}^2}$$

Estimating the measurement error around the nominal value $\frac{e\psi_\mathrm{m}}{k_\mathrm{B}T} = 0.22$, with $\kappa^{-1} = 9.5$ nm, the measured error in slit height h_e=1 nm (Supplementary Fig. 1d) and assuming a rather large (30%) uncertainty on the value of σ_w =0.3 e/nm^2, namely, σ_e=0.1 e/nm^2, we obtain

$$\frac{\psi_\mathrm{m,e}}{\psi_\mathrm{m}} = \sqrt{\left(0.87\times10^{-2}\right)^2 + \left(5.26\times10^{-2}\right)^2 + \left(2.7\times10^{-2}\right)^2} = 5.97\%$$

We now refer back to Supplementary Equation (3) to determine the total error. Substituting the experimentally determined value of 0.05 for the quantities $\left(\frac{t_\mathrm{r,e}}{t_\mathrm{r}}\right)$ and $\left(\frac{t_\mathrm{esc,e}}{t_\mathrm{esc}}\right)$, and taking $\ln\left(\frac{t_\mathrm{esc}}{t_\mathrm{r}}\right) \approx 7$, we find that the estimated overall error in the charge measurement works out to $\frac{q_\mathrm{e}}{q} = \sqrt{\left(5.97\right)^2 + 2\left(0.71\right)^2}\ \% = 6.05\%$

The main contribution to the measurement error thus stems from the uncertainty on the mid-plane potential, ψ_m which in turn depends most strongly on a geometric parameter, namely, the slit height, $2h$.

List of variables and parameters

Symbol	Variable or parameter name
A	Escape-time probability density distribution fit parameter
b	Mean inter-charge spacing in linear polyelectrolytes
c	Salt concentration
D	Diameter of cylinder in quasi-1D molecular model of polyelectrolytes
D_{m}	Molecular diffusion coefficient
Δt_{lag}	Lag-time in SMD measurement
e	Elementary unit charge
ε_0	Permittivity of free space
ε_{m}	Dielectric coefficient of a medium m
ε_{p}	Dielectric coefficient of the interior of a protein
f	Fluctuation contribution to the trap depth
$F(\boldsymbol{r})$	Spatial electrostatic free energy as a function of particle position, $\boldsymbol{r}$
$F_{\mathrm{z}}(r_{\mathrm{t}})$	Axial (z)-minimum of electrostatic free energy as a function of radial position of particle in trap, r_{t}
ϕ_0	Non-electrostatic contribution to ionization equilibrium
ϕ_{s}	Solvation energy of an ionized group
Γ	Structural charge density due to surface ionizable groups on the slit walls
H	$2h$
κ^{-1}	Debye length
K_{a}	Acid dissociation constant
k_{B}	Boltzmann's constant
L	Fully extended length of a nucleic acid or intrinsically disordered protein molecule
$l_{\mathrm{b,m}}$	Bjerrum length in a medium, m
N	Number of escape events or hops
n_{dye}	Number of frames to bleaching for a given dye species
q^*_{str}	Net electrical charge of the molecule estimated prior to chemical modification by dye
q_{c}	Calculated effective charge
q_{eff}	Effective electrical charge
q_{m}	Measured effective charge
q_{s}	Charge enclosed by or distributed over the molecular surface
q_{str}	Net structural electrical charge including the contribution of dye molecules
q_{theory}	Effective charge predicted by other theoretical approaches
R	Radius of sphere representing a globular protein
ρ	Volumetric number density of ionizable species
r_{H}	Hydrodynamic radius
r_{t}	Radial location of particle in trap
σ_{w}	Regulated charge density of the slit walls

T	Temperature
t_{cycle}	Cycle time in fluorescence imaging
t_{esc}	Average escape time of the molecule
t_{exp}	Exposure time in fluorescence imaging
t_{lag}	Lag time in fluorescence imaging
t_{r}	Position relaxation time of the trapped molecule
t_{sim}	Average escape time from Brownian-Dynamics simulation
t'_{sim}	Inferred simulated escape time after camera sampling
W	Depth of the trap or potential well
x_{e}	Error on a parameter or variable, x
$\psi(\boldsymbol{r})$	Local electrostatic potential
ψ_{m}	Electrical potential at the slit mid-plane

3. Supplementary figures and tables

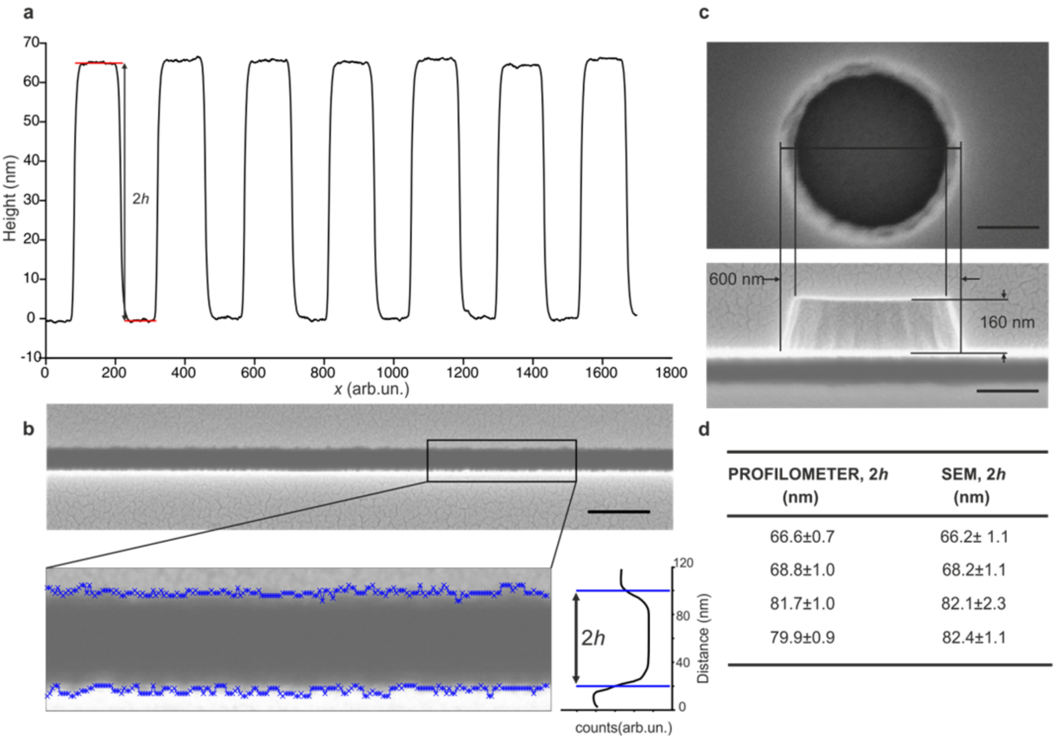

PROFILOMETER, 2h (nm)	SEM, 2h (nm)
66.6±0.7	66.2± 1.1
68.8±1.0	68.2±1.1
81.7±1.0	82.1±2.3
79.9±0.9	82.4±1.1

Supplementary Fig. 1. **Characterization of a representative escape-time electrometry device.** (**a**) SiO_2 surface-topography was measured using profilometry and AFM, prior to fabrication of closed fluidic slits by bonding to an optical-microscopy-compatible glass substrate. (**b**) Subsequent to bonding, nanoslits were cleaved and the cross-section subjected to scanning electron microscopy. An automated analysis of the height of the gap in the SEM images was performed using various edge detection criteria. (**c**) An SEM of the cross-section of the trapping nanostructure. (**d**) Slit height measurements agree remarkably in the profilometry and SEM approaches, with the more noisy SEM values rather reflecting edge roughness created by breakage. Profilometry measurements of average slit height, 2h and corresponding uncertainty, h_e ≈ 1 nm were used in the theoretical modelling. All scale bars denote 200 nm.

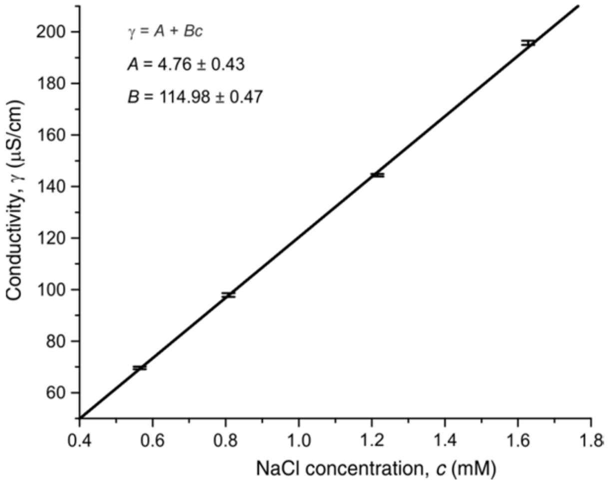

Supplementary Fig. 2. **Converting measured solution conductivity to ionic strength.** The solid line denotes the calibration function used to convert measured reservoir conductivity to solution ionic strength, *c*. The uncertainty on concentrations of the calibration standards (<0.2%) are smaller than the data symbols. The overall uncertainty in measured *c* is ≈0.4%.

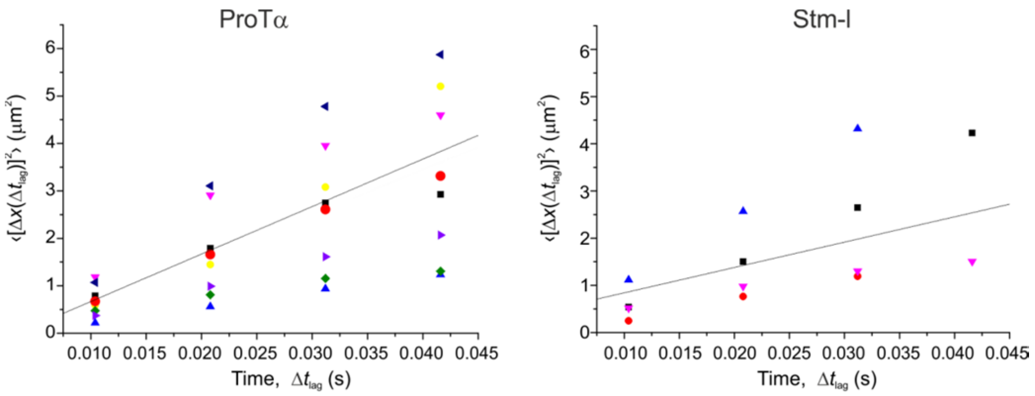

Molecule	$D_{m,FCS}$ (μm²/s)	$D_{m,SMD}$ (μm²/s)	r_H (nm)
ProTα	49.4 ± 2.8	46.9 ± 7.7	4.64 ± 0.7
Stm-I	24.9 ± 1.6	26.8 ± 11.1	8.11 ± 3.35

Supplementary Fig. 3. **Single molecule diffusion (SMD) measurements on ProTα and Stm-1.** Diffusion of single molecules confined in 1-dimensional "line" traps in an ET*e* device [1] was imaged over a period of ~1 s using continuous illumination with $t_{\mathrm{exp}} = 10\,\mathrm{ms}$. Mean square displacement, $\left\langle \left[\Delta x(\Delta t_{\mathrm{lag}}) \right]^2 \right\rangle$ values were determined for each trajectory and plotted as a function of lag-time, Δt_{lag}, with symbol color identifying data from a single molecule. A global linear fit to all the data series (black line) performed according to Ref. [21] yields the molecular diffusion coefficient, $D_{\mathrm{m,\,SMD}}$. The obtained values for ProTα and Stm-1 are tabulated below and compared with the respective measurements from FCS. The inferred hydrodynamic radii, r_{H} are in good agreement with those obtained from bulk FCS measurements (see Supplementary Table 1).

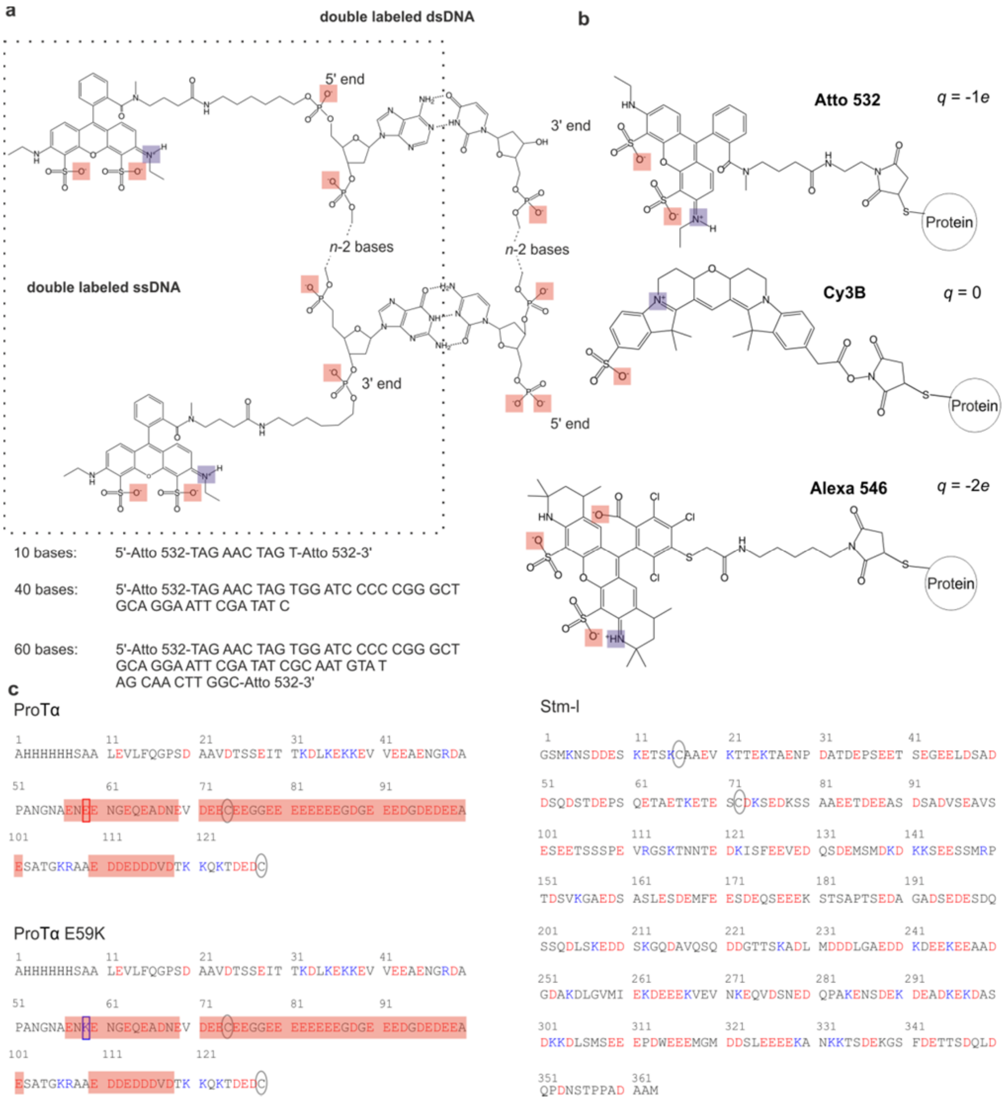

Supplementary Fig. 4. **Sequences of DNA fragments and IDPs.** (a) DNA sequences and chemical structures of Atto 532-derivatized ssDNA and dsDNA, with charge carrying atoms highlighted in blue and red. A labelled ssDNA n bases in length carries a structural charge, $q_{\text{str}} = -(n+3)\,e$ after labelling, while a dsDNA fragment n bp in length carries an additional structural charge of $-(n+1)\,e$ from the unlabeled hybridized strand. (**b**) Chemical structures of the fluorescent dyes Atto 532, Cy3B and Alexa 546. (**c**) Amino acid sequences of ProTα and Stm-l, with the single amino acid exchange site in ProTα indicated by a rectangle and dye-coupling sites by a grey ellipse. Negatively charged residues are colored red and positive, blue. Stretches of negatively charged residues in ProTα are highlighted in red.

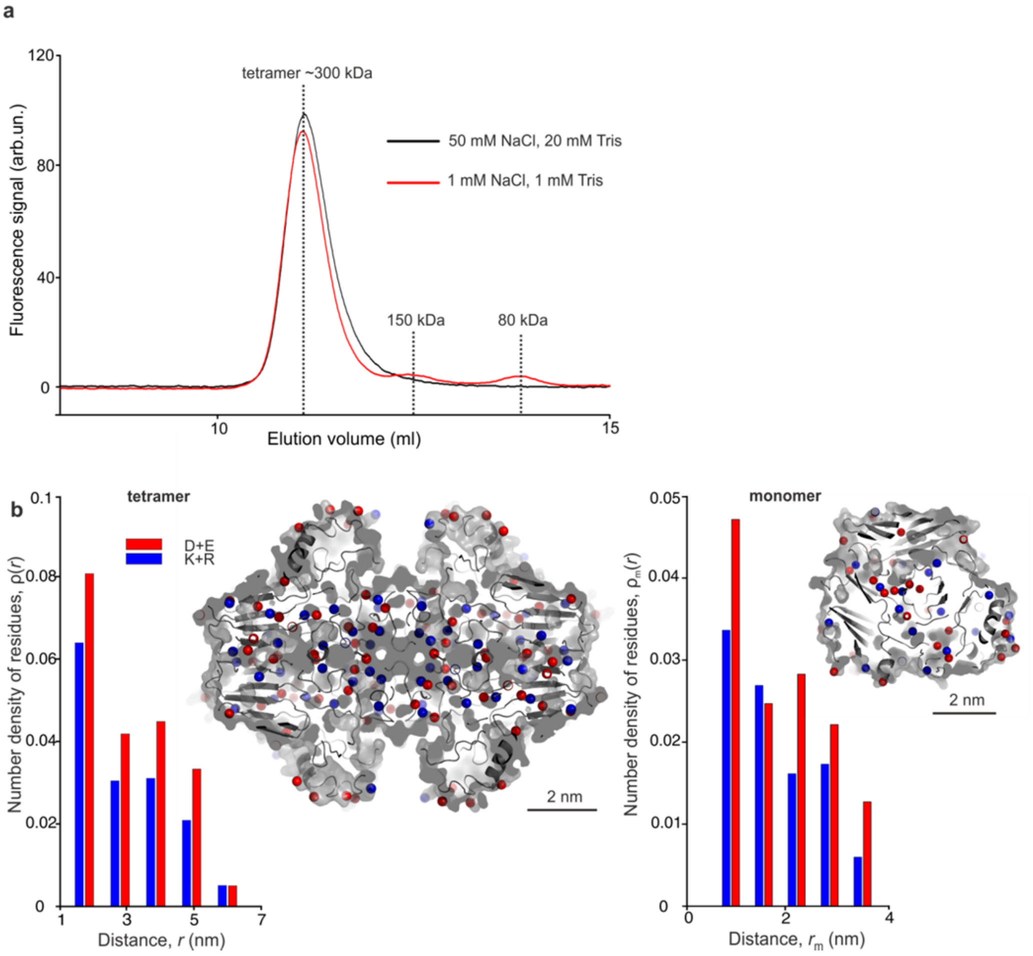

Supplementary Fig. 5. **Structural characterization and analysis of Gusβ.** (**a**) Size-exclusion chromatography of Gusβ in 50 mM NaCl, 20 mM Tris Buffer on a Superdex 200 Increase column, after pre-incubation for 1 hour in the indicated buffers. (**b**) Radial number density distribution, $\rho_i(\boldsymbol{r})$ of charged residues, D+E (red) and K+R (blue), relative to the geometric center of Gusβ (left). $\rho_{\mathrm{m}}(\boldsymbol{r})$ represents the corresponding distribution for a single monomer (right), clearly demonstrating the presence of charged residues in the globular interior. Insets display charge-carrying atoms in 1.5 nm and 1.1 nm thick slices through the geometric centers of the tetramer and monomer respectively.

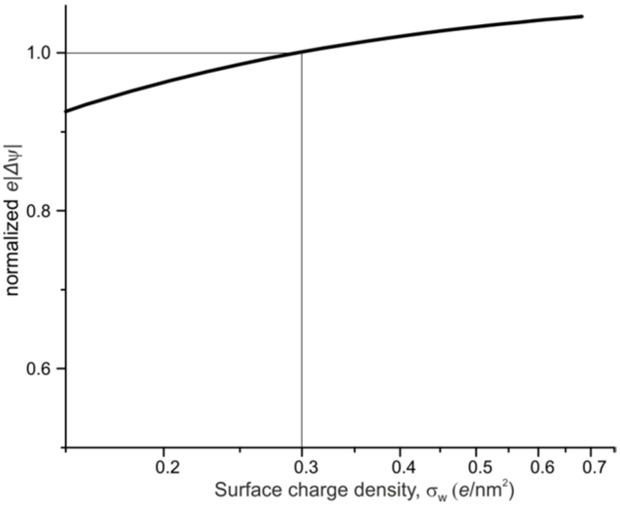

Supplementary Fig. 6. **Dependence of the unit charge trap depth, $e|\Delta\psi|$ on slit surface charge density.** For example for measurements in 0.8 mM NaCl + 1 mM Tris (total salt concentration, $c \approx 1$ mM), pH 9, and slits of height $2h = 66$ nm, we use a slit surface charge density of $\sigma_w = -0.3$ e/nm^2, which comes from a single pK_a charge regulation boundary condition for silica surfaces [16], and agrees well with our own and literature measurements of silica nanoslit conductance [22]. Including a 0.15 nm thick Stern layer with a capacitance of 2.9 F/m^2 decreases the value of $\Delta\psi$ by <1%.

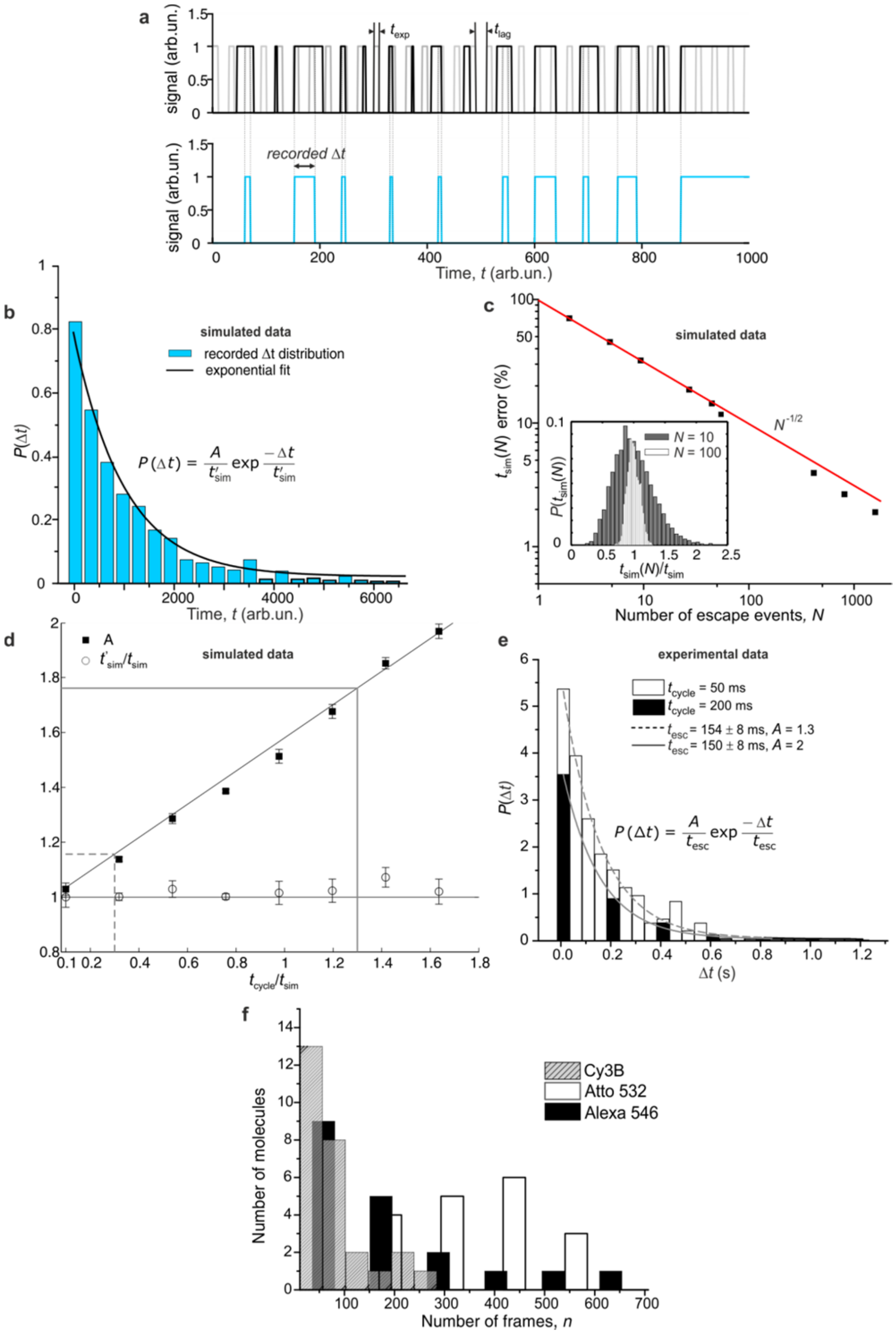

Supplementary Fig. 7. ***In silico* validation of the ET*e* experimental method.** (**a**) A distribution of $N = 10^4$ escape times with a mean value t_{sim} generated from a Brownian Dynamics simulation (black trace) is sampled by a rectangular pulse train representing the time-structure of the camera's sampling (grey trace), yielding a simulated recorded escape trace below (blue line). (**b**) The histogram of these escape times is fit with a single exponential, $P(\Delta t) = \frac{A}{t'_{\text{sim}}} \exp \frac{-\Delta t}{t'_{\text{sim}}}$ (black trace). The decay rate corresponds to the inferred escape time, t'_{sim}, which can be compared under various camera sampling conditions with that of the input Poisson process, t_{sim} (see parts (**d,e**)). (**c**) Dependence of the expected fractional uncertainty on $t_{\text{sim}}(N)$ on the number of recorded escape events, N. The red line denotes $t_{\text{sim}}(N) = N^{-1/2}$. The inset presents simulated histograms of average escape times for 10^4 realizations, each comprising N=10 or 100 events. (**d**) The ratio $\frac{t'_{\text{sim}}}{t_{\text{sim}}}$ examined for $N = 2000$ recorded events using a range of sampling times given by $t_{\text{cycle}} = t_{\text{exp}} + t_{\text{lag}}$, reveals the possibility of accurate reconstruction of t_{sim} over a wide range of sampling conditions, i.e., $t'_{\text{sim}} \approx t_{\text{sim}}$ over a wide range of t_{cycle}. The fit value of A however depends strongly on sampling conditions, and increases with t_{cycle}. Note that using $t_{\text{cycle}} \approx 0.1 t_{\text{sim}}$ gives a fit value $t'_{\text{sim}} = t_{\text{sim}}$. The average 3% uncertainty on the fit value of t'_{sim} over the entire range of $\frac{t_{\text{cycle}}}{t_{\text{sim}}}$ reflects the statistical expectation rather well, see (**c**). (**e**) Experimental measurements of t_{esc} acquired with different sampling times, t_{cycle} indeed reflect the simulation prediction well (solid and dotted grey lines in (**d**)). (**f**) Experiments were performed to measure the bleaching time of the Atto 532 label. Fluorescently labelled, trapped ProTα molecules were illuminated continuously ($t_{\text{lag}} \approx 0$), with the same optical intensity as in the ET*e* measurements and using the same exposure time, $t_{\text{exp}} = 10$ ms. The number of frames to bleaching, n_{dye} was recorded for 20-30 molecules. The measured values $n_{\text{Atto 532}}$ = 344, $n_{\text{Alexa 546}}$= 193 and n_{Cy3B}= 80 far exceed the mean number of frames-to-escape in the ET*e* measurements, which was typically 4.

	Molecule	Buffer 1 mM Tris +	T (°C)	Cond. (µS/cm)	$2h$ (nm)	W ($k_B T$)	t_{esc} (s)	q (-e)
DNA	**10 b**	**0.3-0.4 mM NaCl, pH 8.8-9.1**	**23.1**	**72**	**70±1**	**5.01**	**0.017±0.001**	**7.2±0.1**
			23.3	51	76.3±0.8	6.52	0.074±0.005	8±0.1
			23.1	55	76.3±0.8	6.57	0.079±0.005	8.7±0.2
			23.5	58	69.8±0.3	6.22	0.054±0.008	7±0.2
	60 b	**0.8-1.3 mM NaCl, pH 8.8-9**	**23.1**	**138**	**68±1**	**6.55**	**0.222±0.007**	**26.4±0.2**
			23.1	180	68±1	5.48	0.077±0.015	33.9±1.8
			23.1	150	70±1	5.03	0.049±0.001	23.2.±0.2
			24.3	113	68.8±1	8.11	1.04±0.055	25.1±0.3
			24.3	112	68.8±1	8.13	1.07±0.056	24.7±0.3
	40 bp	**1.1-1.3 mM NaCl, pH8.7-8.8**	**23.1**	**152**	**71±1**	**6.49**	**0.149±0.003**	**35.9±0.1**
			23.1	161	72.3±1.4	5.84	0.078±0.002	37.3±0.3
			23.1	137	72.3±1.4	7.58	0.443±0.013	39.5±0.2
			23.4	156	72.3±1.4	5.91	0.083±0.010	35.9±1.1
	60 bp	**1.1-1.3 mM NaCl, pH 8.8-8.85**	**23.0**	**148**	**72.3±1.4**	**7.25**	**0.452±0.009**	**43.3±0.2**
			23.1	156	71±1	6.59	0.233±0.012	38.7±0.4
			23.1	172	72.3±1.4	5.73	0.099±0.003	41.8±0.3
			23.1	153	71±1	6.73	0.267±0.015	38.3±0.5
			23.1	144	72.3±1.4	8.66	1.85±0.091	52.4.±0.4
Protein	**ProTα**	**0.8-1.2 mM NaCl, pH 8.8-8.9**	**24.4**	**113**	**76.4±0.6**	**7.03**	**0.350±0.023**	**30.9±0.4**
			23.0	156	71±1	5.62	0.086±0.001	30.2±0.1
			23.1	128	71±1	6.52	0.208±0.005	25.8±0.1
			24.8	147	65.5±0.7	6.63	0.233±0.003	25.1±0.1
			25	148	65.2±1.2	7.15	0.39±0.009	27.7±0.1
			24.1	135	72.3±1.4	6.77	0.270±0.035	33.3±0.8
			23.0	124	71±1	6.73	0.258±0.004	25.6±0.05
	Stm-I	**1.9-2.1 mM NaCl, pH 8.8-9**	**23.1**	**230**	**68±1**	**7.41**	**0.971±0.049**	**93.3±1.3**
			23.1	240	68±1	6.20	0.3±0.014	78.4±0.9
			23.1	270	68±1	5.68	0.182±0.016	92.5±2.3
			23.7	270	72.3±1.4	4.78	0.075±0.002	90.9±0.8
	Gusβ	**0.9-1 mM NaCl, pH 8.75-8.9**	**23.1**	**135**	**72.3±1.4**	**5.48**	**0.086±0.001**	**23.8±0.1**
			23.1	137	72.3±1.4	5.41	0.080±0.003	23.9±0.2
			24.4	120	67.5±1	6.28	0.188±0.004	18.1±0.1
			24.7	124	66.3±1.4	6.51	0.237±0.009	19.1±0.1
			25.1	123	65.9±0.4	7.11	0.431±0.009	20.7±0.1
			24.6	124	66.3±1.4	7.37	0.560±0.023	22.8±0.2
			24.9	121	74.6±0.8	5.52	0.090±0.009	22.0±0.6

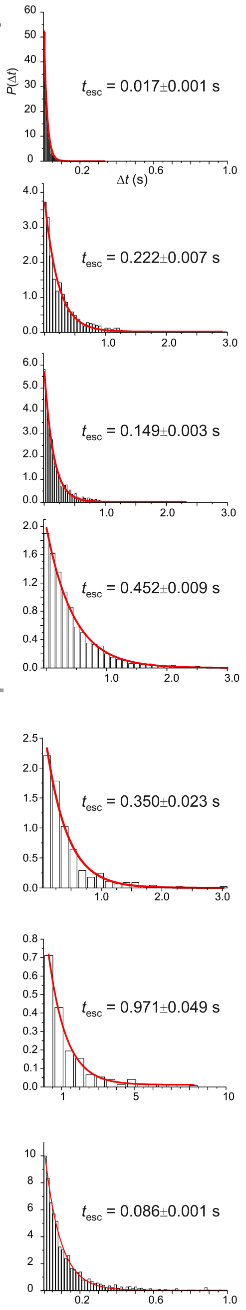

Supplementary Fig. 8. **Experimental details on all measurements contributing to q_m in Figure 3.** The column “Buffer” details the range of salt concentrations and pH probed over all listed measurements for each species. On the right are normalised histograms of recorded escape times and corresponding exponential fits of t_{esc} for a representative measurement, denoted in boldface.

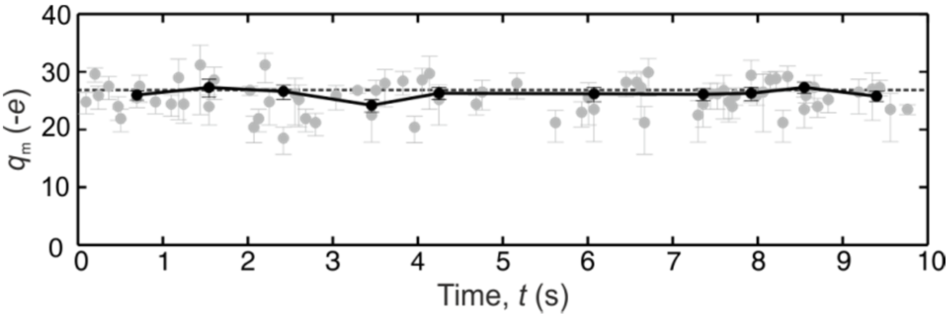

Supplementary Fig. 9. **Simulation of a real-time escape-time electrometry experiment.** We simulated a series of single-molecule trapping events for a 60 b ssDNA molecule, as shown in Supplementary Fig. 7. Binning the trace of escape times in groups of N = 3 (grey data) and 21 (black data) consecutive events, for a well of depth, $W = 6.4\ k_B T$ - corresponding to the experimental measurement in Fig. 5d (top panel) - yields values of inferred temporal charge with corresponding uncertainties. The statistical variation in the inferred real-time charge values, q_m is very close to the experimental data.

Supplementary Table 1. **Structural charge and geometric parameters of measured molecules.** q^*_{str} represents a sequence-based estimate from equation (1) at the experimental pH, prior to chemical modification by fluorescent dye moieties, and using intrinsic pK_a values from Ref. [10]. L denotes the full contour length of the molecule, D the diameter and b the average spacing between charges in fully extended linear polyelectrolytes. $l_{b,w} =$ 0.714 nm is the Bjerrum length in water at 25 °C and r_H represents the measured hydrodynamic radius of the molecule. ‡ b=4-7 Å for ssDNA.

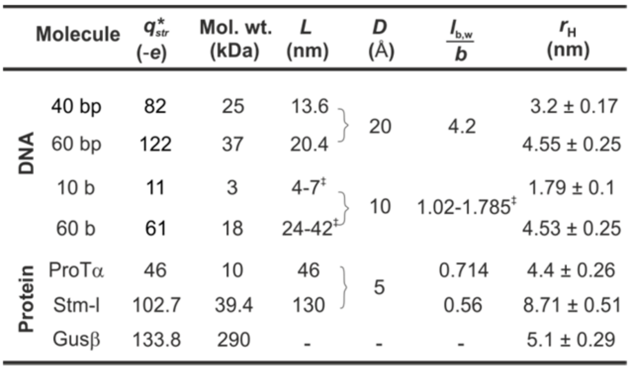

	Molecule	q^*_{str} (-e)	Mol. wt. (kDa)	L (nm)	D (Å)	$\frac{l_{b,w}}{b}$	r_H (nm)
DNA	40 bp	82	25	13.6	20	4.2	3.2 ± 0.17
	60 bp	122	37	20.4			4.55 ± 0.25
	10 b	11	3	4-7‡	10	1.02-1.785‡	1.79 ± 0.1
	60 b	61	18	24-42‡			4.53 ± 0.25
Protein	ProTα	46	10	46	5	0.714	4.4 ± 0.26
	Stm-I	102.7	39.4	130		0.56	8.71 ± 0.51
	Gusβ	133.8	290	-	-	-	5.1 ± 0.29

Supplementary Table 2. **The effective electrical charge of nucleic acids and proteins measured using ET*e*, and compared with our calculations and other theoretical predictions.** All values of charge in units of –e. [†]sequence-based estimate from equation (1) at experimental pH, including the contribution of dye moieties. For DNA, the contribution of dyes is taken as additive in all theoretical estimates, while for proteins, q_{str} remains effectively unaltered. [‡]4-7 Å base-spacing; q_{theory} lists the predicted effective charge from effective charge (charge renormalization) theories, and from an atomistic structure-based calculation for the globular protein. [‖]Ref. [18]; [¶]Ref. [23]; [§]Ref. [24] ; [#]calculated from pK-1/2 values based on PDB structure (http://biophysics.cs.vt.edu/H++, version 3.2) [14]. q_{s} represents the electrical charge of the molecule resulting from charge regulation of the ionizable groups, calculated using our model (see section on 'Theoretical approach'). Our calculated effective charge, q_{c} carries an estimated 1-5% uncertainty due to numerical error in ΔF . Measurement errors reported for q_{m} are s.e.m. Complete experimental details on the measurements are presented in Supplementary Fig. 8.

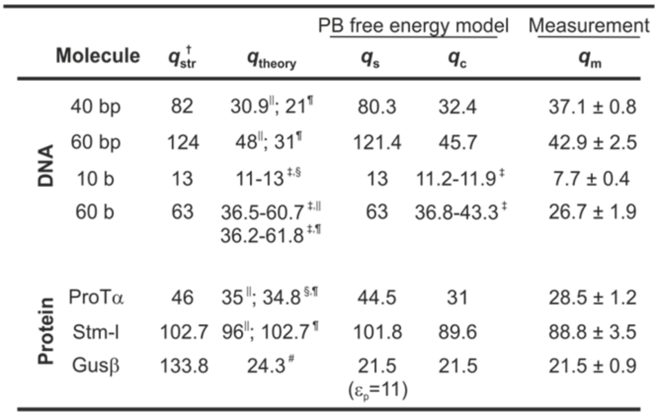

				PB free energy model		Measurement
	Molecule	$q_{\mathrm{str}}^{\dagger}$	q_{theory}	q_{s}	q_{c}	q_{m}
DNA	40 bp	82	30.9[‖]; 21[¶]	80.3	32.4	37.1 ± 0.8
	60 bp	124	48[‖]; 31[¶]	121.4	45.7	42.9 ± 2.5
	10 b	13	11-13[‡,§]	13	11.2-11.9[‡]	7.7 ± 0.4
	60 b	63	36.5-60.7[‡,‖] 36.2-61.8[‡,¶]	63	36.8-43.3[‡]	26.7 ± 1.9
Protein	ProTα	46	35[‖]; 34.8[§,¶]	44.5	31	28.5 ± 1.2
	Stm-I	102.7	96[‖]; 102.7[¶]	101.8	89.6	88.8 ± 3.5
	Gusβ	133.8	24.3[#]	21.5 (ε_{p}=11)	21.5	21.5 ± 0.9

4. Captions for Videos

Supplementary Video 1

The video displays a time series of images of fluorescently labelled single ProTα molecules thermally sampling an array of electrostatic traps, superimposed on an SEM of the nanostructured trapping topography (Panel A, scale bar denotes 2 μm). The sampling rate in the experiment was 20 Hz ($t_{\mathrm{cycle}} = 50\,\mathrm{ms}$), but displayed frames represent a sampling of 4 Hz. Panel B displays the fluorescence signal (red trace) from a single trap (demarcated by a white box in (A)). In a typical experiment, escape-time data from all traps in an array are pooled and fit with a single exponential to give the measured escape time, t_{esc} (Panel C). The video is slowed down by ×5.

Supplementary Video 2

The video presents a short stretch of a real time ET*e* measurement on a single 60 b ssDNA molecule (molecule #4 in Fig. 5). Panel A presents fluorescence images of a single molecule and its trajectory in real-time superimposed on an SEM of the nanostructured surface. Scale bar denotes 500 nm. The sampling rate in the experiment was around 200 Hz ($t_{\mathrm{cycle}} \approx 5\,\mathrm{ms}$). All frames are displayed. Panel B displays durations, $t_{\mathrm{esc},i}$ of individual escape events, *i*. In this case, every 3 escape events or 'hops' yields an average escape time measurement, t_{esc} (dashed green line) which is converted into a measurement of q_{m} (black symbols, panel (C)). Panel C presents real-time measurements of t_{esc} and q_{m} at an average time resolution of 130 ms. Note that the third measurement point arises from relatively rapid escape of the molecule indicating a lower than average temporal effective charge. The video is slowed down by ×60.

References

1 Krishnan, M., Mojarad, N., Kukura, P. & Sandoghdar, V. Geometry-induced electrostatic trapping of nanometric objects in a fluid. *Nature* **467**, 692-695 (2010).

2 Müller-Späth, S. *et al.* Charge interactions can dominate the dimensions of intrinsically disordered proteins. *Proceedings of the National Academy of Sciences* **107**, 14609-14614 (2010).

3 Rozycka, M. *et al.* Intrinsically Disordered and Pliable Starmaker-Like Protein from Medaka (Oryzias latipes) Controls the Formation of Calcium Carbonate Crystals. *PLOS One* **9** (2014).

4 Dertinger, T. *et al.* Two-Focus Fluorescence Correlation Spectroscopy: A New Tool for Accurate and Absolute Diffusion Measurements. *ChemPhysChem* **8**, 433-443 (2007).

5 Kellner, R. *et al.* Single-molecule spectroscopy reveals chaperone-mediated expansion of substrate protein. *Proceedings of the National Academy of Sciences* **111**, 13355-13360 (2014).

6 Benke S., R. D., Wunderlich B., Nettels D., Glockshuber R., Schuler B. The assembly dynamics of the cytolytic pore toxin ClyA. *Nature Communications* **6**, 6198 (2015).

7 Hofmann, H. *et al.* Polymer scaling laws of unfolded and intrinsically disordered proteins quantified with single-molecule spectroscopy. *Proceedings of the National Academy of Sciences* **109**, 16155-16160 (2012).

8 Krishnan, M. Electrostatic free energy for a confined nanoscale object in a fluid. *Journal of Chemical Physics* **138**, 114906 (2013).

9 Ninham, B. W. & Parsegian, V. A. Electrostatic potential between surfaces bearing ionizable groups in ionic equilibrium with physiologic saline solution. *Journal of Theoretical Biology* **31**, 405-428 (1971).

10 Pace, C. N., Grimsley, G. R. & Scholtz, J. M. Protein Ionizable Groups: pK Values and Their Contribution to Protein Stability and Solubility. *Journal of Biological Chemistry* **284**, 13285-13289 (2009).

11 Tanford, C. & Kirkwood, J. G. Theory of protein titration curves. 1. General equations for impenetrable spheres. *Journal of the American Chemical Society* **79**, 5333-5339 (1957).

12 Bashford, D. & Karplus, M. pKas of ionizable groups in proteins - atomic detail from a continuum electrostatics model. *Biochemistry* **29**, 10219-10225 (1990).

13 Baker, N. A. Poisson-Boltzmann methods for biomolecular electrostatics. *Methods in Enzymology* **383**, 94-118 (2004).

14 Gordon, J. C. *et al.* H++: a server for estimating pK(a)s and adding missing hydrogens to macromolecules. *Nucleic Acids Research* **33**, W368-W371 (2005).

15 Isom, D. G., Castaneda, C. A., Cannon, B. R. & Garcia-Moreno, B. E. Large shifts in pK(a) values of lysine residues buried inside a protein. *Proceedings of the National Academy of Sciences of the United States of America* **108**, 5260-5265 (2011).

16 Behrens, S. H. & Grier, D. G. The charge of glass and silica surfaces. *Journal of Chemical Physics* **115**, 6716-6721 (2001).

17 Belloni, L. Ionic condensation and charge renormalization in colloidal suspensions. *Colloids and Surfaces a-Physicochemical and Engineering Aspects* **140**, 227-243 (1998).

18 Netz, R. R. & Orland, H. Variational charge renormalization in charged systems. *European Physical Journal E* **11**, 301-311 (2003).

19 Manning, G. S. Electrostatic free energies of spheres, cylinders, and planes in counterion condensation theory with some applications. *Macromolecules* **40**, 8071-8081 (2007).

20 Aubouy, M., Trizac, E. & Bocquet, L. Effective charge versus bare charge: an analytical estimate for colloids in the infinite dilution limit. *Journal of Physics a-Mathematical and General* **36**, 5835-5840 (2003).

21 Savin, T. & Doyle, P. S. Static and dynamic errors in particle tracking microrheology. *Biophysical Journal* **88**, 623-638 (2005).

22 Stein, D., Kruithof, M. & Dekker, C. Surface-charge-governed ion transport in nanofluidic channels. *Physical Review Letters* **93**, 035901 (2004).

23 Manning, G. S. Limiting laws and counterion condensation in polyelectrolyte solutions. I. Colligative properties. *Journal of Chemical Physics* **51**, 924-933 (1969).

24 Manning, G. S. Approximate solutions to some problems in polyelectrolyte theory involving nonuniform charge distributions. *Macromolecules* **41**, 6217-6227 (2008).

6

Spectrally Resolved ET*e*

> "One gets to the heart of the matter by a series of experiences in the same pattern, but in different colors."
>
> *Robert Graves*

This chapter introduces the findings presented in our paper "*Spectrally resolved single-molecule electrometry*" [4], in which we have used ET*e* to measure two molecular species at the same time. As discussed in Chapter 3.3, the main source of error in an ET*e* measurement arises from the uncertainty in the determination of the electrostatic midplane potential ψ_m. The precision of the method is function of the number of escape events, N, and scales as $1/(\sqrt{N} q_\mathrm{eff} \psi_\mathrm{m})$. For a molecule of $q_\mathrm{eff} = -30e$, in a typical experiment performed at $\kappa h = 3.5$ ($\psi_\mathrm{m} = 0.17 k_\mathrm{B} T$), this statistical error is $\sim 2\%$ for 100 escape events.

Under the same conditions, the uncertainty on the midplane potential – particularly the channel height – inherently limits the accuracy. In a single measurement, where the nominal channel height may depart from the mean value by 2-3 standard deviations, the inaccuracy can be up to $\sim 15\%$ (see Section 3.3 for further details).

In order to achieve high accuracy – as well as precision – and to circumvent the need to extensively characterizing every device, we use the second molecular

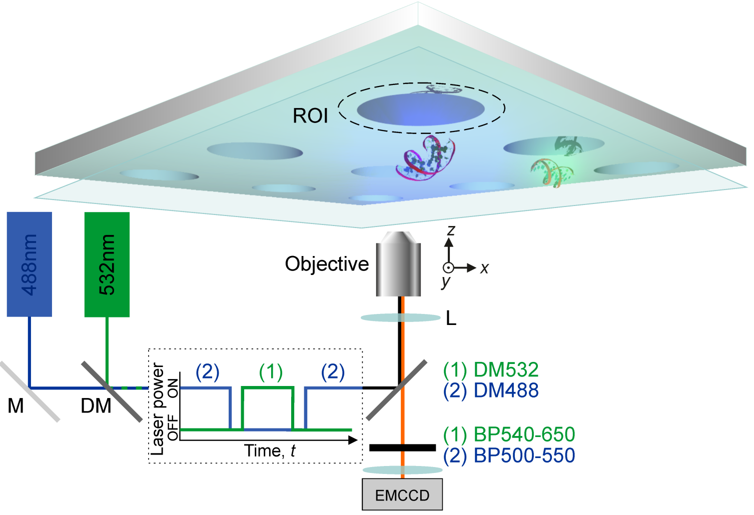

Figure 6.1: Schematic of the double color fluorescence setup, adapted from Ref.[4]. The green and blue laser (and their respective emission filter sets) are toggled to image and measure molecules labelled with two different ATTO dyes.

species as a "calibration molecule". This is typically a 60bp dsDNA molecule of well characterized q_{eff}. Given the charge of the calibrator, once we measure the well depth $W \approx q_{\text{eff}}\psi_{\text{m}}$, the midplane potential is easily inferred. Measuring two molecules at the same time, in the very same area of the device, ensures that the electrostatic potential experienced by both species is indeed the same and the effective charge of the unknown species can be determined with both precision and accuracy.

The wide-field setup was updated in order to incorporate a second excitation wavelength (Laser MDL-III-488, PhotonTec Berlin GmbH). The two laser lines were alternated toggling between two dichroic and filter sets. The green components are described in Chapter 3, while the blue filter set consists of a Dichroic (LPXR H488, Semrock) and a combination of a Shortpass (FESH0550, Thorlabs) and few Longpass filters (FGL495 and FELH0500, Thorlabs and F76-490, AHF) in the emission path, as depicted in Figure 6.1.

6.1 The Dyes

The dyes chosen in order to label the macromolecules, ATTO 532 and ATTO 488 (ATTO-TEC GmbH), are very bright and similar in both structure and net

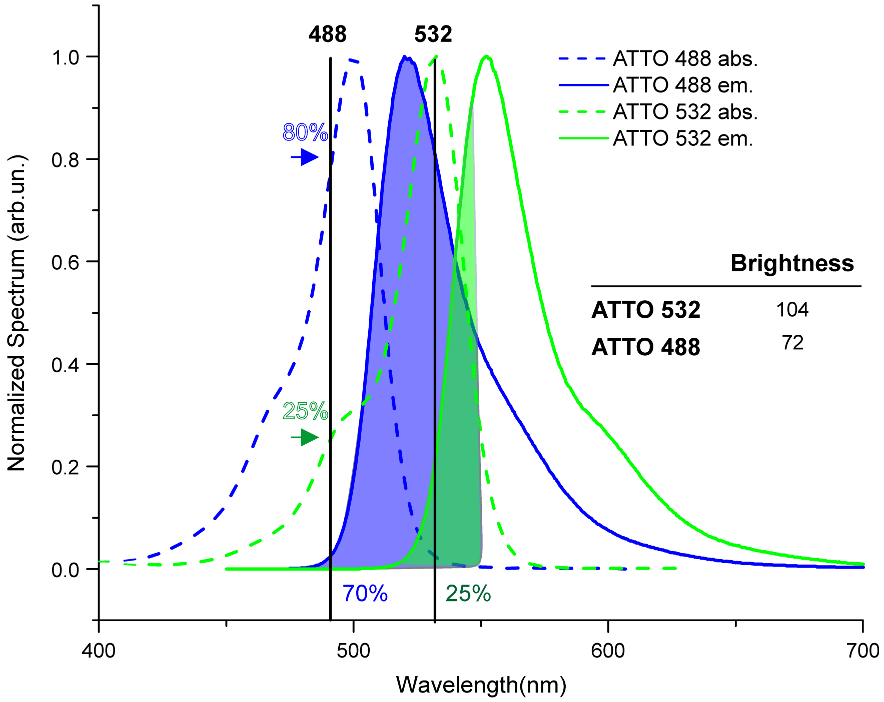

Figure 6.2: The figure depicts emission (solid lines) and absorbance (dashed lines) spectra of the ATTO dyes used in this work. The vertical lines indicate the laser lines. The area highlighted shows the effective area of the emission spectra that will reach the detector, given the filter set used for the blue molecules.

charge. The molecules studied were labelled with either of the ATTO dyes (we attached two of the same dye per each molecule), and measured in the same area of a ETe device in an alternating fashion, for a few seconds each.

In order to make sure to clearly separate the species, we have verified that only the ATTO 532 labelled molecules were visible under green excitation and viceversa. Inspection of the two dyes emission and excitation spectra reveals that, under green excitation, the ATTO 488 dye is only weakly excited ($<$ 5% excitation efficiency, see Fig.6.2) and therefore any bleed-through of the emission of the blue molecule is unlikely to be detected. However, under 488 nm excitation, the ATTO 532 dye can be excited with 25% excitation efficiency and might contribute to a weak spurious fluorescence signal in the other emission channel. To give an estimate, if we were to collect all the emission above 500 nm, under our typical blue illumination conditions the ATTO488-labelled molecules would have an SNR $\sim$ 10, while the green molecule (excited sub-optimally but

characterized by higher brightness, see Figure 6.2), would have an SNR ~ 3.5, high enough to be detected and potentially skew the measured average t_{esc} of the blue species.
In order to avoid any artifact in the measurement, we collected the blue signal only up to 550 nm, losing roughly 30% of the blue emission but, importantly, reducing > 75% of the green signal bleed-through. Overall we find that doing so, under blue excitation, the chosen combination of filters attenuates the spurious green fluorescence by a factor $\sim 7-8$, compared to the desired blue one. Adjusting the 488 nm laser power and the detector exposure-time in order to obtain an SNR of ~ 6 for the blue molecules, the green bleed-through is lost in the background noise and does not create any artifact in the measurement.

6.2 Spectrally resolved ETe vs PAGE

We used Spectrally-resolved ETe to distinguish minute differences between dsDNA fragments. The preparation of dsDNA molecule via annealing (Chapter 3.2.1) demands exact mixing of complementary ssDNA strands, each carrying an ATTO dye. This process relies on precise determination of each strand concentration (via UV-VIS spectrometry) and careful pipetting of the two in the annealing buffer. Clearly, due to imperfect mixing, a small fraction of ssDNA might remain in the sample, un-annealed. As shown in Fig.4 of our manuscript [4], Native Polyacrylamide Gel Electrophoresis (PAGE) can easily distinguish between few bp differences in dsDNA and even detect small contamination of ssDNA, which tends to run slightly faster in an electrophoretic field than its double stranded counterpart.

By performing a single-molecule, spectrally resolved ETe measurement, we can also distinguish between dsDNA fragment that only differ by 4 bp (60bp-ATTO488, the "calibrator molecule" vs. 56bp-ATTO532). Furthermore, we observe the presence of weakly emitting, fast escaping, molecules in both the green and blue emission channels. These are most likely ssDNA molecules, which only carry one dye and our independent ETe measurements have indicated to carry roughly half of the effective charge, resulting in shorter t_{esc} [3]. Note that in fact charge renormalization would predict the same q_{eff} for ss and dsDNA of the same length, but we find that this is not the case: ssDNA is in general less charged than its double stranded counterpart. This is probably due to geometric features of ssDNA that render the rigid rod description of the electrostatic inadequate.

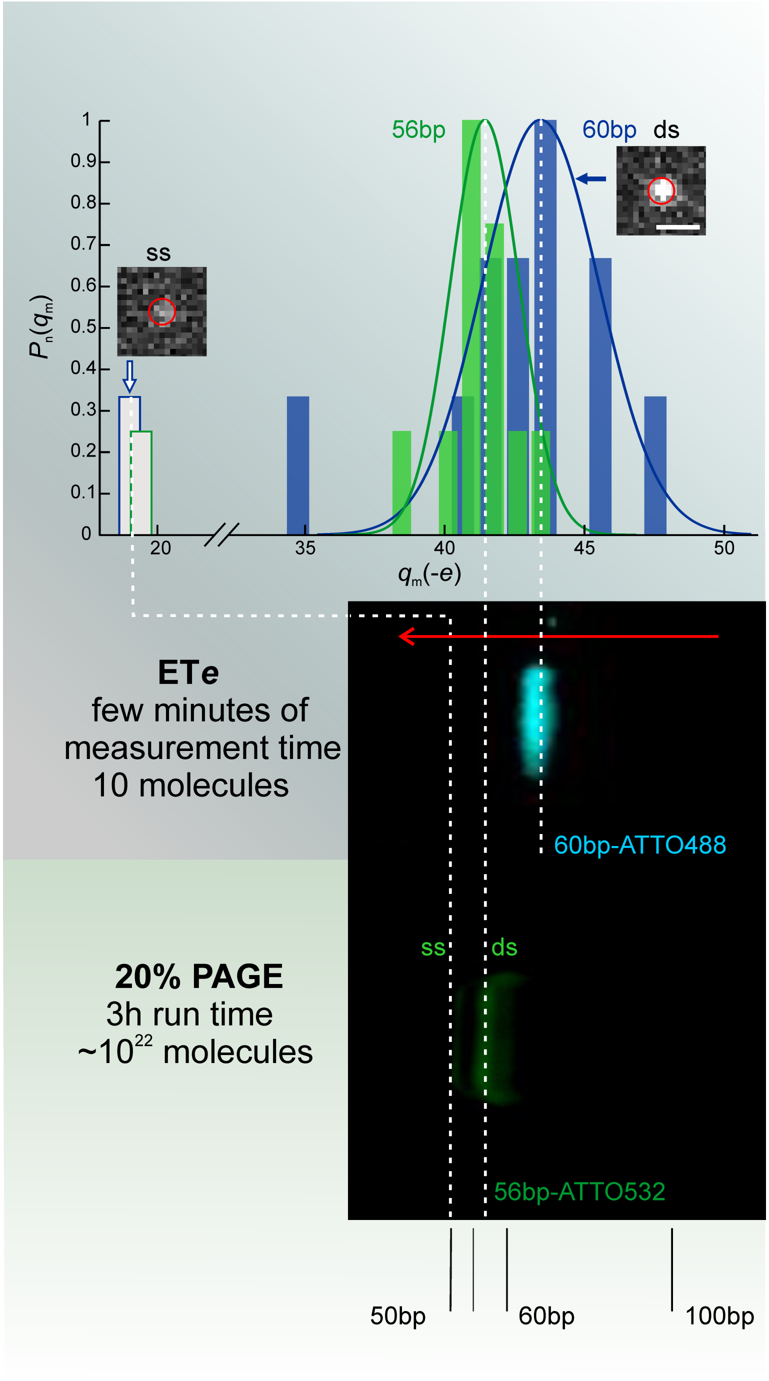

Figure 6.3: Comparison of PAGE and ET*e* results. The image is adapted from Ref.[19]; the gel in the bottom is represented in false color. The red arrow indicates the direction of the electrophoretic mobility.

A typical PAGE experiment requires micromolar concentration of DNA (10^{22} molecules) and several hours of run-time in order to separate minute differences; in addition DNA mobility in gel may show anomalous behaviours, due to undesirable interaction of the molecules with the gel matrix [79]. For example, we have observed that our double-labelled fragments tend to run detectably slower than the corresponding ladder band, probably due to the presence of the attached dyes.

On the other hand, spectrally resolved ET*e* has a few key advantages: it requires very low amounts of molecules (we typically measure ~ 10 for each color) and it is remarkably fast, needing only few minutes of measuring-time in total (Figure 6.3). By distinguishing molecules not only by color, but also by other more subtle detection features like fluorescence intensity, we foresee the application of this novel technique for detecting and sorting mixtures of macromolecules, at the single-molecule level.

THE JOURNAL OF CHEMICAL PHYSICS **148**, 123307 (2018)

Spectrally resolved single-molecule electrometry

F. Ruggeri[1] and M. Krishnan[1,2,a)]
[1]Department of Chemistry, University of Zürich, Winterthurerstrasse 190, CH 8057 Zürich, Switzerland
[2]Department of Physics, University of Zürich, Winterthurerstrasse 190, CH 8057 Zürich, Switzerland

(Received 11 October 2017; accepted 20 November 2017; published online 13 December 2017)

Escape-time electrometry is a recently developed experimental technique that offers the ability to measure the effective electrical charge of a single biomolecule in solution with sub-elementary charge precision. The approach relies on measuring the average escape-time of a single charged macromolecule or molecular species transiently confined in an electrostatic fluidic trap. Comparing the experiments with the predictions of a mean-field model of molecular electrostatics, we have found that the measured effective charge even reports on molecular conformation, e.g., folded or disordered state, and non-uniform charge distribution in disordered proteins or polyelectrolytes. Here we demonstrate the ability to use the spectral dimension to distinguish minute differences in electrical charge between individual molecules or molecular species in a single simultaneous measurement, under identical experimental conditions. Using one spectral channel for referenced measurement, this kind of photophysical distinguishability essentially eliminates the need for accurate knowledge of key experimental parameters, otherwise obtained through intensive characterization of the experimental setup. As examples, we demonstrate the ability to detect small differences (~5%) in the length of double-stranded DNA fragments as well as single amino acid exchange in an intrinsically disordered protein, prothymosin α. *Published by AIP Publishing.* https://doi.org/10.1063/1.5008936

I. INTRODUCTION

Electrical charge is a fundamental property of biological matter and plays a central role in the function and interaction of biological molecules.[1,2] For example, "supercharged" isoforms of evolutionarily conserved proteins are known to confer extreme physiological capacities on certain species, presumably owing to their enhanced stability to aggregation at high concentration.[3–5] It is also well known that the addition and removal of small amounts of structural charge in the form of phosphate groups or other post-translational modifications modulate not only such basic phenomena as protein stability but also sub-cellular localization or function and can regulate macroscopic processes such as metabolism at the systemic levels.[6] A recent study demonstrated at the molecular level that the addition of as few as two phosphate groups to a protein induced a folding-unfolding transition and altered its binding affinity by orders of magnitude.[7] Not surprisingly, several disease states are correlated with altered phosphorylation of proteins, e.g., disordered proteins such as tau and α-synuclein involved in Alzheimer's and Parkinson's disease, and multimeric proteins such as the stress-activated p53, implicated both in ageing and cancer.[8,9] Furthermore there is strong evidence that molecular electrostatics plays a dominant role in phase segregation processes mediated by charged disordered proteins and nucleic acids in the cell.[10,11] The ability to perform a direct, sensitive, high-resolution measurement of the charge of a macromolecule in solution would thus have strong implications from both a fundamental as well as a biomedical perspective.

Contrary to the situation in vacuum, the electrical charge of a macromolecule in solution is governed strongly by thermodynamic processes in the electrolyte that render both theoretical predictions and experimental measurements of the quantity non-trivial. At the simplest level, a direct sum over a macromolecule's charged groups yields a qualitative estimate of its formal structural electrical charge, at a given solution pH,

$$q_{\mathrm{str}} = \sum_i \frac{z_i e}{1 + 10^{z_i(\mathrm{pH}-\mathrm{p}K_i)}}. \tag{1}$$

Here i denotes each ionizable group, pK_i is the negative logarithm of its acid dissociation constant, $z_i = +1$ or -1 indicates the valence of charge of a basic or an acidic group, respectively, and e is the elementary charge. In practice however, collective interactions in a densely packed system of charges can dramatically modify the molecule's effective charge in solution via two separate phenomena, namely, charge regulation and charge renormalization. The former concerns an alteration in the charged state of an ionizable group in the context of the molecular environment, while the latter deals with the highly non-linear screening of molecular charge by counterions in the surrounding electrolyte phase. Both phenomena generally result in a reduced "effective" charge of an electrically charged object and have each received extensive theoretical attention, from polyelectrolytes and proteins to colloidal particles and charged surfaces in solution.[12–19]

A variety of experimental approaches have been applied to the problem of electrical charge measurement on a nanoscale entity in the fluid phase. Electrokinetic methods that probe

---

[a)]Electronic mail: madhavi.krishnan@uzh.ch the electrical potential (ζ-potential) near the surface of an object in an applied electric field yield qualitatively correct results, but the measurement is not highly sensitive at the quantitative level. This is due at least in part to the highly non-linear and even non-monotonic response of a particle's electrical mobility to its charge.[20] Along similar lines, capillary electrophoresis can offer single-charge resolved detection of weakly charged species, but the strong dependence of mobility on an *a priori* unknown drag coefficient renders direct determination of charge on an unknown molecule difficult; in some instances, chemically generated "charge ladders" of the protein of interest circumvent this issue.[21] Notwithstanding, polarization fields and molecular deformation in an applied field inherently limit the ability of the electrokinetic approach to sensitively probe the charge of a macromolecule in solution.[20] Moving out of the solution-phase, native electrospray-ionization mass spectrometry can generate high resolution charge spectra of a macromolecule of interest, but there is considerable debate on whether and how the measured spectrum relates to the charge of the molecule in solution, with measurements often contradicting each other even at the qualitative level.[22,23]

We recently demonstrated the ability to measure the effective charge of a single macromolecule in solution with sub-elementary charge precision and in real time.[24] The method relied on our recently developed equilibrium thermodynamics-based approach to trapping electrically charged matter in solution.[25] Such a trap does not require externally applied fields, but rather exploits the equilibrium repulsive electrostatic interaction between a charged object in solution and like-charged confining parallel plates. Geometric tailoring of the parallel plates results in a local interaction potential minimum that is capable of confining an electrically charged molecule for long periods.[25,26]

For an object confined in a potential well in the fluid phase, the escape process is governed by overdamped diffusive crossing of an energy barrier and is well described by Kramers' theory in the regime $W > 6k_BT$.[24] Here the average time to escape the potential well is given by

$$t_{\mathrm{esc}} = t_{\mathrm{r}} \exp \frac{W}{k_BT}, \tag{2}$$

where t_{r} is a time scale representing the position relaxation time of the molecule, which in turn depends not only on geometric features of the potential well but also on the molecule's diffusion coefficient, $D = k_BT/6\pi\eta r_{\mathrm{H}}$. Here, r_{H} is the hydrodynamic radius of an equivalent sphere that experiences the same frictional drag as the object of interest, and η is the viscosity of the medium.[27]

Relying on this strong non-linear dependence, we converted the measured average escape time of a trapped molecule into a highly precise measurement of the barrier height, W. We note that the barrier height in our case is in essence the interaction free energy of the molecule with the confining parallel-plate slit relative to infinite separation.[28,29] It is also worth noting that this electrostatic interaction energy, W, expressed as $W = q_{\mathrm{eff}}\psi_{\mathrm{m}} + f$, directly depends on q_{eff}, the molecule's effective charge. q_{eff} is in turn not only a function of the molecule's true structural charge but notably also of its 3D conformation.[29] Here ψ_{m} is the electrical potential at the midplane of the slit and f is a small contribution to the total free energy from the finite out-of-plane thermal fluctuations of the molecule.

Importantly, the high measurement precision offered by the approach stems from the exponential dependence of the measurand (the escape time, t_{esc}) on the measurable (the measured effective charge of the molecule, q_{m}), as reflected in Eq. (2). Since escape times are exponentially distributed, the fractional measurement uncertainty on t_{esc} from a sample of N statistically independent "hops" of a molecule is simply $1/\sqrt{N}$. Since $q_{\mathrm{m}} \simeq \ln\left(\frac{t_{\mathrm{esc}}}{t_{\mathrm{r}}}\right)\frac{k_BT}{\psi_{\mathrm{m}}}$, the corresponding fractional uncertainty on q_{m} is given by $\frac{k_BT}{q_{\mathrm{m}}\psi_{\mathrm{m}}}\frac{1}{\sqrt{N}}$.[24] Thus for $N = 100$, the logarithmic dependence of q_{m} on t_{esc} implies ~2% precision in determining q_{m} in a measurement time on the order of 10 s. This level of measurement precision on the electrical charge of an entity in solution is unprecedented.

Furthermore, the ability to perform the measurement on a single molecule immediately raises the prospect of detecting tiny differences between individual molecules in a heterogeneous distribution of molecular states arising from, e.g., different phosphorylation patterns, mutations in charged residues, or different conformational states. Thus the Escape-Time Electrometry (ET*e*) approach offers tremendous scope for detection and measurement of structural, conformational, and compositional heterogeneity of macromolecules in solution, e.g., folding intermediates, mutations in proteins, and post-translational modifications such as phosphorylation, to name a few.

Although a statistically limited experimental error of say <5% on t_{esc} implies a precision of <2% in charge determination in a single measurement, the accuracy in a single measurement is not expected to be as high. This is because in practice, under our experimental conditions, the experimental uncertainty of ~1 nm on the slit height results in an estimated overall peak-to-peak single-measurement uncertainty of 20% in charge determination.[24] In our original demonstration, this device-related measurement uncertainty was reduced to the level of 2%–6% by averaging over several independent measurements.[24] We did note however that a sequential electrometry measurement on different molecular species in a single device permitted us to address some of the variability in experimental parameters and to thus approach statistically limited precision in a single measurement. Thereby, we demonstrated the ability to distinguish between species carrying very similar amounts of charge.[24] Nonetheless, given the high precision offered by the method, the prospect of attaining both precision and accuracy in a single measurement on different species or molecules in parallel would be highly desirable.

Here we examine the possibility of a parallel electrometry measurement on spectrally distinguishable molecules under identical experimental conditions in a single experiment. If one of the molecules in the measurement serves the function of a "calibrator," then the charge of the other spectrally distinct species—or single molecule—can be determined with an accuracy approaching the statistically limited precision. Alternatively, if absolute values of effective charge are not of interest, but the aim is rather to detect minute differences between molecules, here again the parallel, spectrally distinguishable approach would eliminate all other potential sources of variation and enable the attainment of measurement resolution approaching the statistical limit. We demonstrate this new measurement principle and approach using fluorescently labeled nucleic acid fragments and an intrinsically disordered protein, prothymosin α (ProTα).[30,31]

II. MATERIALS AND METHODS

A. Fluorescently labeled biomolecules

All DNA oligomers in our experiments were purchased from either Microsynth AG (Switzerland) or IBA GmbH (Germany) and carried two fluorescent labels, either ATTO 488 or ATTO 532. The dyes were linked to the 5′ and 3′ termini in the case of ssDNA and to both 5′ termini for the double-stranded fragments. We also examine a 60bp dsDNA fragment carrying a single ATTO 488 label on the 5′ end of a single strand and a second identical dye an interior location of the complementary strand [Fig. 3(a)]. In the latter case, the dye was linked via an amino dT C6 modification to Thymine 30. A modified version of the intrinsically disordered protein, prothymosin α (ProTα),[30,31] carrying a single amino acid exchange E59K was produced using site directed mutagenesis as previously described.[24] Both ProTα species were labeled with either ATTO 488 or ATTO 532 maleimide (ATTO-Tec, Germany) at cysteine residues.

B. Optical setup and electrometry measurements

In this work, we use free energy landscapes created in parallel-plate SiO_2 slits of typical nominal height, $2h$ = 70–90 nm, containing surface nanostructured indentations of diameter 600 nm [Fig. 1(b)] and depth 150 nm, as previously described.[24] A suspension of fluorescently labeled DNA or protein in a buffer containing 1 mM Tris and 0.5-1.5 mM NaCl is introduced into the lattice at a concentration of 10-50 pM by capillary flow.[24] After a few minutes, the flow is arrested and molecular motion in lattices of traps is imaged under purely diffusive conditions by wide-field

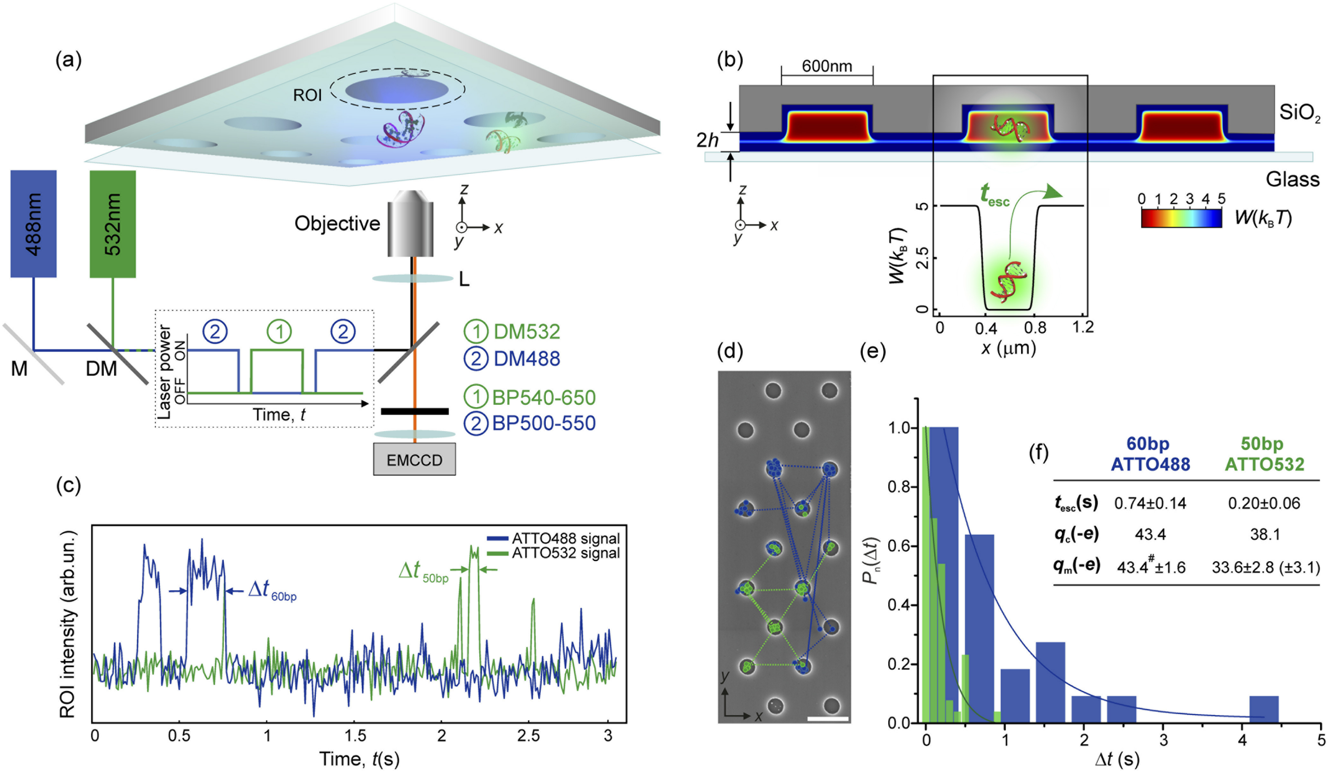

	60bp ATTO488	50bp ATTO532
t_{esc}(s)	0.74±0.14	0.20±0.06
q_c(-e)	43.4	38.1
q_m(-e)	$43.4^{\#}$±1.6	33.6±2.8 (±3.1)

FIG. 1. (a) Schematic representation of the optical setup used for a spectrally resolved single-molecule electrometry experiment. Wide-field fluorescence microscopy employing temporally alternating excitation beams at 488 nm and 532 nm is used to image single macromolecules labeled with ATTO 488 and ATTO 532 diffusing in a lattice of electrostatic fluidic traps. M: silver mirror, DM: dichroic mirror, L: lens, BP: bandpass filter, EMCCD: camera. (b) Representative calculation of the free energy landscape, $W(\boldsymbol{r})$ in the lattice of traps. $2h$ denotes the height of the parallel-plate slit, and the typical nanostructure diameter is 600 nm. (c) The fluorescence intensity of a Region of Interest (ROI) given by the dashed contour in (a), centered on a single trap, monitored in time in both emission channels, clearly shows longer-lived trapped states for 60bp dsDNA-ATTO488 (blue) and shorter trapping times for 50bp dsDNA-ATTO532 (green) (see the supplementary material). (d) Single-particle tracking trajectories of a representative single molecule of each species superimposed on a scanning electron micrograph (SEM) of the underlying nanostructured surface. Scale bar is 1 μm. (e) Probability density distributions, $P(\Delta t) = \frac{A}{t}\exp(-\Delta t/t)$, of experimentally recorded escape times Δt, where $A \approx 1$. The distributions are normalized such that $P_n(\Delta t) = \frac{P(\Delta t)}{P_{max}(\Delta t)}$. (f) Measured average escape time, t_{esc}, in a single lattice over 2-3 molecules for each species ($N \sim 30$), and calculated and measured values of effective charge, q_c and q_m, respectively, for 60bp-ATTO488 and 50bp-ATTO532. $^{\#}$ denotes that q_m for 60bp DNA has been set equal to q_c, permitting a direct calibrated measurement for the other species (50bp DNA). Measurement uncertainties are standard error of the mean (s.e.m.). Values indicated in parentheses for 50bp DNA include the measurement uncertainty on the 60bp DNA "calibration molecule."

fluorescence microscopy. We typically work with landscapes created by a hexagonal lattice of approximately 40 traps where the extent of each lattice is typically 15 µm × 15 µm. In this work, we study molecules in 3-10 lattices for each measurement.

We use optical excitation at 488 nm from a diode laser (PhotonTec Berlin, Germany) and at 532 nm from a diode-pumped solid-state (DPSS) laser (Pusch OptoTech GmbH, Germany). We collect fluorescence emission in two spectral bands—500-550 nm and 540-650 nm—using two temporally alternating dichroic mirrors. The excitation wavelength alternates synchronously with the corresponding emission filters [Fig. 1(a)]. Images of molecular diffusion in the lattice are acquired using a back-illuminated electron multiplying charge coupled device (EMCCD) camera (iXon, Andor, Inc., United Kingdom) with exposures of duration $t_{\mathrm{exp}} = 5$–20 ms and sampling time of 20-100 ms during a total observation time of about 10 s per molecular trajectory. The depth of the wells, W in this work, is typically 5 k_BT, yielding trap residence times of ~200 ms. Furthermore, in this work, the Debye length $\kappa^{-1} \approx 0.3/\sqrt{C} = 10$ nm and is the characteristic length scale of screening of electric fields in an electrolyte containing monovalent salt at a concentration $C = 10^{-3}$ mol/L.

III. RESULTS

A. Measurements on the same molecular species labeled with different fluorescent dyes

A key goal of our electrometry approach is to be able to routinely attain close to 1% measurement precision, and corresponding resolution, in the measured effective charge on two different molecular species, or even two individual molecules of each species, in a single measurement. Spectral splitting of the signal from the species under consideration seems to offer a promising route to this end, as it offers simultaneous measurement under virtually identical experimental conditions—mainly, slit height, salt concentration, and pH.

In an electrometry measurement using two spectrally distinct labels however, a central interest concerns the contributions of the dye molecules themselves to the total molecular charge. Most water-soluble fluorescent dyes used to label biomolecules carry some amount of net charge (typically 1-2e), either positive or negative. In previous work, we presented measurements of the effective charge of ProTα, labeled with spectrally comparable fluorescent dyes carrying different net charge.[24] Our measurements did in fact reveal net charge values for molecules labeled with Cy3B and Alexa 546 that were different from those labeled with ATTO 532, showing that the measurement is sensitive to the charge state of the label. An ideal spectrally referenced measurement would involve the use of spectrally distinguishable dye species that alter the charge of the molecule of interest in a quantitatively identical fashion, if they do so at all. In this work, we focus on two fluorescent dye labels ATTO 488 and ATTO 532 whose structures are shown in Fig. 2(a). We chose ATTO 488 and ATTO 532 as they are chemically very similar and are both expected to carry a net charge of $-1e$, over a wide pH range. They also offer excellent brightness and the required photostability for our measurement.[32,33]

In order to examine the contribution of spectrally distinct dye molecules to the measurement, we performed parallel ETe measurements as described in Sec. II. We find that the variation in slit height, $2h$, from one lattice of traps to the next is reflected in the measured time scales and corresponding effective charges of both species are measured in parallel. To further motivate this point, we present dual color ETe data in experiments where the slits are etched by two different methods: a solution phase wet-etch process using Hydrofluoric (HF) acid and a gas-phase reactive-ion etch (RIE). The former is known to result in large variations of slit height from one lattice of traps to the next ($h_e \sim 2$–3 nm), while RIE—our method of choice, in general—yields uniform slit heights, albeit with an expected nominal rms uncertainty, h_e, of around 1 nm.

First, we studied two species of 10 base ssDNA molecules, each labeled at both ends with either ATTO 488 or ATTO 532 in slits fabricated using RIE. We find that parallel spectrally resolved electrometry on both species agrees within the statistically expected precision [Fig. 2(b)] and the variations in the measured average escape time from one lattice to the next are mainly statistically limited, as expected. We find that the uncalibrated values of measured charge for both species, q_{m}^*, inferred from averaging over $N \sim 200$ escape events recorded in each spectral channel over all lattices, reveal no measurable difference in charge between the two species ($<0.2e$), in keeping with the statistical expectation. This suggests that the two dye species affect the total electrical charge of the molecule in an identical fashion [Fig. 2(c)].

We then studied two species of 60bp dsDNA molecules, each labeled at both 5′ ends with either ATTO 488 or ATTO 532, in a device where the slits were fabricated using etching in HF. Here large correlated variations in the measured escape time scale from one lattice to the next for both measured species reflect common measurement conditions, most likely the local slit height, $2h$ [Figs. 2(d) and 2(e)]. This results in a broad distribution of inferred uncalibrated charge values, q_{m}^* [Fig. 2(e)]. Using the effective charge of 60bp dsDNA labeled with ATTO 532, known both from a calculation as well as measurements under the same experimental conditions in previous work, we infer the "true" local slit height in each lattice. This permits a calibrated measurement of the charge of the blue-labeled species (q_{m}). Figure 2(e) displays both the uncalibrated and spectrally calibrated measured values for the ATTO 488 labeled species. Not only is the mean calibrated value significantly different from the direct measurement but importantly the distribution of measured values is also significantly narrower. These observations exemplify how spectral referencing eliminates a significant source of uncertainty in a single measurement and ultimately enables both accurate and precise measurements on a single molecule [Fig. 2(f)]. We note however that these ensemble-averaged measurements reveal a slightly lower measured charge for the 60bp-ATTO488 species as compared to the ATTO 532 labeled counterpart. This may be due to either residual measurement noise from the large slit height variation that has not averaged out or more likely the presence of a few weakly charged molecules (possibly a small

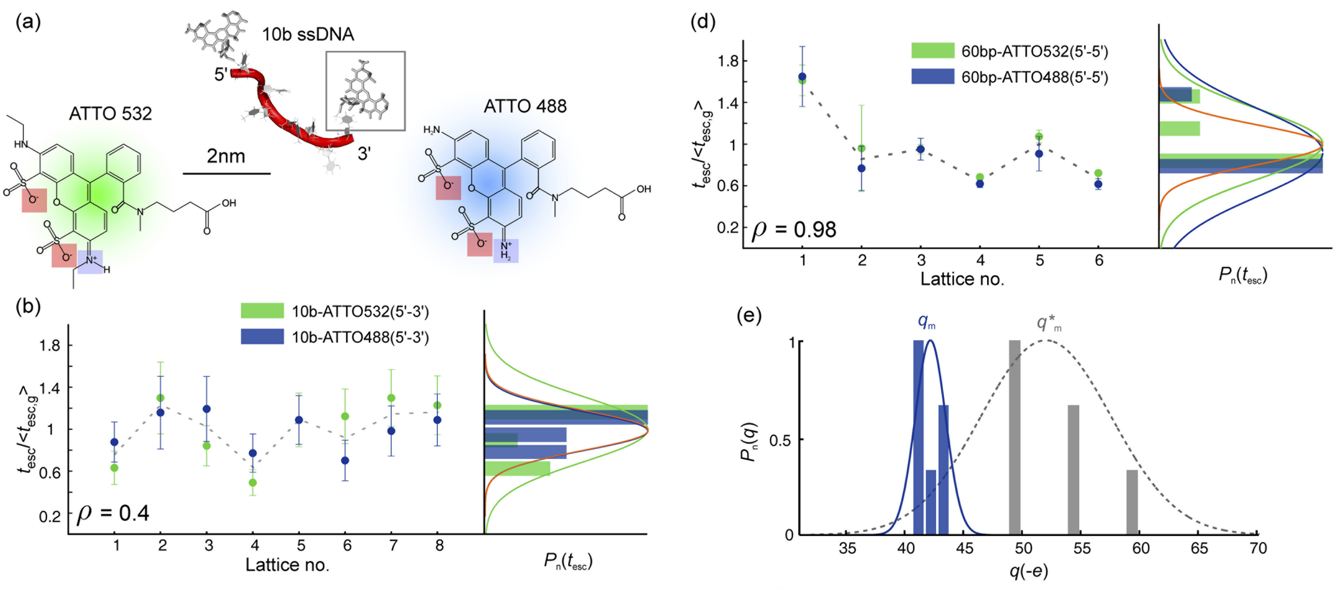

(c)

Molecule	t_{esc}(ms)	q_c(-e)	q^*_m(-e)
10b-ATTO532	46.7±5	10.9	9.6±0.5
10b-ATTO488	47.5±3	10.9	9.7±0.3

(f)

Molecule	q_c(-e)	q^*_m(-e)	q_m(-e)
60bp-ATTO532	43.4	53.6±1.9	$43.4^{\#}$±0.5
60bp-ATTO488	43.4	52.0±2.3	42.1±0.5(±0.7)

FIG. 2. (a) Schematic representations of end-labeled nucleic acid molecules, and the chemical structures of the dyes ATTO 488 and ATTO 532, indicating the expected charged state of the ionizable groups under our measurement conditions (light blue and light red). (b) Values of $t_{\rm esc}$ for 10 base ssDNA labeled with two different dyes, measured in several lattices of traps in the same experiment, normalized by the average measured value of the ATTO 532 labeled species, $\langle t_{\rm esc,g}\rangle$ (green). The dashed line indicates the average $t_{\rm esc}$ for both species in each lattice. Indicated in parentheses are the locations of the ATTO labels for each molecular species. Histograms of $t_{\rm esc}$ for each species (right panel) show nearly statistically limited measurement precision (orange curve) in both cases. The blue and green gaussian curves indicate average and standard deviations for each species. (c) The table displays measured $t_{\rm esc}$ for 10 base ssDNA labeled with either ATTO 488 or 532, averaged over the measurements on 8 lattices (N ~ 200) shown in panel (b). Also indicated are the calculated and measured (uncalibrated) effective charge values, $q_{\rm c}$ and $q^*_{\rm m}$, respectively. The values of $q^*_{\rm m}$ are in remarkable mutual agreement, suggesting that the two dyes most likely affect the overall effective charge of the molecule in a quantitatively identical fashion. Measurement uncertainties are s.e.m. (d) Values of $t_{\rm esc}$ for 60bp dsDNA labeled with two different dyes measured in several independent lattices of traps in slits fabricated using HF etching, normalized by the average value of the ATTO 532 labeled species (green). Histograms of $t_{\rm esc}$ for each species (right) reveal a measurement uncertainty that is larger than the expected statistically limited precision (orange) in both cases. However the mean values for each species averaged over all lattices in both (b) and (d) are in good agreement. While the cross-relation coefficient, ρ, is high in (d) indicating strongly correlated variation in measurement due to the variation in slit height, ρ is lower in (b) where the lattice-to-lattice measurement variation is mostly statistically limited. (e) Uncalibrated charge measurements, $q^*_{\rm m}$, on 60bp-ATTO488, inferred from about 5 to 10 molecules per lattice, using the nominal measured slit height, $2h$ (gray histogram). Calibrated measured values, $q_{\rm m}$, obtained by fixing the charge of the simultaneously measured 60bp-ATTO532 to the calculated value, $q_c = -43.4e$ (blue histogram). The distribution of measured $q_{\rm m}$ (blue gaussian curve) is much narrower that $q^*_{\rm m}$ (dashed gray curve). (f) The table presents uncalibrated directly measured effective charge values, $q^*_{\rm m}$ in 6 lattices, averaged over 5-10 molecules per lattice, and the corresponding values obtained upon calibration, $q_{\rm m}$. Measurement uncertainties are s.e.m.

fraction of unannealed ssDNA) in the 60bp-ATTO488 sample, as will be discussed later.

B. Exploring the effect of dye position: Probing local molecular electrostatics

For a hypothetical molecule carrying identical ionizable groups on its surface, interaction among the solvent-exposed groups leads to a local non-zero surface electrical potential, $\psi_{\rm s}$. Since the chemical potential of the protons is constant throughout the system, the non-zero potential in the vicinity of the groups results in a local pH, different from that in the bulk. In fact the greater the magnitude of electrical potential at the charged groups, the stronger the departure of their degree of ionization, α, from that in isolation, as given by Eq. (3),[16,34]

$$\alpha = \frac{1}{1 + 10^{z_i({\rm pH}-{\rm p}K)}\exp\left(z_i e\psi_{\rm s}/k_{\rm B}T\right)}. \tag{3}$$

This behavior essentially embodies the phenomenon termed "charge regulation." Equation (3) can be generalized to any local potential, ψ, and can therefore be used to describe the behavior of more complex charge distributions and local environments, including a low-dielectric, non-solvent-exposed milieu representing the interior of folded molecules.[29]

Previous studies have discussed the effect of "supramolecular p$K_{\rm a}$ shift" according to which the photophysics and/or charged state of organic dye molecules is altered by the dielectric environment of neighbouring molecules in the host matrix or the local electrostatic environment due to molecule to which the dyes are chemically conjugated. In fact studies on the fluorescein dye have shown that conjugation to ssDNA and dsDNA molecules shifts the dye p$K_{\rm a}$ up by ~0.5 as well as alters the charged state of the fluorophore.[35] In fluorescein, the phenolic group (p$K_{\rm a}$ = 6.5) dissociates to form a dianion which is responsible for intense fluorescence at neutral pH under excitation at 490 nm. Conjugation to a strongly negatively charged polyelectrolyte molecule such as DNA creates a lower pH in the local environment of the dye moiety as compared to the bulk, which shifts its pK_a to an apparently higher value, affecting the dye's photophysics. The pK_a shift of conjugated fluorescein is thus taken to be indicative of the local environment and has even been used to spatially map the local electrostatic potential in RNA molecules.[36,37]

Assuming the linker introduces approximately 1 nm distance between the nucleic acid and the dye, the electrostatic potential at the end-labeled dye molecule under our measurement conditions is $\psi \sim -75$ mV ($3k_BT/e$) [Fig. 3(a)]. Since the dyes are highly acidic (p$K_a \sim 3$) and the measurement p$H = 8.8$, Eq. (3) suggests that the charged state of each end-coupled ATTO dye molecule is not different from its value in free solution. Therefore each dye molecule is expected to add a net structural charge of $-1e$ to the derivatized molecule [Fig. 2(a)]. However the renormalized charge contribution of each dye attached to the molecule could be as low as around $-0.5e$. Indeed our measurements on end-labeled molecules have convincingly demonstrated that the two labels ATTO 488 and ATTO 532 affect the total charge of the molecule in an identical fashion and thus probably have the same ionization behavior. We further address the possibility that local electrostatic effects at the interior of the macromolecule may alter the protonation/deprotonation equilibria of the dye molecule and therefore its charge. If this indeed were the case, the measurement would have to potentially contend with a spurious label-placement dependent contribution to the measured total charge of the molecule.

Figure 3(a) displays the local electrostatic environment of a dye molecule conjugated to an end and an interior location

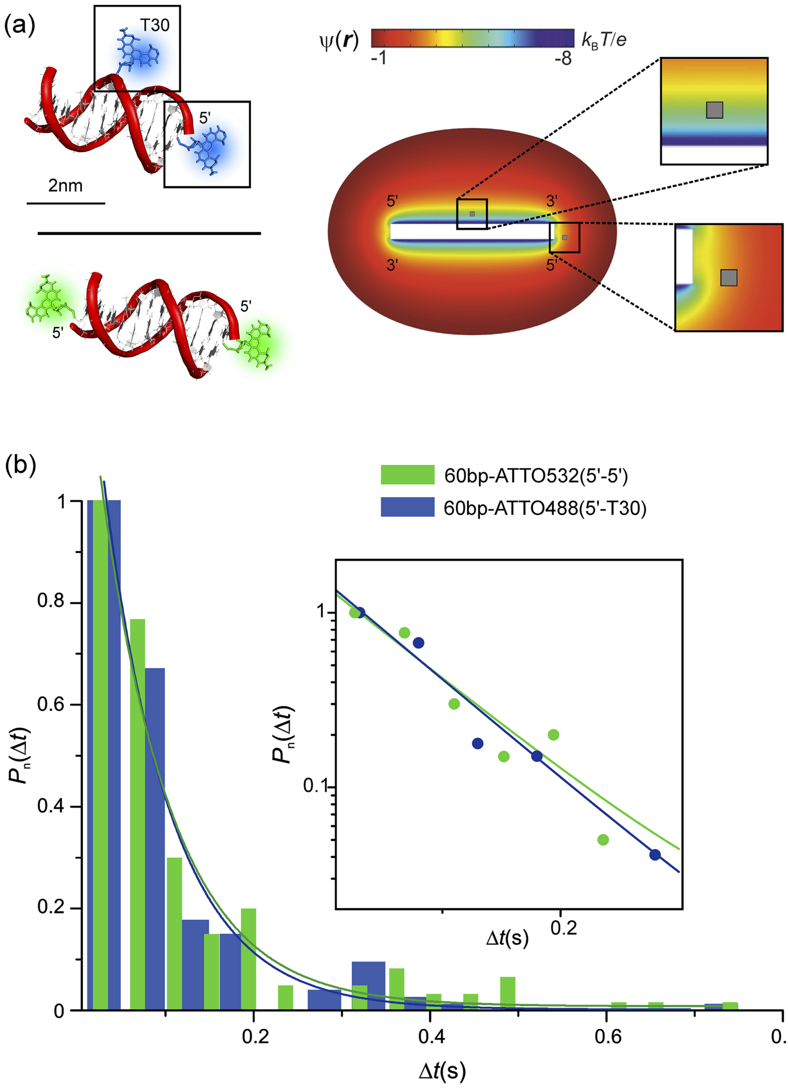

FIG. 3. (a) Schematic representation of two species of 60bp dsDNA molecules, one labeled with ATTO 532 at both 5′ ends and the other labeled with ATTO 488 at the 5′ end and an internal location (T-30). Calculated electrostatic potential distribution, $\psi(\boldsymbol{r})$, around a 60bp dsDNA molecule under our experimental conditions. Gray squares indicate expected approximate locations of the dye molecule relative to the dsDNA fragment, assuming the length of the linker attaching the dye to the molecule is ∼1 nm. (b) Normalized probability distributions, $P_n(\Delta t)$, of measured trap times, Δt, for the two species. (c) The measurements agree within the statistical uncertainty suggesting that dye location has no influence on the measured effective charge. Measurement uncertainties are s.e.m.

(c)

Molecule	t_{esc}**(s)**	q_c**(-e)**	q_m**(-e)**
60bp-ATTO532 (5'-5')	0.080±0.007	43.4	$43.4^{\#}$±1
60bp-ATTO488 (5'-T30)	0.076±0.007	43.4	42.8±1.1 (±1.5)

of a dsDNA fragment. The calculation suggests a difference in electrical potential of around 100 mV between the bulk solution and the interior site of dye attachment. Although these values of local electrical potential (75 and 100 mV) imply pK_a shifts of 1.3 units and 1.7 units, respectively, the effect on the charged state of the ATTO dyes is not expected to be significant, especially at our relatively high measurement p$H \sim 8$.

In order to experimentally probe the influence of local electrostatics on the charged state of the dye label, we compared the measured effective charge of two species of double-labeled dsDNA molecules. One species of dsDNA carries a single dye label at each end of the molecule, while the other carries a single label at one end and a second label at an interior location. If the comparatively large negative local electrical potential at the interior site were to influence the ionization equilibria of the dye molecule strongly enough to alter its net charge, this would be an important consideration in an electrometry measurement that seeks to measure differences of $\sim 1e$ between molecules or molecular species.

Our spectrally split parallel electrometry measurement on the two molecular species, which differ only in the location of a single, otherwise effectively identical dye molecule [Fig. 3(a)], reveals no measurable difference in effective charge [Figs. 3(b) and 3(c)]. The reported effective charges of both species of 60bp dsDNA molecules are based on measurements where the number of hops $N = 160$. We expect 3% measurement resolution under these conditions, which places the expected measurable charge difference between the two spectrally distinguishable species at $\sim 1.3e$.

We further point out that the midplane electrical potential, ψ_m, in this experiment was small by design, resulting in a smaller value of t_{esc} for 60 bp dsDNA compared to the measurements in Figs. 1(e), 1(f), and 2(d)–2(f). Under these conditions, any spurious weakly charged species in solution (as discussed later) would be very unlikely to contribute a detectable trapped state to the ensemble measurement. Our observations thus strongly suggest that the location of the label does not measurably influence the total effective charge of the molecule. This confirms that the charge of both ATTO 488 and ATTO 532 is unaffected by the highly

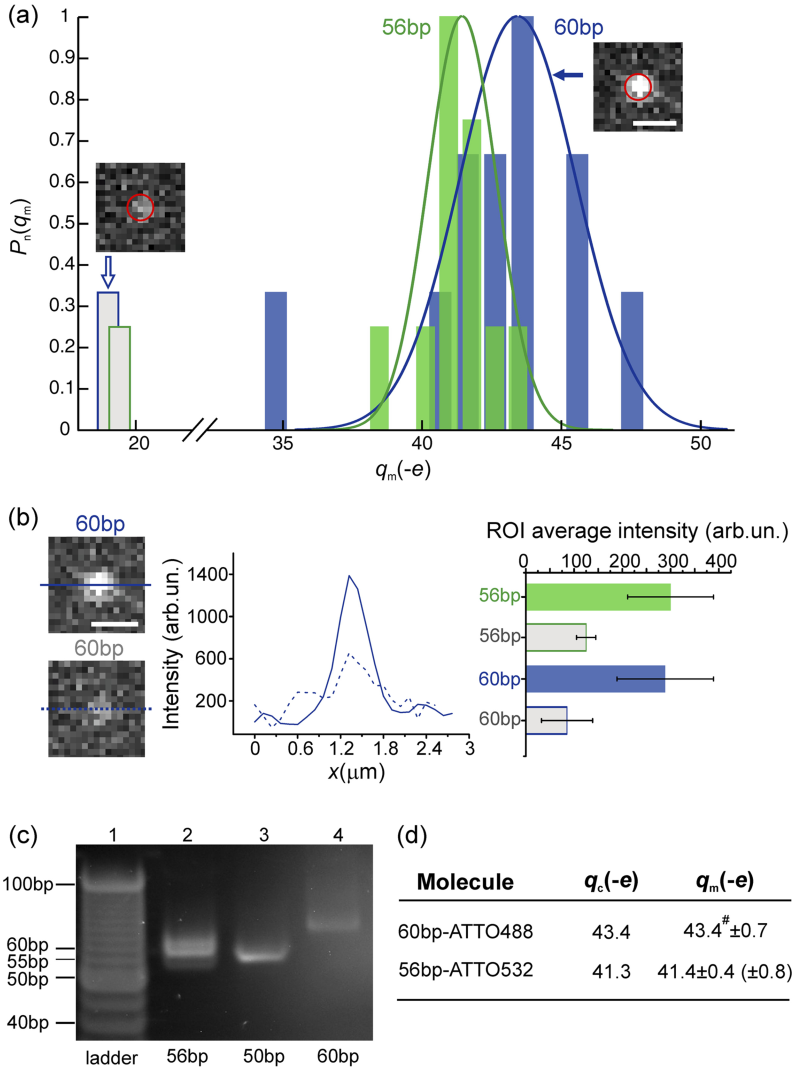

Molecule	$q_c(-e)$	$q_m(-e)$
60bp-ATTO488	43.4	$43.4^{\#} \pm 0.7$
56bp-ATTO532	41.3	41.4 ± 0.4 (± 0.8)

FIG. 4. (a) Histograms of spectrally resolved single-molecule measurements on 56bp-ATTO532 and 60bp-ATTO488. Measurements are reported for individual molecules with $N \sim 20$ hops per molecule, resulting in a typical uncertainty of $\sim 2e$ per measurement on an individual molecule. Solid lines depict gaussian distributions of mean and standard deviation corresponding to the measured dominant fraction of each sample. We also detect the presence of a low abundance weakly charged *and* weakly emitting species (gray bars). Typical images for molecules in the two fractions are presented in each case for 60bp-ATTO488. Red circles denote the occupied trap. Scale bar is 1 µm. (b) Typical intensity profiles for the stably trapped, bright and highly charged species (solid line) and the weakly trapped, poorly emitting, low abundance species (dashed line). Bars represent average ROI intensities over all frames where the molecules register as trapped. The combination of weak emission and short-lived trapping suggests that the low abundance species represents a small excess of unannealed single-labeled ssDNA fragments in solution. (c) 20% native polyacrylamide gel electrophoresis of 5bp DNA ladder (lane 1), 56bp-ATTO532 (lane 2), 50bp-ATTO532 (lane 3), and 60bp-ATTO488 (lane 4) reveal the presence of a rapidly migrating species of low abundance in the 56 bp sample. Molecules in lanes 2-4 display lower mobility than the corresponding fragments in lane 1, likely due to the presence of the dye labels. (d) q_m values of both species, obtained by setting the charge of the dominant fraction of 60bp-ATTO488 to $q_c = -43.4e$. The measurements reveal a difference of about $2e$ between the species, in excellent agreement with the theoretical expectation. Reported errors are s.e.m. over 11 single-molecule measurements per species.

negative local electrical potential due to the strongly charged macromolecule.

The insensitivity of these ATTO dyes to local electrostatics is likely the result of their highly acidic sulfonate groups ($pK_a << pH$, generally). This key feature in combination with their excellent brightness and photostability renders these ATTO dyes excellent labels for spectrally referenced fluorescence-based electrometry measurements.

C. Measuring small differences of charge in biomolecules

Finally we explore the prospect of using spectrally resolved single-molecule electrometry in order to detect small differences of charge (~5%) in biomolecules such as nucleic acids and proteins.

Parallel electrometry measurements on 50bp dsDNA-ATTO532 and 60bp dsDNA-ATTO488 reveal a factor 4 difference in t_{esc} for a modest difference in effective charge of ~12% [Figs. 1(e) and 1(f)]. This suggests that a measurement uncertainty on t_{esc} of ~10%, corresponding to $N = 100$ hops, should place a charge resolution of ~5% well within reach.

We therefore performed parallel ETe on 56bp dsDNA-ATTO532 and 60bp dsDNA-ATTO488, which are expected to differ in effective charge by $2e$. The histogram in Fig. 4(a) displays the results of ~10 single molecule measurements that on average yield a difference in electrical charge close to the theoretically expected value. Note that in these measurements, we fix the charge of one species to the theoretical value. As before, this permits us to minimize the uncertainty on the remaining system parameters, thereby enabling both accurate and precise measurements on the unknown molecule.

The data in Fig. 4(a) show that while the two samples are dominated by a species with a long-lived trapped state, the measurement also detects a second, low-abundance species with very rapid escape dynamics. This "fast fraction" also has a much lower optical intensity than the dominant fraction and we find that its effective charge is very close to our previous measurements on doubly labeled 60 base ssDNA ($q_m = -26.7 \pm 1.9e$). Thus we believe that the species represents a sparse population of singly labeled unannealed ssDNA also present in solution. Gel electrophoresis data indeed confirm the presence of a closely migrating species of slightly higher mobility in the 56bp dsDNA sample [Fig. 4(c)].

Interestingly, examining the measurements on isolated molecules—as opposed to an analysis of pooled single-molecule signals—is key not only to being able to detect small differences between species in different channels but also ultimately to distinguishing different molecular species or states in a given spectral channel.

It is worthwhile to note here that the spatial dimension in the experiment enters the measurement in a subtle way, permitting a chain of nearest neighbor hops in the lattice to be assigned to a distinct molecule. Pooling the measured Δt on individual single molecules and extracting an average value for the measurand would wash out small differences between similar species and make it hard, if not impossible, to glean the underlying charge distribution from the escape time measurement. Indeed an ensemble-level measurement of this kind on the two species reveals statistically indistinguishable time scales, $t_{esc,60bp} = 530 \pm 20$ ms and $t_{esc,56bp} = 550 \pm 15$ ms. Thus we report a preliminary realization of "charge spectrometry" on an ensemble of single molecules in solution.

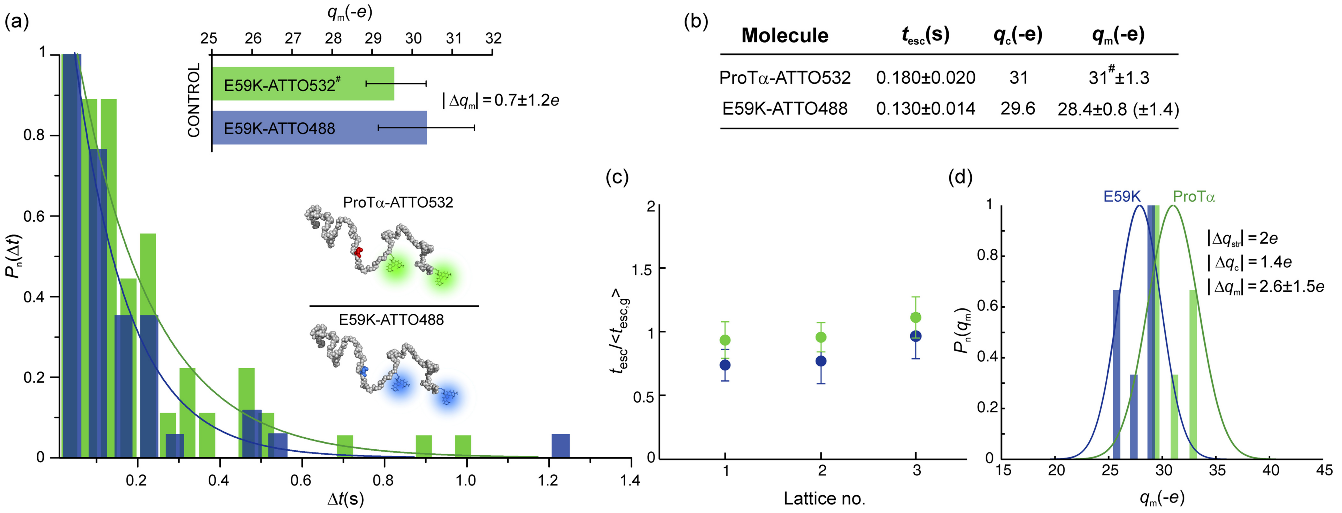

Molecule	t_{esc}(s)	$q_c(-e)$	$q_m(-e)$
ProTα-ATTO532	0.180±0.020	31	$31^{\#}$±1.3
E59K-ATTO488	0.130±0.014	29.6	28.4±0.8 (±1.4)

FIG. 5. (a) Histograms of escape times measured for two species of the disordered protein ProTα, where the ATTO 488 labeled species carries a single amino acid exchange denoted by E59K [residue highlighted in red (E) and blue (K)]. The histograms represent $N \simeq 60$ events for each species. The blue labeled species clearly reveals a value of t_{esc} measurably smaller than that of its unmodified counterpart. Control measurements of ProTα-E59K, labeled with either ATTO 488 or ATTO 532, reveal no measurable difference in molecular effective charge (top panel). (b) Measured t_{esc} from (a), converted to q_m, setting $q^*_{m,ATTO532} = q_c = -31e$, reveal good agreement with theoretical expectations. Measurement uncertainties are s.e.m. (c) Values of t_{esc} for each species measured in three lattices of traps in the same experiment, normalized by the average value of the ATTO 532 labeled species (green). ProTα mutant E59K displays a systematically lower t_{esc} even at the level of the single lattice. (d) Histograms of measured q_m values over 6 lattices, sampled by 2-3 molecules each. Gaussian curves indicate mean and standard deviation for each dataset.

Finally, we demonstrate the detection of single amino acid exchange in the acidic intrinsically disordered protein ProTα. ProTα is a disordered polypeptide 128 amino acids in length, with a nominal net structural charge of $-46e$. Most of this charge is contained within a C-terminal stretch of 31 amino acids. Previously we have performed sequential electrometry measurements of ProTα and a mutant version, E59K, which contains a single Glutamate(E) residue replaced by a Lysine(K).[24] Both species were labeled with the same fluorescent dye, ATTO 532, and the measurement revealed a clear separation of escape time scales with a ratio of a factor 2, corresponding to a difference in charge, $\Delta q_{\mathrm{m}} = 3e$, between the species.

We performed spectrally referenced measurements on ATTO 488-labeled ProTα-E59K and ATTO 532-labeled ProTα. Measuring the two species in parallel we collected $N \simeq 60$ hops on ~5 molecules and determine the charge of each species. We find an average difference in effective charge of $\Delta q_{\mathrm{m}} = 2.6 \pm 1.5e$ between the two species, which is in reasonable agreement with the theoretically expected value of $\Delta q_{\mathrm{c}} = 1.4e$ [Fig. 5].

IV. CONCLUSIONS

We have demonstrated the ability to perform spectrally referenced high-precision measurements of the effective charge of single biological macromolecules in solution. Spectral calibration of the electrometry measurement is a key development that enables facile, direct measurements that are both accurate and precise.

Although the parameters that quantitatively influence the experiment are considered well known by direct measurement, the residual uncertainty in a key quantity, such as the slit height, has a non-negligible effect on the measurement accuracy. For example, spatial variations of the slit height of the order of about 1 nm, which can occur over a distance of ~50 µm, imply that unless the local height in the vicinity of a single molecule is accurately known, a single direct measurement under our current experimental conditions could carry an inaccuracy of 20%–30%. The inaccuracy would increase for experiments performed at higher salt concentrations where the ratio $\frac{h_e}{\kappa^{-1}}$ is even larger. While white light interferometry is capable of delivering direct measurements of gap heights and can even achieve sub-Angstrom precision on this measure, the accuracy is not expected to be better that about 1 nm. Thus we use a molecule of known charge and size, and spectral characteristics distinct from the molecule of interest, in order to calibrate the entire measurement. This eliminates the need for averaging over multiple realizations in order to obtain an accurate result[24] and could also potentially entirely obviate more demanding forms of setup characterization.

Future experiments will seek to simultaneously measure a large number of single molecules in parallel in order to characterize the spectrum of stable conformational or charged states populated by an ensemble of putatively identical macromolecules in solution. Since the current time resolution of the charge measurement is around 100 ms, the approach will accurately probe molecular conformations that are stable over this observation timeframe. Tracking a molecule's transport in the lattice for a long enough total observation time will also permit real time monitoring of slow structural changes that occur on time scales of around 100 ms or longer.

SUPPLEMENTARY MATERIAL

See supplementary material for an example of spectrally resolved single-molecule electrometry measurement of 60bp-ATTO488 and 50bp-ATTO532.

ACKNOWLEDGMENTS

We gratefully acknowledge the support of the Swiss National Science Foundation, European Research Council, and the University of Zürich. We thank Franziska Zosel and Ben Schuler for the generous gift of fluorescently labeled ProTα. Nanofabrication was carried out at the FIRST Center for Micro- and Nanoscience, ETH Zürich.

[1] M. F. Perutz, "Electrostatic effects in proteins," Science **201**, 1187–1191 (1978).
[2] A. Wada and H. Nakamura, "Nature of the charge distribution in proteins," Nature **293**, 757–758 (1981).
[3] D. B. Thompson, J. J. Cronican, and D. R. Liu, "Engineering and identifying supercharged proteins for macromolecule delivery into mammalian cells," Methods Enzymol. **503**, 293–319 (2012).
[4] M. S. Lawrence, K. J. Phillips, and D. R. Liu, "Supercharging proteins can impart unusual resilience," J. Am. Chem. Soc. **129**, 10110–10112 (2007).
[5] S. Mirceta, "Evolution of mammalian diving capacity traced by myoglobin net surface charge," Science **340**, 1234192 (2013).
[6] S. C. L. Kamerlin, P. K. Sharma, R. B. Prasad, and A. Warshel, "Why nature really chose phosphate," Q. Rev. Biophys. **46**, 1–132 (2013).
[7] A. Bah, R. M. Vernon, Z. Siddiqui, M. Krzeminski, R. Muhandiram, C. Zhao, N. Sonenberg, L. E. Kay, and J. D. Forman-Kay, "Folding of an intrinsically disordered protein by phosphorylation as a regulatory switch," Nature **519**, 106–109 (2015).
[8] A. M. Bode and Z. G. Dong, "Post-translational modification of p53 in tumorigenesis," Nat. Rev. Cancer **4**, 793–805 (2004).
[9] L. Martin, X. Latypova, and F. Terro, "Post-translational modifications of tau protein: Implications for Alzheimer's disease," Neurochem. Int. **58**, 458–471 (2011).
[10] J. T. G. Overbeek and M. J. Voorn, "Phase separation in polyelectrolyte solutions. Theory of complex coacervation," J. Cell. Comp. Physiol. **49**, 7–26 (1957).
[11] W. M. Aumiller and C. D. Keating, "Phosphorylation-mediated RNA/peptide complex coacervation as a model for intracellular liquid organelles," Nat. Chem. **8**, 129–137 (2016).
[12] G. S. Manning, "Limiting laws and counterion condensation in polyelectrolyte solutions. I. colligative properties," J. Chem. Phys. **51**, 924–933 (1969).
[13] G. S. Manning, "Molecular theory of polyelectrolyte solutions with applications to electrostatic properties of polynucleotides," Q. Rev. Biophys. **11**, 179–246 (1978).
[14] G. S. Manning, "Electrostatic free energies of spheres, cylinders, and planes in counterion condensation theory with some applications," Macromolecules **40**, 8071–8081 (2007).
[15] R. R. Netz and H. Orland, "Variational charge renormalization in charged systems," Eur. Phys. J. E **11**, 301–311 (2003).
[16] B. W. Ninham and V. A. Parsegian, "Electrostatic potential between surfaces bearing ionizable groups in ionic equilibrium with physiologic saline solution," J. Theor. Biol. **31**, 405–428 (1971).
[17] S. Alexander, P. M. Chaikin, P. Grant, G. J. Morales, P. Pincus, and D. Hone, "Charge renormalization, osmotic-pressure, and bulk modulus of colloidal crystals: Theory," J. Chem. Phys. **80**, 5776–5781 (1984).
[18] M. Aubouy, E. Trizac, and L. Bocquet, "Effective charge versus bare charge: An analytical estimate for colloids in the infinite dilution limit," J. Phys. A: Math. Gen. **36**, 5835–5840 (2003).

[19] M. Lund and B. Jönsson, "Charge regulation in biomolecular solution," Q. Rev. Biophys. **46**, 265–281 (2013).

[20] R. W. O'Brien and L. R. White, "Electrophoretic mobility of a spherical colloidal particle," J. Chem. Soc., Faraday Trans. 2 **74**, 1607–1626 (1978).

[21] J. M. Gao, M. Mammen, and G. M. Whitesides, "Evaluating electrostatic contributions to binding with the use of protein charge ladders," Science **272**, 535–537 (1996).

[22] I. Gitlin, J. D. Carbeck, and G. M. Whitesides, "Why are proteins charged? Networks of charge-charge interactions in proteins measured by charge ladders and capillary electrophoresis," Angew. Chem., Int. Ed. **45**, 3022–3060 (2006).

[23] J. D. Carbeck, J. C. Severs, J. Gao, Q. Wu, R. D. Smith, and G. M. Whitesides, "Correlation between the charge of proteins in solution and in the gas phase investigated by protein charge ladders, capillary electrophoresis, and electrospray ionization mass spectrometry," J. Phys. Chem. B **102**, 10596–10601 (1998).

[24] F. Ruggeri, F. Zosel, N. Mutter, M. Różycka, M. Wojtas, A. Ożyhar, B. Schuler, and M. Krishnan, "Single-molecule electrometry," Nat. Nanotechnol. **12**, 488–495 (2017).

[25] M. Krishnan, N. Mojarad, P. Kukura, and V. Sandoghdar, "Geometry-induced electrostatic trapping of nanometric objects in a fluid," Nature **467**, 692–695 (2010).

[26] N. Mojarad and M. Krishnan, "Measuring the size and charge of single nanoscale objects in solution using an electrostatic fluidic trap," Nat. Nanotechnol. **7**, 448–452 (2012).

[27] H. Kramers, "Brownian motion in a field of force and the diffusion model of chemical reactions," Physica **7**, 284–304 (1940).

[28] M. Krishnan, "Electrostatic free energy for a confined nanoscale object in a fluid," J. Chem. Phys. **138**, 114906 (2013).

[29] M. Krishnan, "A simple model for electrical charge in globular macromolecules and linear polyelectrolytes in solution," J. Chem. Phys. **146**, 205101 (2017).

[30] K. Gast, H. Damaschun, K. Eckert, K. Schulzeforster, H. R. Maurer, M. Mullerfrohne, D. Zirwer, J. Czarnecki, and G. Damaschun, "Prothymosin-alpha: A biologically-active protein with random coil conformation," Biochemistry **34**, 13211–13218 (1995).

[31] S. Müller-Späth, A. Soranno, V. Hirschfeld, H. Hofmann, S. Rüegger, L. Reymond, D. Nettels, and B. Schuler, "Charge interactions can dominate the dimensions of intrinsically disordered proteins," Proc. Natl. Acad. Sci. U. S. A. **107**, 14609–14614 (2010).

[32] M. Davies, B. Rühle, C. Li, K. Müllen, T. Bein, and C. Bräuchle, "Insights into nanoscale electrophoresis of single dye molecules in highly oriented mesoporous silica channels," J. Phys. Chem. C **118**, 24013–24024 (2014).

[33] T. Kiuchi, M. Higuchi, A. Takamura, M. Maruoka, and N. Watanabe, "Multitarget super-resolution microscopy with high-density labeling by exchangeable probes," Nat. Methods **12**, 743–746 (2015).

[34] B. V. Derjaguin, *Theory of Stability of Colloids and Thin Films* (Springer US, 1991).

[35] R. Sjoback, J. Nygren, and M. Kubista, "Characterization of fluorescein-oligonucleotide conjugates and measurement of local electrostatic potential," Biopolymers **46**, 445–453 (1998).

[36] K. Friederich and P. Woolley, "Electrostatic potential of macromolecules measured by pK_a shift of a fluorophore. 1. The 3′ terminus of 16s RNA," Eur. J. Biochem. **173**, 227–231 (1988).

[37] K. Friederich, P. Woolley, and K. G. Steinhäuser, "Electrostatic potential of macromolecules measured by pK_a shift of a fluorophore. 2. Transfer RNA," Eur. J. Biochem. **173**, 233–239 (1988).

7

Entropic Trapping

> "I think you should always bear in mind that entropy is not on your side."
>
> *Elon Musk*

This Chapter introduces our recently published manuscript *"Entropic trapping of a singly charged molecule in solution"* [6]. Here we have exploited the molecule translational entropy contribution, f, to the total well depth W (see Eqn.1.11), to increase the dynamic range of the ETe technique and quantify the configurational entropy of a trapped molecule.

The use of *conformational* entropy, which is the entropy related with the number of conformations a molecule can assume, has been extensively studied for biomolecules [80, 81]. Practical applications range from nanoparticle functionalization [82, 83], to polymer brushes coating [84], to name a few. *Configurational entropy* however, which is relevant to our work, has to do with the location of the constituents in the system, which are considered as hard spheres and have no internal degrees of freedom.

An early description of configurational entropy for colloidal systems was given by

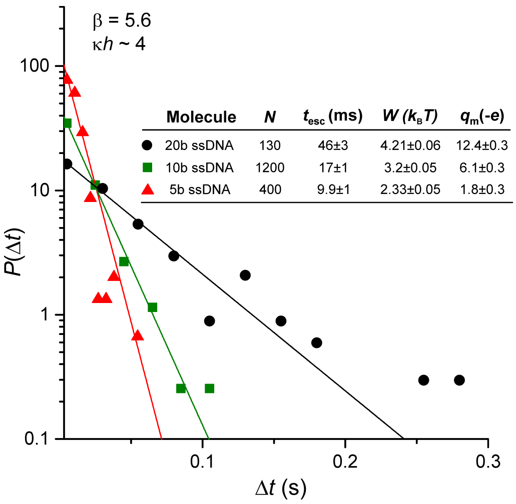

	Molecule	N	t_{esc} (ms)	W (k_BT)	q_m(-e)
●	20b ssDNA	130	46±3	4.21±0.06	12.4±0.3
🟩	10b ssDNA	1200	17±1	3.2±0.05	6.1±0.3
▲	5b ssDNA	400	9.9±1	2.33±0.05	1.8±0.3

Figure 7.1: Escape time probability distribution of 3 short ssDNA molecules - 5,10 and 20 bases - measured under the same conditions using traps of well depth largely due to configurational entropy. The inset table summarizes the measured well depth and $q_{\rm m}$ for each molecule.

Onsager [85], who explained how the apparent higher ordering state of a mixture of long rods, which tend to align, is actually due to a minimization of their excluded volume, which increases the translational entropy of each individual rod. Of similar nature are also depletion forces [86] and phase transitions in colloidal mixtures. Configurational entropy is also a relevant parameter for describing the fusion process in glass forming liquids [87, 88].

We have studied and exploited the *configurational entropy of a particle in the trap* by varying the geometry of the trapping nanostructure and in particular the ratio of heights inside and outside the pocket, $\beta = (2h + d/2h)$.
Chapter 5.3 has shown that tuning of the midplane potential, in order to achieve an higher total well depth, is limited by the range of system parameters – namely κ and $2h$ – that we can achieve experimentally. The nanofluidic channels, for example, tend to collapse for very shallow gaps (see Fig.2.8), hindering the measurement.

Tailoring of the pocket geometry, on the other hand, offers a simple alternative to expand the applicability of ET*e* to weakly charged molecules (Fig.7.1), down to a singly charged fluorophore. At the practical level, this has been achieved by modifying our fabrication procedure, in order to create deeper indentations in the channels. We have used a thicker PMMA E-beam resist to pattern the SiO_2 substrate and included Argon gas in our Reactive Etch recipe, giving straighter etch profiles (see details about Fabrication in Chapter 2.2.2). The maximum depth of pockets we have achieved is $d \sim 330$ nm, which gives a geometrical factor $\beta \sim 6$.

An uncharged object, which doesn't experience any electrostatic interaction in the patterned nanoslit, is still more likely to be found in a pocket than in the slit region, simply because of its larger height, that allows more "states" or "configurations" in the z-dimension. The resulting "entropic trap", corresponding in this case to the "ideal-gas" description, is given by $k_\mathrm{B}T\ln\beta$ and is roughly 2 $k_\mathrm{B}T$ for $\beta = 6$.

Instead a charged object, tightly confined in the middle of the slit space – usually within the first few Debye lengths, $\alpha\kappa^{-1}$, where $\alpha \sim 1 - 2$ – will experience an even higher configurational entropy contribution, given by $k_\mathrm{B}T\ln\beta' \approx k_\mathrm{B}T\ln(\alpha\kappa^{-1} + d/\alpha\kappa^{-1}) > k_\mathrm{B}T\ln\beta$. This additional trap depth can be as high as 4 $k_\mathrm{B}T$ for a molecule carrying roughly 100 charges.

By performing ETe we have measured the total well depth and thus – for the first time to our knowledge – directly characterized this additional entropic contribution, which has allowed us to trap a larger range of molecules under the same experimental conditions, dramatically increasing the dynamic range of the technique.

NANO LETTERS
Cite This: Nano Lett. XXXX, XXX, XXX−XXX
Letter
pubs.acs.org/NanoLett

Entropic Trapping of a Singly Charged Molecule in Solution

Francesca Ruggeri[†] and Madhavi Krishnan[*,†,‡]

[†]Department of Chemistry, University of Zürich, Winterthurerstrasse 190, CH 8057 Zürich, Switzerland
[‡]Department of Physics, University of Zürich, Winterthurerstrasse 190, CH 8057 Zürich, Switzerland

Supporting Information

ABSTRACT: We demonstrate the ability to confine a single molecule in solution by spatial modulation of its local configurational entropy. Previously we established electrostatic trapping of a charged macromolecule by geometric tailoring of a repulsive electrical interaction potential in a parallel plate system. However, since the lifetime of the trapped state depends exponentially on the electrical charge of the molecule, the electrostatic interaction alone is often insufficient in magnitude to stably confine molecules carrying a net charge of magnitude ≤5*e*. Here we show that the configurational entropy of a thermally fluctuating molecule in a geometrically modulated system can be exploited to spatially confine weakly charged molecules in solution. Measurement of the configurational entropy contribution reveals good agreement with theoretical expectations. This additional translational contribution to the total free energy facilitates direct optical imaging and measurement of the effective charge of molecules on the size scale of ∼1 nm and a charge as low as 1*e*, physical properties comparable with those of a monovalent ion in solution.

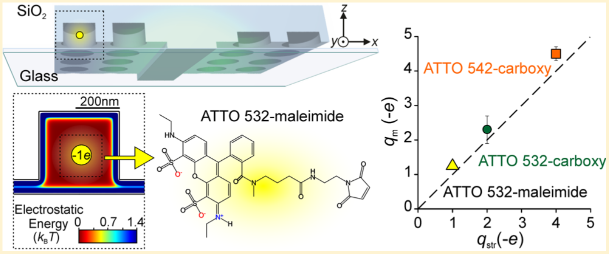

KEYWORDS: *Configurational entropy, single-molecule trapping, effective charge measurement, electrostatic double layer forces*

The development of new experimental approaches to the spatial control and manipulation of single nanoscale entities in the fluid phase remains an area of great current interest. A wealth of techniques exploiting externally applied optical fields,[1−7] time-dependent electrical fields, both deterministic[8−10] and stochastic,[11] as well as thermophoretic[12] and hydrodynamic fields[13] have been reported to address this experimental need.

We recently introduced an external-field-free technique to trap electrically charged molecular scale matter in solution.[14−16] The approach utilized a geometry induced local minimization of an electrostatic interaction free energy for an object in solution and thus circumvented the unfavorable a^3 scaling of trap depth with an object size, a, common to polarizability dependent external-field-based approaches.[17] Here we demonstrate that an additional contribution to the well depth from the translational entropy of the object itself may be harnessed to substantially enhance trap stability. Exploiting configurational entropy enables us to extend the operation of the geometry-driven trapping concept into the regime of weakly charged entities, which carry a charge on the order of 1*e*, where the electrostatic contribution to the interaction energy is very small, ∼1 k_BT, where k_B is the Boltzmann's constant and T is temperature.

The use of entropy to spatially confine long polymer molecules in a geometrically tailored landscape has been reported previously, primarily in the context of polyelectrolyte separations.[18−20] Local variations in height in a confined system modulate the conformational entropy of a polymer by altering the number conformational states accessible to the molecule. The deeper regions in the system give rise to entropic traps that retain molecules for a period much longer than the typical diffusive transport time scale. In general, one relevant confining length scale has to be at least of the same order as the molecule's radius of gyration in order to effectively probe its conformational degrees of freedom.[21−23]

Here we show that the entropic principle may be applied to spatially trap "hard-sphere" entities such as globular macromolecules, and even small organic molecules, that possess no relevant internal conformational degrees of freedom. This is due to the *configurational* entropy of the hard-sphere object, arising from translational freedom in the axial dimension, which can change substantially as a function of spatial position in a corrugated landscape. We find that with the appropriate choice of dimensions, well depths of up to 5 k_BT may be expected due to configurational entropy alone. In terms of time scales, this implies a ∼100-fold enhancement of the residence time given by free diffusion. The effect has been previously examined in theoretical studies on particle transport in corrugated channels, and the local enhancement of states accessible by the particle is sometimes interpreted in terms of a reduction in a local or overall diffusion coefficient.[24−26] Although configurational entropy in many body systems has been examined extensively in thermodynamic measurements at the macroscopic scale,[27−31] few experiments thus far have probed the translational entropy

Received: March 13, 2018
Revised: April 18, 2018
Published: April 24, 2018

DOI: 10.1021/acs.nanolett.8b01011
Nano Lett. XXXX, XXX, XXX−XXX

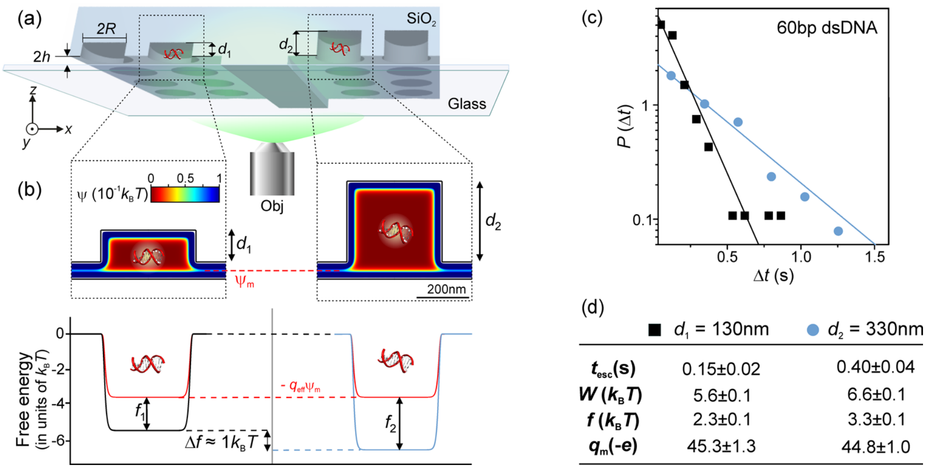

	■ d_1 = 130nm	● d_2 = 330nm
t_{esc}(s)	0.15±0.02	0.40±0.04
W (k_BT)	5.6±0.1	6.6±0.1
f (k_BT)	2.3±0.1	3.3±0.1
q_m(-e)	45.3±1.3	44.8±1.0

Figure 1. (a) Schematic representation of the experimental setup. We measured the average escape time, t_{esc}, of 60 ds DNA in a device where nanoslits of height $2h$ are patterned in an alternating fashion with lattices of nanostructured circular indentations of depths, d_1 = 130 nm and d_2 = 330 nm, and radius, R = 200 nm. (b) While the electrostatic well depth, $q_{eff}\psi_m$, is the same in both cases, the trap created by the deeper indentation entails a larger fluctuation contribution, $\Delta f = f_2 - f_1$, by approximately 1 k_BT in this case. (c) Probability density distributions of experimentally recorded escape times, Δt, fit with a form $P(\Delta t) = \frac{A}{t}\exp(-\Delta t/t)$, where $A \approx 1$. (d) Measured average escape time, t_{esc}, well depth, W, fluctuation contribution, f, and measured values of effective charge, q_m, for 60ds DNA for the two cases. The ratio of the measured escape times, $t_{esc,2}/t_{esc,1}$ = 2.66 ± 0.44, is in excellent agreement with the expected value, $\exp\left(\frac{\Delta f}{k_BT}\right)$ = 2.72. (See text for details and the Supporting Movie.)

associated with the spatial fluctuations of a single entity, e.g., an atom, or molecule in solution.

Experimental Setup and Measurement Approach. In order to explore the possibility of using configurational entropy to trap a single molecule, and to experimentally measure this quantity, we employ our recently developed thermodynamic approach to trapping electrically charged matter in aqueous solution.[14,15] The working principle of such a trap is based on the equilibrium repulsive electrostatic interaction between a charged object in solution and like-charged confining parallel plates (Figure 1a). Geometric tailoring of the parallel plates, by a nanostructured indentation of depth, d, and radius, R, both larger than the Debye length, results in a local interaction energy minimum that is capable of confining an electrically charged molecule for long periods. The Debye length $\kappa^{-1} = \sqrt{\epsilon_m\epsilon_0 k_BT/2cN_Ae^2}$ represents the range of the electrostatic interaction in solution and is typically 10 nm in this work. Here N_A is Avogadro's number, ϵ_m = 78.5 is the dielectric constant of water, ϵ_0 is the permittivity of free space, and c is the bulk salt concentration in the experiment. In the limit of strong electrostatic interactions (e.g., high molecular charge), we have measured molecular residence times in the trap as long as ~30 min.[16] Residence times can be tuned by the geometry of the trapping nanostructure and salt concentration in solution.[16,32,33]

In this work, we use free-energy landscapes created in a parallel plate slit of typical height, $2h$ = 70−80 nm. One of the confining surfaces carries lattices of nanostructured indentations of the radius, R = 200−400 nm (Figure 1a), and depth, d = 100−330 nm. Fluorescently labeled macromolecules in solution are introduced into the lattice at a concentration of 150 pM by capillary flow in a buffer containing 1 mM Tris and 0.25−2 mM NaCl.[16] The flow is arrested, and molecular motion in the lattice is imaged under purely diffusive conditions by wide-field fluorescence microscopy as previously described.[16] We study charged macromolecules such as short DNA fragments, namely, 10 and 20 b ssDNA and 60 bp dsDNA (Microsynth AG, Switzerland), intrinsically disordered proteins, Starmaker-like (Stm-l)[34] and Prothymosin α (ProTα),[35,36] and also examine small fluorescent organic dye molecules with different nominal structural charges, q_{str}, namely, ATTO 532-maleimide ($q_{str} = -1e$), ATTO 532-carboxy ($-2e$), and ATTO 542-carboxy ($-4e$) (ATTO-Tec, Germany). Prior to the experiment, the ATTO 532-maleimide dye dissolved in buffer was reduced with a 2-fold molar excess of 2-mercaptoethanol and sonicated extensively, in order to minimize aggregation.

For an object confined in a potential well in the fluid phase, overdamped diffusive crossing of a barrier is well described by Kramers' theory in the regime $W > 5k_BT$, where the average time to escape the potential well is given by $t_{esc} = t_r\exp(W/k_BT)$.[16,37] Here t_r is a time scale representing the position relaxation time of the molecule. Brownian dynamics simulations that take into consideration the full 3D morphology of the potential well are used to convert the measured average escape time, t_{esc}, of a trapped molecule to a well depth, W.[16,33] (See the Supporting Information for further details.) Since the well depth in turn depends directly on the effective charge of the molecule, q_{eff},[38] we have previously achieved highly precise measurements (precision ~1%) of the effective charge of a variety of biomolecules using the escape-time-based measurement approach described above, which we term "escape-time electrometry" (ETe).[16] The depth of the wells, W, in previous work is typically 5−6 k_BT, yielding trap residence times of ~50−200 ms.

For molecules of effective charge $|q_{eff}| < 5e$, under comparable experimental conditions, the electrostatic interaction alone contributes not more than about 1 k_BT to the trap depth, W. This is often too small to yield molecular residence times of about 5−10 ms, a minimum to facilitate observation of trapping and long-term imaging using conventional detectors and fluorophore labels.[39] We demonstrate that configurational entropy can be used to greatly enhance trapping times in the

DOI: 10.1021/acs.nanolett.8b01011
Nano Lett. XXXX, XXX, XXX−XXX

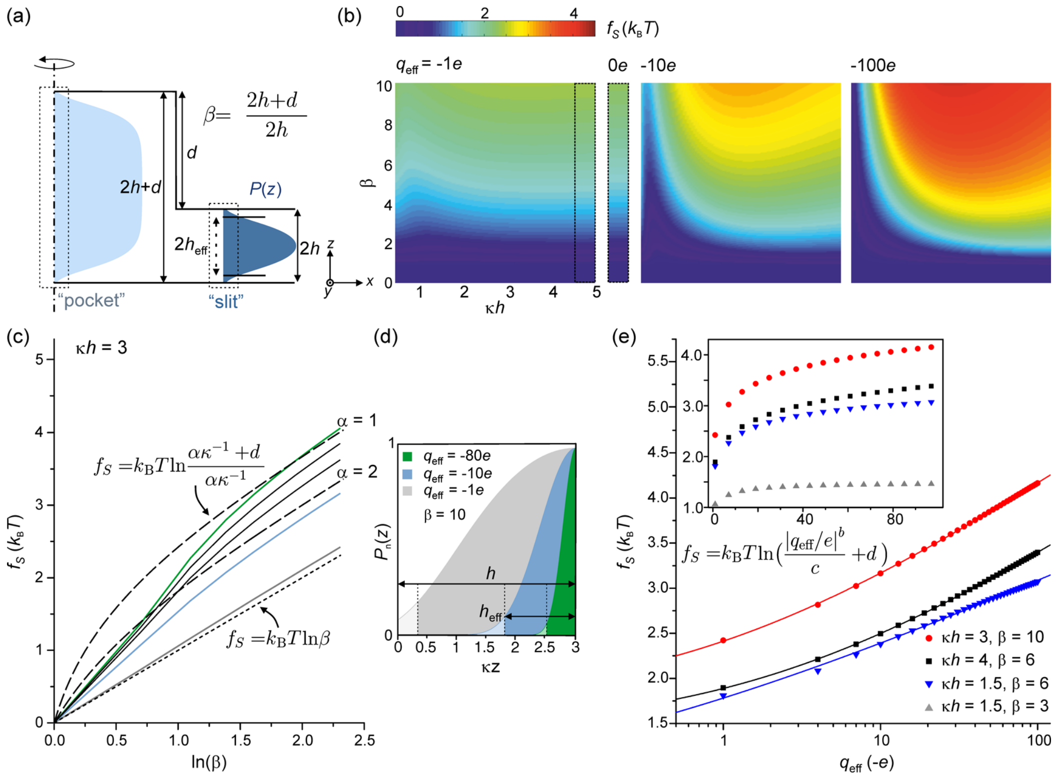

Figure 2. (a) Cross-sectional view of a trapping nanostructure. β denotes the ratio of heights in the system. Representative axial probability distributions of particle position, $P(z)$, in the "pocket" and "slit" domains (blue). (b) Calculated axial fluctuation entropy, f_S, for various combinations of β, system size, κh, and q_{eff}. $q_{\text{eff}} = 0$ depicts the "ideal-gas" case. (c) f_S vs ln β for values of $q_{\text{eff}} = -1e$ (gray), $-10e$ (light blue), $-30e$, $-50e$, and $-80e$ (green) from bottom to top, and $\kappa h = 3$. The behavior between $q_{\text{eff}} = -10e$ (light blue) and $q_{\text{eff}} = -80e$ (green), in the regime $\beta > 4$, is better captured by a phenomenological expression of the form $k_BT\ln\left(\frac{\alpha\kappa^{-1}+d}{\alpha\kappa^{-1}}\right)$, where $\alpha \simeq 1{-}2$ (dashed lines). (d) Normalized probability distributions, $P_n(z)$, in the slit half-space for various q_{eff} and $\beta = 10$. Calculations yield the magnitude of effective slit height, $2h_{\text{eff}}$, underlying the obtained value of f_S, and we find that ~98% of the total axial sampling probability is contained within h_{eff}. Note that, in the limit of a large particle charge, $2h_{\text{eff}} = \alpha\kappa^{-1}$ in the slit, and the corresponding effective height in the "pocket" region is $\alpha\kappa^{-1} + d$. (e) f_S vs q_{eff} for various combinations of β and κh. The fits shown are of the form $f_S = k_BT\ln\left(\frac{|q_{\text{eff}}/e|^b}{c} + d\right)$, where $b = 0.5$ for larger values of κh and β (circles $c = 0.18$, $d = 5.6$; squares $c = 0.4$, $d = 4.1$); $b = 0.3$ for small κh (inverted triangles $c = 0.24$, $d = 1.8$). For small values of both κh and β, f is essentially independent of q_{eff} (upright triangles, inset). $\kappa h = 4$, $\beta = 6$ (squares) is typical for these experiments.

regime of weak electrostatic interactions. Interestingly, inclusion of the configurational entropic contribution also enables measurements of the effective charge on single molecules in the weak electrostatic regime, albeit with a comparatively lower precision (5–20%) in a single measurement. Subtracting the electrostatic contribution to the trap depth, characterized in previous work, we report measurements of the configurational entropy of single molecules in a confined spatially modulated system.

Free Energy of a Single Molecule in a Geometrically Tailored Landscape. The single-particle partition function serves as an appropriate starting point for a complete thermodynamic analysis of a particle in a spatially modulated free-energy landscape.[40] We write the partition function for a point particle whose center is located at $r(x,y)$ in the landscape as $q_r = \int_0^{z_{\max}} \exp(-F_r(z)/k_BT)dz$ where $z_{\max}$ denotes the maximum axial extent of the gap at r. In the "slit" region, $z_{\max} = 2h$, while in the "pocket" region, $z_{\max} = 2h + d$ (Figure 2a). The local axial occupation probability density of the particle is given by $p_r(z) = \frac{\exp(-F_r(z)/k_BT)}{q_r}$.

In our analysis, $F_r(z) = U_r(z) - TS_r(z)$ represents the electrostatic interaction free energy of the particle located at (r,z). Where needed for comparison with the measurement, $F_r(z)$ can be calculated for a given set of experimental parameters as previously described.[16,41] Briefly, it is a volume integral over the whole system, including contributions from both the electrical field energy, U, as well as the entropy of mixing of the ions in solution, S, as originally derived by Overbeek.[42] As has been shown already, for all practical purposes, the electrostatic interaction free energy for an object in the landscape may be written in a simpler form as $F_r(z) = q_{\text{eff}}\psi_r(z)$.[38] Here, the parameter q_{eff} represents the effective charge of a molecule carrying a structural charge, q_{str}, and $\psi_r(z)$ is the electrical potential in the slit at (r,z), in the absence of the particle.

The total free energy, w, of the particle as a function of its location in the landscape, r, is thus $w_r = -k_BT\ln q_r$. This total free energy includes the contribution of axial position fluctuations of the particle and can be decomposed into an electrostatic interaction energy part and a spatial fluctuation entropy component, such that $w_r = u_r - Ts_r$. Here u and s refer to the average electrostatic interaction energy and entropy, respectively, of an axially fluctuating particle at r and are given by

$$u_r = \int_0^{z_{\max}} p_r(z) F_r(z) dz \tag{1}$$

and

$$s_r = -k_B \int_0^{z_{\max}} p_r(z) \ln p_r(z) dz \tag{2}$$

For a given value of q_{eff}, the above integrals are all a function of spatial electrical potential, $\psi(x,y,z)$ alone, which is readily obtained by solving the nonlinear Poisson−Boltzmann equation in the nanostructure as previously described.[14] We use constant charge boundary conditions on the slit walls that correspond to a value of $\psi_s = -2.8 k_B T/e$ for the surface potential of the walls, which we have found to hold under our experimental conditions.[33] From eq 1, we further note that fluctuations render the particle's mean electrostatic energy, $u_r = q_{\text{eff}} \int_0^{z_{\max}} p_r(z) \psi_r(z) dz$ slightly larger than its electrostatic energy at the midplane of the slit, $q_{\text{eff}}\psi_{m,r}$, typically by about 5%. Here $\psi_{m,r}$ denotes the electrical potential midway between the parallel surfaces at any lateral location $r(x,y)$ (Figure 1b).

We may thus write w_r in a more physically intuitive form as $w_r = q_{\text{eff}}\psi_{m,r} + f_r$, where the first term indicates the total particle free energy at r in the absence of particle position fluctuations. The second term, $f_r = f_{S,r} + f_{U,r}$, denotes the fluctuation contribution, consisting of a larger entropic part, $f_{S,r} = -Ts_r$, and a smaller energetic component, $f_{U,r} = u_r - q_{\text{eff}}\psi_{m,r}$. Finally, we write the total well depth as the difference between the particle free energy outside and inside the trap, $W = w_r|_{\text{slit}} - w_r|_{\text{pocket}} = q_{\text{eff}}\psi_m + f$. Here $f = f_S + f_U$, and the absence of the subscript r denotes a quantity that is the difference between values at two in-plane spatial locations r, namely, the "slit" and the "pocket" (Figure 2a). In general, we use ψ_m to simply refer to the electrical potential at the midplane in the slit region, as the corresponding electrical potential in the "pocket" region is zero in most experimental situations.

The Gibbs entropy eq 2 gives the additional entropy due to position fluctuations of the center of mass of the particle. Note that, as we are interested in free-energy differences, we have dropped a multiplicative constant in the arguments of the logarithms. We find that in the "ideal-gas" limit of a point particle with no interactions, or equivalently, for an uncharged system, the well depth, $W = w_r|_{\text{slit}} - w_r|_{\text{pocket}} = f_S$, reduces to $k_B T \ln \beta$ as expected, where the parameter $\beta = \left(\frac{2h+d}{2h}\right)$ denotes the ratio of heights in the system (Figure 2a). Analyzing further the dependence of f_S on experimental parameters, namely, β, κh, and q_{eff} (Figure 2), we find an interesting dependence of the configurational entropy on the charge of the object, q_{eff}, and the system size parameter, κh. We note that for strongly charged entities the translational entropy contribution can be substantially larger that the "ideal-gas" expectation. This essentially implies that the effective height, h_{eff}, available for particle fluctuations in the slit region is much smaller than the physical hard-wall slit height (Figure 2a,d). In fact, we find that, in the regime of strong electrostatics, the slit region provides confinement within an axial extent on the order of the Debye length, κ^{-1}. Since in this work $\kappa^{-1} \sim 10$ nm is much smaller than the slit height $2h \sim 70$ nm, the configurational entropic contribution increases by about 2 $k_B T$ for a highly charged object (Figure 2c).

Furthermore, under a given set of experimental conditions, namely, κh and β, we find that f_S also displays some dependence on the charge of the object (Figure 2e). The strongest dependence we encounter is a $\ln \sqrt{|q_{\text{eff}}/e|}$ in the regime of large β and intermediate value of $\kappa h \sim 3$. This behavior can be explained by the fact that, in the pocket region, the molecule encounters an approximately square-well potential of axial extent $2h + d$, regardless of its charge (Figure 2a). In the slit, however, the same molecule encounters a parabolic electrical interaction energy, $F(z) = q_{\text{eff}}\psi(z) \propto q_{\text{eff}}(z-h)^2$, resulting in the observed overall $\ln \sqrt{|q_{\text{eff}}/e|}$ dependence. Interestingly in the limit of weak screening, $\kappa h = 1.5$, and moderate height ratio, $\beta = 3$, although electrostatic interactions are strong per se, the configurational entropy in both spatial domains responds in a similar fashion to molecular charge, rendering the overall behavior of f_S essentially independent of effective charge, over a 2 order of magnitude range in q_{eff} (Figure 2e, inset). Finally we note that particle position fluctuations in the radial dimension in the trap are explicitly accounted for in BD simulations of the 2D escape process (Supporting Information, Section I).

Probing the Effect of Configurational Entropy. Initially we probed the contribution of configurational entropy, f_S, to the total trap depth, W, by measuring escape times of a given molecular species in traps created by nanostructured indentations of two different depths ($\beta_1 = 2.85$, $\beta_2 = 5.71$) in the same device and observed a ratio of average escape times that agreed well with the theoretical expectation (Figure 1d, Supporting Movie). In order to perform a broader quantitative comparison of measurements of f_S with the theoretical expectation, we measured t_{esc} on different molecules, 60bp dsDNA, ProTα, and Stm-l, and obtained measured values of W for values of β ranging from 2 to 6 and κh ranging from 3.8 to 5.6 (Supporting Information).

The calculated values of effective charge, q_c, for 60ds DNA, ProTα, and Stm-l are $-43.4e$, $-31e$, and $-89.6e$, respectively, under our experimental conditions.[16,32] We assumed that the molecules carry an effective charge $q_{\text{eff}} = q_c$ in each case and determined the theoretically expected value of the fluctuation entropy using eq 2 in the expression $f_{S,c} = Ts_r|_{\text{pocket}} - Ts_r|_{\text{slit}}$. The experimentally measured value of $f_{S,m}$ in turn was obtained using the measured value of W and eq 1 in the relation $f_{S,m} = W - (u_r|_{\text{slit}} - u_r|_{\text{pocket}})$. Note that previous measurements of the effective charge of these molecular species agreed well with the calculated q_c values.[16]

Figure 3a displays a comparison of measurements and theoretically expected values of f_S for the three molecular species for various values of β. We note good agreement between theory and experiment with an r.m.s. deviation over all measurements considered within ∼10%. We point out that the measured values presented are from single experiments using the nominal value of $2h$ in eqs 1 and 2.[16,32] Since the nominal slit height in a given measurement may differ from the true value by up to 3 nm, the agreement could in fact be much better than shown.[16,32]

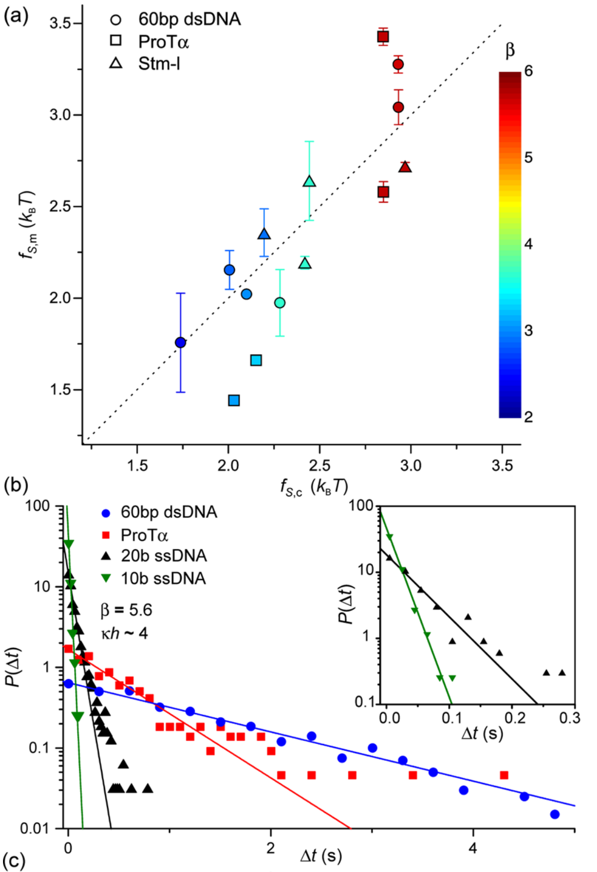

(c)

Molecule	N	t_{esc} (s)	W (k_BT)	$f_{S,m}/W$	q_m(-e)	q_m(-e) [Ref 16]
60bp dsDNA	670	1.4±0.05	7.07±0.04	0.5	43.4#±0.6	42.9±2.5
ProTα	200	0.54±0.03	6.15±0.05	0.4	26.9±0.6	28.5±1.2
20b ssDNA	130	0.046±0.003	4.21±0.06	0.6	12.4±0.3	-
10b ssDNA	1200	0.017±0.001	3.2±0.05	0.7	6.1±0.3	7.7±0.4

Figure 3. (a) Comparison of measured, $f_{S,\mathrm{m}}$, and calculated, $f_{S,\mathrm{c}}$, values of the axial fluctuation entropy, f_S, for three molecular species, 60bp dsDNA (circles), ProTα (squares), and Stm-l (triangles) using values of β from 2 to 6. (b) Measurements of average escape times, t_{esc}, for 10b ssDNA, 20b ssDNA, ProTα, and 60ds DNA, under the same experimental conditions ($\beta = 5.6$ and $\kappa h \sim 4$). (c) The table presents the fractional contribution of $f_{S,\mathrm{m}}$ to the total well depth, W, the number of escape events, N, recorded for each species, and the average measured escape time, t_{esc}. # denotes that q_{m} for 60bp DNA was set equal to $q_{\mathrm{c}} = -43.4e$, permitting a calibrated measurement of all of the other species in the same experiment. Measurement uncertainties are standard error of the mean (s.e.m.). The values obtained for q_{m} in the fluctuation entropy dominated regime are in excellent agreement with previous measurements (last column[16]).

Effective Charge Measurements on Weakly Charged Molecules. Using our model described above, which we find correctly accounts for the additional particle fluctuation entropy, we demonstrate that it is possible to operate in the entropy-governed trapping regime and still determine the unknown effective charge of a molecule using the ETe approach. Configurational entropy enhances molecular residence times in the trap by at least a factor of 3 compared to the electrostatic limit. Figure 3b reports measurements of the effective charge of various biomolecular species in the regime where the trap depth is dominated by configurational entropy, i.e., $f_S/W \geq 0.4$. The obtained q_{eff} values compare well with previous measurements in the electrostatically dominated limit (Figure 3c).[16] The ability to use ETe to measure the molecular effective charge in a regime dominated by configurational entropy suggests the feasibility of applying the approach not only to highly charged macromolecules ($|q_{\mathrm{eff}}| > 5e$) but also to weakly charged, small organic molecules or even ions in solution.

To conclude, we demonstrate the ability to spatially confine and measure the effective charge of single organic molecules that are typically about 1 nm in diameter and carry a net structural charge of $q_{\mathrm{str}} = -1e$, $-2e$, and $-4e$ (Figure 4). Since these molecules have a hydrodynamic radius of ~0.5 nm, both their size and charge are reminiscent of hydrated monovalent and multivalent ions in solution.[43,44] Performing ETe on these molecular species, we note very comparable average escape times despite the large disparity in charge in these molecules (Figure 4b–d). This is due to the fact that W in these measurements arises largely from configurational entropy and is thus essentially charge independent. Nonetheless, the weak electrostatic contribution to W permits effective charge measurements on these molecules. We find that our measured values are indeed close to the nominal q_{str} values. The measurements also agree with the calculated effective charge values, q_{c} obtained by modeling each dye as a sphere of radius given by the hydrodynamic radius, carrying a uniformly distributed total net charge of q_{str}, as previously described.[38]

Despite the fact that the measurement uncertainty on t_{esc} is statistically limited, given by $\frac{1}{\sqrt{N}}$, where N is the number of escape events recorded, we note a rather large uncertainty on q_{m} of around 10–15% in a single measurement on weakly charged molecules (Figure 4d). This is due to the fact that, in the low well-depth regime, $W < 5k_BT$, and particularly for a small molecule where t_{esc} is close to the sampling time, simulations show that the measured t_{esc} displays a dependence on W much weaker than $\exp(W/k_BT)$ (Supporting Information, Figure S2b). It follows that the fractional uncertainty of a single measurement in this regime can be approximated as $k_BT/(0.6q_{\mathrm{eff}}\psi_{\mathrm{m}}\sqrt{N}) \sim 5$–20%, with $q_{\mathrm{eff}}\psi_{\mathrm{m}}$ ranging from 0.4 to 1 k_BT. (See the table in the Supporting Information.) The overall accuracy can be improved either by including a "calibration molecule" in a single measurement or by averaging over several independent measurements.[16,32] Our observations suggest that, by using ion sensitive fluorescent dyes, it should be possible in the future to trap and measure the effective or renormalized charge of inorganic ions in solution.[45,46] It may also be possible to use these measurements to infer the spatial distribution of charge or to better understand the interplay of individual ionizable groups in small molecules in solution.

Conclusions. A quantitative view of the role of configurational entropy could play an important role in optical microscopy-based measurements of interaction energies of particles and molecules in solution. Moreover, the ability to trap and visualize single molecules in the regime of negligible electrostatic repulsion (electrostatic part of well depth as low as about 0.4 k_BT, Figure 4d and the table in the Supporting Information) strongly suggests that trapping based on configurational entropy alone should be possible in a completely uncharged system, where neither the molecule nor the surfaces carry electrical charge. For instance, in an "entropic fluidic trap" composed of slit surfaces coated with a

DOI: 10.1021/acs.nanolett.8b01011

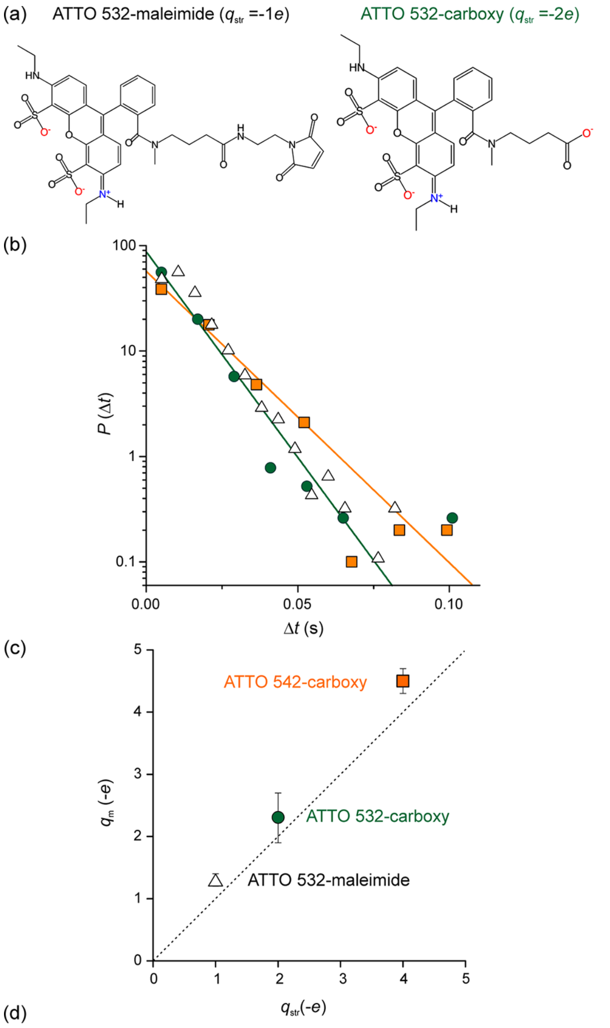

(d)

Molecule	κh	β	N	t_{esc} (ms)	W (k_BT)	$f_{S,m}/W$	q_{str} (-e)	q_c (-e)	q_m (-e)
ATTO 542-carboxy	3.5	5.6	700	13.9±0.4	3.37±0.06	0.7	4	3.85	4.5±0.2
ATTO 532-carboxy	3.5	5.6	500	10.5±0.5	2.75±0.10	0.8	2	1.98	2.3±0.4
ATTO 532-maleimide	2	5.7	1700	14±0.3	3.36±0.05	0.6	1	0.99	1.3±0.1

Figure 4. (a) Chemical structures of the ATTO 532 dye molecules with maleimide and carboxylic acid functional groups. (b) Probability density distributions, $P(\Delta t)$, of recorded escape times for ATTO 542-carboxy (orange squares) and ATTO 532-carboxy (green circles), measured under the same conditions (β = 5.6, κh = 3.5) and for ATTO 532-maleimide (empty triangles) measured using κh = 2. (c) Comparison of the measured effective charge, q_m, and nominal structural charge, q_{str}, for the three molecular species. Error bars are s.e.m. and represent the statistical measurement uncertainty alone (Supporting Information, Section II). (d) Details on the experimental conditions for the three species and their mean escape times, t_{esc}, averaged over 10–20 molecules per species.

neutral lipid bilayer, for a molecule of radius, a, confined in a slit such that $h - a$ = 10 nm with a nanostructure depth d = 600 nm, well depths of over $4k_BT$ can be achieved due to configurational entropy alone.

Our findings also carry strong implications for the electrostatic trap-based biomolecular charge measurement principle we recently introduced. This work establishes the applicability of the ETe approach for molecular effective charge measurements of magnitude $|q_{eff}|$ ranging from 1 to 100e. The ability to measure the effective charge in the regime of very weak electrostatics ($q_{eff}\psi_m < 1k_BT$) suggests that the ETe measurement principle can be readily applied to charged biomolecules in solutions with higher salt concentrations, where electrostatic interactions are typically diminished. Configurational entropy also greatly enhances the dynamic range of the measurement in a single experiment. This opens up the possibility of measuring in real-time changes over an order of magnitude (Figure 3) in the effective charge of a single diffusing entity using, e.g., the previously described lattice diffusion approach.[33] This ability would be useful in studying a number of dynamic inter- and intramolecular processes that strongly impact biomolecular electrostatics, including binding, nucleation and aggregation, folding and conformational changes, and ion-specific effects.

■ ASSOCIATED CONTENT

Ⓢ Supporting Information

The Supporting Information is available free of charge on the ACS Publications website at DOI: 10.1021/acs.nanolett.8b01011.

> Details on Brownian dynamics simulations and error propagation (PDF)
> Supporting Movie (AVI)

■ AUTHOR INFORMATION

Corresponding Author

*E-mail: madhavi.krishnan@uzh.ch.

ORCID

Madhavi Krishnan: 0000-0003-1274-7155

Notes

The authors declare no competing financial interest.

■ ACKNOWLEDGMENTS

We gratefully acknowledge the Swiss National Science Foundation, the European Research Council and University of Zurich for financial support. We thank Ben Schuler and Andrzej Ożyhar for gifts of the proteins ProTα and Stm-l. Nanofabrication was carried out at FIRST Center for Micro- and Nanoscience, ETH Zurich.

■ REFERENCES

(1) Svoboda, K.; Block, S. M. *Opt. Lett.* **1994**, *19*, 930–932.
(2) Grigorenko, A. N.; Roberts, N. W.; Dickinson, M. R.; Zhang, Y. *Nat. Photonics* **2008**, *2*, 365.
(3) Yang, A. H. J.; Moore, S. D.; Schmidt, B. S.; Klug, M.; Lipson, M.; Erickson, D. *Nature* **2009**, *457*, 71.
(4) Juan, M. L.; Gordon, R.; Pang, Y.; Eftekhari, F.; Quidant, R. *Nat. Phys.* **2009**, *5*, 915.
(5) Zhang, W.; Huang, L.; Santschi, C.; Martin, O. J. F. *Nano Lett.* **2010**, *10*, 1006–1011.
(6) Pang, Y.; Gordon, R. *Nano Lett.* **2012**, *12*, 402–406.
(7) Huft, P. R.; Kolbow, J. D.; Thweatt, J. T.; Lindquist, N. C. *Nano Lett.* **2017**, *17*, 7920–7925.
(8) Hughes, M. P.; Morgan, H. *J. Phys. D: Appl. Phys.* **1998**, *31*, 2205.
(9) Cheon, D.; Kumar, S.; Kim, G.-H. *Appl. Phys. Lett.* **2010**, *96*, 013101.
(10) Guan, W.; Joseph, S.; Park, J. H.; Krstić, P. S.; Reed, M. A. *Proc. Natl. Acad. Sci. U. S. A.* **2011**, *108*, 9326–9330.
(11) Cohen, A. E.; Moerner, W. E. *Proc. Natl. Acad. Sci. U. S. A.* **2006**, *103*, 4362–4365.
(12) Braun, M.; Bregulla, A. P.; Günther, K.; Mertig, M.; Cichos, F. *Nano Lett.* **2015**, *15*, 5499–5505.

DOI: 10.1021/acs.nanolett.8b01011
Nano Lett. XXXX, XXX, XXX–XXX

(13) Tanyeri, M.; Johnson-Chavarria, E. M.; Schroeder, C. M. *Appl. Phys. Lett.* **2010**, *96*, 224101.

(14) Krishnan, M.; Mojarad, N.; Kukura, P.; Sandoghdar, V. *Nature* **2010**, *467*, 692−695.

(15) Mojarad, N.; Krishnan, M. *Nat. Nanotechnol.* **2012**, *7*, 448−452.

(16) Ruggeri, F.; Zosel, F.; Mutter, N.; Różycka, M.; Wojtas, M.; Ożyhar, A.; Schuler, B.; Krishnan, M. *Nat. Nanotechnol.* **2017**, *12*, 488−495.

(17) Ashkin, A.; Dziedzic, J. M.; Bjorkholm, J. E.; Chu, S. *Opt. Lett.* **1986**, *11*, 288−290.

(18) Smisek, D.; Hoagland, D. *Science* **1990**, *248*, 1221−1223.

(19) Rousseau, J.; Drouin, G.; Slater, G. *Phys. Rev. Lett.* **1997**, *79*, 1945−1948.

(20) Liu, L.; Li, P.; Asher, S. A. *Nature* **1999**, *397*, 141.

(21) Han, J.; Craighead, H. G. *Science* **2000**, *288*, 1026−1029.

(22) Reisner, W.; Larsen, N. B.; Flyvbjerg, H.; Tegenfeldt, J. O.; Kristensen, A. *Proc. Natl. Acad. Sci. U. S. A.* **2009**, *106*, 79−84.

(23) Liu, X.; Skanata, M. M.; Stein, D. *Nat. Commun.* **2015**, *6*, 6222.

(24) Zwanzig, R. *J. Phys. Chem.* **1992**, *96*, 3926−3930.

(25) Martens, S.; Straube, A. V.; Schmid, G.; Schimansky-Geier, L.; Hänggi, P. *Phys. Rev. Lett.* **2013**, *110*, 010601.

(26) Verdel, R.; Dagdug, L.; Berezhkovskii, A. M.; Bezrukov, S. M. *J. Chem. Phys.* **2016**, *144*, 084106.

(27) Adam, G.; Gibbs, J. H. *J. Chem. Phys.* **1965**, *43*, 139−146.

(28) Adams, M.; Dogic, Z.; Keller, S. L.; Fraden, S. *Nature* **1998**, *393*, 349.

(29) Fainerman, V. B.; Kovalchuk, V. I.; Lucassen-Reynders, E. H.; Grigoriev, D. O.; Ferri, J. K.; Leser, M. E.; Michel, M.; Miller, R.; Möhwald, H. *Langmuir* **2006**, *22*, 1701−1705.

(30) Dinsmore, A. D.; Yodh, A. G.; Pine, D. J. *Nature* **1996**, *383*, 239.

(31) Dinsmore, A. D.; Wong, D. T.; Nelson, P.; Yodh, A. G. *Phys. Rev. Lett.* **1998**, *80*, 409−412.

(32) Ruggeri, F.; Krishnan, M. *J. Chem. Phys.* **2018**, *148*, 123307.

(33) Ruggeri, F.; Krishnan, M. *Phys. Rev. E* **2017**, *96*, 062406.

(34) Różycka, M.; Wojtas, M.; Jakób, M.; Stigloher, C.; Grzeszkowiak, M.; Mazur, M.; Ożyhar, A. *PLoS One* **2014**, *9*, e114308.

(35) Gast, K.; Damaschun, H.; Eckert, K.; Schulzeforster, K.; Maurer, H. R.; Mullerfrohne, M.; Zirwer, D.; Czarnecki, J.; Damaschun, G. *Biochemistry* **1995**, *34*, 13211−13218.

(36) Müller-Späth, S.; Soranno, A.; Hirschfeld, V.; Hofmann, H.; Rüegger, S.; Reymond, L.; Nettels, D.; Schuler, B. *Proc. Natl. Acad. Sci. U. S. A.* **2010**, *107*, 14609−14614.

(37) Kramers, H. *Physica* **1940**, *7*, 284−304.

(38) Krishnan, M. *J. Chem. Phys.* **2017**, *146*, 205101.

(39) Bosch, P. J.; Correa, I. R.; Sonntag, M. H.; Ibach, J.; Brunsveld, L.; Kanger, J. S.; Subramaniam, V. *Biophys. J.* **2014**, *107*, 803−814.

(40) McQuarrie, D. A. *Statistical Mechanics*; University Science Books: Mill Valley, CA, 2000; pp 113−117.

(41) Krishnan, M. *J. Chem. Phys.* **2013**, *138*, 114906.

(42) Theodoor, J.; Overbeek, G. *Colloids Surf.* **1990**, *51*, 61−75.

(43) Pau, P. C. F.; Berg, J. O.; McMillan, W. G. *J. Phys. Chem.* **1990**, *94*, 2671−2679.

(44) Müller, C. B.; Loman, A.; Pacheco, V.; Koberling, F.; Willbold, D.; Richtering, W.; Enderlein, J. *EPL* **2008**, *83*, 46001.

(45) Manning, G. S. *J. Phys. Chem. B* **2007**, *111*, 8554−8559.

(46) Sharma, H.; Kaur, N.; Singh, A.; Kuwar, A.; Singh, N. *J. Mater. Chem. C* **2016**, *4*, 5154−5194.

ENTROPIC TRAPPING OF A SINGLY CHARGED MOLECULE IN SOLUTION

SUPPORTING INFORMATION

Francesca Ruggeri[1] and Madhavi Krishnan[1,2]
[1]*Department of Chemistry, University of Zürich, Winterthurerstrasse 190, CH 8057 Zürich, Switzerland*
[2]*Department of Physics, University of Zürich, Winterthurerstrasse 190, CH 8057 Zürich, Switzerland*

SECTION I: BROWNIAN DYNAMICS SIMULATIONS IN 2D AND 3D

In order to quantitatively relate the average measured escape time, t_{esc} of a particle to the depth of the potential well, W, we perfomed Brownian Dynamics (BD) simulations of the escape process as described previously [1, 2]. We first determine the full three-dimensional distribution of electrical potential in a single trap by solving the nonlinear Poisson-Boltzmann equation in the fluidic nanostructure. A molecule of charge q_{eff}, noted as q from hereafter, sampling the free energy landscape, experiences both thermal fluctuations in 3 dimensions and a force given by $-\nabla q\psi(\mathbf{r})$ at any point $\mathbf{r}$ in the landscape. Here $\psi(\mathbf{r})$ is the local the electrical potential at $\mathbf{r}$ in the absence of the particle [3].

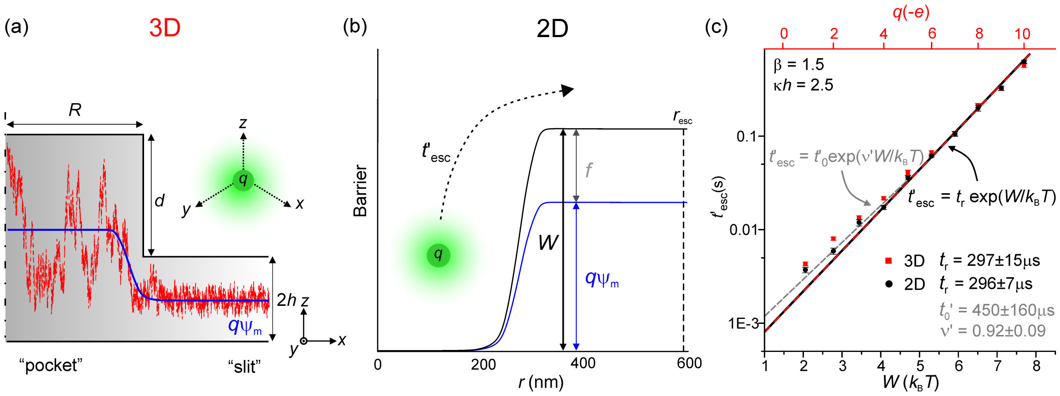

Figure S1: (a) Axisymmetric representation of the trapping nanostructure. $2h$ is the slit height, d is the pocket depth and R the pocket radius = 300 nm. Red dashed trace indicates a representative z-trajectory of a particle of charge q sampling the 3D space of the trap. ψ_{m} is the electrostatic midplane potential in the slit region. (b) In the equivalent 2D simulation, the total well depth W (in black) experienced by the trapped molecule is $W = q\psi_{\mathrm{m}} + f$, where f is the additional entropic contribution due to axial fluctuation of the molecule. r is a radial coordinate referenced to the center of the nanostructure. The escape boundary, r_{esc} (black dashed line), which must be crossed for an escape event to occur, is placed 300 nm away from the physical boundary of the nanostructure, $r_{\mathrm{esc}} = R + 300$ nm [2]. t'_{esc} denotes the escape time based on instantaneous particle position. (c) Comparison of escape times based on instantaneous particle positions, t'_{esc} for both 3D and 2D approaches. In the regime of $W = 5 - 8k_{\mathrm{B}}T$, the behaviour can be fit with the form $t'_{\mathrm{esc}} = t_{\mathrm{r}}\exp(W/k_{\mathrm{B}}T)$ according to Kramers' theory (overlapping black and dashed red lines).Here t_{r} is the position relaxation time of the particle which depends on the particle hydrodynamic radius, r_{H}, and is a fit parameter [1, 2]. The simulation results shown correspond to parameter values: $r_{\mathrm{H}} = 4.5$ nm, $\beta = (2h + d)/2h = 1.5$ and $\kappa h = 2.5$, where κ is the inverse Debye length. The is no significant difference between a full 3D simulation (red squares) and a 2D simulation (black circles) in the regime of $W > 5k_{\mathrm{B}}T$, as the fit parameter t_{r} is almost identical in the two cases. Error bars are smaller than the symbols. For $W < 5k_{\mathrm{B}}T$ the data is better represented by a fit of the form $t'_0\exp(\nu' W/k_{\mathrm{B}}T)$ (dashed grey line), where $\nu' < 1$ and $t'_0 \sim 1.4t_{\mathrm{r}}$, discussed later in Section II.

We simulate a particle trajectory by iteratively solving the discretized overdamped Langevin equation, which reads as follows in one dimension:

$$\mathbf{x}(t+\delta t) = \mathbf{x}(t) - \mu \nabla q\psi(\mathbf{x}(t)) + \sqrt{2D\delta t}\,\mathbf{w}(t) \tag{S1}$$

Here, $\mathbf{x}(t)$ represents the instantaneous position of the molecule at time, t in one dimension, and D is the molecule's diffusion coefficient which depends on its hydrodynamic radius, r_H, and the viscosity of the medium, η as $D = k_\mathrm{B}T/6\pi\eta r_\mathrm{H}$. $\mathbf{w}(t)$ represents a displacement due to the random thermal force acting on the particle that satisfies $\langle \mathbf{w}(t)\rangle = \mathbf{0}$ and $\langle \mathbf{w}(t)\mathbf{w}^\top(t')\rangle = \boldsymbol{I}$ if $\mid t-t' \mid \leq \delta t$, $\mathbf{0}$ otherwise. Further $\mu = \delta t/6\pi\eta r_\mathrm{H}$, where the simulation time-step, $\delta t = 10\,\mu\mathrm{s}$ is much larger than the momentum relaxation time ∼10 ns for a typical molecule.

At $t = 0$, the particle is located at $x = y = 0$ and $z = (2h + d)/2$, where $2h$ is the slit height and d the nanostructure depth. We use Eq.S1 to propagate the instantaneous position of the particle, $\mathbf{x}(t)$, forward in time for each spatial dimension, until its radial position $r = \sqrt{x^2 + y^2}$ exceeds an arbitrary radial escape threshold, r_esc [2] (Fig.S1(b)). The time needed to reach r_esc from the bottom of the well corresponds to an escape event, or hop, Δt. Once the molecule has escaped, the simulation restarts and another escape trajectory is computed. The durations of the escape events are exponentially distributed and we typically average over a number of hops, $N \sim 10^3$, to obtain the average escape time t'_esc. Note that this analysis is performed without time-averaging of the spatial position and the simulation is repeated for different values of q.

We then compare the results of t'_esc vs q from a full 3D simulation, which is computationally very demanding, with an equivalent 2D simulation (Fig.S1(c)), in which a molecule of charge q is only permitted motion in (x, y). Here the molecule is forced to sample a two-dimensional energy manifold whose value at any point (x, y) is given by the minimum electrostatic energy in z at every radial coordinate. Importantly in order to simulate 3D behavior using an equivalent 2D problem we add to the depth of the well, which would otherwise be simply $q\psi_\mathrm{m}$, the fluctuation contribution f. Thus in the 2D simulations we use a well depth given by $W = q\psi_\mathrm{m} + f$, where f is the fluctuation contribution calculated for each case as described in the main text (Fig.S1(b)). Identical to the 3D case, the molecule is considered to have escaped when its samples the region outside the radially symmetric boundary given by r_esc. We find excellent agreement (r.m.s. within 2%) between the average escape times, t'_esc computed using the two approaches in the regime of $W \geq 5k_\mathrm{B}T$, where most of our experiments are performed. A representative molecular trajectory in z depicted in Fig.S1(a) clearly reveals that the axial fluctuation of the molecule in the "slit" are of much smaller amplitude than in the "pocket" region. This difference gives rise to the configurational entropy contribution to the total trap depth.

We point out that in order to relate experimentally measured escape times, t_esc to measured well depths, we perform the 2D BD simulation analysis using time-averaged co-ordinates $< r >_{t_\mathrm{exp}}$, rather than instantaneous positions r, as previously described [2]. The duration of an exposure time, t_exp is typically 5 ms in our experiments. Further, we examine the motion process in a 2D landscape of traps, corresponding to the experimental situation. This is because neighbouring wells in the landscape effectively act as absorbing boundaries for molecules and need to be included in order to accurately reconstruct the escape process [2].

SECTION II: ESTIMATING UNCERTAINTIES IN THE CHARGE MEASUREMENT ON WEAKLY CHARGED MOLECULES

The measurement error, x_{e} on a quantity x, which is a function of the variables f, g, h, etc., each with uncertainties f_{e}, g_{e}, h_{e}, etc., can be expressed as follows:

$$x_{\mathrm{e}} = \sqrt{\left(\frac{\partial x}{\partial f}\right)^2 f_{\mathrm{e}}^2 + \left(\frac{\partial x}{\partial g}\right)^2 g_{\mathrm{e}}^2 + \left(\frac{\partial x}{\partial h}\right)^2 h_{\mathrm{e}}^2 + \ldots} \tag{S2}$$

In the regime of $W \geq 5k_{\mathrm{B}}T$, the relationship between measured escape time, t_{esc}, and molecule effective charge, noted here as q, is well described by Kramers' theory and is given by:

$$q\psi_{\mathrm{m}} + f = k_{\mathrm{B}}T \ln\left(\frac{t_{\mathrm{esc}}}{t_{\mathrm{r}}}\right) \tag{S3}$$

However the experiments shown in Fig.4, in which we measure the effective charge of 3 dye molecules, were performed in the regime of $W < 5k_{\mathrm{B}}T$, where the dependence of t_{esc} on W departs from that given in Eq.S3.

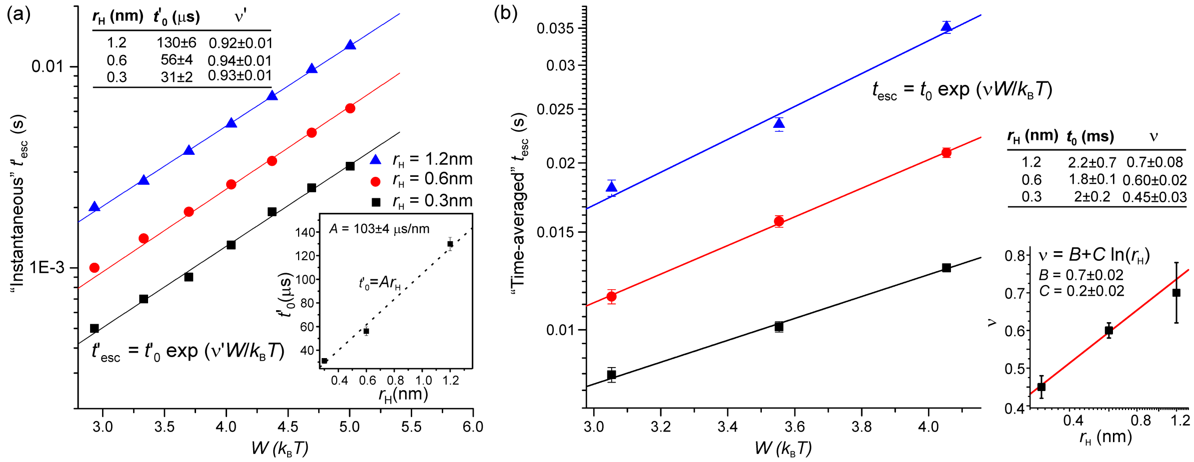

Figure S2: (a) The plot presents simulated t'_{esc} in the low W regime ($W \leq 5k_{\mathrm{B}}T$) for molecules of r_{H} ranging from 0.3 to 1.2 nm, analyzing the instantaneous coordinates of an object escaping from a single well. The fits shown are of the form $t'_0 \exp(\nu' W/k_{\mathrm{B}}T)$. (b) Simulated t_{esc} using time-averaged coordinates of molecules sampling a landscape of traps. In general, for a given combination of W and r_{H}, t_{esc} is substantially larger in this case. The inset table shows the values of the fit parameter t_0 and ν for different r_{H}. Inset plot shows ν vs r_{H}, fit by a logarithmic form, $\nu = B + C\ln(r_{\mathrm{H}})$.

In order to study this behaviour, we performed BD simulations in the range of $W \sim 3 - 5k_{\mathrm{B}}T$, as described in Section I (Fig.S2(a)). Figure S2 compares the results of simulated escape from a single well, obtained using instantaneous positions (as in Section I), and time-averaged approach, which also includes the effects given by the trap landscape geometry. In the experiment, a molecule must reside in a given trap for $\Delta t \geq t_{\mathrm{exp}}$ in order to accumulate enough signal on the detector and be recognized as trapped. In the simulation, we use the same criterion on the minimum residence time when analyzing a particle position trajectory, as previously described [2]. In general, for a given well depth, the "time-averaged" t_{esc} is substantially longer than the "instantaneous" t'_{esc} (Fig.S2).

In both cases, we find - as expected - that in the low well depth regime t_{esc} depends less strongly on W, by a factor ν. This fit parameter is < 1 for $W \leq 5k_{\mathrm{B}}T$ and is equal to 1 for $W > 5k_{\mathrm{B}}T$ where the Kramers' prediction well describes the behavior (Fig.S1(c)). Fitting the simulation with a functional form given by

$$t_{\mathrm{esc}} = t_0 \mathrm{exp}\left(\frac{\nu W}{k_{\mathrm{B}}T}\right) = t_0 \mathrm{exp}\left[\frac{\nu(q\psi_{\mathrm{m}} + f)}{k_{\mathrm{B}}T}\right] \tag{S4}$$

we find that, when operating with instantaneous positions (Fig S2(a)), the prefactor t_0', depends linearly on the size of the molecule (inset in Fig.S2(a)), and is also slightly larger than the relaxation time, t_{r} at high well depths by a factor ∼1.4 (Fig.S1(c)). Upon position averaging, however, the escape time no longer depends in a simple linear fashion on r_{H}. The inset Table in Fig.S2(b) shows that in this case the prefactor t_0 is a constant, larger in magnitude and close to t_{exp}, that no longer carries information on the radius of the molecule. The fit parameter ν captures the weaker response of the measured timescale on well depth. This different t_{esc} vs. W behaviour is most likely due to a finite (size-dependent) return probability of the molecule during the observation time [2]. For molecule of $r_{\mathrm{H}} = 0.6$nm, which corresponds to the size the dyes measured [4], we find that $\nu = 0.6 \pm 0.02$.

We now write the fractional error q_{e}/q according to Eq.S2 as:

$$\frac{q_{\mathrm{e}}}{q} = \sqrt{\left(\frac{1}{q^2}\right)\left(\frac{\partial q}{\partial \psi_{\mathrm{m}}}\right)^2 \psi_{\mathrm{m,e}}^2 + \left(\frac{1}{q^2}\right)\left(\frac{\partial q}{\partial t_{\mathrm{esc}}}\right)^2 t_{\mathrm{esc,e}}^2 + \left(\frac{1}{q^2}\right)\left(\frac{\partial q}{\partial r_{\mathrm{H}}}\right)^2 r_{\mathrm{H,e}}^2} \tag{S5}$$

The first term on the RHS of Eq.S5, from now on denoted as $(q_e/q)_{\psi_{\mathrm{m}}}$, represents the uncertainty in determining the electrical potential at the midplane of the slit, ψ_{m}. This aspect has been discussed at length in our previous work [1], and arises from the uncertainty in determining the slit height ($2h$) with an accuracy better than $h_{\mathrm{e}} = 1$ nm and is estimated at about 5% when averaging over 4-5 independent experiments (typical Debye length $\kappa^{-1} \sim 9$nm and $2h \sim 70$nm). In a single experiment however where the height of the slit may depart from the mean value by as much as 2 or $3h_{\mathrm{e}}$, this (single) measurement inaccuracy can be as large as 15%. For the measurement of the dye ATTO532-maleimide, performed using a larger Debye length ($\kappa^{-1} \sim 20$ nm) and thus higher ψ_{m}, the estimated fractional uncertainty on a single measurement is calculated to be as low as 6% (∼ 2% upon averaging).

The second term of Eq.S5, that we denote as $(q_e/q)_{t_{\mathrm{esc}}}$, arises from statistical uncertainty in measuring t_{esc} in a temporally limited experiment. Given that the escape events Δt are exponentially distributed, the measurement error $t_{\mathrm{esc,e}}$ on their average value, t_{esc}, is function of the number of detected hops, N, as follows:

$$t_{\mathrm{esc,e}} = \frac{t_{\mathrm{esc}}}{\sqrt{N}} \tag{S6}$$

According to Eq.S4, $(\partial q/\partial t_{\mathrm{esc}}) = (k_{\mathrm{B}}T/\nu t_{\mathrm{esc}}\psi_{\mathrm{m}})$. Using Eq.S6, $(q_e/q)_{t_{\mathrm{esc}}}$ gives

$$\left(\frac{q_e}{q}\right)_{t_{\mathrm{esc}}}^2 = \left(\frac{1}{q^2}\right)\left(\frac{\partial q}{\partial t_{\mathrm{esc}}}\right)^2 t_{\mathrm{esc,e}}^2 = \left(\frac{1}{q^2}\right)\left(\frac{k_{\mathrm{B}}T}{\nu t_{\mathrm{esc}}\psi_{\mathrm{m}}}\right)^2 t_{\mathrm{esc,e}}^2 = \left(\frac{k_{\mathrm{B}}T}{\nu q\psi_{\mathrm{m}}\sqrt{N}}\right)^2 \tag{S7}$$

Note that in this analysis we assume that f in Eq.S4 is constant, since the fluctuation contribution is largely charge-independent as discussed in the main text. We finally analyze the last term of Eq.S5, denoted by $(q_e/q)_{r_\mathrm{H}}$, which represents the fractional contribution of the uncertainty on hydrodynamic radius, r_H to the total single measurement charge error.

As shown above (Fig.S2(b)), in the BD time-averaged approach at low W, the fit parameter ν in Eq.S4 captures the dependance of t_esc on the size of the molecule and scales with r_H in a logarithmic fashion, $\nu = B + C\ln(r_\mathrm{H})$, where $B = 0.7 \pm 0.02$ and $C = 0.2 \pm 0.02$. Therefore we can write $(q_e/q)_{r_\mathrm{H}}$ as function of ν as follows:

$$\left(\frac{q_e}{q}\right)^2_{r_\mathrm{H}} = \left(\frac{1}{q^2}\right)\left[\left(\frac{\partial q}{\partial \nu}\right)\left(\frac{\partial \nu}{\partial r_\mathrm{H}}\right)\right]^2 r^2_{\mathrm{H,e}} \tag{S8}$$

Using Eq.S4 this can be rearranged as:

$$\left(\frac{q_e}{q}\right)^2_{r_\mathrm{H}} = \left(\frac{1}{q^2}\right)\left\{\left[-\frac{k_\mathrm{B}T}{\psi_\mathrm{m}\nu^2}\ln\left(\frac{t_\mathrm{esc}}{t_0}\right)\right]\left(\frac{C}{r_\mathrm{H}}\right)\right\}^2 r^2_{\mathrm{H,e}} = \left[-\frac{Ck_\mathrm{B}T}{q\psi_\mathrm{m}\nu^2}\ln\left(\frac{t_\mathrm{esc}}{t_0}\right)\right]^2\left(\frac{r_\mathrm{H,e}}{r_\mathrm{H}}\right)^2 \tag{S9}$$

The fractional error $(r_\mathrm{H,e}/r_\mathrm{H})$ in Eq.S9 is estimated from an independent Dual-focus Fluorescence Correlation Spectroscopy (2fFCS) measurement [2] and is typically 5%.

The following Table summarizes the fractional errors for each dye molecule, and the overall uncertainty, (q_e/q).

Molecule	**$q_\mathrm{str}(-e)$**	**$q\psi_\mathrm{m}(k_\mathrm{B}T)$**	**$W(k_\mathrm{B}T)$**	**$(q_e/q)_{t_\mathrm{esc}}$**	**$(q_e/q)_{\psi_\mathrm{m}}$**	**$(q_e/q)_{r_\mathrm{H}}$**	**q_e/q**
ATTO 542-carboxy	4	0.72	3.37±0.06	9%	5%	3.4%	11%
ATTO 532-carboxy	2	0.36	2.75±0.10	20%	5%	6.2%	22%
ATTO 532-maleimide	1	1	3.36±0.05	4%	2%	5.4%	7%

8

Measuring the Size of a Single Molecule

> “These motions were such as to satisfy me, after frequently repeated observation, that they arose neither from currents in the fluid, nor from its gradual evaporation, but belonged to the particle itself.”
>
> *Robert Brown*

8.1 A brief Overview of Alternative Techniques

Fluorescence Correlation Spectroscopy (FCS) is a sensitive ensemble-averaged method which estimates the molecule hydrodynamic radius via auto-correlating the fluorescence fluctuations given by a small number of molecule (nM concentration) passing through the detection volume of a confocal microscope [89]. We have used 2-focus FCS (2fFCS) – which has the advantage of a better defined detection volume resulting in more accurate measurements [73] – to characterize most of the molecules then studied with ET*e* [3] (Fig.8.1).

Short fragments of dsDNA (<100 bp), which has a persistence length of ∼ 40 nm [90], can be thought as rigid rods under our experimental conditions. Indeed our FCS measurement of r_{H} – which is in essence the radius of a hard sphere diffusing as fast as the molecule under observation – is in good agreement with the predicted size for the equivalent cylinders [91](see inset in Fig.8.1b).
On the other hand we have found that the radius of ssDNA, of persistence length ∼ 3nm – corresponding to roughly 10 bases under low salt concentration conditions [92] – follows a power law behaviour as previously shown by Doose and collaborators. [93].

(a)

	Molecule	q^*_{str} (-e)	Mol. wt. (kDa)	r_{H} (nm)
dsDNA	40 bp	82	25	3.2 ± 0.17
	50 bp	102	31	3.9 ± 0.2
	60 bp	122	37	4.55 ± 0.25
ssDNA	10 b	11	3	1.79 ± 0.1
	20 b	21	6	2.4 ± 0.12
	60 b	61	18	4.53 ± 0.25
Protein	ProTα	46	10	4.4 ± 0.26
	ProTα-E59K	44	10	4.3 ± 0.22
	ProTα-Cy3B	44	10	4.73 ± 0.25
	ProTα-Alexa546	48	10	5.06 ± 0.25
	Stm-I	102.7	39.4	8.71 ± 0.51
	Gusβ	133.8	290	5.1 ± 0.29

(b)

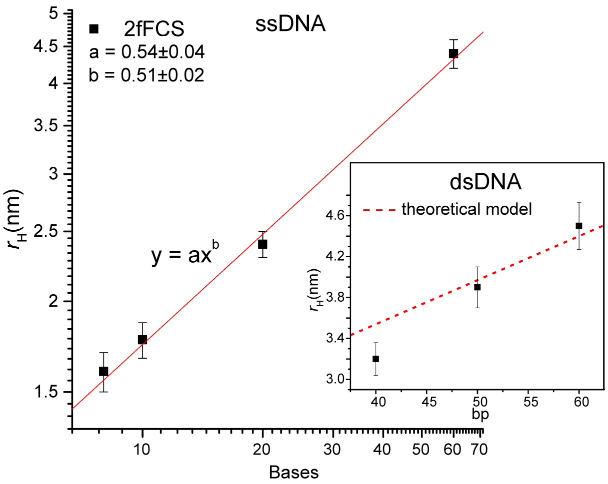

Figure 8.1: (a) The table summarizes the structural charge, q_{str}, the molecular weight and the measured hydrodynamic radius, r_{H}, for all the molecules studied in Refs. [3, 4, 5]. The values of r_{H} result from and independent 2fFCS measurement. (b) The values of r_{H} for ssDNA from (a) are fit with a polynomial form $y = ax^b$, similarly as in Ref.[93](red solid line). The dsDNA data instead is compared with a cylindrical model prediction [94], $r_{\mathrm{H}} = l_{\mathrm{c}}/2\ln(l_{\mathrm{c}}/d_{\mathrm{DNA}})$ (red dashed line). Here the diameter, $d_{\mathrm{DNA}} = 2$ nm and the contour length, l_{c}, is 0.34 nm per base pair.

Alternative techniques to infer the size of a biomolecule in solution include the study of the object trajectory to obtain a Means Squared Displacement (MSD) value, which scales with the molecule diffusion coefficient, D [95, 96]. Direct tracking of a nanometer sized object, however, is often challenging in an unbounded system: one needs long observation times to collect enough signal, but small macromolecules typically diffuse beyond the imaging depth of a single-molecule microscope in less than a millisecond [97]. Tracking of small molecules can be achieved in the case of diffusion at a solid-liquid interface, where motion is substantially reduced by local adsorption or subdiffusion [98, 99].

Mobility measurements using the Anti-Brownian Electrokinetic (ABEL) trap have characterized molecules as small as a single fluorophore [40], but require a fairly complicated setup. An alternative experimental approach consists in a "single-image" diffusion measurement [100, 97]: the signature of the molecule diffusion in 2D is given by a single fluorescence snapshot, in which the "blob" width contains information on the molecular motion during the observation time, convolved with the instrument PSF.

8.2 Lattice Diffusion of a Single Molecule in Solution

Combined information about the effective charge and size of a biomolecule could yield valuable insight into its structure in solution. The charge per unit length is a crucial parameter to determine the degree of charge renormalization in a polyelectrolyte [101]. Given the same structural charge, the effective charge in solution for a globular biomolecule is expected to be significantly reduced compared to an equivalent one dimensional polyelectrolyte. Additional charge regulation effects, depending on the geometry of the molecule, may decrease q_{eff} further [19, 3]. Given this, it is clear that the molecule structure in 3D and its effective charge are quantities deeply related, and knowledge of the molecule dimensions would be important to understand its electrostatic properties.

We note that, at the practical level, information on the molecule radius is also necessary to determine its position relaxation time, t_{r} (see Eqn.1.10) and thus crucial for our BD simulations. A simultaneous determination of q_{eff} and r_{H} not only eliminates the need of an independent FCS measurement, but is also highly desirable to evaluate possible hydrodynamic effects due to confinement, which might result in an apparent smaller D [102].

The "on-off" concept proposed in our recently published work "*Lattice diffusion of a single molecule in solution*" allows us to measure both size and charge from a single molecule trajectory at the same time. In brief, the time spent by the molecule in a trap, as usual, gives q_{eff}. The inter-well travel time, in which the molecule fluorescence intensity is spread over a larger area, appearing too weak to be detected (the “off” state), directly yields the molecule hydrodynamic radius. We have modelled transport across a 2D landscape of traps [103, 104, 105, 106] with BD simulations, in order to correctly interpret the experimentally measured timescales (see Chapter 4) and we have validated the method with fluorescent nanospheres, which are very bright and easy to characterize by a simultaneous MSD measurement. Finally, we have compared our experimental results with previous 2fFCS measurements finding excellent agreement, and suggesting no measurable confinement-induced hydrodynamic effects under our experimental ETe conditions.

PHYSICAL REVIEW E **96**, 062406 (2017)

Lattice diffusion of a single molecule in solution

Francesca Ruggeri[1] and Madhavi Krishnan[1,2,*]
[1]*Department of Chemistry, University of Zürich, Winterthurerstrasse 190, CH 8057 Zürich, Switzerland*
[2]*Department of Physics, University of Zürich, Winterthurerstrasse 190, CH 8057 Zürich, Switzerland*

(Received 5 September 2017; published 13 December 2017)

The ability to trap a single molecule in an electrostatic potential well in solution has opened up new possibilities for the use of molecular electrical charge to study macromolecular conformation and dynamics at the level of the single entity. Here we study the diffusion of a single macromolecule in a two-dimensional lattice of electrostatic traps in solution. We report the ability to measure both the size and effective electrical charge of a macromolecule by observing single-molecule transport trajectories, typically a few seconds in length, using fluorescence microscopy. While, as shown previously, the time spent by the molecule in a trap is a strong function of its effective charge, we demonstrate here that the average travel time between traps in the landscape yields its hydrodynamic radius. Tailoring the pitch of the lattice thus yields two different experimentally measurable time scales that together uniquely determine both the size and charge of the molecule. Since no information is required on the location of the molecule between consecutive departure and arrival events at lattice sites, the technique is ideally suited to measurements on weakly emitting entities such as single molecules.

DOI: 10.1103/PhysRevE.96.062406

I. INTRODUCTION

Diffusion in a free-energy landscape is a phenomenon of central importance in condensed matter physics, chemical reactions, and molecular biology. Highly disparate natural phenomena such as atom migration on surfaces or in crystals, molecular chemical transformation, macromolecular interactions, and protein folding can in fact be described in terms of common underlying statistical principles governing transport across energy barriers. Indeed, surface science offers a most tangible example of the phenomenon [1]. Atoms preferentially adsorb at specific sites on the periodic surface lattice which represent locations of the lowest potential energy for adsorption. Driven by thermal energy, adsorbed atoms hop in a random fashion across relatively small energy barriers from one minimum to the next. Depending on the height of the barrier relative to the thermal energy scale, transport of the surface adsorbate can be substantially slowed down or virtually unimpeded as in a fully mobile two-dimensional gas. Direct imaging of atomic and molecular migration using field-ion and scanning-tunneling microscopy has facilitated the measurement of important physical parameters in the transport process such as the activation energy and the attempt frequency. These studies have been instrumental in exploring fundamental features of transition state theory [2–6].

Furthermore, transport in periodic potentials is ubiquitous in biological systems. For example, thermal migration of motor proteins along the periodic interaction energy landscape of a microtubule plays an important role in regulating microtubule length in the cellular cytoskeleton [7]. DNA-binding proteins and enzymes use diffusion along the molecular contour in order to locate specific binding sites. This diffusive search strategy is thought to include a “hopping” mode of transport reminiscent of the classic lattice diffusion problem [8].

Previous experimental studies on particle motion in periodic potentials in the fluid phase have examined diffusive and field-driven transport of single colloidal particles and DNA, in spatially modulated gravitational and optical fields, and configurational entropy landscapes [9–13]. Typically these investigations use field-driven transport to separate a mixture of molecular species, exploiting the nonlinear response in object mobility to a spatially varying potential [14,15]. However, not much prior effort has been directed at quantitative studies on purely diffusive transport of a single molecule in a well-defined free-energy landscape. A microscopic view of this transport process under well-controlled conditions is not only highly relevant for direct measurements on the properties and interactions of an isolated macromolecule in solution, as we show in our work, but may also contribute toward an improved understanding of molecular transport in naturally occurring modulated systems, e.g., living cells [16,17].

Here we examine diffusive transport of single nanometer-scale molecules in a 2D free-energy landscape in the fluid phase. Analogous to the experiments on atom diffusion on a surface, we use optical microscopy to study the thermal migration of a single fluorescently labeled macromolecule in a well-controlled electrostatic interaction free-energy landscape in solution. We further exploit the principles of overdamped transport in a periodic free-energy landscape in order to directly measure the physical properties of a single macromolecule—namely, its size and effective electrical charge in solution.

II. EXPERIMENTAL METHODS

A. Experimental design and measurement principle

In order to create an ordered landscape of potential wells for a single macromolecule, we employ our recently developed thermodynamic approach to trapping electrically charged matter in aqueous solution [18]. The working principle of such a trap is based on the equilibrium repulsive electrostatic interaction between a charged object in solution and like-charged confining parallel plates (Fig. 1). Geometric tailoring of the parallel plates results in a local interaction potential minimum that is capable of confining an electrically charged

---

[*] madhavi.krishnan@uzh.ch

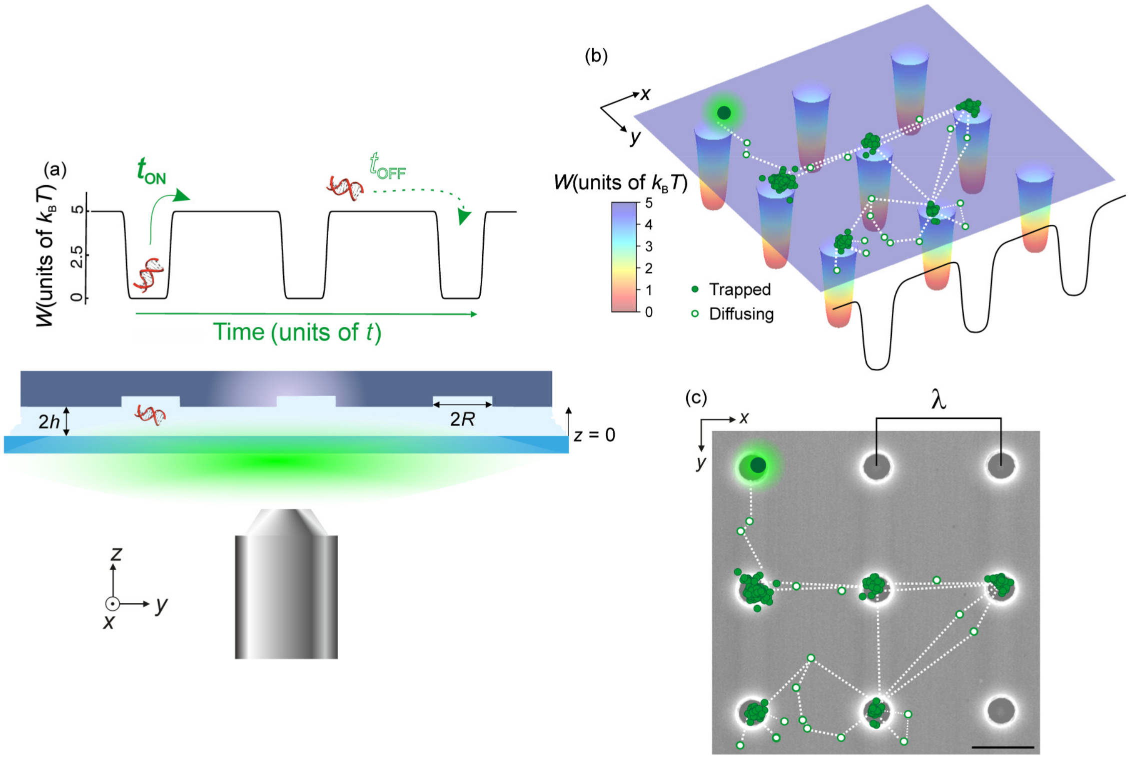

FIG. 1. (a) Schematic representation of the experimental setup displaying a single biomolecule in a lattice of electrostatic traps, observed using wide-field fluorescence microscopy. $2h$ indicates the slit height while $2R$ is the diameter of the nanostructured surface indentations that create local electrostatic potential minima. (b) A simulated trajectory of a diffusing molecule superimposed on a representative free-energy landscape, $W(\mathbf{r})$. (c) The same trajectory as in panel (b) superimposed on a scanning electron micrograph (SEM) of the underlying nanostructured surface. Closed symbols denote locations of the particle at lattice sites and open symbols denote free-diffusive transport in the interwell region. λ denotes the the lattice pitch. Scale bar denotes 1 μm.

molecule for long periods (∼30 min). Molecular residence time scales in a trap can be tuned by the geometry of the trapping nanostructure and salt concentration in solution [18,19].

Briefly, in our experiment, we work with free-energy landscapes created in a gap of typical height, $2h = 73$–75 nm, containing surface nanostructured indentations of radius, $R = 150$ or 300 nm [Fig. 1(a)] and depth, 150 nm, as previously described [19]. Fluorescently labeled macromolecules or particles in solution are introduced into the lattice at a concentration of 10–50 pM by capillary flow in a buffer containing 1 mM Tris and 0.5–2 mM NaCl [19]. We studied fluorescent nanoparticles and macromolecules, such as short DNA fragments (10 b ssDNA and 40 and 60 bp dsDNA, purchased from Microsynth AG, Switzerland) as well as an intrinsically disordered starmaker-like protein, Stm-l [20]. The molecules in our work are labeled with the fluorescent dye Atto532 while the nanoparticles (FluoSpheres, ThermoFisher Scientific) are carboxylated latex spheres labeled with Nile Red. The flow is arrested and molecular motion in the lattice is imaged under purely diffusive conditions by wide-field fluorescence microscopy.

We use optical excitation at 532 nm from a DPSS laser (Pusch OptoTech GmbH, Germany) and collect fluorescence emission beyond 552 nm. Images of object motion are acquired using a back-illuminated Electron Multiplying CCD (EMCCD) camera (iXon, Andor Inc., United Kingdom) with continuous exposures of duration $t_{\mathrm{exp}} = 5$ ms during a total observation time of about 1 s per molecular trajectory. The depth of the wells, W, in this work is typically 5 $k_{\mathrm{B}}T$, yielding trap residence times of ∼50 ms. For an object in a potential well in the fluid phase, overdamped diffusive crossing of a barrier is well described by Kramers' theory in the regime $W > 6\, k_{\mathrm{B}}T$, where the average time to escape the potential well is given by [19]

$$t_{\mathrm{esc}} = t_{\mathrm{r}} \exp \frac{W}{k_{\mathrm{B}}T}. \tag{1}$$

Here t_{r} is a time scale representing the position relaxation time of the molecule, which in turn depends not only on geometric features of the potential well but also importantly on the molecule's diffusion coefficient, $D = k_{\mathrm{B}}T/6\pi\eta r_{\mathrm{H}}$. Here, r_{H} is the hydrodynamic radius of an equivalent sphere that experiences the same frictional drag as the object of interest, and η is the viscosity of the medium [21]. Relying on this strong nonlinear dependence, we converted the measured average escape time t_{esc} of a trapped molecule into a highly precise (∼1%) measurement of the barrier height, W [19]. Note that the barrier height in our case is in essence the interaction free energy of the molecule with the confining parallel-plate slit [22,23]. It is also worth emphasizing that this electrostatic interaction energy directly reflects the molecule's effective charge, q_{eff}, which is in turn a function not only of its total structural charge but notably also of its three-dimensional (3D) conformation [23].

In our original proof-of-concept electrometry experiment on single molecules, conversion of the measured escape time to a well depth also required accurate knowledge of the free diffusion coefficient or hydrodynamic radius r_H of the molecule [19]. This information was therefore obtained from an independent fluorescence correlation spectroscopy or single-molecule diffusion measurement. Furthermore, although we have shown previously that the electrical charge as well as the size of a particle in an electrostatic potential well can be obtained in a single measurement by, e.g., high-precision tracking of particle position [24] or alternatively by high-temporal resolution optical monitoring of particle fluctuations, doing so typically requires a high signal-to-noise ratio (SNR $>$ 10) in detection, which is generally out of reach in experiments involving weakly emitting single molecules. In addition, the limited photon count rate and overall photon budget would pose a challenge for precise measurements on molecular-scale entities where the position fluctuation dynamics can be up to two orders of magnitude faster than for nanoparticles.

We emphasize that in this work the Debye length, $\kappa^{-1} \approx 0.3/\sqrt{C} = 10$ nm, is the characteristic length scale of screening of electric fields in an electrolyte containing monovalent salt at a concentration, $C = 10^{-3}$ mol/L. Since in these experiments, the lattice pitch, $\lambda \sim 300\,\kappa^{-1}$ [Fig. 1(c)], the interwell region of the landscape, is free of electrical fields in the xy plane and the in-plane transport of the molecule should be well described by free diffusion in two dimensions. We show later using validation experiments on nanoparticles that this is indeed the case. There are, however, strong axial forces (in z) in these regions which keep the particle tightly confined to the midplane of the slit. The solution-phase two-dimensional (2D) free-energy landscapes in our present work therefore differ significantly from those encountered in surface-atom diffusion in that in our case the wells are local regions of potential energy minima in an otherwise curvature-free energy landscape [Figs. 1(b) and 2(a)].

Crucially, such a design permits us to observe molecular transport in both the trapped and freely diffusive regimes.

Monitoring the thermal migration of a single macromolecule in the lattice, we indeed observe two different regimes in molecular transport: a trapped state and a free-diffusive state that alternate in time and whose durations can be readily measured. The acquired images of lattice migration are analyzed using an intensity threshold to yield "on times," t_{ON}, where the molecule is confined at a trap location and a large signal accumulates locally on the detector (the same as t_{esc} in our previous work), and "off-times," t_{OFF}, where it performs free diffusion traveling from one trap to the next and no substantial signal is received [Fig. 3(b)]. Comparing measurements of these two time scales with the predictions of a Brownian dynamics (BD) simulation, we demonstrate the ability to extract information on both the size and effective charge of the molecule from a single transport trajectory. Interestingly, the hopping motion of a molecule in the lattice yields a telegraphic on-off signal in optical detection which permits

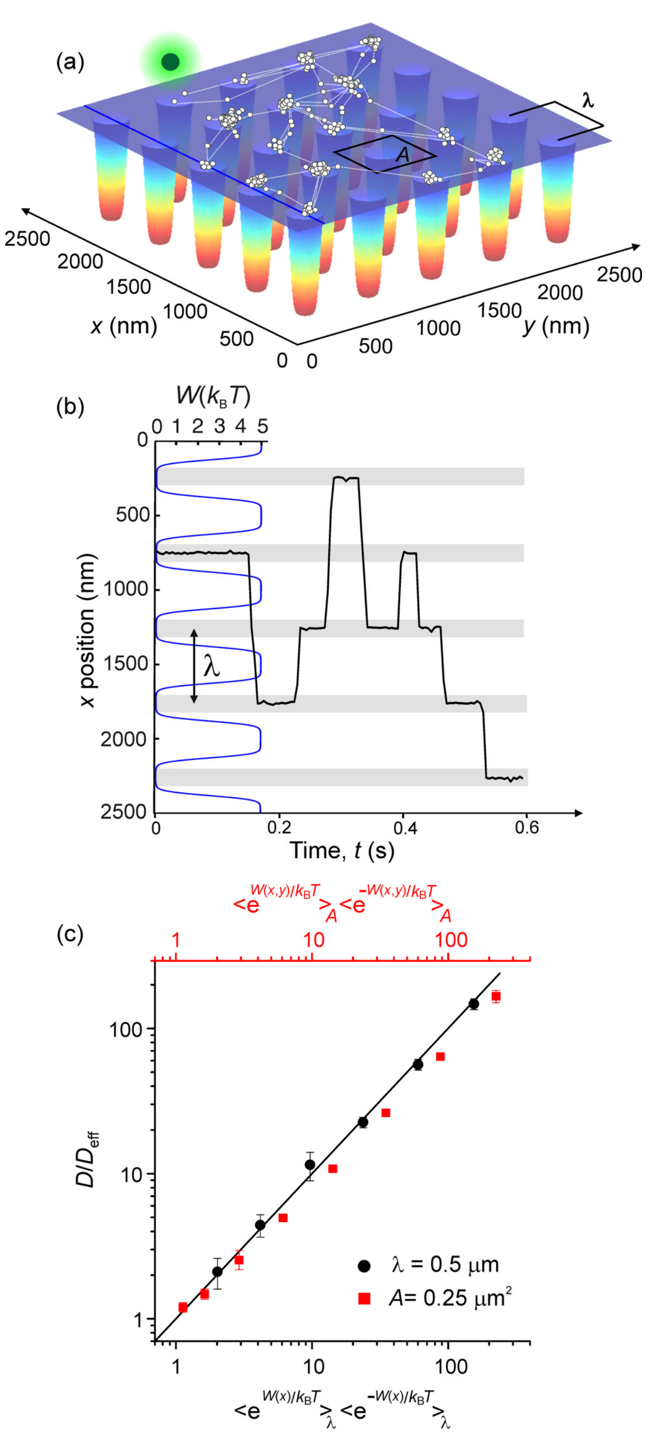

FIG. 2. (a) A simulated single-molecule trajectory superimposed on a two-dimensional lattice of electrostatic traps. λ denotes the lattice pitch, while A demarcates a single unit cell. (b) A simulated diffusive trajectory (black trace) in a one-dimensional periodic potential (blue vertical trace) along the solid blue line shown in panel (a). Shaded gray regions depict the part of molecular trajectory confined to the bottom of a given well. (c) The effective diffusion coefficient, D_{eff}, extracted from a mean-squared-displacement (MSD) analysis of simulated trajectories in both one (black circles, bottom axis) and two dimensions (red squares, top axis). The resulting D/D_{eff} values compare with the Lifson-Jackson expression, Eq. (2) (solid black line).

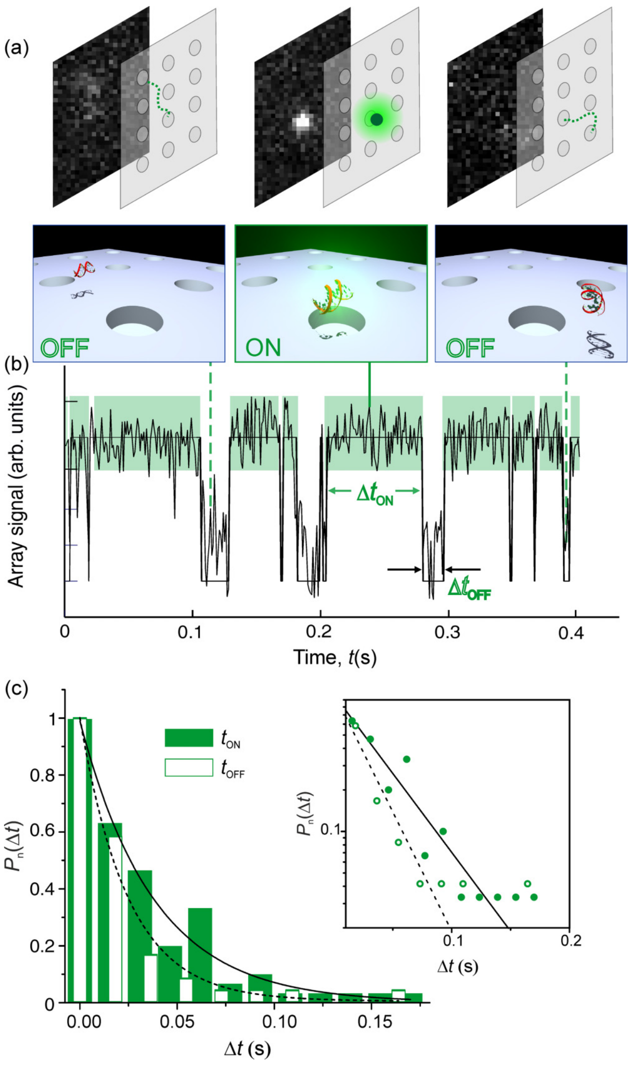

FIG. 3. (a) Experimental raw fluorescence images and corresponding schematic representations depicting a single 60 bp dsDNA molecule sampling a lattice of traps. (b) A simulated temporal trace of the total optical intensity from the lattice sites. The signal is high for a duration Δt_{ON} when the molecule is trapped at a lattice site and sufficient photons accumulate locally on the detector (green bands); the signal is low for a period Δt_{OFF} during free diffusion of the molecule between lattice sites. (c) Probability density distributions, $P(\Delta t) = \frac{A_{\mathrm{fit}}}{t}\exp(-\Delta t/t)$, of experimentally recorded times Δt_{OFF} (white bars) and Δt_{ON} (green bars), for a single trajectory of a 60 bp dsDNA molecule, where $A_{\mathrm{fit}} \approx 1$. The distributions are normalized such that $P_{\mathrm{n}}(\Delta t) = \frac{P(\Delta t)}{P_{\max}(\Delta t)}$. The fits yield average values $t_{\mathrm{OFF}} = 25 \pm 2$ ms and $t_{\mathrm{ON}} = 38 \pm 4$ ms.

precise measurements to be performed at very low SNR (∼3) [Fig. 3(a) and Fig. 12 in Appendix B]. We thus introduce a lattice-diffusion principle that is ideally suited to measurements on weakly emitting single macromolecules in solution.

B. Interpreting the detected single-molecule signal

We define the signal received from the molecule as the difference between the total optical intensity due to the molecule and that due to the detector background. When a weakly emitting entity occupies a potential well, its radius of spatial confinement (∼250 nm) is comparable with the optical point spread function. As a result, a measurable local signal builds up on a spatially sensitive detector such as a camera. In contrast, when the molecule leaves a well and diffuses in the "field-free" interwell zone of the landscape, the received signal does not exceed the local detector background and therefore gives rise to a "dark time" during the measurement, which we term t_{OFF} (see the movie in the Supplemental Material [25]).

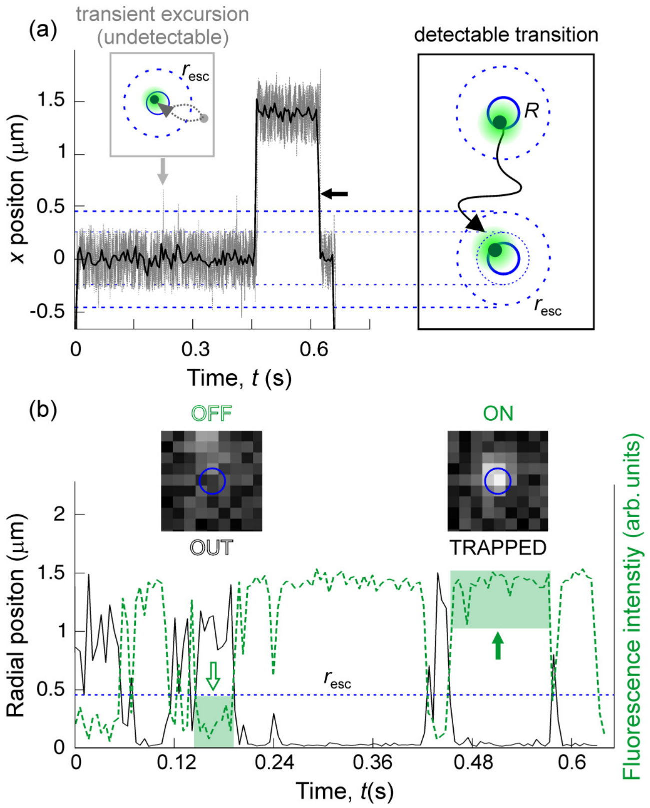

FIG. 4. (a) A simulated particle trajectory at a time resolution of 1 μs (gray dashed line), time averaged to a resolution of 5 ms (black solid line) in order to reflect experiments where the exposure time $t_{\mathrm{exp}} = 5$ ms. The accompanying schematics depict the circumference of the surface indentations (solid blue lines) and various escape boundaries (dotted blue lines). We highlight transient rapid excursions of the molecule out of and back into the trap which go undetected (light gray arrow), as well as transitions of the molecule from one trap to the next which are detected in the simulation and experiment as a "hop" between lattice sites (black arrow). (b) Generation of a series of optical images corresponding to molecular coordinates in a trajectory (black trace, left axis) shows that the signal from the lattice is high when a molecule is trapped at a lattice site and low otherwise (green dashed trace, right axis). The location of the escape boundary, r_{esc}, applied to the simulated trajectory data is tuned such that the resulting on and off-time scales agree with those from the simulated optical signal. These time scales are then compared with the corresponding experimental measurements.

Analysis of the detected optical signal from a single molecule diffusing in a 2D lattice yields the two average time scales: an on time, t_{ON}, and an off-time, t_{OFF} [Figs. 3(a)

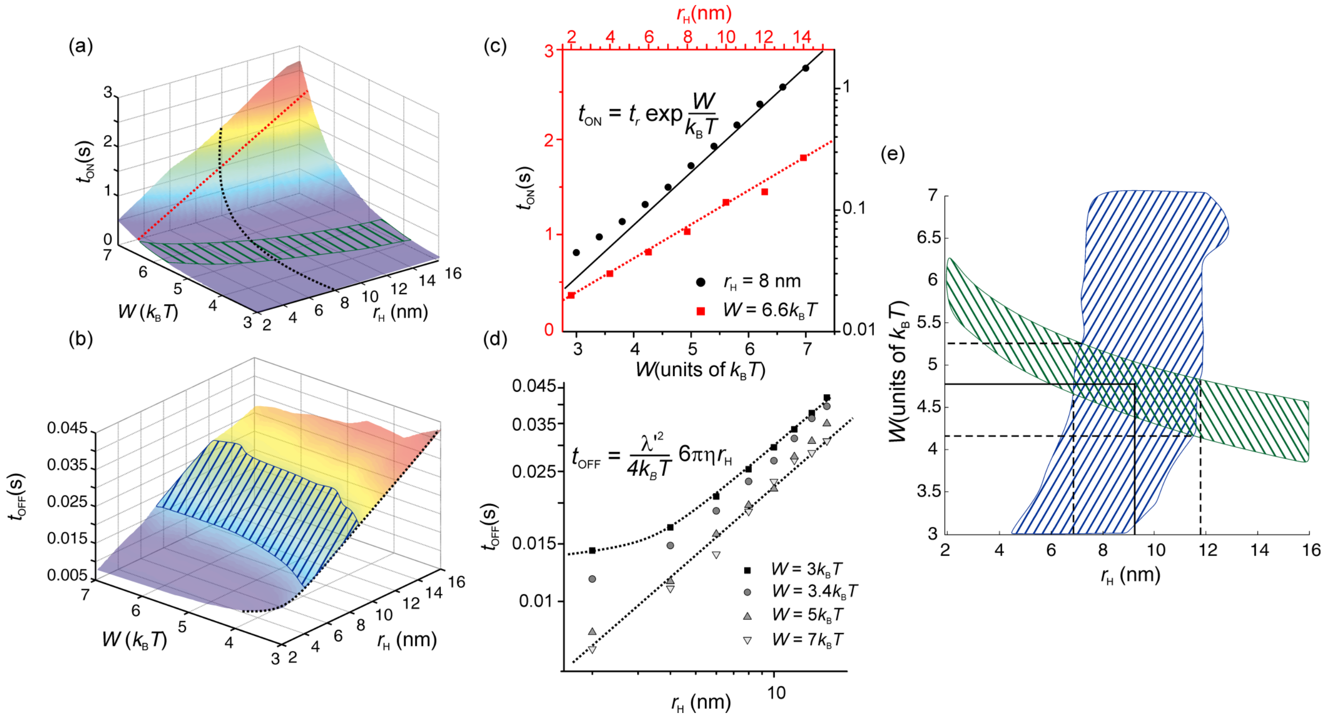

FIG. 5. [(a), (b)] Simulated t_{ON} and t_{OFF} values for relevant combinations of W and r_{H}. (c) Plots of t_{ON} vs W at $r_{\mathrm{H}} = 8$ nm (black circles, bottom and right axis) and t_{ON} vs r_{H} for $W = 6.6\ k_{\mathrm{B}}T$ (red squares, top and left axis) along the contour lines shown in panel (a). t_{ON} depends linearly on r_{H} but is exponential in W. (d) t_{OFF} vs r_{H} for various values of W. The relationship is linear in the high well-depth regime ($W > 5k_{\mathrm{B}}T$), but starts to plateau for low r_{H} and $W < 6k_{\mathrm{B}}T$. Dashed lines are guides to the eye. (e) The hatched regions on the plots in panels (a) and (b) depict combinations of W and r_{H} that satisfy a measured t_{ON} and t_{OFF} value independently, including measurement uncertainty (here shown for a single Stm-1 molecule of $t_{\mathrm{ON}} = 0.2 \pm 0.065$ s and $t_{\mathrm{OFF}} = 0.023 \pm 0.005$ s). The intersection of the set of solutions for both time scales yields mean measured values of r_{H} and W (and thus q_{m}) (solid black lines). The statistical error on the measurements are given by the lateral and vertical extents of the hatched regions (dashed black lines) (see Appendix D).

and 4(b)]. Similar to memoryless escape from a potential well, we find that, as expected, off-times are also exponentially distributed [Fig. 3(c)]. Importantly, the mean off-time, t_{OFF}, depends linearly on the molecular hydrodynamic radius, r_{H}, while t_{ON} depends exponentially on the effective charge of the molecule and relatively weakly on r_{H} [Fig. 5(c)]. A BD simulation of the hopping process yields t_{ON} and t_{OFF} times over the $\{W(q_{\mathrm{eff}}), r_{\mathrm{H}}\}$ space of interest and thereby serves to convert an experimental measurement of the two measured time scales into unique values of q_{m} and r_{H}, with respective uncertainties for a single molecule.

III. BROWNIAN DYNAMICS SIMULATION OF PARTICLE DIFFUSION IN A FREE-ENERGY LANDSCAPE

Analytical expressions for the average escape time for a particle in a potential well, or transport coefficients in a landscape, are generally only available for particular analytical functional forms of the underlying potential and entail landscapes of infinite extent [21,26,27]. As escape times do depend on subtle features such as local curvatures of the landscape, e.g., at the bottom of the well and at the barrier [28], and our experiments involve lattices of finite extent in both dimensions, we performed BD simulations of particle motion in periodic landscapes in order to extract quantitative predictions that accurately reflect our experiments.

A. Generating the free-energy landscape

The first step in the simulation study is to determine the full three-dimensional distribution of electrical potential in a single well by solving the nonlinear Poisson-Boltzmann (PB) equation in the fluidic trapping nanostructure [18]. We have verified that in our work, the spatial electrostatic free energy for a charged object can be simply obtained by multiplying the local electrical potential $\psi(\mathbf{r})$ by a parameter q_{eff}, which is the effective charge of the object [23]. We point out that since the position of the particle is strongly weighted toward the local minimum of interaction energy, the electrical potential in the region of the midplane of the slit largely determines the overall behavior. Thus, the electrostatic free energy, which is the dominant contribution to W in this work, is well estimated by $q_{\mathrm{eff}}\psi_{\mathrm{m}}$, where ψ_{m} is the electrical potential at the midplane of the slit.

Furthermore, the problem has a free-energy contribution of typically 30% from particle spatial fluctuations in the axial (z) dimension. We have verified by simulation that the dimensionality of the problem can be reduced to two by including an entropic correction for axial fluctuations both inside and outside the trap, and an additional ~6% contribution to the electrostatic energy arising from axial fluctuations in the slit region [19]. Thus, the depth, W, of each well in the landscape can be expressed as $W = q_{\mathrm{eff}}\psi_{\mathrm{m}} + f$, where the first term is due to the electrostatic interaction free energy of a particle at the midplane of the slit and f is the contribution to the total free energy from the finite out-of-plane thermal fluctuations of the particle. Note that in formulating the well depth, W, we deliberately ignore the system free energy when the particle is at the bottom of the well, as the electrical potential here is zero by design.

The geometry of a single potential well is further influenced by the diameter of the surface nanostructure, height of the slit, and the salt concentration in solution, which are all included in the PB calculation. We thus obtain the free-energy landscape for a single primitive cell in the lattice which we then use to generate a 2D landscape of the required lateral pitch and spatial extent in x and y for the simulation [Fig. 2(a)].

B. Effective diffusion coefficient of a particle in the lattice

The experiments we report here involve a square or rectangular lattice of effectively identical radially symmetric potential wells of depth, W, with each well occupying a single lattice site. Analytical treatments of diffusive transport in an infinite one-dimensional periodic arrangement of wells show that the effective diffusion coefficient, D_{eff}, of a molecule strongly depends on W and in the overdamped limit is given by the Lifson-Jackson relation [29–32]:

$$D = D_{\text{eff}} \left\langle \exp \frac{W(x)}{k_B T} \right\rangle_{\lambda} \left\langle \exp \frac{-W(x)}{k_B T} \right\rangle_{\lambda}, \tag{2}$$

where D is the particle's free diffusion coefficient.

We use the effective diffusion coefficient as the starting point of our analysis of single-molecule transport in a periodic potential. We iteratively solve the discretized overdamped Langevin equation for particle motion in a 2D free-energy landscape of "infinite" extent:

$$\mathbf{x}(t+\delta t) = \mathbf{x}(t) - \mu \nabla W[\mathbf{x}(t)] + \sqrt{2D\Delta t}\, \mathbf{w}(t). \tag{3}$$

Here, $\mathbf{x}(t)$ represents the instantaneous position of a particle at time, t, in one dimension, and $\mu = \delta t / 6\pi\eta r_H$. $\mathbf{w}(t)$ represents a displacement due to the random thermal force acting on the particle that satisfies $\langle \mathbf{w}(t) \rangle = \mathbf{0}$ and $\langle \mathbf{w}(t)\mathbf{w}^{\top}(t') \rangle = I$ if $|t - t'| \leqslant \delta t$, and $\mathbf{0}$ otherwise. Note that the simulation time step, $\delta t = 10$ μs, is much larger than the momentum relaxation time, which is ~10 ns for a typical molecule.

At $t = 0$, the particle is located at the center of a trap in the landscape. We then use Eq. (3) to propagate the instantaneous position of the particle, $\mathbf{x}(t)$, forward in time over a typical observation period of 30 s. A typical such trajectory in one dimension, time averaged over the exposure time t_{exp}, is shown in Fig. 2(b). In order to validate our simulations against theoretical expectations, we apply a mean-squared-displacement (MSD) analysis to about five particle trajectories and extract effective lattice diffusion coefficients, D_{eff}, for the particle. We verify that the simulated D_{eff} values satisfy the Lifson-Jackson relation in both one and two dimensions for values of W ranging from 3 to 8 $k_B T$ [29,33] [Fig. 2(c)]. Experiments on micron-scale particles in a periodic landscape have verified the Lifson-Jackson relation [34] and demonstrated a measurement of the effective diffusion coefficient, D_{eff}, of a particle [9]. However, knowledge of D_{eff} alone yields neither the well depth, W, nor the particle's free diffusion coefficient, D, which reflects its hydrodynamic radius, r_H.

C. Trapped and free diffusive-state lifetimes for a single particle

Our study requires us to go beyond the analysis of an effective diffusion coefficient for molecular transport in a lattice. Our goal is to accurately determine both the trapped and free diffusive time scales for a single particle migrating in a periodic lattice in order to obtain measures for both W and D (r_H) from a single transport trajectory. A recent study on colloidal particle transport in a quasicrystalline lattice illustrates the subtleties involved and shows how the lack of crystalline order in the landscape introduces more complex free diffusive behavior, thus necessitating averaging over an ensemble of particles in order to measure both W and r_H [34].

In order to correctly relate the time scales of interest observed in experiment to those available from simulations, we perform further analysis of the simulated trajectories involving important additional features. One such feature is the definition of an absorbing "escape boundary" represented by a radially symmetric contour at r_{esc} centered on the trap [Fig. 4(a)].

When analyzing a simulated transport trajectory of an object diffusing in the landscape, we register a trapped state of duration Δt_{ON} when the particle enters the region within the predefined domain circumscribed by r_{esc} at time t, then reaches the bottom of the trap - denoted by a circular region of radius, $R/2$ centered on the trap - and subsequenty leaves the domain given by r_{esc} at a time $t' > t$. Here $\Delta t_{\text{ON}} = t' - t$. Δt_{OFF} is then the interval between two sequential on-states. In addition, since the imaging process involves a finite time window of observation, the experimentally measured particle position in fact physically reflects its location averaged over the duration of an exposure time $\langle r \rangle_{t_{\text{exp}}}$, rather than its instantaneous position, r. Furthermore, in the escape-from-a-potential well problem, it is well known that the location of the absorbing boundary condition can strongly influence the value of the average escape time or the trapped state lifetime [35] (Appendix A). Simulation results presented in Fig. 4(a) illustrate two important features: (1) The average escape time of the instantaneous position, r, depends strongly on the location of the escape boundary, and (2) escape times based on a time-averaged position, $\langle r \rangle_{t_{\text{exp}}}$, should be substantially longer than that based on an instantaneous position, r.

We analyze via simulation the dependence of t_{ON} on r_{esc} the location of the escape boundary (Fig. 11 in Appendix A). Given the average diffusion length during an exposure time of duration, t_{exp}, is $l_{\text{diff}} = \sqrt{4Dt_{\text{exp}}}$, we find that for $\lambda < l_{\text{diff}}$, the measured time scale t_{ON} does not strongly depend on the location of the boundary. This is because the proximity of traps ensures that escape from one well is highly likely to result in absorption at the neighboring lattice site. When $\lambda > l_{\text{diff}}$, however, as in these experiments reported here, the simulated escape time, t_{ON}, does strongly depend on the location of the escape boundary (see Fig. 11 in Appendix A). This is due to the fact that in this regime a particle that escapes a given well and crosses r_{esc} has, on short time scales, a finite probability of return to the same well rather than diffusion to and capture at the neighboring well [34].

Furthermore, as already described, the experimental readout in the case of single molecules is not a temporally varying particle position in the lattice but rather a high or low optical signal at the lattice sites [Fig. 3(a)]. It is therefore essential to determine the true location of the absorbing boundary condition in the simulation that would correctly reflect the optical on-off time scales measured in experiments. In addition, other experimental factors such as SNR and detector background could also influence the measurement of the time scales of interest. Since time averaging and subtle features of the optical detection described above make it *a priori* unclear where to place the escape boundary in the particle-coordinate output of the BD simulation, r_{esc} has to be obtained by matching particle position-based predictions of the on-off time scales against those from simulated optical signal data.

We therefore also perform an image-based analysis of simulated thermal migration of the molecule in the lattice including most, if not all, of the important attributes of the imaging process and system, e.g., exposure time, typical signal and background intensities, background noise, and the optical point spread function [Fig. 4(b)]. These simulated images of molecular transport are generated in an additional step after the BD simulation, using trajectories generated for various values of particle size and charge. An example of a particle position trace and the corresponding optical signal are shown in Fig. 4(b).

The optical traces are analyzed in terms of intensity thresholds on the signal, in a manner identical to the experimental data, to yield values of t_{OFF} and t_{ON} for a single hopping trajectory about 30 s in length. Importantly, the time scales obtained from this full image-based analysis can be compared with those from the corresponding "raw" particle coordinates in order to determine the location of the escape boundary, r_{esc}, that accurately recovers the same t_{ON} and t_{OFF} values [Fig. 4(b)]. As a general rule for the lattices in these experiments, we find that a radially symmetric absorbing boundary located at $r_{\mathrm{esc}} = R + 300\,\mathrm{nm}$ yields values of t_{OFF} and t_{ON} within 10% of the full image-based analysis. The advantage of working with simulations based on the coordinates of the particle, $\langle r \rangle_{t_{\mathrm{exp}}}$, rather than detected optical images is that the former approach is computationally less demanding and faster than the image-based route.

Interestingly, we find that for strongly emitting objects (photon count rate >10 kHz), where particle motion can be directly tracked at all times, self-consistent results are obtained as long as the experimentally measured position traces are analyzed using the same escape boundary criterion as the simulated traces, regardless of the actual location of the boundary.

As t_{OFF} and t_{ON} each depend on both q_{eff} and r_{H}, the simulation analysis yields two surface plots for the time scales as a function of the two measurables of interest (Fig. 5). We note that t_{OFF} not only depends linearly on the molecular hydrodynamic radius, r_{H}, but also depends strongly on geometric parameters such as the lattice pitch, λ, and further displays a weak dependence on the depth of the traps, W [Fig. 5(d)]. t_{ON} in turn, as previously shown, depends exponentially on W (or q_{eff}) and only linearly on r_{H} [Fig. 5(c)]. The simulation result thus serves to convert an experimental measurement of the two time scales t_{ON} and t_{OFF} into unique values of the two unknowns, namely the measured effective charge, q_{m}, and hydrodynamic radius, r_{H}, with respective uncertainties for a single molecule.

Finally, we point out that the precision on the inferred value of q_{m} is ultimately limited by the statistical uncertainty inherent to determining the diffusion coefficient, D, of a single molecule from a temporally limited migration trajectory in the lattice. Measurement precision improves with the number of recorded transitions, N_{hop}. For example, $N_{\mathrm{hop}} = 100$ in a measurement with $t_{\mathrm{OFF}} = t_{\mathrm{ON}} = 25$ ms implies precision of 9% and 17% in the charge and size measurements, respectively, in a total measurement time of $\sim$2 s (see Appendix D). Armed with a full-fledged simulation-based quantitative analysis of the problem, we then proceed to an experimental validation of the predictions as well as measurements of the properties of single molecules.

IV. EXPERIMENTAL VALIDATION USING FLUORESCENT NANOSPHERES

The simulations reveal a linear dependence of t_{OFF} on r_{H} in the large-W regime, reflecting the fact that t_{OFF} is nothing but the average diffusion time of the object over a distance given by an effective lattice pitch, λ' [Fig. 6(a)]. In order to experimentally test the accuracy of the relationship between t_{OFF} and r_{H} predicted by the simulation, we performed measurements of nanoparticle diffusion in a free-energy landscapes created in slits of height $2h = 200$ nm.

In contrast to molecules, nanoparticles emit strong signals in optical excitation and can therefore be spatially tracked with high precision during the entire transport trajectory. A mean-squared-displacement (MSD) analysis of nanosphere motion in the free-diffusive regime directly yields its hydrodynamic radius, r_{H}. The same data can also be used to extract average interwell travel times, which we have referred to as t_{OFF} for a weakly emitting molecule. Thus we compare the value of r_{H} obtained from t_{OFF} measurements in a given lattice, with a parameter-free, direct determination of the same quantity in the same measurement via the MSD approach and find good agreement [Fig. 6(d)]. This result validates our r_{H} measurement principle and warrants its further application to measurements on single molecules. Note that at a particle diameter to slit height ratio of $a/h \simeq 0.2$ the viscous drag on the particle is expected to increase by 20% [37,38]. The slightly inflated value of particle radius, r_{H}, obtained in the lattice MSD measurement compared to bulk measurements is in fact in line with this expectation.

For the measurements on macromolecules, described in the following section, assuming the molecules behave as hard spheres of radius, r_{H}, we expect drag enhancement factors due to confinement ranging from 6% for 10 base DNA to 23% for the disordered protein Stm-l [39]. The measurement averages for r_{H} (Table I), however, reveal no systematic departure from the free solution measurements, suggesting that the true reduction in diffusion coefficient is probably much smaller than the above estimates for hard spheres.

V. MEASUREMENTS ON SINGLE MACROMOLECULES IN SOLUTION

We now focus on measurements of effective charge and hydrodynamic radius on single macromolecules in solution. We have verified using simulations that quantitatively identical escape times are obtained by replacing the spatial electrical potential distribution in the slit from the nonlinear PB equation by an axial potential given by the superposition of two simple

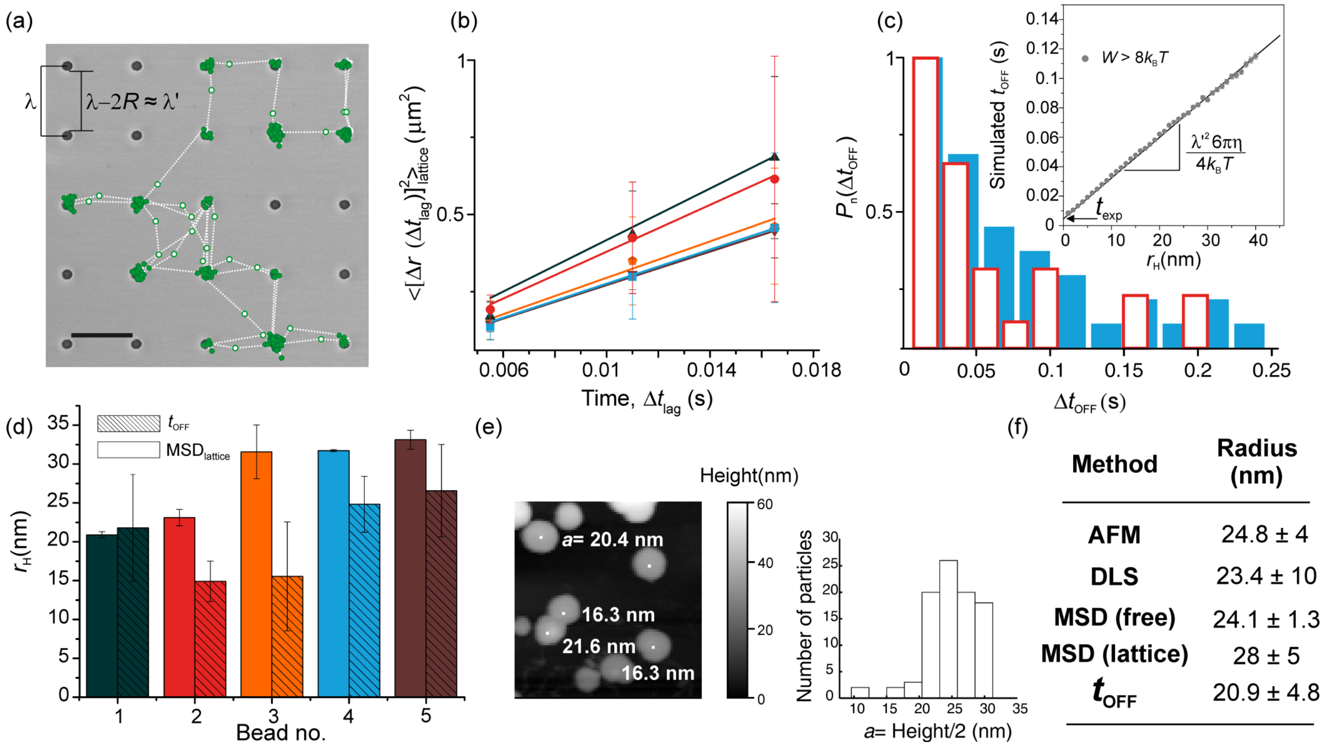

FIG. 6. (a) A representative trajectory of a fluorescent nanosphere of nominal radius $a = 24$ nm diffusing in a square lattice of pitch, $\lambda = 2$ μm and $R = 150$ nm, overlaid on an SEM image of the nanostructured surface. The effective pitch λ' inferred from the fit in panel (c) is close to the value $\lambda - 2R$, which corresponds to the edge-to-edge distance of two neighboring traps. The trapped (solid green symbols) and free-diffusive regimes (open symbols) of the particle trajectory are identified. Scale bar denotes 2 μm. (b) Single-particle trajectories in the free-diffusive regime (open symbols) are used to evaluate the mean-squared displacement (MSD), $\Delta\mathbf{r}(\Delta t_{\mathrm{lag}})$, as a function of lag time, Δt_{lag}, in two dimensions. A fit of the form $\langle[(\Delta\mathbf{r}(\Delta t_{\mathrm{lag}})]^2\rangle = 4D\Delta t_{\mathrm{lag}} + \epsilon^2$, where ϵ represents the particle localization uncertainty, yields D [36]. Here, $\Delta t_{\mathrm{lag}} = 5.5$ ms and each symbol represents a different nanosphere. (c) Normalized probabilty distributions $P_{\mathrm{n}}(\Delta t_{\mathrm{OFF}})$ are presented for two particles in panel (b). The open bars correspond to circular symbols and solid bars to square symbols in panel (b). The simulated t_{OFF} vs r_{H} is linear in the large W regime (inset, gray symbols). The intercept of the linear fit (black line) corresponds to the exposure time, t_{exp}, used in the simulation and experiment, while the slope, as expected, carries information on the effective pitch λ'. Here we find from the experimental dataset $\lambda' = 1.6 \pm 0.01$ μm. (d) Both MSD$_{\mathrm{lattice}}$ and t_{OFF} approaches yield independent measures for r_{H} for individual particles that are in good agreement. Data for individual nanospheres (left to right) correspond to the data series in panel (b) from top to bottom. (e) The hard sphere radius of the beads was characterized via atomic force microscopy (AFM). The height of a sample of spheres spin coated on a glass slide averaged over 90 particles agrees well with the nomimal diameter of the sample. (f) Comparison of size values measured by different approaches including dynamic light scattering (DLS) are in excellent mutual agreement. Please note that while AFM measurements provide information on the hard sphere radius of a particle, the other four approaches directly measure r_{H}.

TABLE I. Measurements of hydrodynamic radius, r_{H}, and effective charge, q_{m}, averaged over all single-molecule measurements reported for each species in Fig. 7. For comparison, we include independent r_{H} measurements using ensemble-averaging techniques, and theoretically expected values of effective charge, q_{c}, including the contribution of the dyes.

	r_{H} (nm)		q_{c}	q_{m}
	FCS/DLS	t_{OFF}	$(-e)$	$(-e)$
Nanospheres	23.4 ± 10	20.9 ± 4.8		181.7 ± 12.6
Stm-l	8.7 ± 0.5	7.9 ± 2.1	89.6	105.5 ± 21.6
60 bp	4.5 ± 0.2	4.7 ± 0.9	43.4	37.9 ± 4
40 bp	3.2 ± 0.2	2.4 ± 0.4	32.7	32.1 ± 5.1
10 base	1.8 ± 0.1	1.5 ± 0.8	10.9	8.3 ± 1.9

exponentials of the form

$$\psi(z) = \psi_{\mathrm{s}}\{\exp(-\kappa z) + \exp[-\kappa(2h - z)]\}, \tag{4}$$

where ψ_{s} is an effective surface potential at each surface of the slit and $2h$ is the height of the slit. This approximation works well because the Boltzmann distribution ensures that the molecule essentially never samples the region very close to the surfaces, where differences in the electrical potential between the nonlinear PB solution and the equivalent linear theory could arise.

We know from our previous measurements in this system that setting $\psi_{\mathrm{s}} = 2.8k_{\mathrm{B}}T/e$ in Eq. (4) yields $q_{\mathrm{m}} = -88.8 \pm 3.5e$, which is nearly identical to the theoretically expected effective charge $q_{\mathrm{c}} = -89.6e$ for the disordered protein Stm-l [19,23]. Stm-l thus serves as the "calibration molecule," which determines the value of the surface potential in Eq. (4) that should hold for all measurements under the same

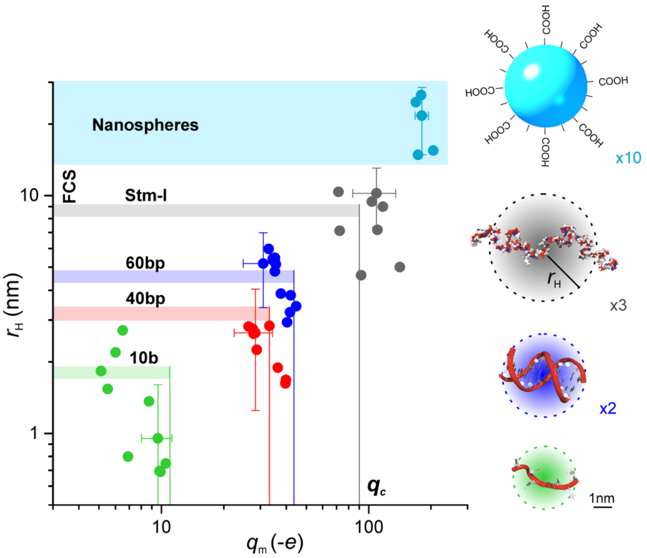

FIG. 7. Measurements of hydrodynamic radius and effective electrical charge of single biomolecules in solution. Each data symbol corresponds to the information obtained for a single object, from top to bottom: 24-nm-radius FluoSpheres (light blue), an intrinsically disordered protein, Stm-l (gray), 60 bp dsDNA (blue), 40 bp dsDNA (red), and 10 base ssDNA (green). Error bars are standard error of the mean (s.e.m.) and are presented for one molecule of each species. Vertical lines denote the theoretically expected charge, q_c, while horizontal bands correspond to radius measurements from fluorescence correlation spectroscopy (FCS) on molecules and DLS for particles (band thickness indicates measurement standard deviation). On the right, structural representations of the measured species are reduced by the scaling factor noted.

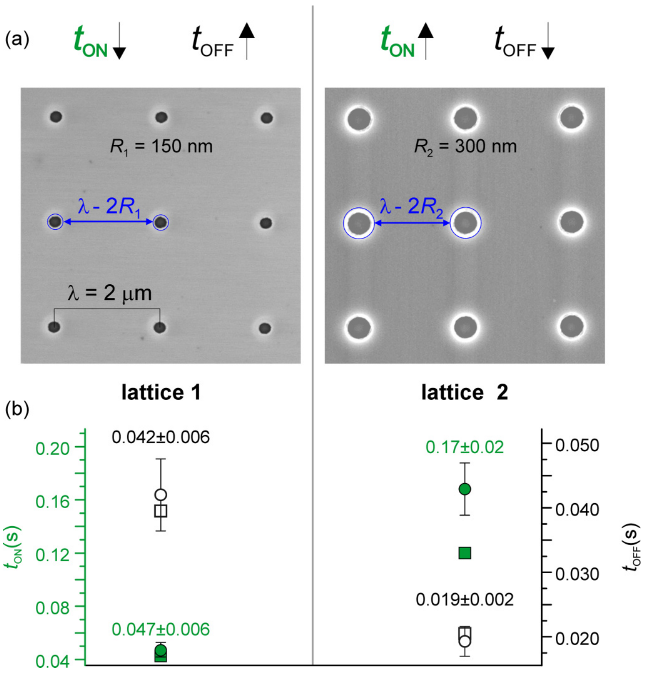

FIG. 8. (a) SEM images of two lattices of pitch $\lambda = 2\ \mu\text{m}$ and nanostructure radius, $R_1 = 150$ nm (left) and $R_2 = 300$ nm (right). Solid circles represent the circumferences of the surface nanostructures and the effective lattice pitch, $\lambda_i' = \lambda - 2R_i$, is indicated in blue. (b) The plot compares the experimentally measured time scales (circles) for the Stm-l molecule with those expected from the simulation (squares), where $q_{\text{eff}} = q_c = -89.6e$ and $r_H = r_{H,\text{FCS}} = 8.7$ nm. Filled symbols represent t_{ON} and open symbols give t_{OFF} values. Reported experimental values are averages over data from five molecules. The errors on the simulated values are smaller than the symbols.

conditions. Note that an effective surface potential of $2.8k_BT/e$ corresponds to a value of $pK_a = 9.5$ in a charge regulation model of the silica-water interface surface, excluding the Stern layer [23,40]. This value is consistent with trends emerging from the most recent experimental and theoretical work on amorphous silica surfaces [41,42].

We introduce solutions of each molecular species into the free-energy landscape and record typically 10 molecular migration trajectories in each case. We report measurements on 10 base single-stranded (ss) DNA, 40 bp double-stranded (ds) DNA, 60 bp dsDNA, and and the starmaker-like intrinsically disordered protein (Stm-l, molecular weight 40 kDa) [20]. The effective charge and hydrodynamic radius values for these molecular species span a range of about one order of magnitude. The combination of measured t_{ON} and t_{OFF} values for each molecule together determines its measured effective charge q_m as well as its hydrodynamic radius, r_H, as shown in Fig. 7. q_m and r_H values averaged over about 10 molecules for each species are shown in Table I.

Note that since the data on each molecular species were not averaged over several independent experiments, the accuracy on all the reported charge values in this work is not expected to be better than within ~20% due to the ca. 1 nm uncertainty in determining the slit height, $2h$, in a single experiment. The accuracy at the level of the single measurement can be improved using sequential measurement in the same lattice that entails first measuring a known standard and then the molecule of interest, or by parallel measurement on spectrally resolvable molecules [19]. Doing so would permit highly accurate single measurements with statistically limited precision.

We further subjected the measurement concept to a test of robustness with respect to the choice of landscape parameters, namely effective lattice pitch and radius of the potential wells. We report measurements performed on the Stm-l molecule in lattices with different nanostructure radii, $R_1 = 150$ nm and $R_2 = 300$ nm, but identical pitch $\lambda = 2\ \mu\text{m}$ [Fig. 8(a)]. We expect both time scales to respond to this change in lattice geometry: on-times, t_{ON}, depend on the area of the trapping nanostructures, while off-times, t_{OFF}, are expected to scale with the area of the "field-free" region of the lattice. In fact, we find that t_{ON} values measured in lattice 2 are 3.6 times larger than in lattice 1, close to the expected value, $(R_2/R_1)^2 = 4$. Conversely, in lattice 2, the measured t_{OFF} is smaller than the value in lattice 1 by a factor 2. Here, the ratio of off-times is expected to correspond to the squared ratio of the effective lattice pitch values, $(\lambda_1'/\lambda_2')^2 = 1.8 \pm 0.1$, where $\lambda_i' \approx \lambda - 2R_i$. The measured data are in remarkable agreement with the simulation predictions for a molecule of effective charge, $q_{\text{eff}} = q_c = -89.6e$ and $r_H = r_{H,\text{FCS}} = 8.7$ nm, which correspond to the properties of Stm-l [Fig. 8(b)].

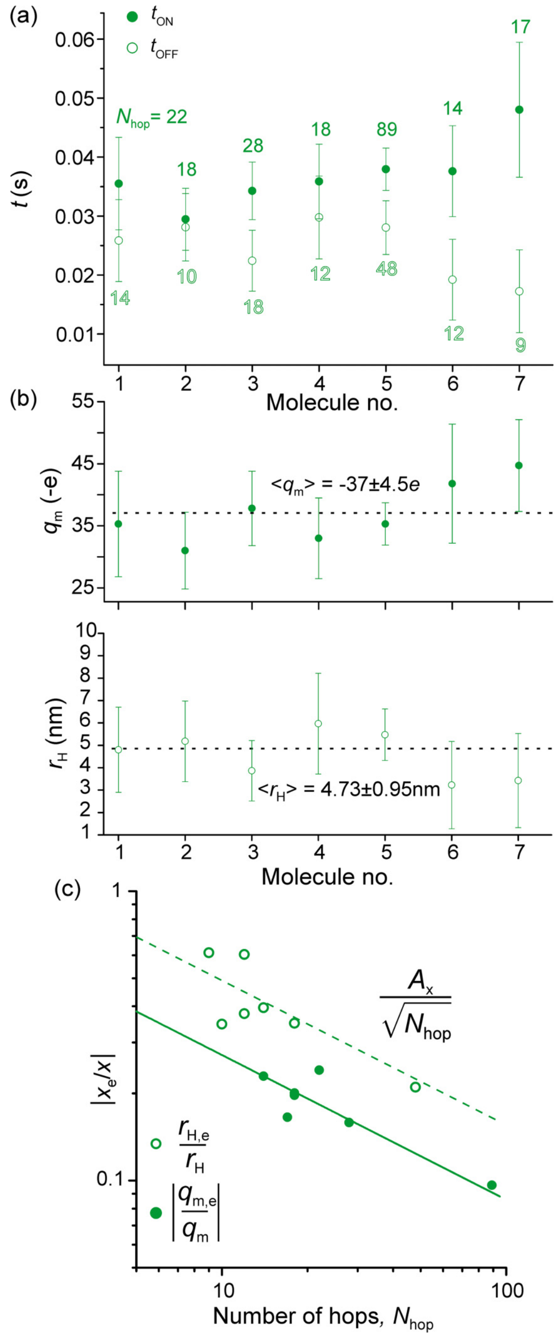

FIG. 9. (a) Measurements of t_{OFF} (empty symbols) and t_{ON} (solid green symbols) for representative single 60 bp dsDNA molecules. Error bars denote s.e.m. over the number of hops, N_{hop}, indicated by each symbol. (b) Inferred r_{H} and q_{m} values for each molecule in panel (a). (c) Plots of measured fractional errors on r_{H} and q_{m} vs N_{hop} for the data in panel (a). The lines represent fits of the form $|x_e/x| = A_x/\sqrt{N_{\mathrm{hop}}}$, where x denotes the measurable: either q_{m} or r_{H}. For r_{H}, we find $A_r = 1.7 \pm 0.1$, in good agreement with the expected value of 1.9 ± 0.15, while for q_{m} we obtain $A_q = 0.87 \pm 0.05$, close to the expected value of 0.82 (see Appendix D for error propagation).

Next we focus on the experimentally attained precision in our single molecule measurements. Data acquired on representative single molecules of 60 bp dsDNA with the values of N_{hop} ranging from 5 to 100 are shown in Fig. 9.

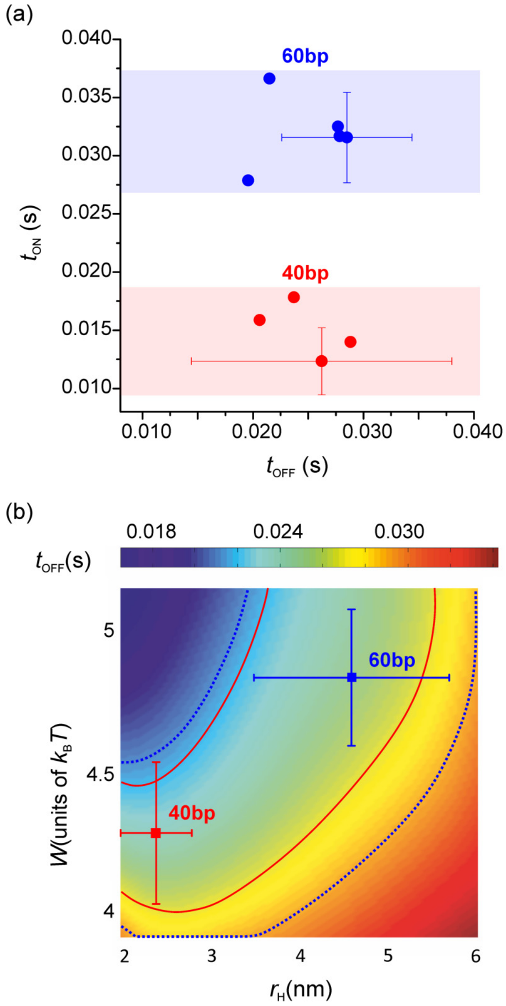

(c)

	r_{H} (nm)	$r_{\mathrm{H,\,FCS}}$ (nm)	q_{m} (-e)	q_{c} (-e)
40bp	2.4 ± 0.4	3.2 ± 0.2	32 ± 3.6	32.7
60bp	4.6 ± 1.1	4.5 ± 0.2	38.4 ± 4.2	43.4

FIG. 10. (a) Measurements of t_{OFF} and t_{ON} compared for ~5 molecules of 40 bp (red symbols) and 60 bp dsDNA (blue symbols). While the values of t_{OFF} are nearly indistinguishable ($\langle t_{\mathrm{OFF,40bp}}\rangle = 24.4 \pm 3$ ms and $\langle t_{\mathrm{OFF,60bp}}\rangle = 25 \pm 4$ ms), the simultaneously measured on-times, t_{ON}, are well resolved ($\langle t_{\mathrm{ON,40bp}}\rangle = 15 \pm 2$ ms and $\langle t_{\mathrm{ON,60bp}}\rangle = 32 \pm 3$ ms). (b) A surface plot of $t_{\mathrm{OFF}} = f(W, r_{\mathrm{H}})$ reveals nonmonotonic behavior of t_{OFF} in the low (W, r_{H}) regime which results in similar $\langle t_{\mathrm{OFF}}\rangle$ values for the two species, despite their different hydrodynamic radii. Overlapping isobands of measured $\langle t_{\mathrm{OFF}}\rangle$ for 40 and 60 bp dsDNA molecules are demarcated by dotted (60 bp) and solid (40 bp) contour lines. Including information on t_{ON}, however, permits unique values of W and r_{H} to be assigned to each species (square symbols). (c) Tabulated averages of measured q_{m} and r_{H} reveal good agreement with the theoretically expected values of q_{c} and r_{H}, independently measured via FCS.

Figure 9(c) shows that the precision we obtain on measurements of both q_{m} and r_{H} is statistically limited, with N_{hop} currently determined by the field of view in the imaging system. Clearly, improvements on this front will lead to more precise measurements on a single molecule, approaching at least the precision shown in the measurements in Table I.

Finally, we demonstrate an interesting effect in the experiment that can arise in the measurement of two similar molecular species. We observe that the comparatively weak trapping of a smaller, less charged molecule—say, species 1 (40 bp DNA)—can result in a measured t_{OFF} value comparable in magnitude to that obtained for the larger, more highly charged, and more stably trapped molecule of species 2 (60 bp DNA) [Fig. 10(a)]. An intuitive conclusion from the magnitudes of the measured (t_{ON}, t_{OFF}) data would point to different effective charges but the same hydrodynamic radius for both species. Notably, however, the simulation analysis assigns (q_{m}, r_{H}) values to the measured (t_{ON}, t_{OFF}) data that are in very good agreement with expectations for both molecules, where not only the effective charge values but also the hydrodynamic radii are significantly different [Fig. 10(c)].

The reason behind this counterintuitive observation is due to a well-depth-dependent effect on the dynamics. Free-diffusive transport terminates once a molecule is absorbed or trapped at a lattice site. If the field at the periphery of the potential well is strong, which generally implies that W is large, the capture probability is high, which means that a molecule that samples this region will very likely be rapidly drawn to the bottom of the well and free diffusive transport terminates. For low values of W, however, the force toward the bottom of the well is smaller, and on short time scales the molecule is statistically highly likely to return to the free diffusion zone; this inflates the measured t_{OFF} in an experiment (Fig. 13 in Appendix C). In general, we find that return probabilities broadly defined, within the finite observation window, strongly influence measured time scales. Correctly accounting for the time-averaged dynamics and well-depth-dependent effects is therefore critical for accurate conversion of the measured time scales into physical parameters of interest.

VI. CONCLUSIONS

Our study introduces lattice diffusion in an electrostatic landscape as a new experimental route to simultaneously measure both the hydrodynamic radius and the effective electrical charge of a single molecule in solution. The approach relies on standard wide-field optical microscopic observation of single fluorescently labeled molecules and also lends itself well to label-free imaging and measurement techniques [43,44]. Although our initial effort to establish the concept required an in-depth simulation-based analysis of Brownian motion in a 2D landscape, we point out that such studies yield simple functional dependences of the expected time scales on the magnitudes of the relevant physical properties of interest [Figs. 5(c) and 5(d)]. These relationships can then be broadly and directly applied to future measurements with simple rescaling to account for variations in experimental or system parameters.

Our combination of experiment and simulation in a periodic landscape has further revealed interesting features relevant for interpreting and understanding experimental observations on diffusive transport in a periodic potential. For example, while for large values of W, t_{OFF} decreases monotonically with decreasing r_{H} and is independent of well depth, as intuitively expected, we find interesting nonmonotonic behavior for small $W\,(< 5\,k_{\mathrm{B}}T)$. Here the measured time spent by an object of a given r_{H} in the field-free region of the lattice can be larger than that expected for high W [Figs. 5(d) and 10(b)]. We find that this effect is due to the finite return probability of the molecule spatially sampling the edge of the well (Appendix C). In other words, the behavior in the regimes of high and low W (or equivalently, effective charge, q_{eff}) are qualitatively delineated by the gradient of the potential at the periphery of the trap.

Further, the experiment we report holds significance for single-molecule studies, both in terms of direct optical measurement of static and dynamic molecular structural properties as well as in order to understand and interpret experimental observations of molecular transport in natural periodic systems. Since both the hydrodynamic radius and effective charge of a macromolecule depend on molecular 3D conformation, our new measurement principle paves the way toward experiments that explore static 3D conformation, or slow temporal changes of conformation, in a single macromolecule in solution.

ACKNOWLEDGMENTS

We gratefully acknowledge the Schweizerischer Nationalfonds zur Förderung der Wissenschaftlichen Forschung (SNSF), the European Research Council, and University of Zürich for financial support. We thank Ben Schuler and Andrzej Ożyhar for the gift of the Stm-l protein. Nanofabrication was carried out at FIRST Center for Micro- and Nanoscience, ETH Zürich.

APPENDIX A: DEPENDENCE OF ON-TIME ON THE LOCATION OF THE ESCAPE BOUNDARY

We analyzed the dependence of t_{ON} on the location of the the escape boundary, r_{esc} using BD simulations. For a lattice of pitch $\lambda = 2\ \mu\mathrm{m}$, we examine molecular residence times in two different regimes: $l_{\mathrm{diff}} \gtrsim \lambda$, corresponding to a molecule of $r_{\mathrm{H}} = 1$ nm, and $l_{\mathrm{diff}} < \lambda$ for a molecule of $r_{\mathrm{H}} = 20$ nm. In the former regime, we find that t_{ON} is nearly insensitive to r_{esc} while in the latter we note up to a factor 2 variation in t_{ON} depending on r_{esc} [Fig. 11(b)].

APPENDIX B: DETECTED OPTICAL SIGNAL FROM MOLECULAR MIGRATION IN THE LATTICE

A lattice area of 100 $\mu\mathrm{m}^2$, typically containing ∼20 lattice sites, is monitored via wide-field fluorescence microscopy. Figure 12(a) shows a subset of a typical array that can be sampled by a single molecule during 1–10 s of observation time. The mean fluorescence intensity of each trap is monitored separately in time. The traces are then rescaled, binarized, and superimposed on each other in order to obtain the overall temporal lattice intensity signal [bold black line in Fig. 12(b)]. The high-intensity bursts in the trace give the time spent at a lattice site and the average thereof yields t_{ON}. The average "dark time" in the trace in which none of the lattice sites appears occupied gives t_{OFF}.

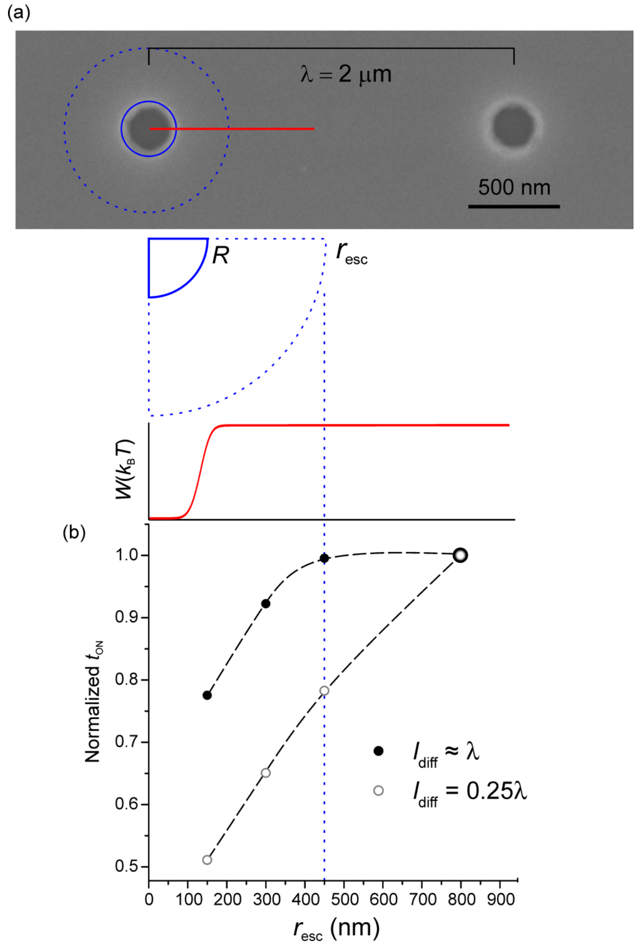

FIG. 11. (a) An SEM image of two trapping nanostructures of radius, $R = 150$ nm at a pitch $\lambda = 2$ μm. The solid circle denotes the circumference of the nanostructure, while the broken circle of radius r_{esc} indicates the escape boundary. The red solid line in the lower panel represents the radial electrostatic free energy profile along the red line in the image above. (b) The simulated value of t_{ON} obtained for each r_{esc} is normalized by the value obtained for $r_{esc} = 800$ nm. The simulated dataset for $r_H = 1$ nm ($\lambda \approx l_{diff}$) shows a weak dependance on r_{esc} (black symbols). For $r_H = 20$ nm, we find a strong variation in this time scale, as the average molecular diffusion length is smaller than the lattice pitch (gray open symbols). The vertical dotted line indicates the r_{esc} used for the analysis of the single-molecule transport for the depicted lattice geometry.

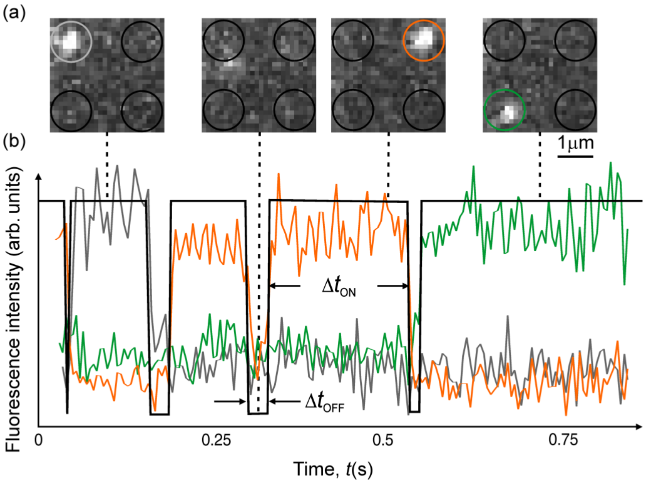

FIG. 12. (a) Wide-field fluorescence images of a lattice of four trapping nanostructures of $R = 150$ nm and $\lambda = 2$ μm. The average intensity of each circular region of interest (ROI) (black), centered on the lattice sites, is monitored in time. (b) Temporal intensity traces corresponding to three individual lattice sites are denoted by a different color. When the molecule occupies a lattice, the intensity recorded in the corresponding ROI is high, while the others appear dark. Each recorded trace is rescaled and binarized in order to compensate for heterogeneity in the illumination across the entire field of view.

APPENDIX C: DEPENDENCE OF OFF-TIME ON WELL DEPTH

In order to study the dependance of t_{OFF} on well depth W and in particular its nonlinear behavior for $W < 5k_BT$, we performed BD simulations. We studied the probability of capture of a molecule at traps in the lattice. The capture probability is defined as the ratio of the number of trapped events, $n(\Delta t_{ON})$ to the total number of events capable of resulting in capture. The latter quantity is given by the number of instances in the trajectory that satisfy $\langle r \rangle_{t_{exp}} < r_{esc}$, with reference to each trap in the lattice.

For a molecule of $r_H = 3$ nm, we find than the probability of being captured by a well decreases with decreasing well depth [Fig. 13(b)]. This is due to the fact that when the trapping force is weak, a small rapidly diffusing molecule sampling the edge of the potential well can evade escape and return to the "field-free" zone, all within a time period $< t_{exp}$. This gives rise to a longer lived t_{OFF} state. By contrast, at greater well depths a molecule sampling the edge of the well is very likely to reach the bottom and remain trapped for at least $t = t_{exp}$, as reflected in the increased capture probability. In general, for larger molecules [e.g., r_H= 9 nm, Fig. 13(b)], given the same exposure time in the observation, the influence of well depth on the capture probability is weaker, as the diffusive dynamics is slower.

APPENDIX D: ESTIMATING MEASUREMENT UNCERTAINTIES

The measurement error, x_e on a quantity x, which is a function of the variables f, g, h, etc., each with uncertainties f_e, g_e, h_e, etc., can be expressed as follows:

$$x_e = \sqrt{\left(\frac{\partial x}{\partial f}\right)^2 f_e^2 + \left(\frac{\partial x}{\partial g}\right)^2 g_e^2 + \left(\frac{\partial x}{\partial h}\right)^2 h_e^2 + \cdots} \quad \text{(D1)}$$

In our experiment, the main source of error in the determination of both molecular effective charge, q_{eff}, and hydrodynamic radius, r_H, arises from the statistical uncertainty in measuring t_{ON} and t_{OFF} in a temporally limited experiment. Here both time scales, Δt_x (where x is either ON or OFF) are exponentially distributed. Thus, the measurement error $t_{x,e}$ on their average value, t_x, is function of the number of detected events or hops,

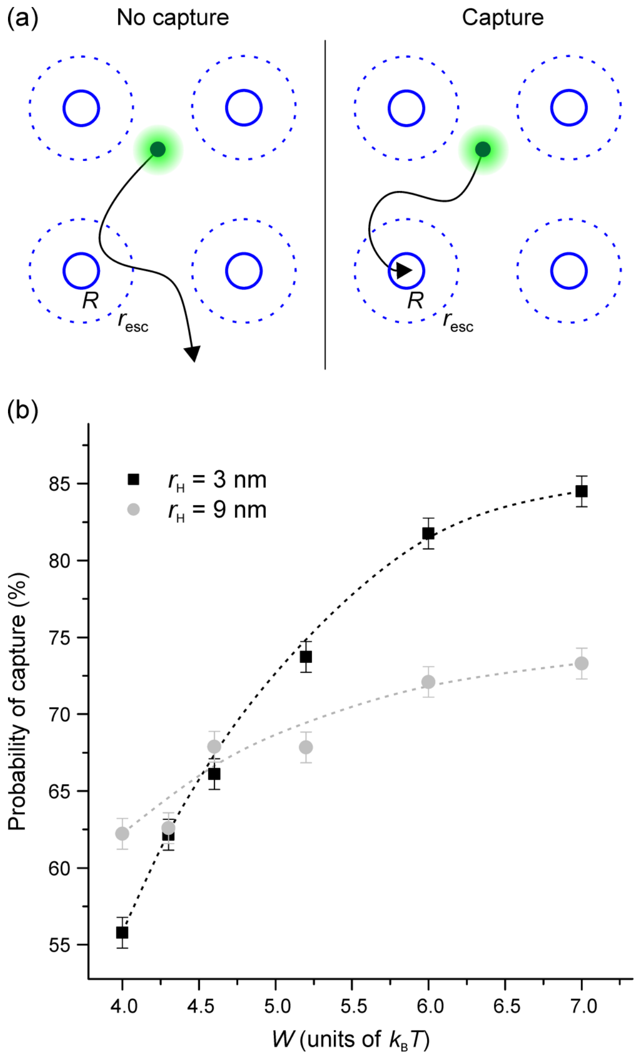

FIG. 13. (a) Schematic of a particle sampling a lattice of four traps. The blue solid line indicates the circumference of the surface indentations of radius R, while the dotted blue line shows the escape boundary r_{esc}. The molecule is considered "captured" if its trajectory results in a trapped state for a period $\geqslant t_{\text{exp}}$ once it traverses r_{esc}. (b) The probability of a molecule being trapped once it samples the area within the escape boundary of a given pocket increases with increasing well depth for a molecule of $r_H = 3$ nm (black squares), while the response is less pronounced for a molecule of larger radius ($r_H = 9$ nm, gray circles). Dashed lines are guides to the eye.

N_{hop}, as follows:

$$t_{\text{x,e}} = \frac{t_{\text{x}}}{\sqrt{N_{\text{hop}}}}. \tag{D2}$$

First, we consider the measurement error on r_H. The measurement uncertainty on r_H is nearly entirely due to the statistical error in measuring an average off-time from a limited number of hops. We have established that the relationship between t_{OFF} and the diffusion coefficient of the molecule of interest, D, is well described by $t_{\text{OFF}} = \lambda'^2/4D$, where λ' is the effective lattice pitch. This expression can be rewritten in terms of r_H using the Stokes-Einstein relation as follows:

$$r_H = \frac{4k_BT}{6\pi\eta\lambda'^2}t_{\text{OFF}} = a_1 t_{\text{OFF}}. \tag{D3}$$

Equation (D1) then gives the uncertainty on the hydrodynamic radius, $r_{\text{H,e}}$:

$$r_{\text{H,e}} = \sqrt{\left(\frac{\partial r_H}{\partial t_{\text{OFF}}}\right)^2 t_{\text{OFF,e}}^2} = a_1 t_{\text{OFF,e}}. \tag{D4}$$

Using the expression for $t_{\text{OFF,e}}$ given by Eq. (D2), we have for the fractional uncertainty on r_H

$$\frac{r_{\text{H,e}}}{r_H} = \frac{a_1}{r_H}\frac{t_{\text{OFF}}}{\sqrt{N_{\text{hop}}}} = \frac{A_r}{\sqrt{N_{\text{hop}}}}. \tag{D5}$$

Holding other parameters constant, the measurement error may be decreased by tuning the parameter a_1, which is inversely proportional to the squared effective pitch λ'. Clearly, a large lattice pitch would improve the accuracy of the method; however, the lattice pitch is limited by the field of view in the measurement. On the other hand, for very small λ', the molecule would see a landscape of contiguous potential wells and never appear in the off-state, thus hindering the measurement. For the conditions of the experiment illustrated in Fig. 9, we determine the value of $A_r = a_1 t_{\text{OFF}}/r_H$ to be 1.9 ± 0.15 ($\lambda' = 1.6 \pm 0.05$ μm, $r_H = 4.7$ nm, and $t_{\text{OFF}} = 25.5$ ms). This is in good agreement with the experimental fit value 1.7 ± 0.1 in Fig. 9(c). Thus, 10% measurement error on t_{OFF} ($N_{\text{hop}} = 100$) would correspond to ~17% error on r_H.

Next, we estimate the error on the measured effective charge, q_m, of the molecule. As described in the Supporting Information of our previous work [19], q_{eff}, hereafter referred to as q, depends on the measured time scale t_{ON} as follows:

$$q\psi_m + f = k_BT \ln\left(\frac{t_{\text{ON}}}{t_r}\right). \tag{D6}$$

Here ψ_m denotes the electrical potential at the midplane of the slit and f is a particle fluctuation contribution to the total trap depth, W. This contribution is almost entirely entropic in origin and is essentially independent of q. t_r in turn reflects a position relaxation time of the particle, which again can be written in terms of a diffusion time scale, $t_r = L^2/4D$. Here L is a length scale on the order of r_{esc}, the radius of the escape boundary. The position relaxation time can therefore be rewritten in terms of r_H as $t_r = \frac{L^2}{4k_BT}6\pi\eta r_H = a_2 r_H$.

Equation (D6) now reads

$$q\psi_m + f = k_BT \ln\left(\frac{t_{\text{ON}}}{a_2 r_H}\right). \tag{D7}$$

Thus the fractional error q_e/q according to Eq. (D1) is

$$\frac{q_e}{q} = \sqrt{\left(\frac{1}{q^2}\right)\left(\frac{\partial q}{\partial \psi_m}\right)^2 \psi_{\text{m,e}}^2 + \left(\frac{1}{q^2}\right)\left(\frac{\partial q}{\partial t_{\text{ON}}}\right)^2 t_{\text{ON,e}}^2 + \left(\frac{1}{q^2}\right)\left(\frac{\partial q}{\partial r_H}\right)^2 r_{\text{H,e}}^2}. \tag{D8}$$

The first term in Eq. (D8) represents the uncertainty in the determination of the midplane potential. This aspect has been discussed at length in our previous work [19], and arises from the uncertainty in determining the slit height with an accuracy better than $h_e = 1$ nm. For a molecule whose radius is known *a priori* from an independent measurement, and where the escape dynamics is well sampled ($N_{hop} > 100$), as in our previous work, this first term would be the main source of error, and is estimated at about 6% when averaging over four to five independent experiments. In a single experiment, however, where the height of the slit maybe depart from the mean value by as much as 2 or $3h_e$, this (single) measurement inaccuracy can be as large as 18%.

In the current experiment, short single-molecule trajectories are also affected by the statistical noise on t_{ON} (second term). It turns out that the total measurement error is in fact dominated by the measurement error on r_H (third term), which is measured simultaneously here.

As reflected in Eq. (D5), $r_{H,e}$ itself is a function of the number of hops, N_{hop}. The second and third terms thus essentially represent the error due to statistical noise, $(q/q_e)_N$, and can be written as follows:

$$\left(\frac{q_e}{q}\right)_N = \sqrt{\left(\frac{1}{q^2}\right)\left(\frac{k_BT}{t_{ON}\psi_m}\right)^2 t_{ON,e}^2 + \left(\frac{1}{q^2}\right)\left(-\frac{k_BT}{\psi_m r_H}\right)^2 r_{H,e}^2}, \tag{D9}$$

which simplifies to

$$\left(\frac{q_e}{q}\right)_N = \frac{1}{\sqrt{N_{hop}}}\frac{k_BT}{q\psi_m}\sqrt{1+\left(\frac{a_1 t_{OFF}}{r_H}\right)^2} = \frac{A_q}{\sqrt{N_{hop}}}. \tag{D10}$$

The first term in Eq. (D9) represents the contribution of statistical noise on t_{ON} to the overall measurement error. As noted in previous work, the logarithmic dependence of q on the escape time (on-time) means that poorly sampled dynamics will still give a relatively precise charge measurement. Also, as the electrostatic well depth $q\psi_m$ is larger, the attenuation of the statistical noise, $1/\sqrt{N_{hop}}$, is greater. In this experiment, we have $\langle q\psi_m\rangle = 2.6\ k_BT$. Thus 10% error in determining t_{ON} corresponds to only ~4% error on q. However, the second term in Eq. (D9)—which arises from the uncertainty on r_H—contributes predominantly to the overall error. Under the experimental conditions concerned, we calculate $A_q = 0.82$, which is very close to the fit value 0.87 ± 0.05 from Fig. 9(c).

To conclude, given $N_{hop} = 100$, we expect ~9% error on the measured q value arising from statistical uncertainty alone. Including the contribution from the uncertainty on the midplane potential, ψ_m, we estimate an overall uncertainty or measurement inaccuracy of ~20% in a single measurement.

[1] R. Gomer, Rep. Prog. Phys. **53**, 917 (1990).
[2] G. Ayrault and G. Ehrlich, J. Chem. Phys. **60**, 281 (1974).
[3] J. V. Barth, H. Brune, B. Fischer, J. Weckesser, and K. Kern, Phys. Rev. Lett. **84**, 1732 (2000).
[4] B. G. Briner, M. Doering, H. P. Rust, and A. M. Bradshaw, Science **278**, 257 (1997).
[5] H. X. Zhou, J. Phys. Chem. **94**, 8794 (1990).
[6] P. Hanggi, P. Talkner, and M. Borkovec, Rev. Mod. Phys. **62**, 251 (1990).
[7] J. Helenius, G. Brouhard, Y. Kalaidzidis, S. Diez, and J. Howard, Nature (London) **441**, 115 (2006).
[8] J. Gorman, A. J. Plys, M.-L. Visnapuu, E. Alani, and E. C. Greene, Nat. Struct. Mol. Biol. **17**, 932 (2010).
[9] X. G. Ma, P. Y. Lai, and P. G. Tong, Soft Matter **9**, 8826 (2013).
[10] M. Pelton, K. Ladavac, and D. G. Grier, Phys. Rev. E **70**, 031108 (2004).
[11] D. Kim, C. Bowman, J. T. Del Bonis-O'Donnell, A. Matzavinos, and D. Stein, Phys. Rev. Lett. **118**, 048002 (2017).
[12] S. W. P. Turner, M. Cabodi, and H. G. Craighead, Phys. Rev. Lett. **88**, 128103 (2002).
[13] V. Garcés-Chávez, R. Quidant, P. J. Reece, G. Badenes, L. Torner, and K. Dholakia, Phys. Rev. B **73**, 085417 (2006).
[14] J. Fu, R. B. Schoch, A. L. Stevens, S. R. Tannenbaum, and J. Han, Nat. Nanotechnol. **2**, 121 (2007).
[15] K. Xiao and D. G. Grier, Phys. Rev. Lett. **104**, 028302 (2010).
[16] J. Skolnick, J. Chem. Phys. **145**, 100901 (2016).
[17] J. A. Dix and A. S. Verkman, Annu. Rev. Biophys. **37**, 247 (2008).
[18] M. Krishnan, N. Mojarad, P. Kukura, and V. Sandoghdar, Nature (London) **467**, 692 (2010).
[19] F. Ruggeri, F. Zosel, N. Mutter, M. Różycka, M. Wojtas, A. Ożyhar, B. Schuler, and M. Krishnan, Nat. Nanotechnol. **12**, 488 (2017).
[20] M. Różycka, M. Wojtas, M. Jakób, C. Stigloher, M. Grzeszkowiak, M. Mazur, and A. Ożyhar, PLoS ONE **9**, e114308 (2014).
[21] H. Kramers, Phys. (Amsterdam, Neth.) **7**, 284 (1940).
[22] M. Krishnan, J. Chem. Phys. **138**, 114906 (2013).
[23] M. Krishnan, J. Chem. Phys. **146**, 205101 (2017).
[24] N. Mojarad and M. Krishnan, Nat. Nanotechnol. **7**, 448 (2012).
[25] See Supplemental Material at http://link.aps.org/supplemental/10.1103/PhysRevE.96.062406 for a movie of lattice diffusion of a single molecule.
[26] B. U. Felderhof, Phys. A (Amsterdam, Neth.) **387**, 1767 (2008).
[27] B. U. Felderhof, Phys. A (Amsterdam, Neth.) **387**, 39 (2008).
[28] S. Chandrasekhar, Rev. Mod. Phys. **15**, 1 (1943).
[29] S. Lifson and J. L. Jackson, J. Chem. Phys. **36**, 2410 (1962).
[30] D. L. Weaver, Phys. A (Amsterdam, Neth.) **98**, 359 (1979).
[31] R. Zwanzig, Phys. A (Amsterdam, Neth.) **117**, 277 (1983).
[32] M. Siler and P. Zemanek, in *Conference on Optical Trapping and Optical Micromanipulation VII* (SPIE, Bellingham, Washington, 2010), Vol. 7762.
[33] R. Verdel, L. Dagdug, A. M. Berezhkovskii, and S. M. Bezrukov, J. Chem. Phys. **144**, 084106 (2016).
[34] Y. Su, P. Y. Lai, B. J. Ackerson, X. Cao, Y. Han, and P. Tong, J. Chem. Phys. **146**, 214903 (2017).
[35] C. W. Gardiner, in *Handbook of Stochastic Methods* (Springer-Verlag, Berlin, Heidelberg, 1985), p. 140.

[36] T. Savin and P. S. Doyle, Biophys. J. **88**, 623 (2005).
[37] S. L. Eichmann, S. G. Anekal, and M. A. Bevan, Langmuir **24**, 714 (2008).
[38] Y. Pawar and J. L. Anderson, Ind. Eng. Chem. Res. **32**, 743 (1993).
[39] J. Happel and H. Brenner, in *Low Reynolds Number Hydrodynamics* (Springer, Netherlands, 1983), p. 286.
[40] S. H. Behrens and D. G. Grier, J. Chem. Phys. **115**, 6716 (2001).
[41] M. Pfeiffer-Laplaud, D. Costa, F. Tielens, M.-P. Gaigeot, and M. Sulpizi, J. Phys. Chem. C **119**, 27354 (2015).
[42] L. Dalstein, E. Potapova, and E. Tyrode, Phys. Chem. Chem. Phys. **19**, 10343 (2017).
[43] D. Cole, G. Young, A. Weigel, A. Sebesta, and P. Kukura, ACS Photon. **4**, 211 (2017).
[44] P. Kukura, M. Celebrano, A. Renn, and V. Sandoghdar, Nano Lett. **9**, 926 (2009).

9

ETe: what could be achieved?

> "To a synthetic chemist, the complex molecules of nature are as beautiful as any of her other creations. The perception of that beauty depends on the understanding of chemical structures and their transformations, and, as with a treasured work of art, deepens as the subject is studied, perhaps even to a level approaching romance."
>
> *Elias James Corey*

We have shown how ETe can be used to measure the effective charge and the size of a molecule in solution. In particular, by following the trajectory of a single molecule, we can measure its charge evolution over time [3].
Given the large dynamic range of the technique, which can measure molecules of q_{eff} spanning 2 orders of magnitude under the same conditions [6], ETe could

be a powerful tool to observe biomolecules conformational changes in real time, at the single-molecule level.

9.1 Detecting Charge Fluctuations

We have simulated a single-molecule ET*e* trajectory of a molecule that fluctuates between two "states" of different effective charge. To simplify the problem, we have assumed that the lifetimes of the states are the same (Figure 9.1).
As a case study, we have considered the same experimental conditions shown in "*Single-molecule electrometry*" [3]. A 60 bases ssDNA fragment ($q_{\text{eff}} \approx -26e$, $r_{\text{H}} = 4.5$ nm), sampling a densely patterned lattice of pockets of $R = 150$ nm and $\lambda \sim 700$ nm and for $\kappa h = 3.8$ will experience a midplane potential of $\sim 0.13 k_{\text{B}}T$, corresponding to a total well-depth of $5k_{\text{B}}T$ and giving the measured average $t_{\text{esc}} \approx 25$ ms. Under these conditions, a modest variation in effective charge (e.g. $\sim 10\%$) produces a large response in t_{esc}, by a factor two. The statistical error, which is the dominant source of noise in a single-molecule measurement as we have verified in Chapter 4.1.2, is in this case $< 10\%$ for a number of hops $N = 5$, so this small amount of events should suffice to resolve the aforementioned difference in effective charge.

The simulated trajectory in Figure 9.1 corresponds to the behaviour of a molecule alternating between two "states", each characterized by a different q_{eff} ($-26e$ and $-29e$) and average escape times of ~ 25 ms and ~ 50 ms respectively, for stretches of approximately 4 seconds at a time. We averaged over a number of hops $N = 5$, 20 and 50, and studied whether we could reconstruct the underlying timescales (Figure 9.1). For large number of events, the individual average escape time measurement, $t_{\text{esc,N}}$ (Fig. 9.1b,c) are well separated in the two cases. The probability density $P(t_{\text{esc,N}})$ also clearly reveals two distinct "populations". As expected, even for $N = 5$, corresponding to a time resolution of $\sim$150 ms (Fig. 9.1a), the average t_{esc} in the two states are clearly distinguishable.

Protein folding kinetics span several order of magnitudes in time [107]. While fast, ro-vibrational transitions usually occur in the picosecond regime [108], large conformational changes, for example due to allosteric regulation [109], can develop over many seconds [110], a regime in which our novel single molecule ET*e* method could easily detect them.

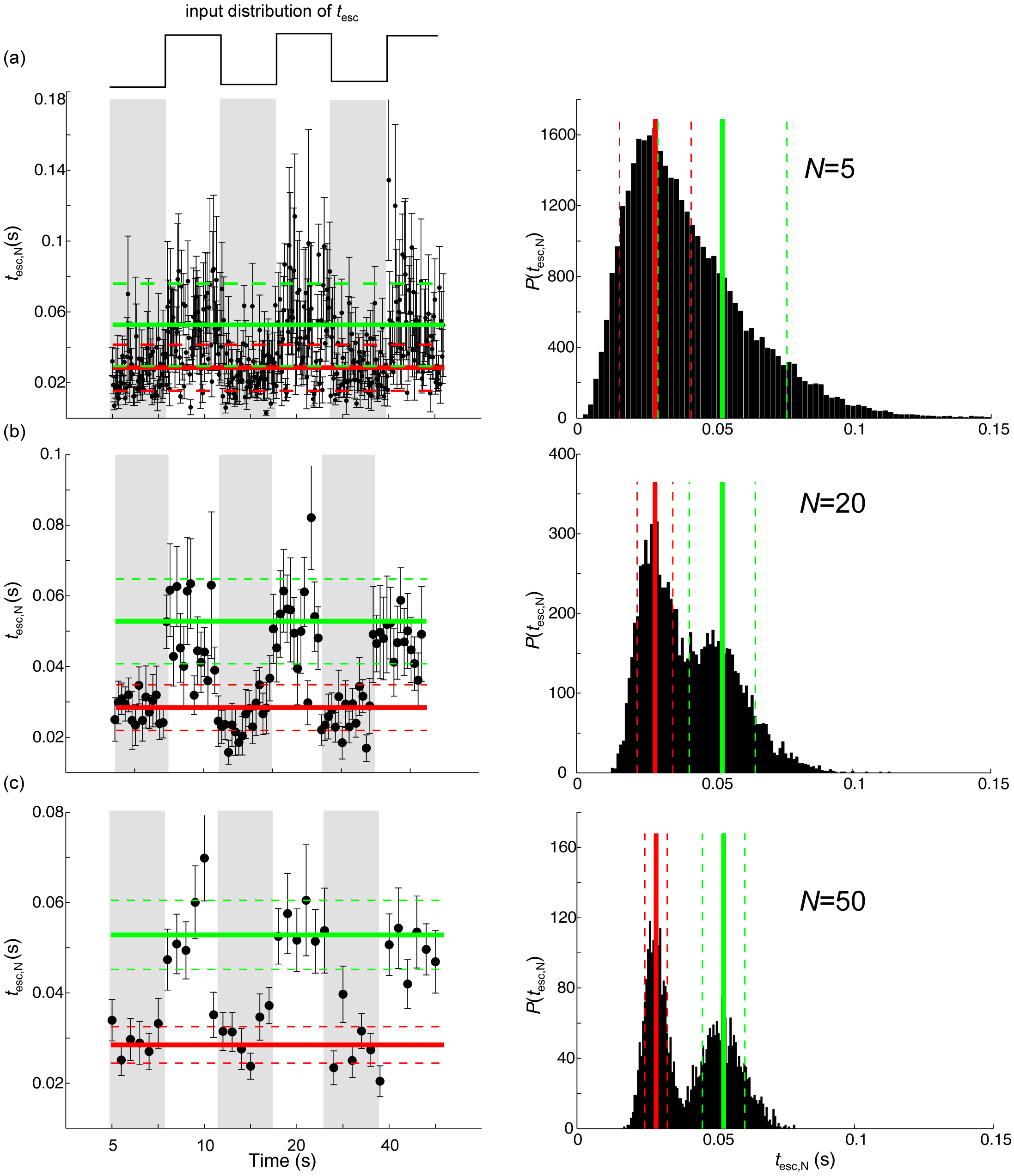

Figure 9.1: Simulated average escape time over N events, $t_{\mathrm{esc,N}}$, of a molecule which fluctuates between two "states" of average t_{esc} = 26ms (solid red line) and 52 ms (solid green line) for 4 seconds at a time. Dashed line indicated the S.D. of $t_{\mathrm{esc,N}}$ during each "state". The right hand plot shows the probability distribution $P(t_{\mathrm{esc,N}})$ over the entire observation time. In the top panel (a), the dynamics is averaged over $N = 5$ events. Panel b, where we have averaged over $N = 20$ events, shows clearly two distinct populations. The bottom panel (c) shows the result for $N = 50$, which corresponds to a time resolution of approximately 1 s.

Not only protein, but also DNA conformational changes are of great interest in biology. The transient formation of DNA and RNA secondary structure is ubiquitous in cellular processes [111] and holds great significance in synthetic biology, e.g. in the context of DNA origami and molecular machines [112].

By carefully tuning the length and sequence, a ssDNA can be designed to arrange into stable secondary structures, which can be implemented for creating DNA motors [113] or nanoscaffolds for drug delivery [114]. DNA hairpins for example can form transiently on a timescale of a few seconds: the length of the hairpin stem, created by the two complementary sections at the extreme of the dna fragment, governs the opening time of the hairpin, while the size of the loop dominates the closing rate [115]. Using the additional information given by an auxiliary FRET signal, achieved by labeling the ends of the DNA fragment with appropriate fluorophores which would give a modulated fluorescence emission depending on their distance [25, 116], ETe could accurately distinguish and characterize the conformations and even measure transition rates.

To conclude, with this thesis we have shown that ETe can measure effective charge and hydrodynamic radius of a single molecule, in real-time. It is fast, precise and accurate, and requires unprecedentedly low amounts of sample (pM concentration). Furthermore, ETe is a versatile technique that can be applied to study many different biomolecules, ranging from big globular proteins (e.g. the enzyme Gusβ, of molecular weight $\sim$ 300 kDa [3]), down to a single dye (1 kDa) [6]. While this technique has already shown the ability of trapping, characterizing and distinguishing a number of macromolecules, we believe it has the potential of being used as a novel tool for structural biology studies, providing new insight on single molecules in solution.

Bibliography

[1] Madhavi Krishnan, Nassiredin Mojarad, Philipp Kukura, and Vahid Sandoghdar. Geometry-induced electrostatic trapping of nanometric objects in a fluid. *Nature*, 467(7316):692–695, 2010.

[2] Nassiredin Mojarad and Madhavi Krishnan. Measuring the size and charge of single nanoscale objects in solution using an electrostatic fluidic trap. *Nature Nanotechnology*, 7(7):448–452, 2012.

[3] Francesca Ruggeri, Franziska Zosel, Natalie Mutter, Mirosława Różycka, Magdalena Wojtas, Andrzej Ożyhar, Benjamin Schuler, and Madhavi Krishnan. Single-molecule electrometry. *Nature Nanotechnology*, 12(5):488–495, 2017.

[4] F. Ruggeri and M. Krishnan. Spectrally resolved single-molecule electrometry. *The Journal of Chemical Physics*, 148(12):123307, 2018.

[5] Francesca Ruggeri and Madhavi Krishnan. Lattice diffusion of a single molecule in solution. *Physical Review E*, 96:062406, 2017.

[6] Francesca Ruggeri and Madhavi Krishnan. Entropic trapping of a singly charged molecule in solution. *Nano Letters*.

[7] Manfred Schliwa and Günther Woehlke. Molecular motors. *Nature*, 422:759, 2003.

[8] Bernard Yurke, Andrew J. Turberfield, Allen P. Mills Jr, Friedrich C. Simmel, and Jennifer L. Neumann. A dna-fuelled molecular machine made of dna. *Nature*, 406:605, 2000.

[9] Henri G. Franquelim, Alena Khmelinskaia, Jean-Philippe Sobczak, Hendrik Dietz, and Petra Schwille. Membrane sculpting by curved dna origami scaffolds. *Nature Communications*, 9(1):811, 2018.

[10] Yu-Shiun Chen, Meng-Yen Hong, and G. Steven Huang. A protein transistor made of an antibody molecule and two gold nanoparticles. *Nature Nanotechnology*, 7:197, 2012.

[11] H Frauenfelder, SG Sligar, and PG Wolynes. The energy landscapes and motions of proteins. *Science*, 254(5038):1598–1603, 1991.

[12] D. E. Koshland. Correlation of structure an function in enzyme action. 142(3599):1533–1541, 1963.

[13] Garrett M. Morris and Marguerita Lim-Wilby. *Molecular Docking*, pages 365–382. Humana Press, Totowa, NJ, 2008.

[14] Irina M. Kuznetsova, Konstantin K. Turoverov, and Vladimir N. Uversky. What macromolecular crowding can do to a protein. *International Journal of Molecular Sciences*, 15(12):23090–23140, 2014.

[15] Irina Gitlin, Jeffrey D. Carbeck, and George M. Whitesides. Why are proteins charged? networks of charge–charge interactions in proteins measured by charge ladders and capillary electrophoresis. *Angewandte Chemie International Edition*, 45(19):3022–3060.

[16] Ganesh H. Iyer, Swagata Dasgupta, and Jeffrey A. Bell. Ionic strength and intermolecular contacts in protein crystals. *Journal of Crystal Growth*, 217(4):429 – 440, 2000.

[17] Susan Miller, Joël Janin, Arthur M. Lesk, and Cyrus Chothia. Interior and surface of monomeric proteins. *Journal of Molecular Biology*, 196(3):641 – 656, 1987.

[18] Michael S. Lawrence, Kevin J. Phillips, and David R. Liu. Supercharging proteins can impart unusual resilience. *Journal of the American Chemical Society*, 129(33):10110–10112, 2007.

[19] M. Krishnan. A simple model for electrical charge in globular macromolecules and linear polyelectrolytes in solution. *The Journal of Chemical Physics*, 146(20):205101, 2017.

[20] H. M. Berman, J. Westbrook, Z. Feng, G. Gilliland, T. N. Bhat, H. Weissig, I. N. Shindyalov, and P. E. Bourne. The protein data bank. *Nucleic Acids Res*, 28(1):235–42, 2000.

[21] Calin Plesa, Stefan W. Kowalczyk, Ruben Zinsmeester, Alexander Y. Grosberg, Yitzhak Rabin, and Cees Dekker. Fast translocation of proteins through solid state nanopores. *Nano Letters*, 13(2):658–663, 2013.

[22] B. Schuler and W. A. Eaton. Protein folding studied by single molecule fret. *Curr Opin Struct Biol*, 18(1):16–26, 2008.

[23] Elza V. Kuzmenkina, Colin D. Heyes, and G. Ulrich Nienhaus. Single-molecule förster resonance energy transfer study of protein dynamics under denaturing conditions. 102(43):15471–15476, 2005.

[24] Sungchul Hohng, Chirlmin Joo, and Taekjip Ha. Single-molecule three-color fret. *Biophysical Journal*, 87(2):1328–1337, 2004.

[25] Roman Tsukanov, Toma E. Tomov, Rula Masoud, Hagai Drory, Noa Plavner, Miran Liber, and Eyal Nir. Detailed study of dna hairpin dynamics using single-molecule fluorescence assisted by dna origami. *The Journal of Physical Chemistry B*, 117(40):11932–11942, 2013.

[26] Barry W. Ninham and V.Adrian Parsegian. Electrostatic potential between surfaces bearing ionizable groups in ionic equilibrium with physiologic saline solution. *Journal of Theoretical Biology*, 31(3):405 – 428, 1971.

[27] Gerald S. Manning. Limiting laws and counterion condensation in polyelectrolyte solutions i. colligative properties. *The Journal of Chemical Physics*, 51(3):924–933, 1969.

[28] R. R. Netz and H. Orland. Variational charge renormalization in charged systems. *The European Physical Journal E*, 11(3):301–311, 2003.

[29] Gerald S. Manning. The molecular theory of polyelectrolyte solutions with applications to the electrostatic properties of polynucleotides. *Quarterly Reviews of Biophysics*, 11(2):179–246, 1978.

[30] Gerald S. Manning. Approximate solutions to some problems in polyelectrolyte theory involving nonuniform charge distributions. *Macromolecules*, 41(16):6217–6227, 2008.

[31] Donald J Winzor. Determination of the net charge (valence) of a protein: a fundamental but elusive parameter. *Analytical Biochemistry*, 325(1):1 – 20, 2004.

[32] Therese W. Herling, Paolo Arosio, Thomas Muller, Sara Linse, and Tuomas P. J. Knowles. A microfluidic platform for quantitative measurements of effective protein charges and single ion binding in solution. *Phys. Chem. Chem. Phys.*, 17:12161–12167, 2015.

[33] Richard W. O'Brien and Lee R. White. Electrophoretic mobility of a spherical colloidal particle. *J. Chem. Soc., Faraday Trans. 2*, 74:1607–1626, 1978.

[34] R. Roy, S. Hohng, and T. Ha. A practical guide to single molecule fret. *Nat Methods*, 5(6):507–16.

[35] Stanley D. Chandradoss, Anna C. Haagsma, Young Kwang Lee, Jae-Ho Hwang, Jwa-Min Nam, and Chirlmin Joo. Surface passivation for single-molecule protein studies. *Journal of Visualized Experiments : JoVE*, (86):50549, 2014.

[36] Laura D. Hughes, Robert J. Rawle, and Steven G. Boxer. Choose your label wisely: Water-soluble fluorophores often interact with lipid bilayers. *PLOS ONE*, 9:1–8, 02 2014.

[37] Allen H. J. Yang, Sean D. Moore, Bradley S. Schmidt, Matthew Klug, Michal Lipson, and David Erickson. Optical manipulation of nanoparticles and biomolecules in sub-wavelength slot waveguides. *Nature*, 457:71, 2009.

[38] A. N. Grigorenko, N. W. Roberts, M. R. Dickinson, and Y. Zhang. Nanometric optical tweezers based on nanostructured substrates. *Nature Photonics*, 2:365, 2008.

[39] Quan Wang, Randall H. Goldsmith, Yan Jiang, Samuel D. Bockenhauer, and W. E. Moerner. Probing single biomolecules in solution using the anti-brownian electrokinetic (abel) trap. *Accounts of Chemical Research*, 45(11):1955–1964, 2012.

[40] Alexander P. Fields and Adam E. Cohen. Electrokinetic trapping at the one nanometer limit. *Proceedings of the National Academy of Sciences*, 108(22):8937–8942, 2011.

[41] Melikhan Tanyeri, Eric M. Johnson-Chavarria, and Charles M. Schroeder. Hydrodynamic trap for single particles and cells. *Applied Physics Letters*, 96(22):224101, 2010.

[42] Marco Braun, Andreas P. Bregulla, Katrin Günther, Michael Mertig, and Frank Cichos. Single molecules trapped by dynamic inhomogeneous temperature fields. *Nano Letters*, 15(8):5499–5505, 2015.

[43] Paolo Cadinu, Binoy Paulose Nadappuram, Dominic J. Lee, Jasmine Y. Y. Sze, Giulia Campolo, Yanjun Zhang, Andrew Shevchuk, Sylvain Ladame, Tim Albrecht, Yuri Korchev, Aleksandar P. Ivanov, and Joshua B. Edel. Single molecule trapping and sensing using dual nanopores separated by a zeptoliter nanobridge. *Nano Letters*, 17(10):6376–6384, 2017.

[44] Xu Liu, Mirna Mihovilovic Skanata, and Derek Stein. Entropic cages for trapping dna near a nanopore. *Nature Communications*, 6:6222, 2015.

[45] Yuanjie Pang and Reuven Gordon. Optical trapping of 12 nm dielectric spheres using double-nanoholes in a gold film. *Nano Letters*, 11(9):3763–3767, 2011.

[46] A. Ashkin, J. M. Dziedzic, J. E. Bjorkholm, and Steven Chu. Observation of a single-beam gradient force optical trap for dielectric particles. *Optics Letters*, 11(5):288–290, May 1986.

[47] Yuanjie Pang and Reuven Gordon. Optical trapping of a single protein. *Nano Letters*, 12(1):402–406, 2012.

[48] Jacob N. Israelachvili. *Intermolecular and surface forces*. Academic Press, London, 1992.

[49] S. Fringes, F. Holzner, and A. W. Knoll. The nanofluidic confinement apparatus: studying confinement-dependent nanoparticle behavior and diffusion. *Beilstein J Nanotechnol*, 9:301–10, 2018.

[50] Single positively charged particle trapping in nanofluidic systems. *Microelectronic Engineering*, 175:43 – 49, 2017.

[51] Madhavi Krishnan. Electrostatic free energy for a confined nanoscale object in a fluid. *The Journal of Chemical Physics*, 138(11):114906, 2013.

[52] Sven H. Behrens and David G. Grier. The charge of glass and silica surfaces. *The Journal of Chemical Physics*, 115(14):6716–6721, 2001.

[53] F. H. van der Heyden, D. Stein, and C. Dekker. Streaming currents in a single nanofluidic channel. *Phys Rev Lett*, 95(11):116104.

[54] Carlos Macias-Romero, Igor Nahalka, Halil I. Okur, and Sylvie Roke. Optical imaging of surface chemistry and dynamics in confinement. *Science*, 2017.

[55] David J. Belton, Olivier Deschaume, and Carole C. Perry. An overview of the fundamentals of the chemistry of silica with relevance to biosilicification and technological advances. *The Febs Journal*, 279(10):1710–1720, 2012.

[56] Jau Tang and R. A. Marcus. Mechanisms of fluorescence blinking in semiconductor nanocrystal quantum dots. *The Journal of Chemical Physics*, 123(5):054704, 2005.

[57] H.A. Kramers. Brownian motion in a field of force and the diffusion model of chemical reactions. *Physica*, 7(4):284 – 304, 1940.

[58] Pan Mao and Jongyoon Han. Fabrication and characterization of 20 nm planar nanofluidic channels by glass-glass and glass-silicon bonding. *Lab Chip*, 5:837–844, 2005.

[59] W. Ouyang and W. Wang. Fabrication and characterization of sub 100/10nm planar nanofluidic channels by triple thermal oxidation and silicon-glass anodic bonding. *Biomicrofluidics*, 8(5).

[60] Wen-Pin Shih, Chung-Yuen Hui, and Norman C. Tien. Collapse of microchannels during anodic bonding: Theory and experiments. *Journal of Applied Physics*, 95(5):2800–2808, 2004.

[61] A. G. Nagy. Sidewall tapering in reactive ion etching. *J. Electrochem. Soc.*, 132(3).

[62] Robert J. Hoekstra, Mark J. Kushner, Valeriy Sukharev, and Phillipe Schoenborn. Microtrenching resulting from specular reflection during chlorine etching of silicon. *Journal of Vacuum Science & Technology B: Microelectronics and Nanometer Structures Processing, Measurement, and Phenomena*, 16(4):2102–2104, 1998.

[63] Michał Bogdan and Thierry Savin. Errors in energy landscapes measured with particle tracking. *arXiv:1708.01217v1.*

[64] Motoyoshi Kobayashi, Frédéric Juillerat, Paolo Galletto, Paul Bowen, and Michal Borkovec. Aggregation and charging of colloidal silica particles: effect of particle size. *Langmuir*, 21(13):5761–5769, 2005.

[65] G. Kokot, M. I. Bespalova, and M. Krishnan. Measured electrical charge of sio2 in polar and nonpolar media. *The Journal of Chemical Physics*, 145(19):194701, 2016.

[66] Derek Stein, Maarten Kruithof, and Cees Dekker. Surface-charge-governed ion transport in nanofluidic channels. *Phys. Rev. Lett.*, 93:035901, Jul 2004.

[67] Qiaosheng Pu, Jongsin Yun, Henryk Temkin, and Shaorong Liu. Ion-enrichment and ion-depletion effect of nanochannel structures. *Nano Letters*, 4(6):1099–1103, 2004.

[68] Dongmei Li, Shilin Fu, and Charles A. Lucy. Prediction of electrophoretic mobilities. 3. effect of ionic strength in capillary zone electrophoresis. *Analytical Chemistry*, 71(3):687–699, 1999.

[69] Russell E. Thompson, Daniel R. Larson, and Watt W. Webb. Precise nanometer localization analysis for individual fluorescent probes. *Biophysical Journal*, 82(5):2775–2783.

[70] K. Gast, H. Damaschun, K. Eckert, K. Schulzeforster, H. R. Maurer, M. Mullerfrohne, D. Zirwer, J. Czarnecki, and G. Damaschun. Prothymosin-alpha - a biologically-active protein with random coil conformation. *Biochemistry*, 34(40):13211–13218, 1995.

[71] Sonja Müller-Späth, Andrea Soranno, Verena Hirschfeld, Hagen Hofmann, Stefan Rüegger, Luc Reymond, Daniel Nettels, and Benjamin Schuler. Charge interactions can dominate the dimensions of intrinsically disordered proteins. 107(33):14609–14614, 2010.

[72] Mirosława Różycka, Magdalena Wojtas, Michał Jakób, Christian Stigloher, Mikołaj Grzeszkowiak, Maciej Mazur, and Andrzej Ożyhar. Intrinsically disordered and pliable starmaker-like protein from medaka (oryzias latipes) controls the formation of calcium carbonate crystals. *PLOS ONE*, 9(12):1–36, 12 2014.

[73] C. B. Müller, A. Loman, V. Pacheco, F. Koberling, D. Willbold, W. Richtering, and J. Enderlein. Precise measurement of diffusion by multi-color dual-focus fluorescence correlation spectroscopy. *EPL (Europhysics Letters)*, 83(4):46001, 2008.

[74] Peter J Bosch, Ivan R Corrêa, Michael H Sonntag, Jenny Ibach, Luc Brunsveld, Johannes S Kanger, and Vinod Subramaniam. Evaluation of fluorophores to label snap-tag fused proteins for multicolor single-molecule tracking microscopy in live cells. *Biophysical Journal*, 107(4):803–814, 2014.

[75] D. Sage, F. R. Neumann, F. Hediger, S. M. Gasser, and M. Unser. Automatic tracking of individual fluorescence particles: application to the study of chromosome dynamics. *IEEE Transactions on Image Processing*, 14(9):1372–1383, 2005.

[76] B. U. Felderhof. Escape by diffusion from a parabolic well across a parabolic barrier. *Physica a-Statistical Mechanics and Its Applications*, 387(8-9):1767–1785, 2008.

[77] B. U. Felderhof. Escape by diffusion from a square well across a square barrier. *Physica a-Statistical Mechanics and Its Applications*, 387(1):39–56, 2008.

[78] Wiebke Arlt, Elizabeth A Walker, Nicole Draper, Hannah E Ivison, Jon P Ride, Fabian Hammer, Susan M Chalder, Maria Borucka-Mankiewicz, Berthold P Hauffa, Ewa M Malunowicz, Paul M Stewart, and Cedric HL Shackleton. Congenital adrenal hyperplasia caused by mutant p450 oxidoreductase and human androgen synthesis: analytical study. *The Lancet*, 363(9427):2128 – 2135, 2004.

[79] Nancy C. Stellwagen. Electrophoresis of dna in agarose gels, polyacrylamide gels and in free solution. *Electrophoresis*, 30:S188–S195.

[80] Stephen D. Pickett and Michael J.E. Sternberg. Empirical scale of side-chain conformational entropy in protein folding. *Journal of Molecular Biology*, 231(3):825 – 839, 1993.

[81] Kendra King Frederick, Michael S. Marlow, Kathleen G. Valentine, and A. Joshua Wand. Conformational entropy in molecular recognition by proteins. *Nature*, 448:325, 2007.

[82] Mirjam E. Leunissen, Remi Dreyfus, Roujie Sha, Nadrian C. Seeman, and Paul M. Chaikin. Quantitative study of the association thermodynamics and kinetics of dna-coated particles for different functionalization schemes. *Journal of the American Chemical Society*, 132(6):1903–1913, 2010.

[83] R. Zhang, B. Lee, C. M. Stafford, J. F. Douglas, A. V. Dobrynin, M. R. Bockstaller, and A. Karim. Entropy-driven segregation of polymer-grafted nanoparticles under confinement. *Proc Natl Acad Sci U S A*, 114(10):2462–2467.

[84] Dan Bracha, Eyal Karzbrun, Gabriel Shemer, Philip A. Pincus, and Roy H. Bar-Ziv. Entropy-driven collective interactions in dna brushes on a biochip. *Proceedings of the National Academy of Sciences*, 110(12):4534–4538, 2013.

[85] Lars Onsager. The effects of shape on the interaction of colloidal particles. *Annals of the New York Academy of Sciences*, 51(4):627–659.

[86] A. D. Dinsmore, A. G. Yodh, and D. J. Pine. Entropic control of particle motion using passive surface microstructures. *Nature*, 383:239, 1996.

[87] K. Ohsaka and E. H. Trinh. Estimation of the configurational entropy of fusion. *Applied Physics Letters*, 66(23):3123–3125, 1995.

[88] Gerold Adam and Julian H. Gibbs. On the temperature dependence of cooperative relaxation properties in glass-forming liquids. *The Journal of Chemical Physics*, 43(1):139–146, 1965.

[89] L. Elson E . Fluorescence correlation spectroscopy: Past, present, future. *Biophys J*, 101(12):2855–70.

[90] Christoph G. Baumann, Steven B. Smith, Victor A. Bloomfield, and Carlos Bustamante. Ionic effects on the elasticity of single dna molecules. *Proceedings of the National Academy of Sciences*, 94(12):6185–6190, 1997.

[91] Maria M. Tirado and José García de la Torre. Translational friction coefficients of rigid, symmetric top macromolecules. application to circular cylinders. *The Journal of Chemical Physics*, 71(6):2581–2587, 1979.

[92] M. Murphy, I. Rasnik, W. Cheng, T. M. Lohman, and T. Ha. Probing single-stranded dna conformational flexibility using fluorescence spectroscopy. *Biophys J*, 86(4):2530–7.

[93] Sören Doose, Hannes Barsch, and Markus Sauer. Polymer properties of polythymine as revealed by translational diffusion. *Biophysical Journal*, 93(4):1224 – 1234, 2007.

[94] Earle Stellwagen, Lu, and Nancy C. Stellwagen. Unified description of electrophoresis and diffusion for dna and other polyions. *Biochemistry*, 42(40):11745–11750, 2003.

[95] Thierry Savin and Patrick S. Doyle. Static and dynamic errors in particle tracking microrheology. *Biophysical Journal*, 88(1):623 – 638, 2005.

[96] X. Michalet. Mean square displacement analysis of single-particle trajectories with localization error: Brownian motion in isotropic medium. *Phys Rev E Stat Nonlin Soft Matter Phys*, 82(4 Pt 1):041914.

[97] S. K. Zareh, M. C. DeSantis, J. M. Kessler, J. L. Li, and Y. M. Wang. Single-image diffusion coefficient measurements of proteins in free solution. *Biophys J*, 102(7):1685–91, 2012.

[98] Michael J. Skaug, Anna M. Lacasta, Laureano Ramirez-Piscina, Jose M. Sancho, Katja Lindenberg, and Daniel K. Schwartz. Single-molecule diffusion in a periodic potential at a solid-liquid interface. *Soft Matter*, 10:753–759, 2014.

[99] Michael J. Skaug, Roland Faller, and Marjorie L. Longo. Correlating anomalous diffusion with lipid bilayer membrane structure using single molecule tracking and atomic force microscopy. *The Journal of Chemical Physics*, 134(21):215101, 2011.

[100] J. Schuster, F. Cichos, and C. von Borczyskowski. Diffusion measurements by single-molecule spot-size analysis. *The Journal of Physical Chemistry A*, 106(22):5403–5406, 2002.

[101] Gerald S. Manning. Counterion condensation on charged spheres, cylinders, and planes. *The Journal of Physical Chemistry B*, 111(29):8554–8559, 2007.

[102] Shannon L. Eichmann, Samartha G. Anekal, and Michael A. Bevan. Electrostatically confined nanoparticle interactions and dynamics. *Langmuir*, 24(3):714–721, 2008.

[103] S. Lifson and J. L. Jackson. On self-diffusion of ions in a polyelectrolyte solution. *The Journal of Chemical Physics*, 36(9), 1962.

[104] R. Festa and E.Galleani d'Agliano. Diffusion coefficient for a brownian particle in a periodic field of force: I. large friction limit. *Physica A: Statistical Mechanics and its Applications*, 90(2):229 – 244, 1978.

[105] D. L. Weaver. Effective diffusion-coefficient of a brownian particle in a periodic potential. *Physica A*, 98(1-2):359–362, 1979.

[106] Ali Naji and Frank L. H. Brown. Diffusion on ruffled membrane surfaces. *The Journal of Chemical Physics*, 126(23):235103, 2007.

[107] Athi N. Naganathan and Victor Muñoz. Scaling of folding times with protein size. *Journal of the American Chemical Society*, 127(2):480–481, 2005.

[108] Christoph Kolano, Jan Helbing, Mariusz Kozinski, Wolfram Sander, and Peter Hamm. Watching hydrogen-bond dynamics in a β-turn by transient two-dimensional infrared spectroscopy. *Nature*, 444:469, 2006.

[109] The changing landscape of protein allostery. *Current Opinion in Structural Biology*, 16(1):102 – 108, 2006.

[110] Bosco K. Ho and David A. Agard. Probing the flexibility of large conformational changes in protein structures through local perturbations. *PLOS Computational Biology*, 5, 04 2009.

[111] D. Bikard, C. Loot, Z. Baharoglu, and D. Mazel. Folded dna in action: Hairpin formation and biological functions in prokaryotes. *Microbiol Mol Biol Rev*, 74(4):570–88, 2010.

[112] Thomas Gerling, Klaus F. Wagenbauer, Andrea M. Neuner, and Hendrik Dietz. Dynamic dna devices and assemblies formed by shape-complementary, non–base pairing 3d components. *Science*, 347(6229):1446–1452, 2015.

[113] Simon J. Green, Daniel Lubrich, and Andrew J. Turberfield. Dna hairpins: Fuel for autonomous dna devices. *Biophysical Journal*, 91(8):2966 – 2975, 2006.

[114] Yashodhara Pawar and John L. Anderson. Hindered diffusion in slit pores: an analytical result. *Industrial & Engineering Chemistry Research*, 32(4):743–746, 1993.

[115] Grégoire Bonnet, Oleg Krichevsky, and Albert Libchaber. Kinetics of conformational fluctuations in dna hairpin-loops. *Proceedings of the National Academy of Sciences*, 95(15):8602–8606, 1998.

[116] Roman Tsukanov, Toma E. Tomov, Yaron Berger, Miran Liber, and Eyal Nir. Conformational dynamics of dna hairpins at millisecond resolution obtained from analysis of single-molecule fret histograms. *The Journal of Physical Chemistry B*, 117(50):16105–16109, 2013.

10

Appendix

Resist spinning recipes:

- Resist AZ1505
    1. Spin positive Resist AZ1505 at 6000rpm for 45s (6s ramp).
    2. Bake for 60s.
    3. DUV Exposure: Wavelength = 220nm, Power = 20mW/cm^2, Exposure time = 1.7s.
    4. Develop with AZ ® 726 MIF (Microchemicals) for 60s.
- Resist AZ2020
    1. Spin negative Resist AZ2020 at 3000rpm for 45s (3s ramp).
    2. Bake for 60s.
    3. DUV Exposure: Wavelength = 365nm, Power = 16mW/cm^2, Exposure time = 0.5s.
    4. Bake for 60s.
    5. Develop with AZ ® 826 MIF (Microchemicals) for 60s.
- Resist PMMA
    1. Spin negative Resist PMMA (1:1 in EL) at 2000rpm for 45s (2s ramp).

2. Bake for 10min.
3. E-beam exposure (double the dose when using pure PMMA)
4. Develop with MIBK:IPA(30:70).

Materials Used:

- Si/SiO2 wafer (Si-Mat)
  Diameter: 100mm
  Type/Dopant: P/Bor
  Orientation $< 100 > +/-0.5$
  Resistivity: 10-20 ohmcm
  Thickness: 525+/-25µm
  TTV: <5µm
  Particle: < 10 @0.3µm

- Glass for anodic bonding BOROFLOAT® 33 Borosilicate Glass (Plan Optik AG)

11

List of Symbols and Abbreviations

> “Brevity is the soul of wit”
>
> *William Shakespeare*

ABEL trap	Anti-Brownian Electrokinetic Trap
α_r	Regulation Factor
β	Ratio of Depth in the Slit, $2h$ over the Depth in the Pocket, $2h + d$
c	Salt Concentration
d	Pocket Depth
D	Molecule Diffusion Coefficient
e	Electrical Charge
ϵ	Dielectric Constant
η	Viscosity
E-beam	Electron Beam Lithography
EMCCD	Electron Multiplying CCD Camera
ETe	Escape-Time Electrometry
Γ	Silica Surface Chargeable Groups Density
FRET	Förster Resonant Energy Transfer
f	Fluctuations Contribution to the Well Depth
κ^{-1}	Debye Length
$l_{\mathrm{B,m}}$	Bjerrum Length in the Medium
l_{c}	Contour Length
l_{diff}	Diffusion Length
λ	Lattice Pitch
MSD	Mean Squared Displacement
μ_i	Ion Mobility
n	Number Density
N	Number of Escape Events
N_{A}	Avogadro's Number
PAGE	Polyacrylamide Gel Electrophoresis
pK	Negative Logarithm of the Dissociation Constant
PSF	Point Spread Function
q_{c}	Calculated Effective Charge
q_{eff}	Effective Charge
q_{m}	Experimentally Measured Effective Charge
q_{str}	Structural Charge
R	Pocket Radius
RIE	Reactive Ion Etching
ROI	Region Of Interest
r_{abs}	Absorbing Boundary Conditions
r_{esc}	Escape Boundary
r_{H}	Hydrodynamic Radius
S.D.	Standard Deviation
SEM	Scanning Electron Microscopy
s.e.m.	Standard Error of the Mean
SNR	Signal-to-Noise Ratio

σ	Charge Density of Silica
t_{esc}	Escape Time
t_{r}	Position Relaxation Time
W	Well Depth
w_{c}	Channel Width
ψ_{m}	Midplane Potential
ψ_{s}	Effective Surface Potential
z	Valence
$2h$	Slit Height
$2h_s$	Slit Height in the Step Region of the Device
2fFCS	Two-focus Fluorescence Correlation Spectroscopy

12

Acknowledgements

I would like to thank my supervisor, Prof. Madhavi Krishnan, for giving me the opportunity to work on such an interesting project. Her mentorship has shaped me as a researcher and as a person, and I will be forever grateful to her for this. I take this opportunity to thank the members of my committee, Prof. Peter Hamm and Prof. Ben Schuler, as well as Prof. Susan Perkin, who kindly agreed to evaluate my thesis as external referee. My work at the University of Zurich has furthermore greatly benefited from the support of a number of colleagues. I would like to particularly mention Prof. David Tilley, Thomas Moehl, Richard Börner and Jan Helbing for many fruitful discussions.

The Department of Chemistry is full of talented people that have contributed to this work, and to make my life easier, in many ways. Thanks to Sabine, Maja, Chantal, Fabienne, Connie, Petra, Larissa and Nathalie from HR, who basically know how to fix any problem. Thanks to Sascha and Mirko: they always had intelligent answers to my very stupid IT questions. I'm particularly grateful to Roland, from the Mechanical Workshop, because anytime I asked him to build something, he always said it was a terrible idea and came up with a far better solution in the blink of an eye. Thanks to the members of FIRST team at ETH, particularly Yargo, Sandro, Tobias and Petra. My time working in the cleanroom was always enjoyable thanks to you guys.

Over the years I had the pleasure of sharing the office and the lab with many

great researchers: Ali, Sven, Lei, Oleg and Gasper (Dr. Postdoc), Sushanta and Maria. Every single one of you has contributed to this thesis with guidance, support or great conversations, scientific and non-scientific. Thanks to Claudio and Olga, you guys are both very loud – and also very fun. A special thanks to Franzi, who has been the best collaborator and biochemistry teacher I could ask for, as well as a true friend. And, by the way, thanks for translating my abstract to German, you are a life-saver.

In my first 3 years in this city, I have had two homes – one officially in Zurichbergstrasse and one, by "adoption", in Tobelhof. I was lucky to share a flat and endless evenings of laughter with Viktor, Apostolis, Fabio, Stephan, Laura and Franzi. A shout-out to The Brunch Club, which is not as active as we would like, but I'm sure we will do better. A special thanks to Aimilia, who is my greek sister at heart. Thanks to Ella and Moh, especially for showing me sword dancing.
Thanks to Mauro and Gabriele, who are my oldest friends. I'm grateful to have been able to share my PhD stories with two of the most clever people I have ever met, even if with some time-zones in between. Our Whatsapp chats have been a real comfort to me. Vale, my BFF: we have both have had our tough times during the past five years, for different reasons. We have grown together and I hope we will continue to do so.

Thanks to my Mum and Dad. They taught me how to be curious and strong and they are simply the coolest parents. Thanks for being supportive all the way – even though, when neighbours or relatives asked them what I was doing for a living, to this day they have been saying I was working as an Aerospace Engineer, because it definitely sounded better.

Finally, thanks to Chris, for being my partner – in more ways than one. Against all odds, we have managed to share our work and our private life, and I wouldn't change a thing. Your endless kindness inspires to be a better person.

CURRICULUM VITAE

NAME: RUGGERI

FIRST NAME: Francesca

DATE OF BIRTH: 29/04/1988

NATIONALITY: Italian

EDUCATION

2012 – 2018 **PhD Candidate, Department of Chemistry**
University of Zürich, Supervisor: Prof. Madhavi Krishnan

2010 – 2012 **MSc Nanotechnology Engineering**
Sapienza Università di Roma, Italy
University of Copenhagen, Denmark

Thesis title: Protein mediated interactions between nanocarriers and giant unilamellar vesicles
Supervisor: Prof. Maritè Cardenas, Prof. Allegra Via

2007 – 2010 **BSc Aerospace Engineering**
Sapienza Università di Roma, Italy

2002 – 2007 **Maturità classica**
Liceo Lucio Anneo Seneca, Rome, Italy